THE BELL SYSTEM TECHNICAL JOURNAL

DEVOTED TO THE SCIENTIFIC AND ENGINEERING
ASPECTS OF ELECTRICAL COMMUNICATION

Volume 55 October 1976 Number 8

Basic Fluid-Dynamic Considerations in the Drawing of Optical Fibers

By F. T. GEYLING

(Manuscript received January 9, 1976)

The optical fiber drawing process is considered in its totality—from source to forming zone to draw-down region and take-up end—as a problem in fluid dynamics. Fiber drawing of most glasses is dominated by viscous stresses, surface tension effects, and quenching rates. This contrasts with the drawing of textile fibers, where other fluid properties and non-Newtonian effects can play important roles. Preliminary time-invariant "base flow" models are developed for glass drawing, using the one-dimensional, small-slope approximation of extensional flow. First-order sensitivities of these base flows to changes in operating conditions are examined via a stability analysis. Two important instability mechanisms, denoted as the tensile and capillary modes of dynamic fiber response, are discussed. Several follow-on objectives arising from this study are described.

I. INTRODUCTION

Stringent tolerances set on optical fibers used in communication systems have generated a need for understanding the fluid dynamics of the fiber drawing process. The responses of this process to various disturbances, especially those resulting in perturbations of the fiber diameter, are of interest.

For steady-state drawing, one seeks analytic models that interrelate the draw-down ratio, draw force, flow rate, and some characteristic temperature. Such models serve two purposes: they predict the effects of changes in the operating parameters and can therefore be used in the control of industrial drawing processes; they also provide a "base state" for the theoretical study of dynamic responses. Such responses could be due to a variety of physical disturbances; for example, mechanical vibrations, thermal transients, ambient gas flow, and even acoustic noise. All of these disturbances may produce variations in the diameter of the finished fiber.

In studying the perturbations of liquid fibers, our philosophy departs somewhat from the more traditional one of stability analysis in textile engineering. Textile fiber studies, in general, strive to avoid fiber rupture and gross distortions of the thread line. (See, for example, Refs. 1 through 9.) In cases where continuous drawing of textile fibers is impossible, much emphasis is placed on the prediction and control of thread length, i.e., the filament lengths attainable between spontaneous ruptures.

The drawing of optical fibers takes filament continuity for granted. However, the ultimate optical application is sensitive to small diametral perturbations, far from rupture. Moreover, optical fibers are usually drawn at higher viscosities and draw forces than textile fibers. Starting from a much higher melt temperature, the subsequent viscosity increase due to quenching of the glass is much more severe than in polymers. Also, in its molten state glass is more nearly Newtonian than most polymers.

Our purpose, then, is to model the mechanisms by which perturbations arise in the glass-drawing process and are frozen into the finished fibers. Based on this understanding, we hope to control fiber dimensions within the tolerances imposed by optical considerations (e.g. Ref. 10).

The fluid dynamics of fiber forming involve a source flow, also referred to as the forming zone, and a draw-down region. The forming zone is usually characterized by a rapidly contracting flow issuing from the bottom of a preform, or pulled from an orifice at the bottom of a crucible (Fig. 1a). In drawing from preforms, we may distinguish between a very sharply contracting configuration (Fig. 1b), commonly encountered with laser heating, and a more gradual contraction that results from furnace heating (Fig. 1c). We include in Fig. 1d the case of an overheated preform, where the forming zone consists essentially of a liquid drop from which the filament is drawn. The different forming-zone configurations shown in Fig. 1 can imply fundamental differences in the flow field, as far as the steady-state and potential instabilities are concerned. For example, there is some evidence[11] to suggest that the overheated preform, Fig. 1d, is capable of self-sustained oscillations at critical draw speeds, whereas, at noncritical speeds, the liquid reservoir in the pendant drop tends to absorb perturbations coming from the take-up end.

The forming zone makes a continuous transition to the draw-down

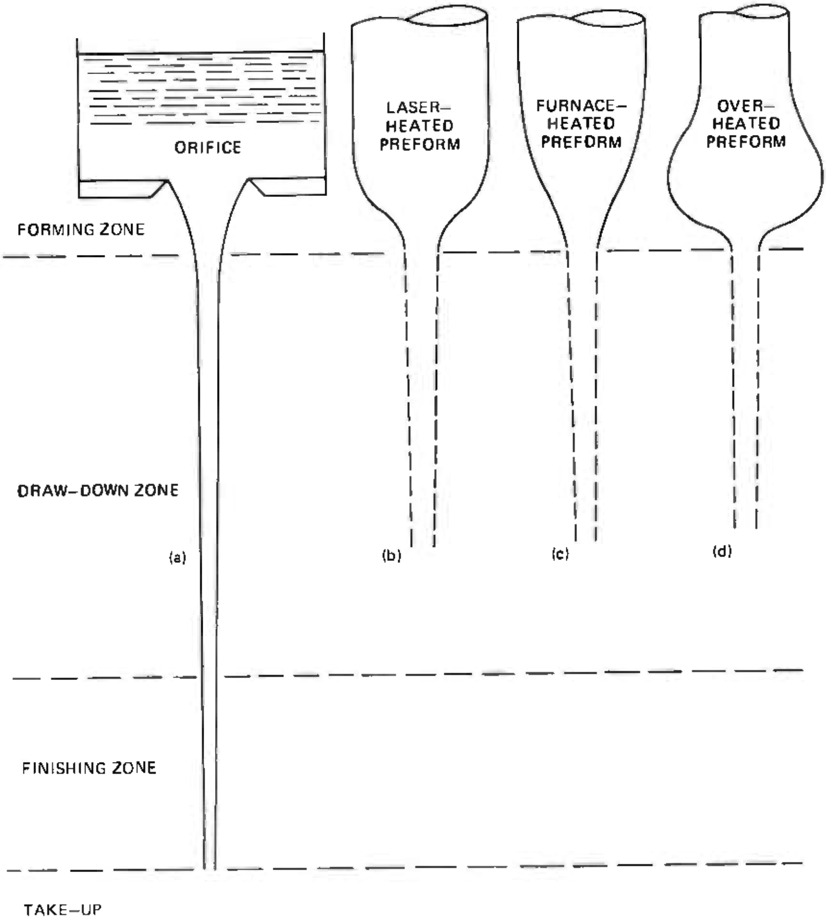

Fig. 1—Fiber-drawing methods.

region, where an essential part of the fiber contraction occurs. Typical draw-down ratios, defined as terminal velocity/source velocity, in this region run between 10 and 100. Most fiber stability studies place major emphasis on the draw-down region, because of its physical importance and mathematical tractability. However, the role of incipient perturbations in the forming zone cannot be ignored. The essential need for modeling this part of the flow field, if only by numerical simulations, is obvious. For completeness, we also recognize that a very small amount of fiber deformation occurs beyond the draw-down region; but this falls within the visco-elastic rather than the fluid-dynamic regime.

Much of the empirical evidence in textile and glass-fiber drawing[1] suggests that fluid dynamics in the draw-down region is governed by the so-called Trouton viscosity, a measure of the ability of fluid filaments to sustain tensile stress as a function of elongational strain rate. Indeed, if fiber breakage occurs in the draw-down region, it exhibits the neck-down and cohesive separation reminiscent of tensile test specimens. Much of the early modeling by Ziabicki[12,13] and subsequent efforts by Pearson,[5,14] Kasé,[6,7] and others are based on this notion, and for this reason we refer to these analyses as "tensile" models.

In parallel, and possibly quite independent of the tensile mechanism, local flow conditions may exist where surface-tension-driven phenomena play a significant role. Such "capillary" responses could occur at the hot tip of the forming zone, where the viscosity is still quite low and the filament begins to take shape. Capillary models of filament response go back to Rayleigh's classical work,[15,16] with subsequent extensions and experimental corroboration by, for example, Taylor,[9] Tomotika,[17,18] and Weber.[19]

The present paper serves several purposes: (*i*) it generates preliminary base-flow models for the draw-down region, using the one-dimensional, small-slope approximation of elongational flow; (*ii*) it makes a preliminary assessment of sensitivities, through differences in base flow, to changes in operating conditions, such as take-up speed and quenching profile; (*iii*) it presents the tensile and capillary models of dynamic fiber response as fundamentally distinct mechanisms; it explores their applicability to different parts of the draw process by suitable modifications and extensions of existing theories; (*iv*) it projects several follow-on efforts aimed at unified models of the steady and perturbed drawing process, viz. more realistic base-flow models, including heat transfer and two-dimensionality at the start of the draw-down region, and transient-response models, which account for these refinements in the base flow together with possible interactions between capillary and tensile mechanisms.

II. REVIEW OF EARLIER WORK

In this section, we discuss some of the literature on tensile and capillary stability analyses of liquid filaments. Table I relates several key publications and identifies their underlying assumptions and physical models.

The first comprehensive study of tensile fiber models was undertaken by Ziabicki et al.[1–4,12,13,20] Motivated by the textile engineers' interest in potential instabilities and fracture mechanisms, the authors reviewed existing phenomenological evidence on filament "spinning."[*] They

---

[*] This traditional terminology, which suggests twisting a fibrous material into strands, will be avoided henceforth as inappropriate to the drawing of liquid filaments.

Table 1 — Overview of tensile and capillary fiber models

Tensile models, physical features discussed.	Viscosity = 3 μ, inertia, surface tension, quenching, finite draw-down.	Viscosity = 3 μ, stability analyses.	Viscosity = 3 μ, stability experiments.
Pertinent literature	Refs. 1–4, 12, 13, 20: analysis and experimental corroboration of relevant physical factors in base state and some dynamic perturbations.	Refs. 5, 14: dynamic analysis of attenuating fibers, including the effects of viscosity perturbations and different base states.	Refs. 6, 7, 21, 22, 25: experiments corroborating cyclic and transient responses of tensile fiber models.
Capillary models, physical features investigated.	Newtonian viscosity and surface tension.	Inertia and surface tension.	Newtonian viscosity, inertia, and surface tension.
Pertinent literature	Ref. 16: cylindrical filaments neglecting inertia. Refs. 17, 18: adaptation to contracting flows and quenching effects.	Refs. 16, 19: theory of inviscid capillary fluid cylinders.	Refs. 16, 17, 18, 19: complete theories of capillary jets. Modification for quenching effects given here.
	Note: Numerous authors have conducted experiments over the years to demonstrate instabilities of capillary jets and filaments under isothermal, i.e., constant viscosity, conditions.		

also cite experimental evidence that when a filament is formed, say in the wake of a free-falling viscous drop, either a tensile ("cohesive") fracture or capillary separation may sever the flow.

In Ref. 12, a suitable tensile theory is developed for the prediction of finite filament lengths, assuming the cross-sectional distribution of longitudinal velocities to be uniform and the steady-state flow to contract with small slope. Reference 20 accomplishes the same for capillary effects by an adaptation of Rayleigh's classical theory (as we have done independently for our own purposes). Ziabicki's subsequent publications include a thorough evaluation of experimental results, corroborating his predictions of filament lengths.*

Ziabicki's comprehensive effort was followed by a series of papers by Pearson and others, aimed predominantly at tensile stability models. Starting from the simplest possible representation[14]—an isothermal filament under constant viscous tension—progressively more elaborate results were achieved by adding fiber quenching, inertia, surface tension, and gravity. A physical interpretation of this work, however, is difficult since the explicit features of diametral perturbation profiles along the fiber, their time dependence, and their sensitivity to properties of the base state seem poorly understood. We will return to this in Section VII. Ziabicki's tensile flow models and the draw-resonances

---

* Like other Western readers, the author has been somewhat late in fully recognizing the significance of Ziabicki's work, much of which was initially recorded in Polish journals. Note, however, Ref. 4 for a more recent, comprehensive account.

predicted by Pearson et al. were corroborated by several experimenters. We cite the work of Kasé[21,22] and Donnelly and Weinberger[25] as examples in this area.

As mentioned earlier, the study of surface-tension-driven perturbations contributes another, as yet separate, view of fiber stability which goes back to Rayleigh's classical work as presented in Refs. 15 and 16. Rayleigh himself studied several simplified cases: (*i*) constant viscosity plus surface tension (no inertia), (*ii*) inertia plus surface tension (no viscosity), and (*iii*) constant viscosity plus inertia plus surface tension. Each analysis yields an exact solution of the hydrodynamic perturbation equations for an incompressible liquid contained by a cylindrical boundary with surface tension. Simplifying assumptions are made only in solving the characteristic equations.

Weber[19] showed that exact solutions of the characteristic equation differ little from Rayleigh's approximation. He also considered the effect of aerodynamic drag on the perturbed filament. Tomotika[17,18] extended Rayleigh's model to allow for an ambient viscous fluid that surrounds the filament and is subjected to a steady elongational flow.

For our own purposes, we need to modify Rayleigh's and Tomotika's work to reflect not only contraction in the base flow but also the viscosity buildup due to quenching. These are essential features of such "capillary" models of fiber drawing and are therefore listed explicitly in Table I. A display of diametral response profiles along the fiber and their dependence on wavelength and base-flow properties is given for comparison with tensile stability models.

III. FUNDAMENTAL EQUATIONS AND THE ASSUMPTION OF ONE-DIMENSIONAL FLOW

Let z = axial coordinate

r = radial coordinate

v = axial velocity component

u = radial velocity component

ρ = fluid density, assumed constant

σ = surface tension,

μ = Newtonian viscosity, a function of temperature.

In the cylindrical coordinate system (r, z), the Eulerian equations of mass and momentum conservation read:

$$v_z + u_r + \frac{u}{r} = 0 \tag{1}$$

$$\rho[u_t + uu_r + vu_z] = \frac{\partial \tau_r}{\partial r} + \frac{1}{r}\tau_r + \frac{\partial \tau_{rz}}{\partial z} - \frac{1}{r}\tau_\theta \tag{2}$$

$$\rho[v_t + uv_r + vv_z] = \frac{\partial \tau_z}{\partial z} + \frac{\partial \tau_{rz}}{\partial r} + \frac{1}{r}\,\tau_{rz}, \tag{3}$$

where τ_r, τ_z, τ_{rz} denote stress components. In all other instances, the subscripts r, z, t denote partial derivatives.

The constitutive relations for an incompressible Newtonian fluid are

$$\begin{aligned} \tau_z &= -p + 2\mu\,\frac{\partial v}{\partial z} \\ \tau_r &= -p + 2\mu\,\frac{\partial u}{\partial r} \\ \tau_\theta &= -p + 2\mu\,\frac{u}{r} \\ \tau_{rz} &= \mu\left(\frac{\partial v}{\partial r} + \frac{\partial u}{\partial z}\right), \end{aligned} \tag{4}$$

where p is the pressure. It is one of the dependent variables, along with u, v, and the free surface configuration $r = a(z, t)$. Equations (1) to (3) have the following boundary conditions:

At $z = 0$:

$$\begin{aligned} v(r, 0, t) &= v_0(r, t) \\ u(r, 0, t) &= u_0(r, t) \\ a(0, t) &= a_0(t). \end{aligned} \tag{5}$$

At $z = L$, the take-up position:

$$v(r, L, t) = v_L(r, t). \tag{6}$$

At $r = a(z, t)$: the kinematic condition

$$v = u\,\frac{\partial a}{\partial z} + \frac{\partial a}{\partial t} \tag{7}$$

together with tangential and normal surface-stress conditions, which we do not reproduce in detail at this point. (See Appendix A.) Once a solution of this boundary value problem has been found, the draw force at any cross-section follows from

$$P(z, t) = 2a\pi\sigma/[1 + (\partial a/\partial z)^2]^{1/2} + 2\pi \int_0^a r\tau_z dr. \tag{8}$$

In particular, $\Delta P(t) = P(L, t) - P(0, t)$ and, to the extent that the solution for τ_z contains μ, ρ, σ, the expression for ΔP depends on these fluid properties.

The complete set of governing equations for the fiber drawing process includes an energy equation from which the temperature distribution $T(r, z, t)$ in the draw-down region is determined. This, in turn, yields μ as function of position and time. Strictly speaking, therefore, the heat-transfer equation is coupled to the fluid-dynamic equations. However, since we give it a separate, detailed treatment elsewhere, we uncouple it from this preliminary discussion and introduce $\mu(r, z)$, for nonisothermal draw-down, as a function presumed obtainable from some heat transfer model.

The general axisymmetric, free-surface flow problem posed by (1) to (7) is a formidable one. However, for the purposes of an engineering analysis and to gain some basic insight, much headway can be made by taking advantage of the fact that $|a_z| = 0(\epsilon) \ll 1$ and $|u/v| = 0(\epsilon) \ll 1$ throughout the draw-down region. This "small slope" assumption expresses the obvious fact that fluid flow in fiber drawing is essentially one-dimensional. The consequences of this kinematic feature are developed in Appendix A, taking advantage of the fact that we are dealing with low-Reynolds-number flow away from regions of strong relaxation in velocity profile. Specifically, we find:

(*i*) $v_r \equiv 0$, i.e., "plug" flow throughout the draw-down region.

(*ii*) $\tau_{rz} \propto \epsilon(\tau_z, \tau_r, \tau_\theta)r/a$

(*iii*) $u \propto \epsilon vr/a$

(*iv*) $\tau_r = \tau_\theta$, uniform over the cross-section

(*v*) $\tau_z = -\sigma/a + 3\mu v_z$, over the cross-section, where 3 μ is the so-called "Trouton" viscosity for extensional flow in a liquid filament.

These features of one-dimensional flow in the draw-down region suggest that mass and momentum conservation may be expressed conveniently in terms of cross-sectional fluxes and stress integrals. Equations of this kind may be obtained formally by integrating over the fiber cross-section: eq. (1) for volume conservation and eq. (3) for the axial momentum balance. Alternatively, we may derive these equations directly by taking a segment, of length dz, from the tapered axisymmetric filament as control volume. We obtain for volume conservation

$$(a^2v)_z + (a^2)_t = 0 \tag{9}$$

and for axial momentum conservation

$$\rho(a^2v^2)_z + \rho(a^2v)_t - 3(a^2\mu v_z)_z - \sigma a_z = 0. \tag{10}$$

For an eventual comparison with the early work of Pearson et al., we also record (10) after the terms in ρ and σ have been dropped. We have the simplified momentum equation

$$a^2\mu v_z = M(t), \tag{11}$$

where M is an arbitrary time function. This equation merely states that the draw force is uniform along the fiber and varies only with t.

For later reference, the time-independent (i.e., steady-state) versions of (9) and (10) yield

$$a^2 v = \text{const.} = Q \tag{12}$$

and

$$C = 3a^2 \mu v_z - \rho Q v + a\sigma, \tag{13}$$

where C is a constant of integration, viz. the cross-sectional draw force reduced by the momentum flux.

IV. STEADY-STATE SOLUTIONS FOR THE DRAWING PROCESS

In this section, we consider solutions of the time-independent equations (12) and (13). These constitute steady-state representations of the drawing process which are of interest for two reasons. First, they model the steady drawing operation and yield some insight into its controlling parameters, i.e., the dependence of draw force and draw-down profile on the draw-down ratio, the viscosity profile, fluid inertia, and surface tension. Second, they provide reference states on which to build dynamic response models for fiber-stability studies. In this context, such solutions are often referred to as base flow models.

It is well-known in fluid-dynamic stability theory that detailed features of the underlying base flow can be quite important to the predicted dynamic response. Hence, it is necessary that we examine several base-flow solutions of the drawing process for the physical features they represent.

Starting from (13), one observes that the first term on the right-hand side represents the viscous stress effect, the second fluid inertia, and the third a contribution from surface tension. We assume the following fiber dimensions and fluid properties at the start of draw-down:

$$\begin{aligned}
v &= 10 \text{ cm/s} \\
a &= 10^{-2} \text{ cm} \\
v_z &= 100/\text{s (e.g., } \Delta v = 100 \text{ cm/s, over } \Delta z = 1 \text{ cm)} \\
\rho &= 2.5 \text{ gm/cm}^3 \\
\sigma &= 200 \text{ dyn/cm} \\
\mu &= 100 \text{ poise for soda lime glass} \\
&= 1000 \text{ poise for fused silica.}
\end{aligned}$$

Note that the temperature at the interface between forming and draw-down zone is very dependent on as yet unknown fluid-dynamic and heat-transfer conditions in the forming zone. Therefore, the assumed values for μ are rather tenuous. 100 poise probably represents a minimum for soda lime glass, as might be expected in fiber drawing from crucibles.

Given these data, the order-of-magnitude relations between terms in (13) are:

	Viscosity μ (poise)	Viscous stress $3\mu a^2 v'$ (dyn)	Inertia $\rho Q v$ (dyn)	Surface Tension σa (dyn)
Soda lime glass	100	3	2.5×10^{-2}	2
Fused silica	1000	30	2.5×10^{-2}	2

Thus, inertia effects amount to barely 1 percent of the viscous term under the most favorable circumstances, while surface tension can be important when μ is near its minimum. However, physical evidence suggests rapid quenching of glass fibers in the draw-down region. Hence, inertia and surface tension effects soon become negligible as the temperature drops by several hundred degrees over the first few millimeters of the draw-down region, causing μ to grow by several orders of magnitude (see, for example, Ref. 23).

Disregarding, for a moment, the quenching effect that actually occurs in the draw-down region, we briefly consider an isothermal base state for two reasons. First, it permits an understanding of secondary physical effects such as inertia and surface tension, without being obscured by viscosity changes. Second, in later dynamic response studies, the isothermal base state serves as a basis of comparison for the stabilizing effect of the quenching that does occur.

Letting the fluid properties in (13) be independent of z, we consider flow conditions such that inertia and surface-tension effects can be viewed as perturbations in relation to the viscous stress. Eliminating the radius a from (12) and (13) and nondimensionalizing according to

$$\Psi = v/v_0, \qquad \zeta = z/L, \qquad (\quad)' = \frac{\partial(\quad)}{\partial \zeta},$$

we find

$$\Psi' - D\Psi = -We\Psi^{\frac{1}{2}} + Re\Psi^2, \tag{14}$$

where $v_0 = v$ at $z = 0$, L = length of draw-down region, and $D = LC/3a_0^2 v_0^2 \mu_0$, the nondimensionalized equivalent of C in (13). The inertia and the surface-tension terms are characterized by a Reynolds number $Re = v_0 L \rho / 3\mu_0$ and a Weber number, $We = \sigma L / 3 a_0 v_0 \mu_0$. The elementary solution for (14) with $We = Re = 0$ is

$$\Psi_{(0)} = e^{\zeta \ln E}, \tag{15}$$

where we have used the boundary conditions

$$\Psi = 1 \qquad \text{at} \qquad \zeta = 0$$
$$\Psi = E \qquad \text{at} \qquad \zeta = 1$$

and $E = v_L/v_0$ is the so-called "draw-down ratio." Note that $D = \ln E$.

Corrections to this simple base-state solution for small We and Re can be found by perturbation methods. A first-order approximation for $We \ll D$ and $Re \ll D$ is found by substituting (15) into the r.h.s. of (14):

$$\Psi_{(1)} = \exp\left[lnE\zeta + \frac{2We}{lnE}\left(e^{-(lnE/2)\zeta} - 1\right) + \frac{Re}{lnE}\left(e^{\zeta lnE} - 1\right)\right]. \quad (16)$$

Resubstituting this into the right side of (14) for a second iteration, terms such as $\exp[e^{\zeta lnE}]$, were approximated by power series prior to quadrature with respect to ζ. Then,

$$\Psi_{(2)} = e^{\zeta lnE}\left\{1 - We\mathcal{H}\left[\frac{Re}{2lnE}, \frac{We}{lnE}, -\frac{lnE}{2}, -\frac{(We + \frac{1}{2}Re)}{lnE}, \zeta\right] + Re\mathcal{H}\left[\frac{2Re}{lnE}, \frac{4We}{lnE}, lnE, -\frac{(4We + \frac{1}{2}Re)}{lnE}, \zeta\right]\right\}, \quad (17)$$

where the expression for $\mathcal{H}[a, b, c, d, \zeta]$ is recorded in Appendix B. Numerical results from (17) are best presented in terms of the nondimensional radius $a/a_0 = \chi$. According to (12)

$$\chi = \Psi^{-\frac{1}{2}}. \quad (18)$$

This has been plotted in Figs. 2 and 3 for a range of values in We and

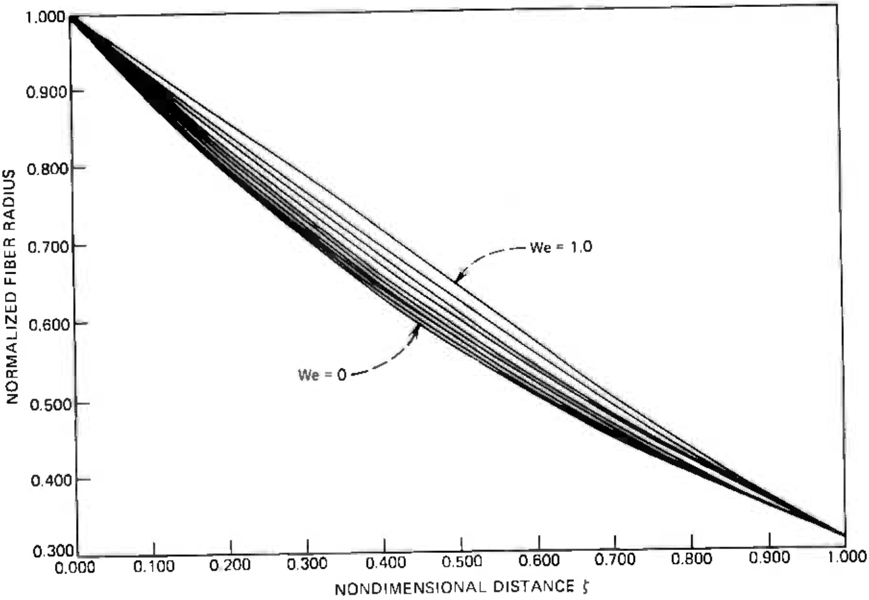

Fig. 2—Perturbation solutions for base-flow profiles with increasing surface tension; $E = 10$, $Re = 0$.

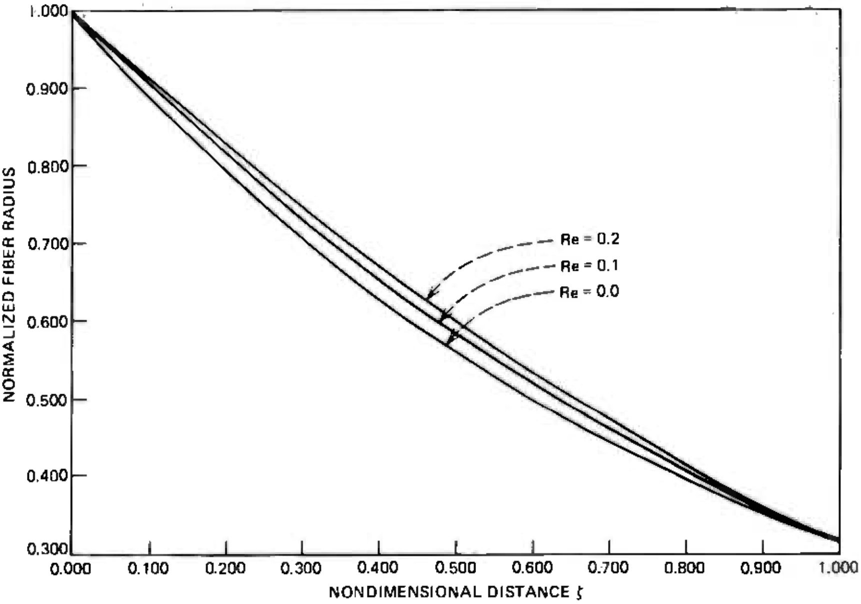

Fig. 3—Perturbation solutions for base-flow profiles with increasing fluid inertia; $E = 10$, $We = 0$.

Re. These results show a tendency for filament contraction to be delayed with increasing surface tension and fluid inertia, a familiar phenomenon from more accurate base-flow models obtained by numerical methods.[24]

Now let us return to the more realistic case of variable viscosity. We denote it $\mu_0\eta(\zeta)$, where the second factor represents only the dimensionless dependence on ζ, with $\eta(0) = 1$. Then (14) becomes

$$\eta\Psi' - D\Psi = -We\Psi^{\frac{1}{2}} + Re\Psi^2. \tag{19}$$

Using an inverse approach, we can, for example, assume $Re \neq 0$, $We = D = 0$ (where $D = lnE$ is no longer true) and $\Psi = e^{\zeta lnE}$, as in (15). This yields

$$\eta = \frac{Re}{lnE} e^{\zeta lnE} \tag{20}$$

and constitutes an inertia-dominated base flow. Experimental data suggest that something like an exponential viscosity buildup along the draw-down region is a fair representation of quenching effects. Note that for this base-flow model,

$$\chi = e^{-(lnE/2)\zeta}, \tag{21}$$

which has the disadvantage that $\chi \rightarrow 0$ for $\zeta \gg 1$. To provide a finite asymptotic value for χ, we may assume a draw-down profile of the form $\chi = fe^{-\alpha\zeta} + g$ with $f + g = 1$, $0 < f, g < 1$, and solve for Ψ from (18) and η from (19).

We summarize the three elementary base-flow models obtained so far with the notation $lnE/2 = \alpha$:

Unquenched base flow; $Re = We = 0$:

$$\chi = e^{-\alpha\zeta}, \qquad \Psi = e^{2\alpha\zeta}, \qquad \eta = 1. \tag{22}$$

Quenched base flow; $Re \neq 0$; $We = 0$;

$$\begin{aligned} &\chi \to 0 \quad \text{for} \quad \zeta \to \infty: \\ &\chi = e^{-\alpha\zeta}, \qquad \Psi = e^{2\alpha\zeta}, \qquad \eta = e^{2\alpha\zeta}. \end{aligned} \tag{23}$$

Quenched base flow; $Re \neq 0$; $We = 0$;

$$\chi \text{ finite for } \zeta \to \infty:$$

$$\chi = (fe^{-\alpha\zeta} + g), \quad \Psi = 1/(fe^{-\alpha\zeta} + g)^2, \quad \eta = e^{\alpha\zeta}/(fe^{-\alpha\zeta} + g). \tag{24}$$

In addition to the inertia-dominated base flows (23) and (24), we can show that

$$\chi = fe^{-\alpha\zeta} + g, \qquad \Psi = \frac{1}{g^2}\left(1 - 2\frac{f}{g}e^{-\alpha\zeta}\right), \qquad \eta = \frac{1}{g}e^{\alpha\zeta} \tag{25}$$

is a solution of the approximate fluid-dynamic and heat-transfer equations, for small α, if we let $Re = We = 0$ and assume

$$\mu = \mu_0 e^{\beta(1-T/T_0)},$$

where T_0 is the initial temperature and $\beta \gg 1$. This represents a quenched base flow that is not inertia-dominated, in keeping with some of the perturbation equations discussed later on. Note that for each of these base-flow models $\partial a/\partial z = 0(\alpha a_0/L)$. Since $\alpha = 0(1)$ but $a_0/L \ll 1$, this means that $|\partial a/\partial z| \ll 1$ and confirms the basic assumption providing for one-dimensional flow, as discussed in Section III. Note also that the viscosity profiles in models (23), (24), and (25), which reflect a cooling process along the fiber, are connected with the draw-down profile through the parameter α. This parameter is indicative of the quenching rate in η, and also controls χ', the slope of the draw-down profile.

The draw-force follows from any of these solutions by the obvious relation, in dimensional form,

$$P = \pi a^2 \tau_z + 2a\pi\sigma = 3\pi a^2 \mu v_z + \pi a\sigma. \tag{26}$$

If we neglect σ and substitute one of the base flows, we find that P

depends on a_0, v_0, μ_0 as well as the draw-down ratio and the quenching rate α; all of which could be expected on physical grounds.

Clearly, we could refine upon the viscosity profiles to be used in simple base-flow models. Since some experimental temperature profiles tend to show an exponential decay and the viscosity temperature relation for many glasses is of the form $\eta \sim e^{k/T}$, we might consider functions of the form

$$\eta = r + s\exp(e^{2\alpha\zeta}).$$

However, such elaborations result in a loss of mathematical simplicity and usually lead to equations for Ψ that require numerical integration. At that point, it seems more appropriate to solve the coupled heat-transfer/flow problem by numerical means. This has been done and is documented elsewhere.[24]

V. PERTURBATION EQUATIONS FOR TENSILE STABILITY MODELS

In this section, we develop the first-order perturbation equations necessary for a linear stability analysis of tensile fiber models. Let the first-order solution of (9), (10), and (11) be denoted

$$\begin{aligned} \bar{a} &= a(z)[1 + \hat{a}(z, t)] \\ \bar{v} &= v(z)[1 + \hat{v}(z, t)] \\ \bar{\nu} &= \nu(z)[1 + \hat{\nu}(z, t)], \end{aligned} \tag{27}$$

where $a(z)$, $v(z)$, and $\nu(z)$ represent radius, velocity, and kinematic viscosity for a suitable base state, in dimensional form for the time being, and $\hat{a}$, $\hat{v}$, $\hat{\nu}$ are dimensionless first-order perturbations of these quantities.

Substituting (27) into (9), the first-order variation of the continuity equation reads

$$\hat{a}_z + \frac{1}{v}\hat{a}_t + \frac{1}{2}\hat{v}_z = 0. \tag{28}$$

Similarly, (10) without the surface-tension term becomes

$$\begin{aligned} \hat{v}_{zz} + \hat{v}_z\left(\frac{\nu_z}{\nu} + \frac{v_z}{v} - \frac{2v}{3\nu}\right) - \frac{1}{3\nu}\hat{v}_t + \hat{a}_z\left(\frac{2v_z}{v} - \frac{2v}{3\nu}\right) \\ - \frac{2}{3\nu}\hat{a}_t + \hat{a}\left(2\nu\frac{v_z}{v} - \frac{2v}{3}\right)_z \Big/ \nu + \hat{v}\left(\frac{\nu v_z}{v} - \frac{2v}{3}\right)_z \Big/ \nu \\ = -\hat{\nu}_z\frac{v_z}{v} - \hat{\nu}\left(\frac{\nu v_z}{v}\right)_z \Big/ \nu \end{aligned} \tag{29}$$

and from (11), the momentum equation without inertia terms,

$$2\hat{a} + \hat{\nu} + \hat{v} + \frac{v}{v_z}\hat{v}_z = \frac{d(t)}{P_0}, \tag{30}$$

where we have used $a^2 \nu v_z = P_0 = \text{const.}$ from (11) and $d(t)$ is a perturbation of $M(t)$. Since the examples in later sections use the base states of Section IV, it is convenient to nondimensionalize the space and time variables as

$$\alpha\zeta = \mathfrak{z} \qquad \frac{v_0 \alpha t}{L} = \tau \tag{31}$$

and use the notation

$$\frac{d(\ \ )}{d\mathfrak{z}} = (\ \ )' \quad \text{and} \quad \frac{d(\ \ )}{d\tau} = (\ \ )^{\cdot}. \tag{32}$$

The specific versions of (28), (29), and (30) now develop as follows. With the base states (22) or (23), eq. (28) becomes

$$\hat{a}' + \tfrac{1}{2}\hat{v}' + \dot{\hat{a}} e^{-2\mathfrak{z}} = 0. \tag{33}$$

Neglecting inertia in the momentum equation, (22) and (30), for the unquenched inertialess base state, yields

$$2\hat{a} + \hat{v} + \dot{\hat{v}} + \tfrac{1}{2}\hat{v}' = \varphi(\tau), \tag{34}$$

where φ is an arbitrary function of τ. On the other hand, the momentum equation (29), using the quenched inertia-dominated base state (23) leads to

$$\hat{v}'' - 4\hat{v} - 4\dot{\hat{a}} e^{-2\mathfrak{z}} - 2\dot{\hat{v}} e^{-2\mathfrak{z}} = -2\dot{\hat{v}}' - 4\dot{\hat{v}}. \tag{35}$$

Turning now to the inertialess, quenched base state (25), we revert to (28) and (30) as basic equations, but reserve the substitution of v and v_z from (25) for a later time.

For some of the examples treated in later sections, it is convenient to eliminate $\hat{v}$ from (34) and (35) by means of (33) and similarly from (28) and (30) for base state (25). The resulting equations for $\hat{a}$ are recorded in Appendix C for later reference.

Conversely, the boundary conditions for some problems demand an equation in $\hat{v}$. This is the case with steady-state responses to changes in the takeup velocity, which we treat in the next section. If (27) is used in (12) and we let $\bar{Q} = Q(1 + \hat{q})$, the first-order variation of that equation yields

$$2\hat{a} + \hat{v} = \hat{q}. \tag{36}$$

Next, consider (13), where we neglect surface tension and perturbations in ν. As noted before, the constant C may be interpreted as a force parameter, carried from the forming zone to the draw-down region. Taking the first variation of (13), letting $\bar{C} = C(1 + \hat{c})$, and eliminating $\hat{a}$ by means of (36),

$$\hat{v}_z - \frac{v}{3\nu}\hat{v} = -\frac{C}{3Q\nu}\hat{c} + \hat{q}\left(\frac{v}{3\nu} - \frac{v_z}{v}\right). \tag{37}$$

Nondimensionalizing the base-flow variables in this equation according to Section IV, we have

$$\hat{\mathfrak{v}}_\zeta - \frac{Re\Psi}{\eta}\hat{\mathfrak{v}} = \frac{k}{\eta} + \left(\frac{Re\Psi}{\eta} - \frac{\Psi_\zeta}{\Psi}\right)\hat{q}, \tag{38}$$

where

$$k = \frac{LC\hat{c}}{3a_0^2 v_0 \mu_0}.$$

Equation (38) is designed to yield changes in the steady-state velocity profile, $\hat{\mathfrak{v}}$, as a function of $\hat{q}$ and k, which are perturbations of the volume flux and force parameter of the base flow.

In summary, this section has developed first-order perturbation equations based on the continuity and momentum equations of Section III. The perturbation equations were given in terms of $\hat{a}$ or $\hat{\mathfrak{v}}$ as needed for the steady-state and dynamic-response studies to be pursued in Sections VI and VII.

VI. PERTURBATIONS OF THE BASE FLOW

In this section, we use the time-independent versions of perturbation equations derived in Section V to display changes in several base-flow solutions due to shifts in such steady-state parameters as the boundary values and the viscosity profile along the fiber. Since these parameters are often accessible to control in real fiber-drawing processes, their effects on the steady flow are of operational interest. Obviously such effects could be determined by differencing neighboring base-flow solutions in the control-parameters space; however, exhibiting the changes (analytically) as first-order perturbations can yield useful insight for the design of feedback controls.

We start by examining the response of steady state (24) to a change $\hat{\mathfrak{v}}_L$ in take-up speed. Substituting the appropriate base-flow expressions for Ψ and η into (38), one has

$$\hat{\mathfrak{v}}' - Re\frac{e^{-\mathfrak{z}}}{\chi}\hat{\mathfrak{v}} = ke^{-\mathfrak{z}}\chi + (Re - 2f)\frac{e^{-\mathfrak{z}}}{\chi}\hat{q}, \tag{39}$$

where

$$\mathfrak{z} = \alpha\zeta \qquad (\ \ )' = \frac{\partial(\ \ )}{\partial\mathfrak{z}} \qquad s = fe^{-\mathfrak{z}} + g$$

and a factor of $1/\alpha$ has been absorbed in Re and k. The boundary condition for (39) is

$$\hat{\mathfrak{v}} = \hat{\mathfrak{v}}_L \quad \text{at} \quad \mathfrak{z} = \mathfrak{z}_L = \alpha. \tag{40}$$

We find

$$\hat{\mathfrak{v}} = V\chi^{-Re/f} - \frac{k\chi^2}{2(1+f)} + \left(\frac{2f}{Re} - 1\right)\hat{q} \tag{41}$$

with

$$V = \left[\hat{v}_L + \left(1 + \frac{2f}{Re}\right)\hat{q}\right]\chi_L^{Re/f} + \frac{k\chi_L}{2(1+f)}\,(2 + Re/f),$$

where $\chi_L = \chi(z_L)$. Given (41), the corresponding changes in fiber radius $\hat{a}$ follow from (36).

Additional features of interest with (41) are $\hat{v}$ at $z = 0$ and perturbations of the draw force at either end. Thus,

$$\hat{v}_0 = \hat{v}(0) = V - \frac{k}{2(1+f)} + \left(\frac{2f}{Re} - 1\right)\hat{q}. \tag{42}$$

For the draw force,

$$\bar{P} = P(1 + \hat{p}) = 3\pi\mu\bar{a}^2\bar{v}_z,$$

which yields

$$\hat{p} = \hat{q} + \frac{v}{v'}\hat{v}' = \hat{q} + \frac{e^{\partial}s\hat{v}'}{2f}.$$

From this,

$$\hat{p}_0 = \hat{q} + \frac{VRe}{2f} + \frac{k}{2(1+f)} \tag{43}$$

and

$$\hat{p}_L = \hat{q} + \frac{VRe}{2f}\chi_L^{-Re/f} + \frac{k\chi_L^2}{2(1+f)}, \tag{44}$$

the changes in draw force, as function of $\hat{v}_L$, $\hat{q}$, and k.

The solution (41) is of little more than conceptual value as long as $\hat{q}$ and k are unknown. Recall from (38) that these parameters represent perturbations in the integration constants of the base-flow solution for the draw-down region: $\hat{q}$, a change in the volume flux, and k, a change in the force parameter of the momentum equation. Such changes must, in general, be expected to enter from the forming zone when the steady state is altered due to $\hat{v}_L$.

Fortunately, $\hat{q} = 0$ for drawing from a preform that is fed at a constant rate. However, the exit flow from a crucible (Fig. 1a) does not provide such a simple condition. If operating at a low head in the reservoir, we would expect the entrance flow into the orifice to be affected by changes in the take-up speed. In neither case does there exist an obvious condition for the force parameter k [i.e., $\hat{c}$ and C, see eq. (38)].

A theory of the forming zone should be able to relate $\hat{v}_0$ and $\hat{p}_0$ on the one hand with $\hat{q}$ and k on the other. Given such relations, these would combine with (42) and (43) to determine $\hat{q}$ and k in terms of $\hat{v}_L$, and hence $\hat{v}$, $\hat{a}$, $\hat{p}$ as functions of $\hat{v}_L$. Depending on the different situations depicted in Fig. 1, the relations of $\hat{v}_0$, $\hat{p}_0$ vs $\hat{q}$, k in the forming zone could vary considerably. In some cases, an understanding of the complex fluid-dynamic and heat-transfer processes of the forming zone (see Fig. 1d) would seem essential for a satisfactory representation of speed-diameter-force relations at the take-up end.

In the remainder of this section, we examine the sensitivity of steady-state flow in the draw-down region to changes in the viscosity profile. Such changes can be viewed as consequences of perturbations in the heat-transfer mechanism. Our primary purpose is to determine response amplitudes for $\hat{a}$, the perturbation in draw-down profile, as functions of $\hat{\nu}_0$, an amplitude parameter of the viscosity perturbation. Once again we encounter the problem of assuming reasonable boundary conditions at $z = 0$ without a dynamic model of the forming zone.

We consider two different cases: the draw-down response without inertia effects imposed on the unquenched, inertialess base state (22), and the response with inertia effects imposed on the quenched, inertia-dominated base state (23). In particular, we shall be working with eqs. (76) and (77) after deletion of the time derivatives.

In both cases, we consider a viscosity perturbation of the form

$$\hat{\nu} = \hat{\nu}_0 \mathfrak{z} e^{-\gamma \mathfrak{z}}, \tag{45a}$$

which represents a distribution of arbitrary amplitude and spread, determined by $\hat{\nu}_0$ and γ, respectively. A family of such functions is displayed in Fig. 4 for $1 \leqq \gamma \leqq 6$. Note that for a given value of γ

$$\frac{\nu}{\hat{\nu}_{0_{\max}}} = \frac{1}{\gamma e}, \tag{45b}$$

the peak viscosity perturbation, normalized w.r.t. $\hat{\nu}_0$.

Let us consider various boundary conditions that may be applicable to solutions of this problem. If we assume that the fiber is drawn from a preform with constant feed and take-up conditions, an obvious boundary condition is

$$\hat{a}(\mathfrak{z}_L) = 0. \tag{46a}$$

In view of $\hat{q} \equiv 0$, it seems reasonable to assume that the forming zone will respond with $\hat{p}(0) = 0$. $\hat{\nu}'(0)$ can be eliminated from these two conditions to yield

$$a'(0) - \frac{a'(0)}{a(0)} \hat{a}(0) = 0. \tag{46b}$$

If three boundary conditions are needed, we take

$$\hat{a}(0) = 0, \tag{46c}$$

and then, according to (46b), also $\hat{a}'(0) = 0$. Finally, for a fourth condition, let

$$\hat{a}'(\mathfrak{z}_L) = 0, \tag{46d}$$

which implies that $p(\mathfrak{z}_L) = 0$, i.e., no perturbation of the draw force

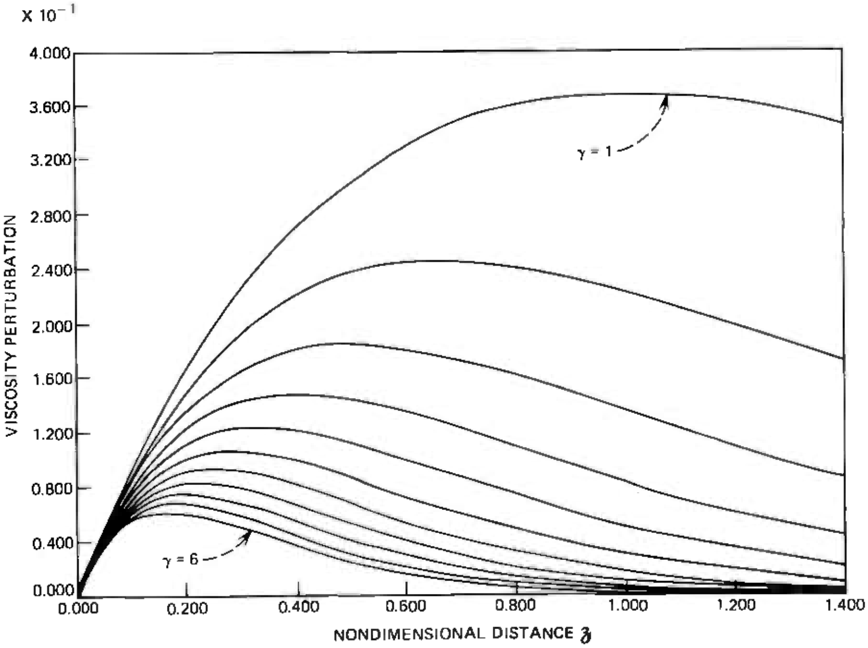

Fig. 4—Profiles of the viscosity perturbation, $\nu/\nu_0 = \mathfrak{z}e^{-\gamma\mathfrak{z}}$.

occurs at the take-up end. Conditions (46) will be invoked as necessary with increasing order of the perturbation equations.

We start by considering the inertialess perturbation eq. (77). We have

$$\hat{a} = -\frac{\hat{\nu}_0}{\gamma}e^{-\gamma\mathfrak{z}}\left(\frac{1}{\gamma} + \mathfrak{z}\right) + B_1\mathfrak{z} + B_2. \tag{47}$$

Results from (47) have been plotted in Fig. 5 to represent the effect of viscosity perturbations on the unquenched base state. Note the nonmonotonic evolution of these curves with increasing γ.

Next, we examine the corresponding results, including effects of fluid inertia. Integrating (76) after deletion of the time derivatives, the quenched inertia-dominated base state (23) leads to

$$\hat{a}''' + 2\hat{a}'' - 4\hat{a}' - 8\hat{a} = \hat{\nu}'' + 4\hat{\nu}' + 4\hat{\nu} + C. \tag{48}$$

C is a constant of integration.

Substituting (45) into (48), we obtain

$$\hat{a}(\mathfrak{z}) = \frac{-\hat{\nu}_0}{(\gamma+2)}\left(\mathfrak{z} + \frac{1}{\gamma+2}\right)e^{-\gamma\mathfrak{z}} + B_1e^{2\mathfrak{z}} + (B_2 + B_3\mathfrak{z})e^{-2\mathfrak{z}} + B_4. \tag{49}$$

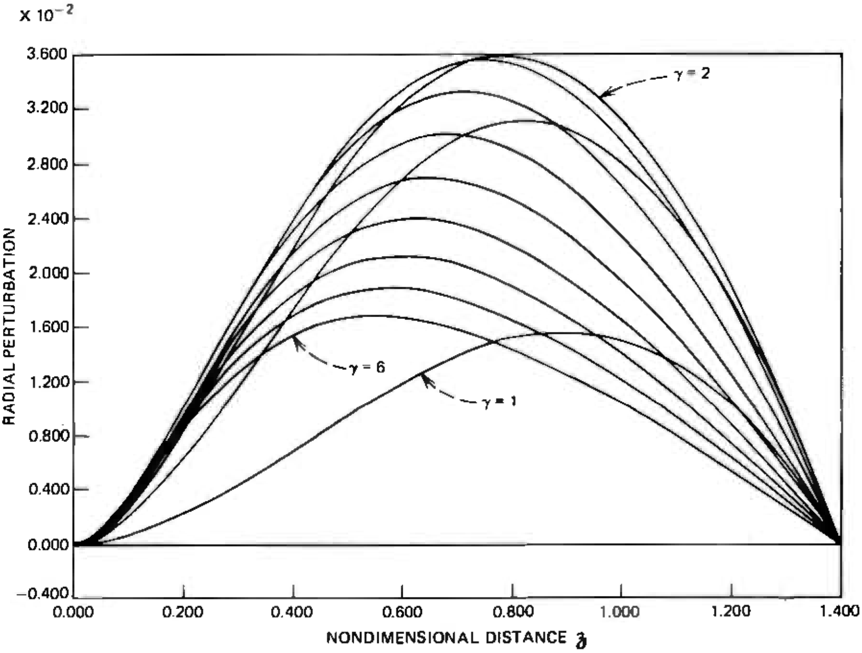

Fig. 5—Draw-down response to the viscosity perturbations of Fig. 4, without fluid inertia, for unquenched base flow.

Figure 6 shows (49), the effect of viscosity perturbations on the quenched, inertia-dominated base state, over the range $1 \leqq \gamma \leqq 6$. Note that the presence of quenching significantly alters the evolution of response curves in Fig. 6, which becomes monotonic with γ. Typical amplitudes in this case are about one-half to one-third as large as for the unquenched base flow (Fig. 5).

The main inference to be drawn from a comparison of Figs. 5 and 6 is that typical peak amplitudes for $\hat{a}/\hat{\nu}_0$ are reduced significantly due to fluid inertia and quenching.

By way of specific example, we consider results for $\gamma = 3.5$:

Maximum for viscosity perturbation (Fig. 4)	$\hat{\nu}/\hat{\nu}_0 = 0.110$
Maximum for response without inertia on unquenched base state (Fig. 5)	$\hat{a}/\hat{\nu}_0 = 0.018$
Maximum for response with inertia on quenched base state (Fig. 6)	$\hat{a}/\hat{\nu}_0 = 0.005$

The latter case, which represents the more realistic model, also predicts the lower response amplitudes. Thus, for example, a 10-percent departure from the nominal viscosity profile would cause only a 0.5-percent departure from the draw-down profile.

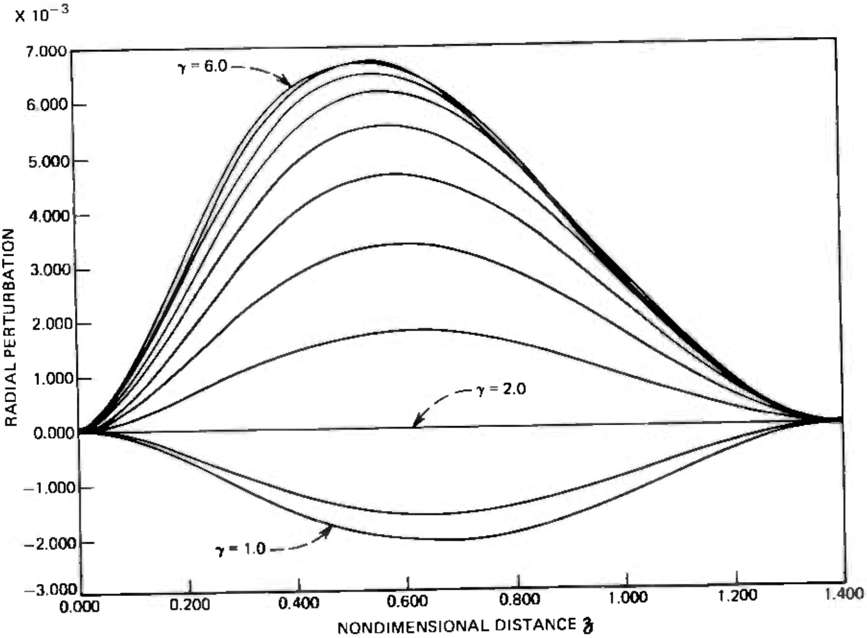

Fig. 6—Draw-down response to viscosity perturbations, with fluid inertia, for quenched base flow.

In summary, the first-order results given in this section yield a qualitative indication of base flow responses to time-invariant changes of the boundary conditions and of the viscosity profile. As stated in Section IV, a more satisfactory treatment of viscosity effects may be achieved by numerical integration of the base-flow equations, which introduce heat-transfer perturbations through the energy equation. However, the question of realistic interface conditions between the drawn-down region and forming zone remains open until the latter is included in our model.

VII. THE DYNAMIC RESPONSE OF TENSILE FIBER MODELS

We turn now to the dynamic response of tensile fiber models for the unquenched and quenched base flows; i.e., we address solutions of the equations in Appendix C, including the time-dependent terms. Unfortunately, the formulation allowing for fluid inertia, eq. (76), does not lend itself to a simple solution. We therefore seek what preliminary insight can be gained from solutions obtainable with (77) and (78), i.e., by neglecting inertia in the perturbation equations.

Starting with (77), which represents perturbations of the unquenched base flow, the operator on the left-hand-side suggests a gen-

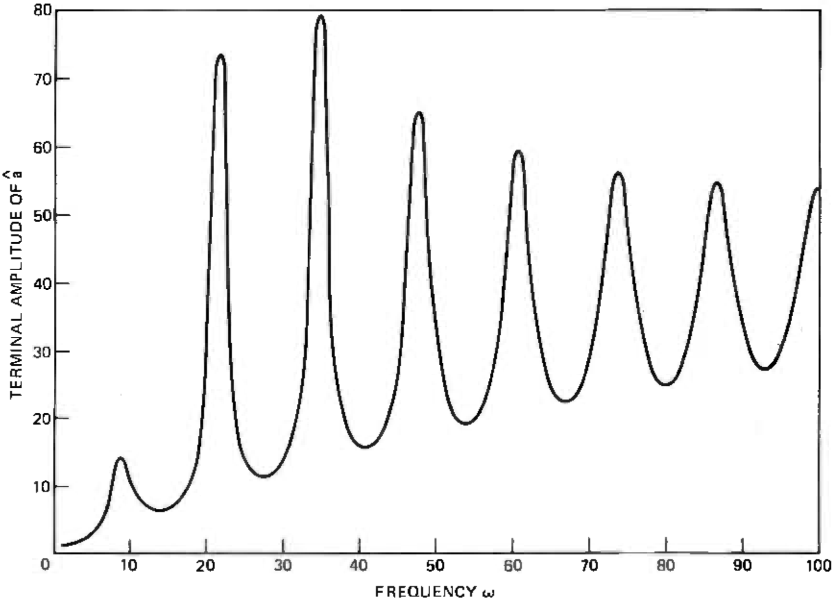

Fig. 7—Tensile fiber model: frequency response of surface perturbation at $\mathfrak{z}_L = 2$ for base state [eq. (22)].

eral solution of traveling waveform

$$\hat{a}' = f(\tau + \tfrac{1}{2}e^{-2\mathfrak{z}}) \tag{50}$$

and

$$\hat{a}_c = \int f(\tau + \tfrac{1}{2}e^{-2\mathfrak{z}})d\mathfrak{z} + \Phi(\tau), \tag{51}$$

where $\Phi(\tau)$ is an arbitrary time function. This solution may be used to represent radial excitations at the source or take-up end or to satisfy boundary conditions in the presence of a particular solution. In the former case, where $\hat{a}(0, \tau) = \sin \omega\tau$, we reconstruct a solution by Pearson and Matovitch[14] of the form

$$\hat{a}(\mathfrak{z}, \tau) = A_1(\mathfrak{z}) \sin \omega\tau + A_2(\mathfrak{z}) \cos \omega\tau \tag{52}$$

with the terminal response amplitude

$$A(\omega, \mathfrak{z}_L) = [A_1^2(\omega, \mathfrak{z}_L) + A_2^2(\omega, \mathfrak{z}_L)]^{\frac{1}{2}}. \tag{53}$$

This is normalized with respect to $\hat{a}_0$, the amplitude of radial perturbations at $\mathfrak{z} = 0$, and plotted, for later comparison, in Fig. 7 as a function of ω, for $\mathfrak{z}_L = 2$. It shows a series of response peaks presumably due to the absence of quenching from the base state (22), used in (77).

These response peaks are commonly referred to in the literature as "draw resonances." The author takes exception to this term since it implies the existence of natural frequencies contingent on the interaction of system inertia and some restoring force, neither of which is obvious in the present model. Nevertheless, experimental evidence confirms the occurrence of highly amplified responses near some of the "critical" frequencies predicted by Pearson's model. Typical radial perturbation profiles for $\hat{a}(\mathfrak{z}, \tau)$ are shown in Fig. 8 for $\omega = 100$, at $T = 0$, the start of a period, and $T = 0.25$, its quarter-point. They illustrate the spatial amplification of surface perturbations occurring along the draw path.

Since the direct physical realization of radial perturbations at $\mathfrak{z} = 0$ may be difficult, we now examine the effect of viscosity perturbations that are convected along the fiber as a consequence of fluctuations in the heat source; i.e.,

$$\hat{\vartheta} = g(\tau + \tfrac{1}{2}e^{-2\mathfrak{z}}). \tag{54}$$

Substitution into (77) yields the inhomogeneous equation

$$\left(\frac{\partial}{\partial \tau} + e^{2\mathfrak{z}} \frac{\partial}{\partial \mathfrak{z}} \right) \hat{a}' = -\dot{g}(\tau + \tfrac{1}{2}e^{-2\mathfrak{z}}), \tag{55}$$

where the dot is also used to designate differentiation with respect to

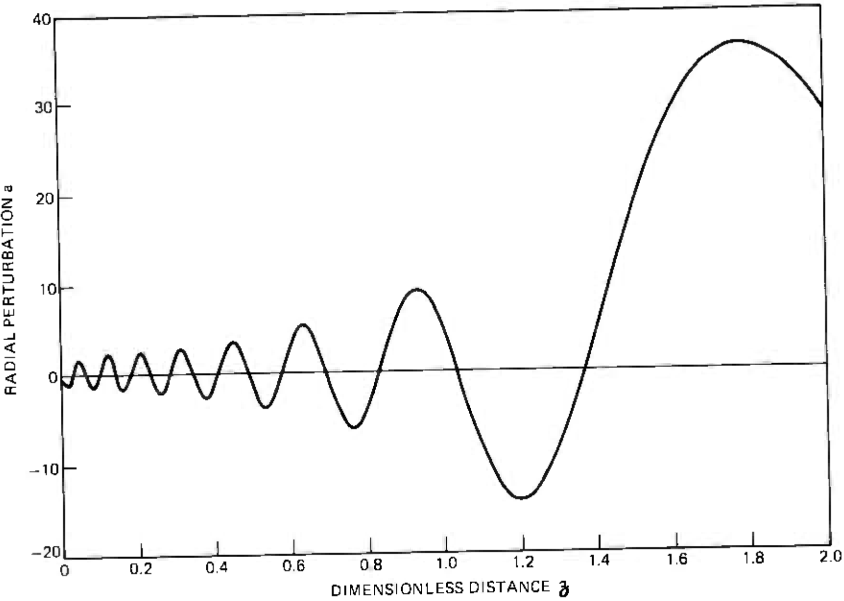

Fig. 8a—Surface perturbation for base state [eq. (22)] with $\omega = 100$, $\mathfrak{z}_L = 2$, at $T = 0$.

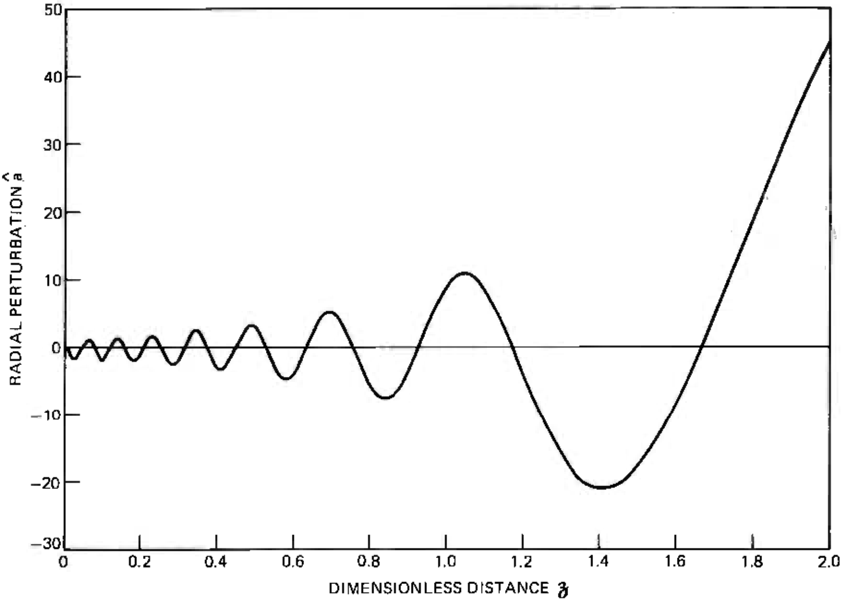

Fig. 8b—$\hat a$ at $T = 0.25$.

the compound space-time argument. If we substitute

$$\hat a' = h(\tau + \tfrac{1}{2}e^{-2\mathfrak{z}})e^{-2\mathfrak{z}},$$

this leads to $h = -\frac{1}{2}\dot g$; hence, the particular solution

$$\hat a = -\tfrac{1}{2}g(\tau + \tfrac{1}{2}e^{-2\mathfrak{z}}) = -\tfrac{1}{2}\hat\nu. \tag{56}$$

This suggests that any space-time history of viscosity changes given in the form (54) translates into changes of fiber radius by the factor $-\frac{1}{2}$. It is a traveling-wave type of response only in the sense that it is convected with the moving fluid.*

To take a specific example, consider a periodic viscosity perturbation, as would be caused by misalignment of the rotating laser beam used in heating the preform,

$$\hat\nu = \sin\omega(\tau + \eta), \tag{57}$$

---

* The negative sign may appear surprising at first. One notes, however, from the continuity equation (33) written as

$$(e^{-2\mathfrak{z}}\partial/\partial\tau + \partial/\partial\mathfrak{z})\hat a = -\tfrac{1}{2}\hat v',$$

that $\hat a$ of the form $g(\tau + \frac{1}{2}e^{-2\mathfrak{z}})$ leads to $\hat v' = 0$. This means that such a form of radial perturbation can travel with the flowing fiber without perturbing the local velocity. Further, if a constant draw force is to be maintained, the expression

$$P/\rho = \pi a^2 \nu v'$$

shows that, with v' unperturbed, an increase in ν requires a decrease in a of half this magnitude.

where $\eta = \frac{1}{2}e^{-2\mathfrak{z}}$, yielding the particular solution

$$\hat{\mathfrak{a}}_p = -\tfrac{1}{2}\sin\omega\tau\cos\omega\eta - \tfrac{1}{2}\cos\omega\tau\sin\omega\eta. \tag{58}$$

The boundary conditions to be satisfied with the help of (51) are then

$$\begin{aligned} \hat{\mathfrak{v}}(0, \tau) &= 0, \qquad \hat{\mathfrak{v}}(\mathfrak{z}_L, \tau) = 0, \\ \hat{\mathfrak{a}}_c(0, \tau) &= \tfrac{1}{2}\sin\omega(\tau + \tfrac{1}{2}). \end{aligned} \tag{59}$$

In this case, the perturbations are driven only by the variations in viscosity.

An appropriate form for f is

$$f(\mathfrak{z}, \tau) = f_1\cos\omega(\tau + \eta) - f_2\sin\omega(\tau + \eta) \tag{60}$$

so that

$$\begin{aligned} \hat{\mathfrak{a}}_c(\mathfrak{z}, \tau) = \tfrac{1}{2}(f_1\cos\omega\tau - f_2\sin\omega\tau)[Ci]_{\omega\eta}^{\omega/2} \\ - \tfrac{1}{2}(f_1\sin\omega\tau + f_2\cos\omega\tau)[Si]_{\omega\eta}^{\omega/2} + \Phi(\tau), \end{aligned} \tag{61}$$

where

$$[Ci]_{\omega\eta}^{\omega/2} = \int_{\omega\eta}^{\omega/2} \frac{\cos w}{w}\, dw$$

$$[Si]_{\omega\eta}^{\omega/2} = \int_{\omega\eta}^{\omega/2} \frac{\sin w}{w}\, dw$$

and f_1, f_2 are integration constants. After determining $\Phi(\tau)$, f_1, and f_2 to satisfy (59), once again a solution of the form (52) is obtained, where A_1 and A_2 are recorded in Appendix D. It is interesting to note that $A(\omega, \mathfrak{z}_L)$ for this case, if normalized in terms of $\mathfrak{v}_0$ and plotted as in Fig. 7 shows exactly the same response spectrum, but with half the amplitudes. Moreover, the profiles of radial perturbations along the fiber for this case strongly resemble the ones obtained for radial excitation at $\mathfrak{z} = 0$ (Fig. 8).

The sharp response peaks given by the above solutions at certain frequencies reflect the absence of quenching in the base flow (22). In search of some allowance for quenching effects, we consider two ad hoc modifications of the tensile fiber model: the base flow (25), which includes moderate quenching together with moderate draw-down, and base flow (23), which represents quenched, inertia-dominated, exponential draw-down.

Using eq. (78), which is based on (25), a solution of this perturbation equation is developed in Appendix D for the case of cyclic perturbations in the starting radius $\hat{\mathfrak{a}}(0, \tau) = \sin\omega\tau$. The resulting expression for $\hat{\mathfrak{a}}(\zeta, \tau)$ is recorded in (88). It turns out that the term $e^{-\gamma\zeta}\sin\omega\tau$ exceeds all other contributions to the dynamic response by several orders of magnitude for all values of ω and γ of interest. Thus, the perturbation in the fiber radius is merely a shift in the exponential draw-down profile of the base state, whose spatial variation is independent of ω and characterized by γ, the quenching parameter of the base-flow viscosity profile $\nu = \nu_0 e^{\gamma\zeta}$. This perturbation oscillates in time with constant phase along the entire draw path. Typical profiles of $\hat{a}$ are shown in Fig. 9, again for $T = 0$, the start of a period, and $T = 0.25$, its quarter-point. A contribution from the nonexponential components in $\hat{a}(\zeta, \tau)$ is only seen at $T = 0$, the zero-crossing of its $\sin \omega\tau$ term. These profiles show none of the spatial amplification evident in Fig. 8, which confirms, at least qualitatively, the attenuating effect of the quenching process. Unfortunately, a limiting comparison between the two models is not possible as the quenching effect is made to vanish, since that also requires a vanishing of the draw-down in base state (25).

If the quenched, inertia-dominated base flow (23) is employed in the inertialess perturbation equation (30), the resulting model is indeed subject to criticism as logically inconsistent. However, as a plausibility argument, we might suggest that inclusion of inertia in the base flow would at least give a qualitative indication of changes to be expected from a more complete allowance for inertia effects. The formal exercise, starting from (23) and (30), closely resembles the derivation of (79).

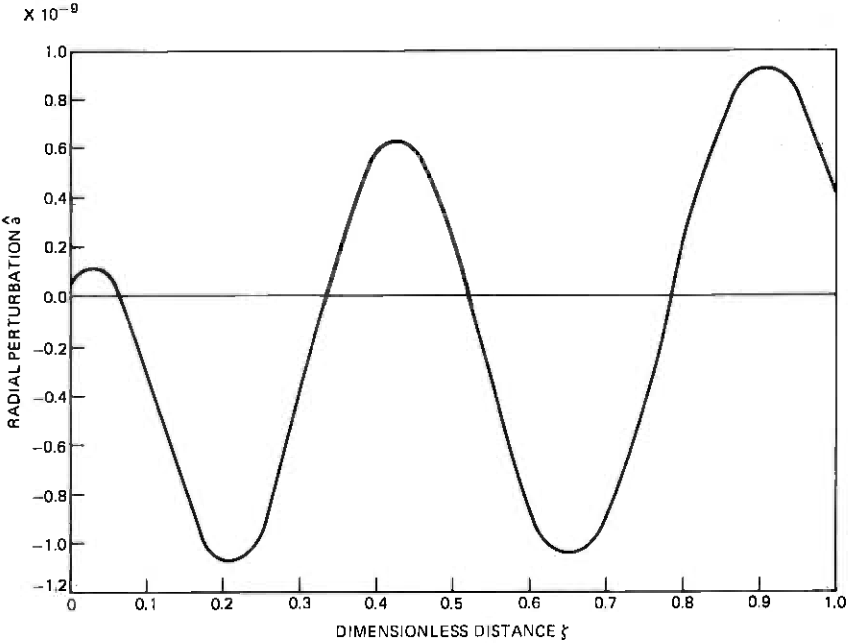

Fig. 9a—Surface perturbation for base state [eq. (25)] with $g = 0.75$, $\omega = 20$, $\gamma = 2$, at $T = 0$.

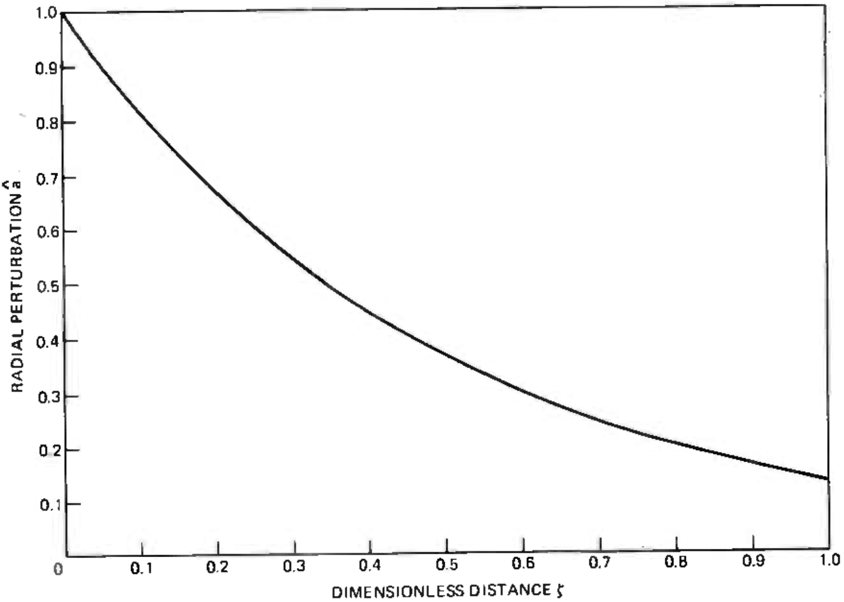

Fig. 9b—$\hat{a}$ at $T = 0.25$.

The resulting frequency response functions evolve quite clearly from curves such as Fig. 7 with considerable smoothing of peaks and valleys. This suppression of the response peaks, due to quenching, certainly agrees with experimental evidence.

The main point to be made in this preliminary assessment of tensile fiber models is that their frequency response curves and surface perturbation profiles bear little resemblance to the perturbations caused by surface tension, which we discuss in the next section. To generate more realistic response predictions for tensile fiber models, including inertia effects and heat transfer, we will have to resort to numerical means.

VIII. THE DYNAMIC RESPONSE OF CAPILLARY FIBER MODELS

We next inquire under what circumstances the well-known phenomena of surface-tension-driven perturbations on liquid filaments apply in the fiber-drawing problem. Indeed, there may be limited portions of the draw path, presumably near the hot tip of the forming zone, where the viscosity drops low enough for surface tension to become significant. At least for low-melting glasses, such as soda lime, this is a possibility, as born out by the comparison of essential terms in the base-flow equations of Section IV. We shall characterize this type of fluid-dynamic behavior as capillary fiber models. As we shall see, their spatial response profiles under harmonic radial excitation are totally different from those of tensile fiber models. By all indications, these two kinds of filament response are fundamentally distinct phenomena. The ultimate question is to what extent they coexist and interact in a real fiber-drawing process.

Rayleigh's classical theory of capillary jets is our point of departure.[15,16] It shows that the growth rate of "varicose" perturbations (axisymmetric harmonic surface modulations) is given by

$$m = \frac{\sigma(\tilde{k}^2 - 1)}{2\mu a[\tilde{k}^2 + 1 - \tilde{k}^2 I_0^2(\tilde{k}) I_1^2(\tilde{k})]}, \tag{62}$$

where

m = real, the rate of growth
a = fiber radius
λ = wavelength of the perturbation
$\tilde{k} = 2\pi a/\lambda$
I_0 and I_1 = modified Bessel functions.

The denominator of (62) turns out to be negative for all $\tilde{k}$.*

If this capillary response model is locally applied to a base-flow model such as (24), assuming that base-state parameters change negligibly over the wavelength λ, we may use it to construct the dynamic response along a contracting fiber. Then the evolution of a small surface disturbance may be synthesized using the stepwise relation between displacement amplitudes at successive instants of time

$$U_{n+1} = U_n \left(\frac{a_{n+1}}{a_n} + \bar{m}\Delta t \right), \tag{63}$$

where

U_n and U_{n+1} = peak amplitudes of sinusoidal surface perturbations at t_n and t_{n+1}, respectively
$\frac{a_{n+1}}{a_n}$ = stepwise scale factor due to fiber draw-down
$\bar{m}$ = m at center of wavelength
$\Delta t = t_{n+1} - t_n$.

Our response simulation convects the end points of a given perturbative wavelength at their respective speeds, while computing local fiber

---

* Note that (62) results from a simplification of the characteristic equation, neglecting inertia effects, which in turn precludes initial conditions on perturbative velocities. However, it can be shown that the quantitative effect of this approximation on m is trivial (Ref. 19).

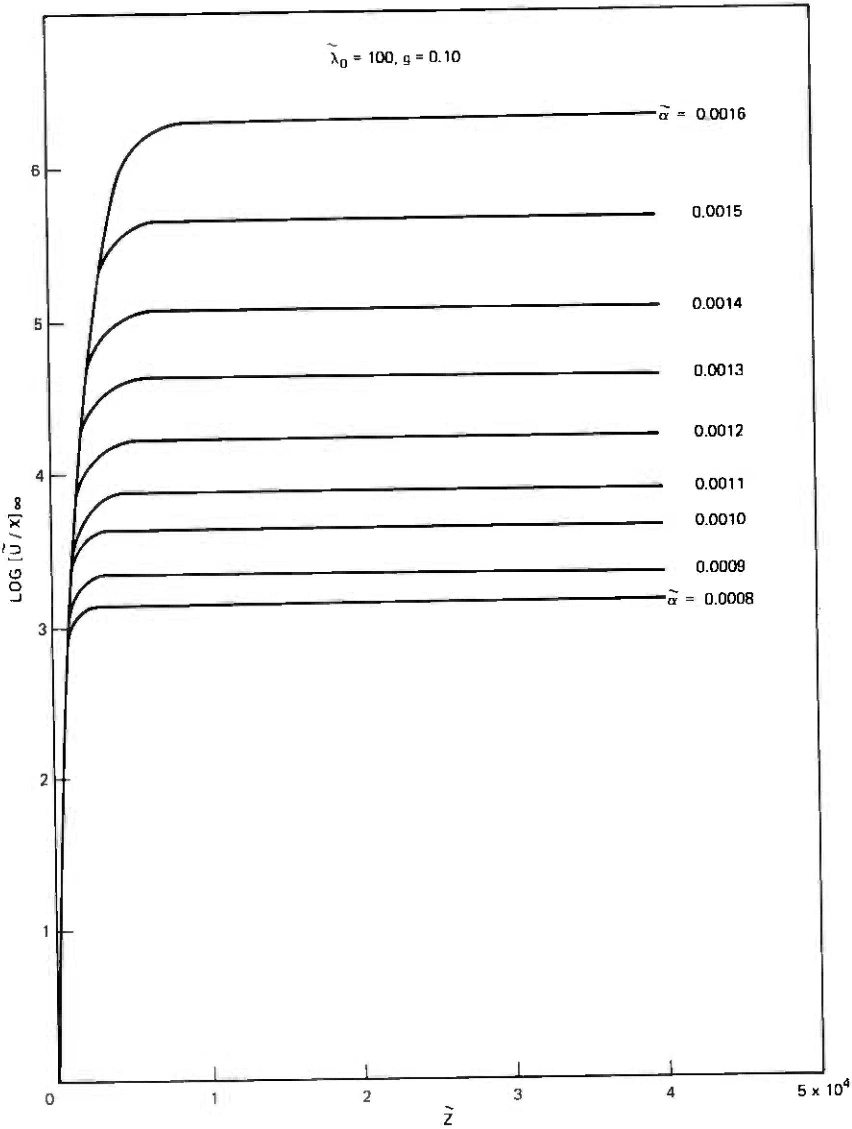

Fig. 10—Response histories for different values of $\tilde{\alpha}$.

properties from the base model (24). We use the notation:

$$\chi = a/a_0 \qquad \Psi = v/v_0 \qquad \eta = \mu/\mu_0$$
$$\tilde{U} = U/U_0, \qquad \tilde{\alpha} = \alpha a_0, \qquad \tilde{\lambda}_0 = \lambda_0/a_0,$$

and

$$\tilde{z} = (s + q)/2a_0,$$

where s, q, are end points of the perturbative wavelength. The nondimensionalized surface tension is assumed to vary as

$$\tilde{\sigma} = \tilde{\sigma}_0 e^{\tilde{\beta}\tilde{\alpha}\tilde{z}},$$

allowing for possible changes along the fiber (small values of $\tilde{\beta}$ approximate a linear dependence).

Figure 10 shows a set of response histories in terms of log $[\tilde{U}/\chi]$ for $g = 0.1$, $\bar{\lambda}_0 = 100$, $\tilde{\sigma}_0 = 0.25$, $\tilde{\beta} = 0$, $\eta_0 = 300$, and $0.0008 \leqq \tilde{\alpha} \leqq 0.0016$, illustrating the build-up to different asymptotic levels as a function of $\tilde{\alpha}$.

Figure 11 shows typical profiles of surface perturbations along the fiber for $\bar{\lambda}_0 = 15.7$, which corresponds to a frequency of 200 Hz. As expected, the varicose response consists of sinusoids whose wavelength is progressively stretched due to fiber draw-down and whose amplitudes are modulated according to a response history such as given in Fig. 10. Note that this behavior differs drastically from the tensile fiber response of Figs. 8 and 9, which are also driven by radial harmonic excitation at the origin.

Figure 12 displays asymptotic response amplitudes for a range of initial wave numbers $2\pi/\bar{\lambda}_0$ and several values of g, the terminal radius in units of a_0 for the base flow. For fixed g and $\tilde{\alpha}$, the response has a maximum in the neighborhood of $\bar{\lambda}_0 = 50$. The low responses at short wavelengths are due to vanishing of the Rayleigh instability as $\bar{\lambda}_0 \rightarrow 2\pi$

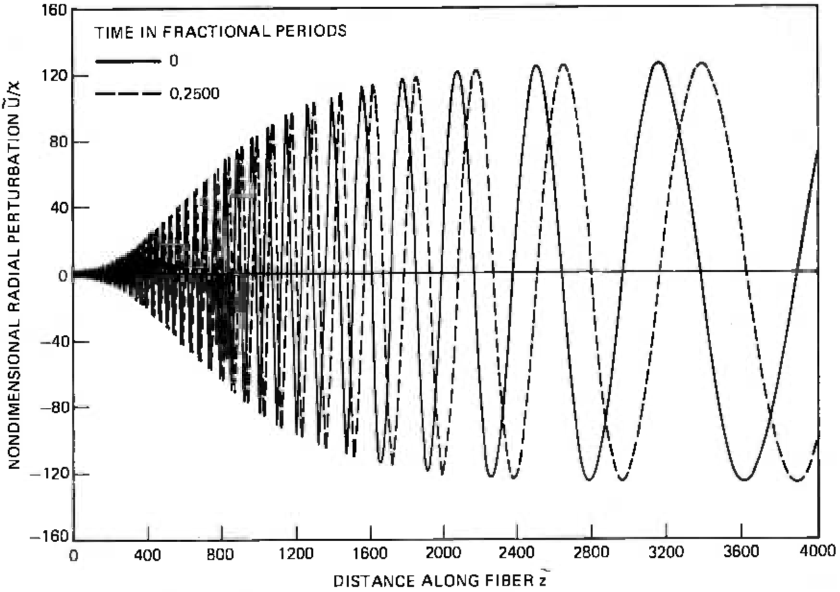

Fig. 11—Plot of deflected surface shapes for $\bar{\lambda}_0 = 15.7$.

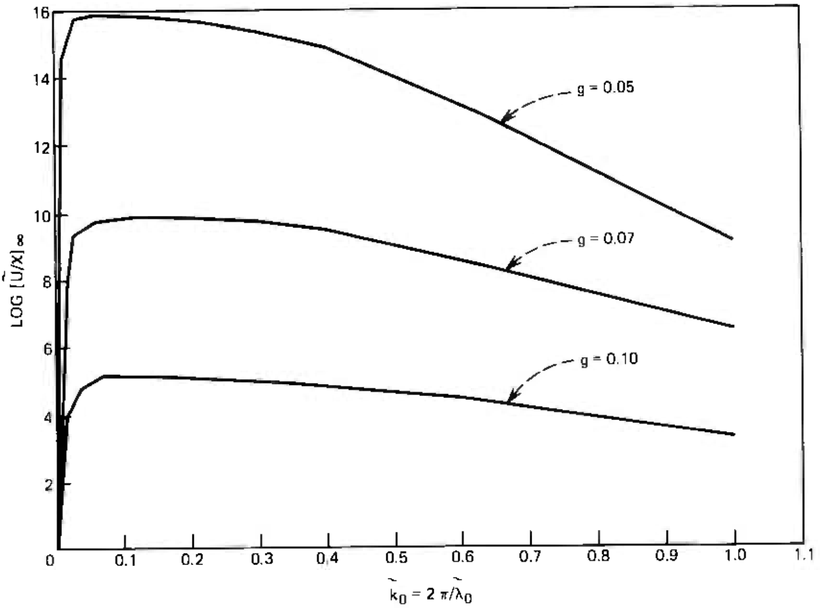

Fig. 12—Amplification factor vs dimensionless wave number for $\tilde{\alpha}$ = 0.001.

while for large $\tilde{\lambda}_0$, hence large $\tilde{z}_0$, the perturbations encounter a rapid viscosity build-up along the fiber. Contrast these response curves with the ones for tensile models, and a fundamental difference is again apparent.

The influence of the terminal radius g, is illustrated in Fig. 13. As expected with a in the denominator of (62), increased draw-down (decreasing g) will enhance terminal perturbations. The second curve on that figure indicates the effect of $\tilde{\beta}$, the growth rate of surface tension. Finally Fig. 14 shows the decrease in response with initial viscosity, η_0 and the increase with rising values of $\tilde{\sigma}_0$, the initial surface tension.

Since the above simulation averages fiber properties over a perturbative wavelength and does not ensure continuity of perturbative surface velocities between time steps, it seemed appropriate to corroborate it by a slightly different model, due to Tomotika,[17,18] which is also germane to our situation. In Tomotika's study, filament contraction is effected by a surrounding medium subjected to extensional shear flow, as in some of Taylor's experiments.[9] This apparent difference in base flow and the need to let ambient viscosity approach zero for our purposes seems to limit the applicability of Tomotika's model to the fiber-drawing problem. However, as we shall see, it agrees quite well with our adaptation of Rayleigh's theory.

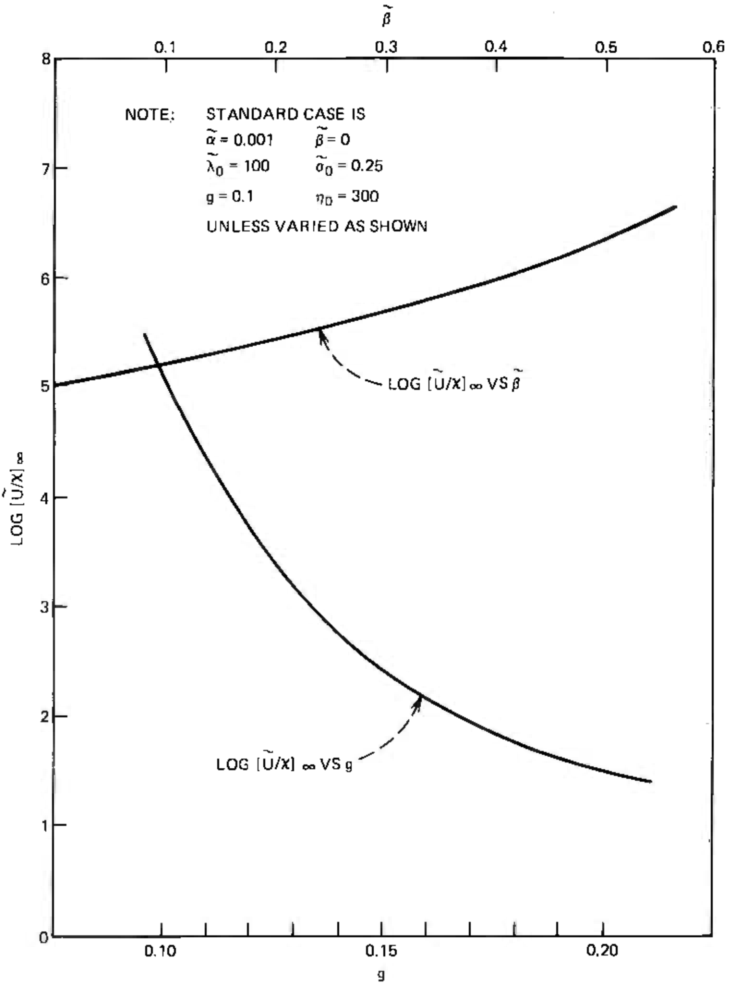

Fig. 13—Amplification factor vs g and $\tilde{\beta}$.

Tomotika finds the following asymptotic expression for interface perturbations as a function of several model parameters:

$$\log\,[\tilde{U}/\chi]_\infty = \tilde{\sigma}\xi\tilde{k}_0^{\frac{1}{2}} \int_0^{\tilde{k}_0} \psi(\tilde{k})d\tilde{k}, \tag{64}$$

where

ξ = ratio of filament to ambient viscosity
$\tilde{k} = 2\pi a/\lambda$ = local wave number of the perturbation
$\tilde{\sigma}$ = nondimensionalized surface tension
$\psi(\tilde{k})$ = a kernel that is detailed in the references.

The behavior of this expression is illustrated in Fig. 15 by plotting it against $\tilde{k}_0$ for various values of ξ. These plots show that, in the absence of quenching, the stabilizing effect of ambient shear flow diminishes steadily with ambient viscosity while the maximum response shifts to higher frequencies. This behavior is altered significantly if exponential changes of filament viscosity and surface tension are introduced to represent quenching effects, similar to our modification of Rayleigh's analysis. Equation (64) then changes to

$$\log\,[\tilde{U}/X]_\infty = \frac{\tilde{\sigma}_0}{3g^2\tilde{k}_0}\int_{g^2\tilde{k}_0}^{\tilde{k}_0} y(1-\tilde{k}^2)\,\varphi(\tilde{k})\,d\tilde{k}, \tag{65}$$

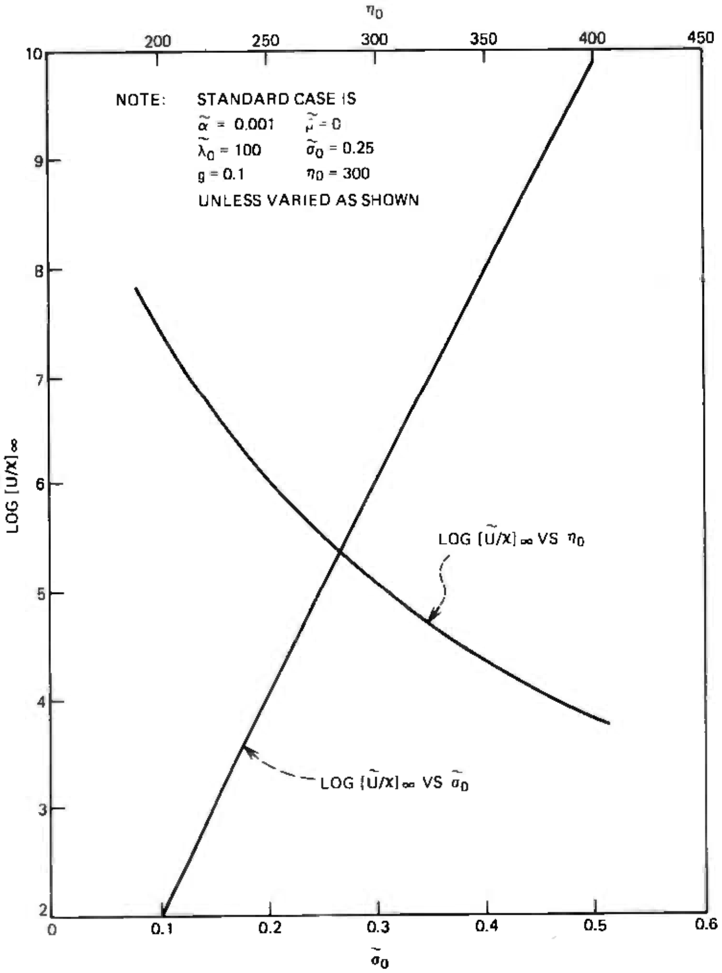

Fig. 14—Amplification factor vs η_0 and $\tilde{\sigma}_0$.

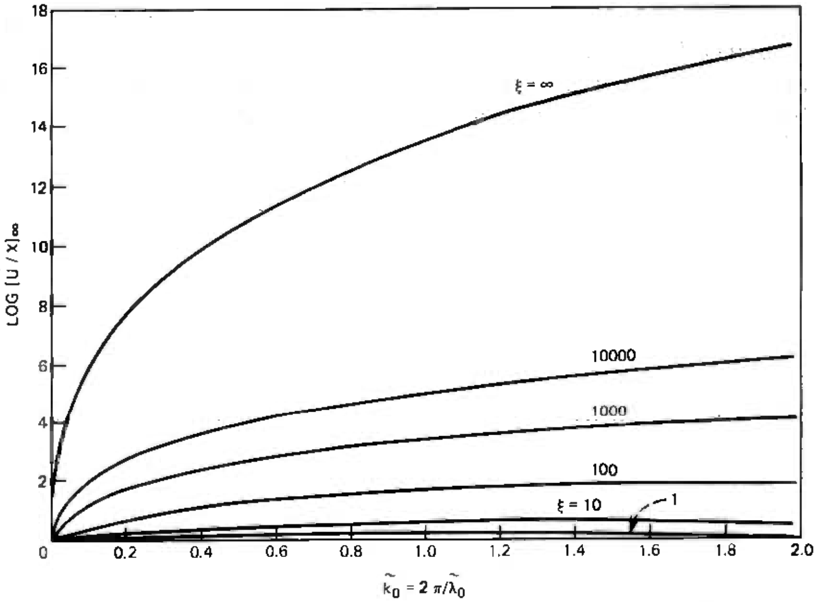

Fig. 15—Amplification factor vs $\tilde{k}_0$ for $\xi \rightarrow \infty$ (Tomotika's model with constant viscosity and surface tension).

where

$$y = e^{\tilde{\beta}\tilde{\alpha}\tilde{z}} = (1-g)^{\tilde{\beta}} \left[\left(\frac{\tilde{k}}{\tilde{k}_0} \right)^{\frac{1}{2}} - g \right]^{-\tilde{\beta}}$$

and $\varphi(\tilde{k})$ is another kernel detailed in the references. Plots of this expression in Fig. 16 show good agreement with Fig. 12 for large ξ (and $g = 0.1$). Plots of (65) for $\xi = 10^6$ and various values of the terminal base flow radius are given in Fig. 17. They show the same response of $[\tilde{U}/\chi]_\infty$ for $g \rightarrow 0$ as Fig. 13.

In summary, these results indicate that the two capillary models of quenched fiber responses, obtained by modifying Rayleigh's and Tomotika's analyses, are essentially equivalent. Note again that none of the response curves, such as Fig. 17, bear any resemblance to those of tensile fiber models.

An additional piece of insight into capillary response mechanisms comes from Weber's work.[19] He reproduces Rayleigh's analysis by a somewhat different approach and obtains an exact equation for m, as well as a simplified expression that agrees with (62). Weber shows that the small errors in (62) are essentially due to the neglect of radial components of the flow field. He demonstrates this conclusively by rederiving (62) from a one-dimensional representation (recorded in Appendix E) which captures all salient features of the capillary re-

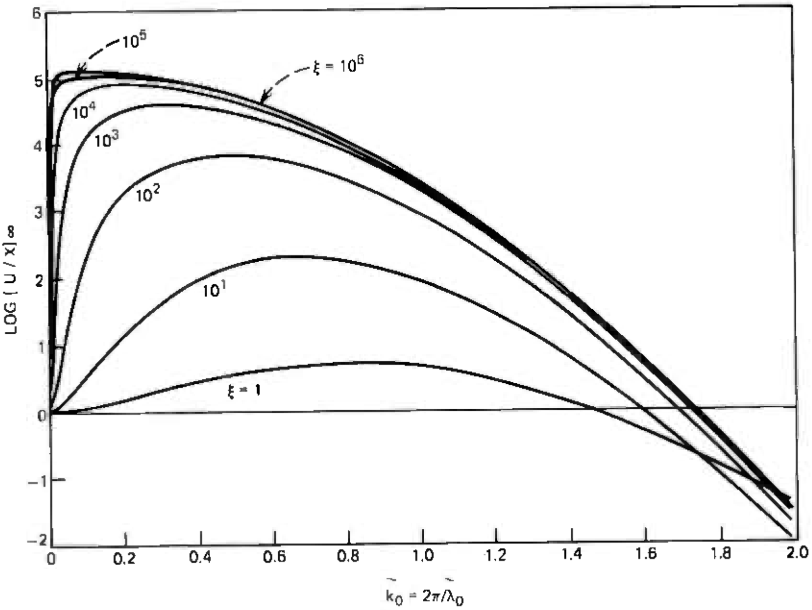

Fig. 16—Amplification factor vs $\tilde{k}_0$ for $\alpha = 0.001$, $g = 0.1$, and $1 \leqq \xi \leqq 10^6$ (modification of Tomotika's analysis for quenched base state).

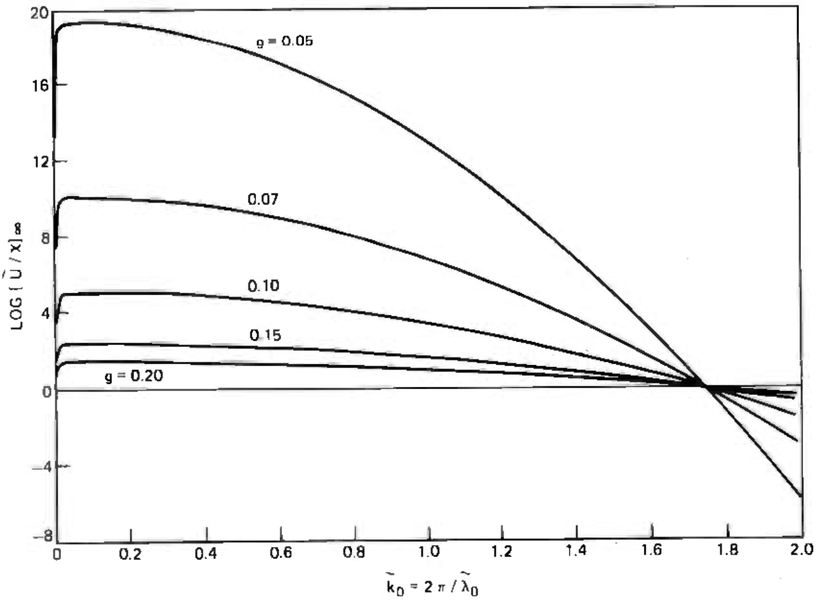

Fig. 17—Amplification factor vs $\tilde{k}_0$ for $\tilde{\alpha} = 0.001$, $\xi = 10^6$, and $0.005 \leqq g \leqq 0.20$ (modification of Tomotika's analysis for quenched base state).

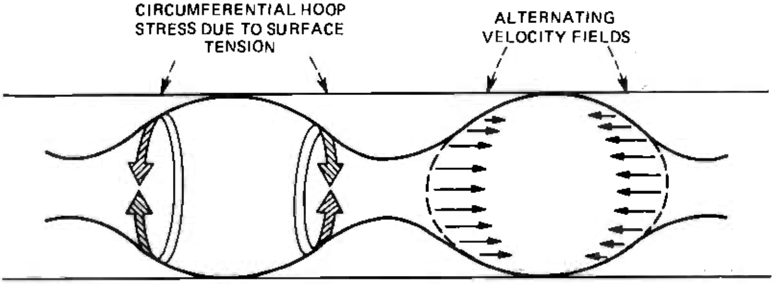

(a) CAPILLARY "PINCH–OFF"

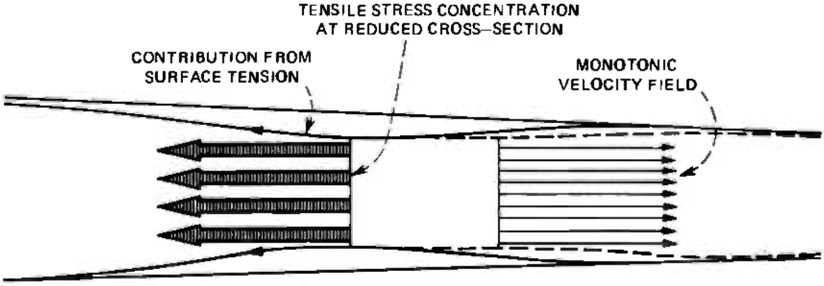

(b) TENSILE "NECK–DOWN"

Fig. 18—Comparison of capillary and tensile instabilities.

sponse mechanism. Thus, multidimensionality is not the criterion that distinguishes capillary from tensile response models. The fundamental difference seems rather to lie in the energy source from which the perturbations are fed: surface tension in one case and axial stress in the other.

Figure 18 attempts to emphasize this distinction in a pictorial fashion: (*i*) In the capillary model, surface tension, by overcoming viscous stresses, tends to accumulate fluid from both directions into periodic "beads," ultimately pinching off individual droplets as the minimum energy configuration. A multiplicity of such separations can occur independently of each other, and the essential physical mechanism is equally as valid for stationary, uniform filaments as it is for contracting base flows. (*ii*) In the tensile model, on the other hand, the "worst" among random localized constrictions, due to surface perturbations, causes a tensile stress concentration which further reduces the cross-sectional area and results in a single, "run-away" tensile separation. This is the familiar necking of any tensile test specimen. The tensile stress associated with draw-down in the base flow is an essential prerequisite for this mechanism. Surface tension will indeed contribute to tensile resistance in the necked down section, but it does not fundamentally alter the separation process.

Thus, the capillary mechanism is a contest between surface tension and viscosity, independent of filament draw-down, whereas in the tensile mechanism the viscous stresses, jointly with surface tension, attempt to resist the draw force.

IX. SUMMARY AND CONCLUSIONS

Several important observations result from the discussions in the preceding sections.

(*i*) Optical fiber drawing differs from textile fiber "spinning" in several essential ways. The flow of glass in the forming zone and draw-down region is dominated by viscous stresses. Inertia and surface tension play secondary roles. (They become noticeable only for the lower-melting glasses and then only in limited portions of the flow field.) This contrasts with polymer fiber forming, where, in some instances, viscosities can be quite low and other effects may be of comparable importance. Moreover, glass fibers are quenched over a wider range of temperatures than polymer fibers. This, together with the extreme temperature-dependence of glass viscosities, causes viscosity profiles along the draw path to rise much more abruptly than in textile fibers. Finally, and perhaps most importantly, molten glass can be considered very nearly Newtonian, which is not true for most polymers. Given the above physical features and the small-slope assumption of gradual draw-down, we can justify one-dimensional base states as useful representations of steady flow in the draw-down region.

(*ii*) Given a base-flow model, its sensitivity to changes in operating conditions, such as the take-up speed and temperature profile, can be estimated by first-order perturbations. It turns out that the draw-down profile is relatively insensitive to significant viscosity changes, assuming that interface conditions between the draw-down region and forming zone have been modeled correctly. For nontrivial forming zones, e.g., Fig. 1a, b, or d, it is difficult to make reasonable assumptions for these conditions. Since we lack a complete understanding of the forming zone, but expect its flow field to change with perturbations in the draw-down region, our results must be considered tentative.

(*iii*) Fundamental differences exist between the tensile and capillary models of dynamic fiber response. The tensile mechanism seems to prevail in most of the draw-down region. For low-melting glasses, we conjecture that the capillary model may apply in the short and very hot transition between forming zone and draw-down region, where surface tension can sustain perturbations that subsequently propagate by the tensile mechanism. The interactions of these two phenomena and their relation to dynamic responses in the forming zone itself are presently not understood. In the following we amplify each of these points to some extent.

The base-flow models we supplied in Section IV are admittedly qualitative. A heat-transfer analysis was circumvented in this preliminary study by assuming exponential viscosity profiles, suggested by qualitative experimental evidence. Exact solutions of the coupled one-dimensional momentum and heat-transfer equations are now being carried out to allow for different kinds of heating in the forming zone and various cooling mechanisms in the draw-down region. The resulting simulation will be able to provide more detailed operational trade-offs between steady drawing parameters. It will also assess the limited influence of fluid inertia, surface tension, and gravity. Finally, this modeling effort presents a natural opportunity for experimental corroboration by suitably instrumented steady-state runs, using laser and/or furnace-heated preforms or crucibles.

As an extension of one-dimensional base-flow models, radial-heat-transfer mechanisms should be simulated, leading to nonuniform cross-sectional viscosity distributions at the start of the draw-down region. These viscosity distributions must be input to a perturbation model of axisymmetric free surface flow which generates the nonplanar velocity profiles expected in the transition between forming zone and draw-down region. Ultimately, the detailed flow fields of forming zones such as Fig. 1b and d may have to be simulated by discretization techniques. If properly combined, these efforts may, hopefully, result in a unified base-flow model that properly allows for interactions between the draw-down region and forming zone in representing steady-state responses to changes in the control parameters of the draw process.

Finally, as mentioned before, it appears that vastly different frequency response curves and longitudinal profiles of surface perturbations characterize tensile and capillary dynamic responses as fundamentally distinct physical mechanisms. (Note the intuitive distinctions given at the end of Section VIII.) They do not seem derivable, in proper relation, from some universal fiber stability analysis. The question is then, what must be done to develop them into parts of a realistic and unified dynamic response model.

Since analytic solutions for tensile responses of nontrivial base flows in the draw-down region are not possible, numerical solutions by modal analysis or space-time integration are being attempted. This is expected to shed further light on the anti-intuitive response profiles obtained from the "inertialess" perturbation equations. Similarly, the capillary model applied so far to an elementary base flow may be implemented, by numerical means, for conditions representative of the transition between forming zone and draw-down region. Combining these extensions of the tensile and capillary response models, it may be possible to relate dynamic records of thermal or mechanical surface perturbations coming out of the forming zone to diameter variations in the finished fiber.

X. ACKNOWLEDGMENTS

I am indebted to Professor G. M. Homsy for numerous discussions of this study, to J. A. Lewis for detailed suggestions, and to P. G. Simpkins and E. Y. Harper for many helpful comments on this manuscript.

APPENDIX A

Implications of the Small-Slope Approximation

We briefly sketch the consequences of the small-slope approximation, $|a_z| \ll 1$ and $|u/v| \ll 1$, as they evolve from (1), (2), (3), and (4) by scaling arguments. Let

$$\begin{aligned} &v = v_0\Psi, \qquad u = u_0\varphi, \qquad \mu = \mu_0\eta, \qquad p = p_0\iota, \\ &a = a_0\chi, \qquad r = a_0\xi, \qquad z = L\zeta, \quad \text{and} \quad t = \frac{L}{v_0}\tau. \end{aligned} \tag{66}$$

Then the small-slope assumption amounts to

$$\left|\frac{u_0}{v_0}\right| = 0\left(\frac{a_0}{L}\right) = \epsilon \ll 1.$$

Substitution of (66) into (4) yields

$$\begin{aligned} \tau_z &= \frac{\mu_0 v_0}{L}\left[-\frac{p_0 L}{\mu_0 v_0}\iota + 2\eta\Psi_\zeta\right] \doteq \frac{\mu_0 v_0}{L}\tilde{\tau}_z \\ \tau_r &= \frac{\mu_0 v_0}{L}\left[-\frac{p_0 L}{\mu_0 v_0}\iota + 2\eta\varphi_\xi\right] \doteq \frac{\mu_0 v_0}{L}\tilde{\tau}_r \\ \tau_\theta &= \frac{\mu_0 v_0}{L}\left[-\frac{p_0 L}{\mu_0 v_0}\iota + 2\eta\varphi/\xi\right] \doteq \frac{\mu_0 v_0}{L}\tilde{\tau}_\theta \\ \tau_{rz} &= \frac{\mu_0 v_0}{L}\eta\left[\frac{1}{\epsilon}\Psi_\xi + \epsilon\varphi_\zeta\right] \doteq \frac{\mu_0 v_0}{L}\tilde{\tau}_{rz}, \end{aligned} \tag{67}$$

where $p_0 L/\mu_0 v_0 = 0(1)$ and will be omitted henceforth. Substituting

(66) and (67) into (3),

$$\frac{\rho v_0 L}{\mu_0}\left[\Psi_\tau + \left(\frac{\mu_0 L}{v_0 a_0}\right)(\varphi\Psi_\xi + \Psi\Psi_\zeta)\right]$$
$$= (-\iota + 2\eta\Psi_\zeta)_\zeta + \frac{1}{\epsilon^2}\frac{1}{\xi}[\xi\eta(\Psi_\xi + \epsilon^2\varphi_\zeta)]_\xi.$$

Considering the case $\rho v_0 L/\mu_0 = Re \ll 1$,

$$0 = \epsilon^2(-\iota + 2\eta\Psi_\zeta)_\zeta + \frac{1}{\xi}[\xi\eta(\Psi_\xi + \epsilon^2\varphi_\zeta)]_\xi.$$

Hence,

$$(\xi\eta\Psi_\xi)_\xi = 0.$$

If no constraint is to be imposed on η, we have

$$\Psi_\xi = 0 \tag{68}$$

and

$$\tau_{rz} = \frac{\mu_0 v_0}{L}\epsilon\eta\varphi_\zeta = 0[\epsilon(\tau_z, \tau_r, \tau_\theta)].$$

Now, from (1),

$$\Psi_\zeta + \left(\frac{\mu_0 L}{v_0 a_0}\right)(\varphi_\xi + \varphi/\xi) = 0$$

and because of (68)

$$\varphi_\xi = \varphi/\xi = -\tfrac{1}{2}\Psi_\zeta. \tag{69}$$

Then,

$$\begin{aligned}\tilde{\tau}_r = \tilde{\tau}_\theta &= -\iota - \eta\Psi_\zeta \\ \tilde{\tau}_{rz} &= -\frac{\epsilon}{2}\eta\xi\Psi_{\zeta\zeta}\end{aligned} \tag{70a}$$

and

$$\tilde{\tau}_z = -\iota + 2\eta\Psi_\zeta. \tag{70b}$$

ι is determined from the normal stress condition at the fiber surface $\xi = \chi$. In dimensional form,

$$\tau_r + a_z^2\tau_z - 2a_z\tau_{rz} = \frac{\sigma(aa_{zz} - a_z^2 - 1)}{a(1 + a_z^2)^{\frac{1}{2}}}. \tag{71}$$

Substituting (66) and (70) into (71) and dropping terms of $0(\epsilon^2)$ and higher, as well as a_{zz}, one finds

$$\iota = \frac{\tilde{\sigma}}{\chi} - \eta\Psi_\zeta \tag{72}$$

for all values of ξ, where $\tilde{\sigma} = \sigma L/\mu_0 v_0 a_0$. With this result, $\tilde{\tau}_z$ from (70a) becomes

$$\tilde{\tau}_z = -\frac{\tilde{\sigma}}{\chi} + 3\eta\Psi_\zeta, \tag{73}$$

where 3η constitutes the "Trouton" viscosity. (The additional $\eta\Psi_\zeta$

term, augmenting $2\eta\Psi_\zeta$ in (70), originated in $\bar{\tau}_r$ of (71). This, in turn, is due to φ_ξ of (67), the cross-sectional contraction that necessarily accompanies the extensional flow of fiber drawing.) We also note from (72) and (70) that

$$(\iota + \eta\Psi_\zeta)_\xi = \tau_{r_\xi} = \tau_{\theta_\xi} = 0, \tag{74}$$

which agrees with the radial equilibrium equation if (66), (68), and (70) are used in (2) and we let $Re \ll 1$.

The tangential surface stress condition at $\xi = \chi$ reads

$$a_z(\tau_r - \tau_z) + (1 + a_z^2)\tau_{rz} = 0 \tag{75}$$

and, if rendered dimensionless, has leading terms of $0(\epsilon)$; hence, it will be ignored. For completeness, we also note that the kinematic boundary condition (7), rendered dimensionless and time-invariant, yields

$$\frac{\Psi_\zeta}{\Psi} = -\frac{2\chi_\zeta}{\chi},$$

which is the time-invariant continuity equation (9).

APPENDIX B

Second-Order Perturbation Term for the Base-Flow Solution [Eq. (17)]

$$\begin{aligned}
\mathcal{K}[a, b, c, d, \zeta] = {} & \zeta\left(1 + \frac{ab^2}{2} + d + \frac{d^2}{2} + \frac{d^3}{6}\right) + \frac{\zeta_c^2}{2}\left(1 + d + \frac{d^2}{2}\right) \\
& + \frac{\zeta^3c^2}{6}(1 + d) + \frac{\zeta^4c^3}{24} \\
& + \frac{1}{lnE}\left[\left(1 + d + \frac{d^2}{2}\right)(ae^{\zeta lnE} - 2be^{-(lnE/2)\zeta})\right. \\
& + (1 + d)\left(\frac{a^2}{4}e^{2\zeta lnE} + 2abe^{(lnE/2)\zeta} - \frac{b^2}{2}e^{-\zeta lnE}\right) \\
& \left. + \frac{a^3}{18}e^{3\zeta lnE} + \frac{a^2b}{3}e^{(3lnE/2)\zeta} - \frac{b^3}{9}e^{-(3lnE/2)\zeta}\right] \\
& - \frac{11}{lnE}\left[(a - 2b)\left(1 + d + \frac{d^2}{2}\right)\right. \\
& \left. + \left(\frac{a^2}{4} + 2ab - \frac{b^2}{2}\right)(1 + d) + \frac{a^3}{18} + \frac{a^2b}{3} + \frac{b^3}{9}\right] \\
& + c\left\{(1 + d)\left[aF(lnE, \zeta) + bF\left(-\frac{lnE}{2}, \zeta\right)\right]\right. \\
& + \frac{a^2}{2}F(2lnE, \zeta) + abF\left(\frac{lnE}{2}, \zeta\right) + \frac{b^2}{2}F(-lnE, \zeta) \\
& \left. + \frac{c^2}{2}\left[aG(lnE, \zeta) + bG\left(-\frac{lnE}{2}, \zeta\right)\right]\right\},
\end{aligned}$$

where

$$F(\gamma, \zeta) = \frac{1}{\gamma}\left[(\zeta - \gamma)e^{\gamma\zeta} + \frac{1}{\gamma}\right]$$

and

$$G(\gamma, \zeta) = \frac{1}{\gamma}\left[\left(\zeta^2 + \frac{2\zeta}{\gamma} + \frac{2}{\gamma^2}\right)e^{\gamma\zeta} - \frac{2}{\gamma^2}\right].$$

APPENDIX C

Differential Equations for First-Order Dynamic Perturbations in the Radius, $\hat{a}$

Using (33) to eliminate $\hat{v}$ from the first-order variations of the momentum equations, we obtain from (35), which reflects the quenched, inertia-dominated base state (23) with inertia effects in the perturbation equation,

$$\begin{aligned}\hat{a}'''' + \hat{a}^{\cdot\prime\prime\prime}e^{-2\mathfrak{z}} + 2\hat{a}''' - 4\hat{a}^{\cdot\prime\prime}e^{-2\mathfrak{z}} - 2\hat{a}^{\cdot\cdot\prime}e^{-4\mathfrak{z}} + 8\hat{a}^{\cdot\cdot}e^{-4\mathfrak{z}} \\ - 4\hat{a}'' - 8\hat{a}' = 4\hat{v}' + 4\hat{v}'' + \hat{v}'''.\end{aligned} \quad (76)$$

From (34), the inertialess momentum equation, and the unquenched, inertialess base state (22), we obtain

$$\hat{a}'' + \hat{a}^{\cdot\prime}e^{-2\mathfrak{z}} = \hat{v}'. \quad (77)$$

Note in (76) and (77) that $(\ )' = \partial(\ )/\partial\mathfrak{z}$ and $(\ )^{\cdot} = \partial(\ )/\partial\tau$, where $\mathfrak{z} = \alpha z/L$ and $\tau = \alpha v_0 t/L$. Finally, from (28) and (30), the inertialess momentum equation with the quenched inertialess base state (25), we can find

$$\left(\frac{\partial}{\partial\zeta} + \frac{1}{\psi}\frac{\partial}{\partial\tau}\right)(\hat{a}' + \alpha\hat{a}) = \frac{e^{-\alpha\zeta}}{2}\hat{v}', \quad (78)$$

where $\psi = v/v_0$ as in (25), $\zeta = z/L$ and $\tau = tv_0/L$. In this case, $(\ )' = \partial(\ )/\partial\zeta$.

APPENDIX D

Detailed Results for Forced Dynamic Responses of the Tensile Fiber Model

The detailed expressions for A_1 and A_2 resulting from (58) and (61) are

$$\begin{aligned}A_1 = \Bigg\{\frac{1}{2}[\cos]^{\omega/2}_{\omega\eta} + \frac{(1-\epsilon)\omega}{4\epsilon(B_1^2 + B_2^2)} \times [(-B_1 \sin\omega/2 + B_2\cos\omega/2) \\ \times [Ci]^{\omega/2}_{\omega/2\epsilon} - (B_1\cos\omega/2 + B_2\sin\omega/2) \times [Si]^{\omega/2}_{\omega/2\epsilon}]\Bigg\}\end{aligned}$$

$$\begin{aligned}A_2 = \Bigg\{\frac{1}{2}[\sin]^{\omega/2}_{\omega\eta} + \frac{(1-\epsilon)}{4\epsilon(B_1^2 + B_2^2)} \times [(B_1\cos\omega/2 + B_2\sin\omega/2) \\ \times [Ci]^{\omega/2}_{\omega/2\epsilon} + (-B_1\sin\omega/2 + B_2\cos\omega/2) \times [Si]^{\omega/2}_{\omega/2\epsilon}]\Bigg\},\end{aligned}$$

where $\epsilon = e^{2\mathfrak{z}_L}$ and

$$
\begin{aligned}
B_1 &= \left[Ci + \frac{\omega}{2\epsilon} Si + \cos \right]_{\omega/2\epsilon}^{\omega/2} \\
B_2 &= \left[Si - \frac{\omega}{2\epsilon} Ci + \sin \right]_{\omega/2\epsilon}^{\omega/2} .
\end{aligned}
\tag{79}
$$

Recall that $\mathfrak{z} = \alpha z/L$.

We now parallel the development of Section VII for the quenched base flow (25). Equation (78) with $\hat{v} \equiv 0$ suggests a solution of the form

$$
\hat{a}(\zeta, \tau) = Re \left\{ f_0 \int_0^{\zeta} \exp[\alpha(\zeta' - \zeta)] \exp[i\omega(\tau - \xi)] d\zeta' + \Phi_0 \exp(i\omega\tau - \alpha\zeta) \right\} ,
$$

where

$$
\xi = \int_0^{\zeta'} \frac{d\zeta^*}{v(\zeta^*)}, \qquad f_0 = f_1 + i f_2, \qquad \Phi_0 = \Phi_1 + i\Phi_2. \tag{80}
$$

Explicitly,

$$
\hat{a}(\zeta, \tau) = A_1 \sin \omega\tau + A_2 \cos \omega\tau,
$$

where

$$
\begin{aligned}
A_1(\zeta) &= \int_0^{\zeta} e^{\alpha(\zeta' - \zeta)} (f_1 \sin \omega\xi - f_2 \cos \omega\xi) d\zeta' - \Phi_2 e^{-\alpha\zeta}, \\
A_2(\zeta) &= \int_0^{\zeta} e^{\alpha(\zeta' - \zeta)} (f_1 \cos \omega\xi + f_2 \sin \omega\xi) d\zeta' + \Phi_1 e^{-\alpha\zeta},
\end{aligned}
\tag{81}
$$

describing the ζ-dependent phase and amplitude of the response. Note that $\zeta = z/L$ and $\tau = tv_0/L$, whereas in (79) $\mathfrak{z} = \alpha\zeta$ and $\tau = \alpha v_0 t/L$.

We use the same boundary conditions as in developing (52). For cyclic radial perturbations at $\zeta = 0$,

$$
\hat{a}(0, \tau) = \sin \omega\tau, \tag{82}
$$

together with the velocity conditions

$$
\hat{v}(0, \tau) \equiv 0 \qquad \hat{v}(1, \tau) \equiv 0.
$$

An expression for $\hat{v}$ is obtained by eliminating $\hat{v}'$ from (28) and (30)

$$
\hat{v} = \frac{2}{v'} \hat{a}^{\cdot} + \frac{2v}{v'} \hat{a}' - 2\hat{a} + 2G(\tau), \tag{83}
$$

where $G(\tau)$ is an arbitrary time function and the differentiation symbols mean $(\ )^{\cdot} = \partial(\ )/d\tau$, $(\ )' = \partial(\ )/\partial\zeta$. Substituting (81) into (83) we find

$$
\hat{v}(\zeta, \tau) = V_1 \sin \omega\tau + V_2 \cos \omega\tau
$$

with

$$\begin{aligned}
V_1(\zeta) = \frac{-2\omega}{\psi'} \int_0^{\zeta} & e^{\alpha(\zeta'-\zeta)}(f_1 \cos \omega\xi + f_2 \sin \omega\xi) d\zeta' \\
& - 2 \int_0^{\zeta} e^{\alpha(\zeta'-\zeta)}(f_1 \sin \omega\xi - f_2 \cos \omega\xi) d\zeta' \\
& + 2e^{-\alpha\zeta} \left[\left(\frac{\psi}{\psi'} \alpha + 1 \right) \Phi_2 - \frac{\omega}{\psi'} \Phi_1 \right] \\
& \qquad + \frac{2\psi}{\psi'} (f_1 \sin \omega\xi - f_2 \cos \omega\xi) + 2G_1 \\
V_2(\zeta) = \frac{2\omega}{\psi'} \int_0^{\zeta} & e^{\alpha(\zeta'-\zeta)}(f_1 \sin \omega\xi - f_2 \cos \omega\xi) d\zeta' \\
& - 2 \int_0^{\zeta} e^{\alpha(\zeta'-\zeta)}(f_1 \cos \omega\xi + f_2 \sin \omega\xi) d\zeta' \\
& - 2e^{-\alpha\zeta} \left[\frac{\omega}{\psi'} \Phi_2 + \left(\frac{\psi}{\psi'} \alpha + 1 \right) \Phi_1 \right] \\
& \qquad + \frac{2\psi}{\psi'} (f_1 \cos \omega\xi + f_2 \sin \omega\xi) + 2G_2.
\end{aligned} \tag{84}$$

Ultimately, (82) leads to

$$\begin{aligned}
& \Phi_1 = 0, \qquad \Phi_2 = -1 \\
& f_1 = (B_1 C_1 + B_2 C_2)/(B_1^2 + B_2^2) \qquad f_2 = (f_1 B_2 - C_2)/B_1 \\
& G_1 = 1 + \frac{1}{\psi_0'} (\alpha + f_2 \cos \omega\xi_0 - f_1 \sin \omega\xi_0) \\
& G_2 = -\frac{1}{\psi_0'} (\omega + f_1 \cos \omega\xi_0 + f_2 \sin \xi_0),
\end{aligned} \tag{85}$$

where

$$\begin{aligned}
B_1 &= \frac{\omega}{\psi_1'} H(1) - K(1) + \frac{\psi_1}{\psi_1'} \cos \omega\xi_1 - 1 \\
B_2 &= -\frac{\omega}{\psi_1'} K(1) - H(1) + \frac{\psi_1}{\psi_1'} \sin \omega\xi_1 \\
C_1 &= \frac{\omega}{\psi_0'} - \frac{\omega}{\psi_1'} e^{-\alpha} \\
C_2 &= \left(\frac{\psi_1}{\psi_1'} \alpha + 1 \right) e^{-\alpha} - \frac{\alpha}{\psi_0'} - 1.
\end{aligned} \tag{86}$$

The subscripts 0, 1 denote evaluation at $\zeta = 0, 1$ respectively, and the quantities H, K are defined as

$$\begin{aligned}
H(\zeta) &= \int_0^{\zeta} e^{\alpha(\zeta'-\zeta)} \sin \omega\xi d\zeta' \\
K(\zeta) &= \int_0^{\zeta} e^{\alpha(\zeta'-\zeta)} \cos \omega\xi d\zeta'.
\end{aligned} \tag{87}$$

With this notation, we ultimately get

$$\hat{a}(\zeta, \tau) = [f_1 H(\zeta) - f_2 K(\zeta) + e^{-\alpha\zeta}] \sin \omega\tau + [f_1 K(\zeta) + f_2 H(\zeta)] \cos \omega\tau. \tag{88}$$

APPENDIX E

Weber's Derivation of the Capillary Stability Equation

This appendix gives a simplified derivation of the stability equation for the capillary fiber model based on assumptions that are quite equivalent to those made for the one-dimensional tensile model. In fact, the rationale used here closely parallels that of Section III.

The analysis proceeds in terms of equilibrium and continuity equations, which we write in dimensional form for the entire filament cross-section. The perturbed surface radius becomes $a + \delta$ and a given cross-sectional element is displaced by vdt along the fiber over the time increment dt. The radius of this element now becomes

$$a + \delta + \frac{\partial \delta}{\partial t} dt + \frac{\partial \delta}{\partial z} vdt. \tag{89}$$

Since the last term is of higher order, it will be neglected.

The constitutive relations are as in (4) and the derivation of an expression for τ_z is quite similar to Appendix A. The main difference arises in the radial stress boundary condition, where, in distinction from the treatment of (72), the longitudinal curvature term cannot be neglected for varicose perturbations. Then the r.h.s. of (72) becomes

$$\sigma \left(\frac{\delta}{a^2} + \delta'' \right) \tag{90}$$

and, instead of (74),

$$\tau_z = \sigma \left(\frac{\delta}{a^2} + \delta'' \right) + 3\mu v'. \tag{91}$$

The continuity equation yields

$$\frac{2}{a} \dot{\delta} + v' = 0. \tag{92}$$

Now, combining (9) and (10),

$$\tau_z' = \rho \dot{v} + \rho v v', \tag{93}$$

where the last term was apparently overlooked by Weber but seems to have little effect on the resulting stability equation.

Substituting (91) and (92) into (93) and assuming surface perturbations of the form $\delta = \delta^* e^{mt} \cos kz/a$, leads to the stability equation

$$m^2 + m \frac{(3\mu)}{\rho a^2} \bar{k}^2 = \frac{\sigma}{2\rho a^3} (1 - \bar{k}^2) \bar{k}^2. \tag{94}$$

The unstable root, of interest here, is

$$m = -\frac{(3\mu)\tilde{k}^2}{2\rho a^2} + \left[\frac{\sigma}{2\rho a^3}(1-\tilde{k}^2)\tilde{k}^2 + \frac{(3\mu)^2\tilde{k}^4}{4\rho^2 a^4}\right]^{\frac{1}{2}}. \qquad (95)$$

REFERENCES

1. A. Ziabicki and R. Takserman-Krozer, "Formation and Breakage of Liquid Threads: I. Mechanism," Rocz. Chem., Ann. Soc. Chim. Polonorum, *37* (1963), p. 1503.
2. Ibid.: V. Range of Occurrence of the Individual Break Processes: General Conclusions," *38* (1964), p. 653.
3. Ibid.: VI. Following the Break Process with High-Speed Photography," *38* (1964), p. 1221.
4. A. Ziabicki, "Principles of Melt Spinning," in *Man Made Fibers*, eds., H. F. Mark, S. M. Atlas, and E. Cernia, Interscience, 1967, pp. 169–240.
5. J. R. A. Pearson and M. A. Matovitch, "Spinning a Molten Threadline, Part I," Ind. and Eng. Chem. Fundamentals, *8* (1969), p. 512.
6. S. Kase and T. Matsuo, "Studies on Melt Spinning: I. Fundamental Equations on the Dynamics of Melt Spinning," J. Appl. Polym. Sci., Part A, *3* (1965), p. 2541.
7. Ibid.: II. Steady State and Transient Solutions of Fundamental Equations Compared With Experimental Results," J. Appl. Polym. Sci., *11* (1967), p. 251.
8. M. M. Denn and C. J. S. Petrie, "Instabilities in Polymer Processing," A. I. Ch. E. Journal, March 1976, p. 209.
9. G. I. Taylor, "The Formation of Emulsions in Definable Fields of Flow," Proc. Roy. Soc., Series A, *146* (1934), p. 501.
10. E. A. J. Marcatili, "What Kind of Optical Fiber for Long-Distance Transmission?," S.P.I.E. Journal, *8* (1970), p. 101.
11. S. S. Kutukov and M. D. Khodakovskii, "Investigating the Movement of Glass in the Forming of Continuous Glass Fiber by High Speed Filming," Inst. of Glass Fiber, translated from Steklo i Keramika, *21*, No. 2 (1964), pp. 3–10.
12. A. Ziabicki and R. Takserman-Krozer, "Formation and Breakage of Liquid Threads, II. Cohesive Break of a Steady Liquid Jet," Rocz. Chem., Ann. Soc. Chim. Polonorum, *37* (1963), p. 1511.
13. Ibid.: IV. Effect of Rheological Behavior on Length of Liquid Threads," *38* (1964), p. 465.
14. J. R. A. Pearson and M. A. Matovitch, "Spinning a Molten Threadline, Part II," Ind. and Eng. Chem. Fundamentals, *8* (1969), p. 605.
15. S. Chandrasekhar, *Hydrodynamic and Hydromagnetic Stability*, Oxford: Clarendon Press, 1961.
16. Lord Rayleigh, "On the Instability of a Cylinder of Viscous Liquid Under Capillary Force," Phil. Mag., *34* (1892), p. 145.
17. S. Tomotika, "On the Instability of a Cylindrical Thread of a Viscous Liquid Surrounded by Another Viscous Fluid," Proc. Roy. Soc., *A150* (1935), p. 322.
18. S. Tomotika, "Breaking up of a Drop of Viscous Liquid Immersed in Another Viscous Fluid Which is Extending at a Uniform Rate," Proc. Roy. Soc., *A153* (1936), p. 302.
19. C. Weber, "Zum Zerfall eines Flüssigkeitsstrahles," Zeitschrift f. ang. Math. und Mech., *11* (1931), p. 136.
20. A. Ziabicki and R. Takserman-Krozer, "Formation and Breakage of Liquid Threads, III. Capillary Break-up of a Steady Viscous Jet," Rocz. Chem. Ann. Soc. Chim. Polonorum, *37* (1963), p. 1607.
21. S. Kasé, "Studies on Melt Spinning: III. Velocity Field Within the Thread." J. Appl. Polym. Sci., *18* (1974), p. 3267.
22. Ibid.: IV. On the Stability of Melting Spinning." *18* (1974), p. 3279.
23. S. Krishnan and L. R. Glicksman, "A Two-Dimensional Analysis of a Heated Free Jet at Low Reynolds Numbers," J. of Basic Eng., *93*, No. 3 (1971), p. 355.
24. F. T. Geyling, "The Glass Fiber Drawing Process and Its Stability Characteristics," 14th International Congress of Theoretical and Applied Mechanics, Delft, Netherlands (1976).
25. G. J. Donnelly and C. B. Weinberger, "Stability of Isothermal Fiber Spinning of a Newtonian Fluid," Ind. and Eng. Chem. Fundamentals, *14* (1975), p. 334.

Copyright © 1976 American Telephone and Telegraph Company
THE BELL SYSTEM TECHNICAL JOURNAL
Vol. 55, No. 8, October 1976
Printed in U.S.A.

An Injection-Molded Plastic Connector for Splicing Optical Cables

By A. H. CHERIN and P. J. RICH

(Manuscript received February 24, 1976)

An injection-molded plastic splice connector for splicing optical cables has been fabricated and evaluated. Five optical cables containing 90-μm OD *graded-index fibers with 55-μm core diameters were spliced, yielding an average splice loss of 0.20 dB for the 425 splice joints measured. Fifty percent of the losses measured were less than 0.1 dB and 95 percent of the splice joints had losses less than 0.8 dB.*

Assembly methods for splicing optical cables using this connector and a multiribbon optical-fiber cutting tool capable of cutting 144 fibers simultaneously are also described.

I. INTRODUCTION

The feasibility of splicing groups of optical fibers in a laboratory environment has been demonstrated by a number of investigators.[1–5] The next phase in the development of optical-fiber splicing is to produce splice connectors, based on the concepts that have shown laboratory feasibility that are adaptable to field use. A field-adaptable splicing technique will require that telephone crafts people be able to splice groups of optical fibers in a routine fashion, with relatively simple tools, in a hostile field environment.

In this paper, an injection-molded splice connector fabricated using a mold designed to optimize reproduction of mold dimensions is described and evaluated. Assembly methods for splicing optical cables using this connector and a multiribbon optical-fiber cutting tool capable of cutting 144 fibers simultaneously are also described.

II. DESCRIPTION OF SPLICE CONNECTOR AND PRECISION-MOLDING TECHNIQUES

A precision metal mold was used to fabricate a 12-ribbon, multigroove substrate with prealigning slots. The molded plastic substrate which forms the base for the optical cable splice connector is shown in Fig. 1. It consists of twelve sections. Each section has a prealignment slot and a set of twelve fiber-alignment grooves spaced 90 μm apart.

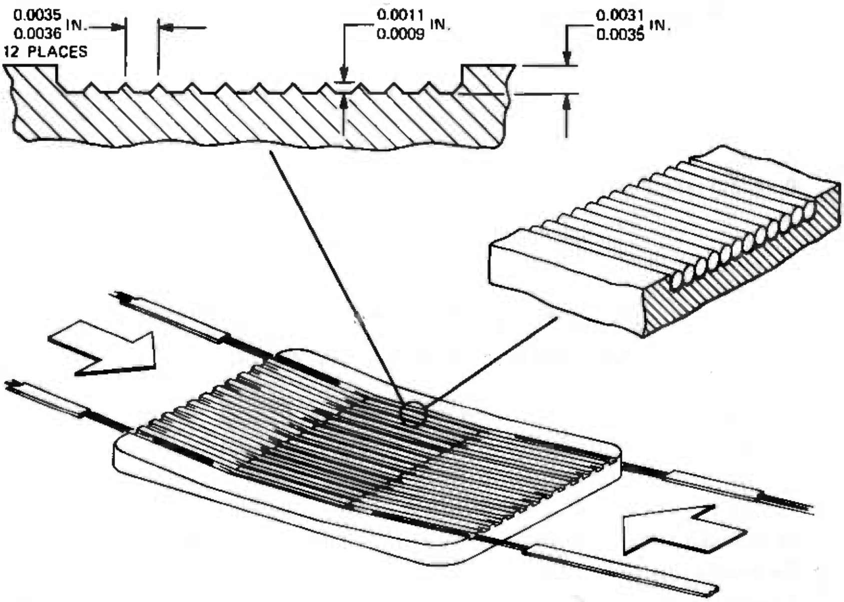

Fig. 1—Precision-molded substrate for 12 × 12 optical-fiber splice connector.

The splice is made by properly seating a precut set of ribbons into grooves and sliding them together to form a butt joint. A coverplate is attached to the substrate and matching material is injected through a slot in the coverplate to complete the splice. The completed splice

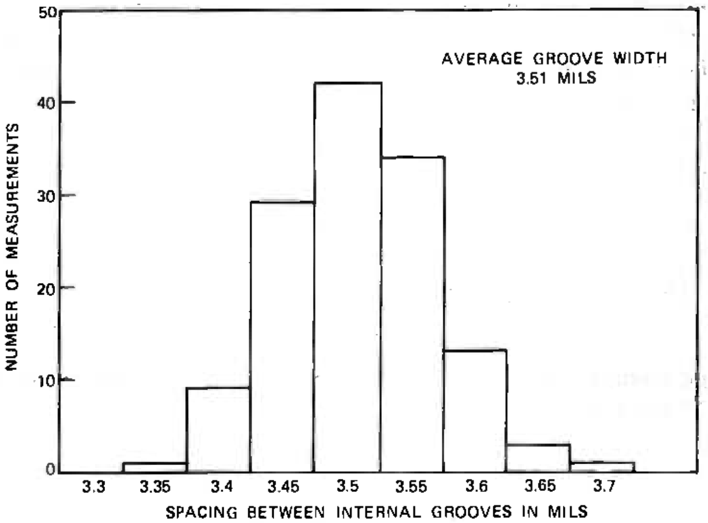

Fig. 2—Histogram of spacing between the internal grooves of metal master.

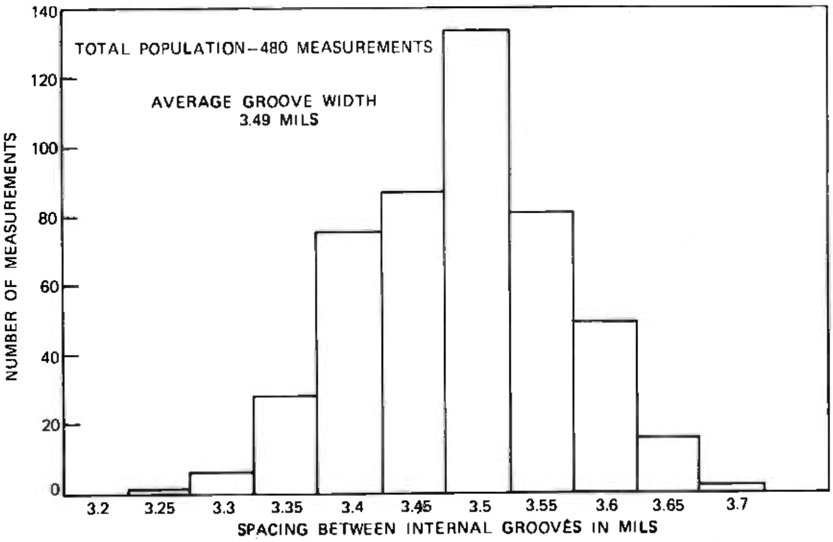

Fig. 3—Histogram of spacing between the internal grooves of molded polycarbonate substrate.

connector can join two optical cables, each consisting of twelve ribbons that house twelve 90-μm OD fibers.

The transverse alignment of the fibers in the grooves of the connector is a critical parameter in attaining low-loss splices. Tight tolerances were placed on the center-to-center spacing between the grooves. The design tolerance for the center-to-center spacing was 3.55 ± 0.05 mils. Less stringent tolerances were placed on the depth of the grooves.

The metal master was measured in an optical toolmakers microscope to determine how well it was machined. Figure 2 is a histogram showing the spacing between the internal grooves. The average groove width was 3.51 mils. Using the metal master in a screw-injection molding machine, a number of polycarbonate substrates were fabricated under different molding conditions. Samples were randomly selected from a batch that was molded to replicate the master as closely as possible. Figure 3 is a histogram showing the spacing between the internal grooves of the molded polycarbonate substrate. The average groove width was 3.49 mils compared with 3.51 mils obtained for the metal master.

Figure 4 is a derived cumulative distribution function of Figs. 2 and 3 showing a comparison of the groove-width dimensions for the master and plastic part. A very small amount of shrinkage, less than 0.1 mil, appears to have occurred in the plastic substrates. Measurement repeatability in obtaining this data with the toolmakers microscope was ±0.05 mil.

III. SPLICE CONNECTOR ASSEMBLY TECHNIQUE

The splicing of optical cables requires the integration of a number of operations including stripping of the cable sheath, ribbon preparation, removal of the plastic coatings from the fibers, fiber-end preparation, and, finally, the assembly and protection of the splice connector itself. Approximately 1 hour and 45 minutes is required to splice two optical cables consisting of 12 ribbons (each containing 12 fibers) together with the molded connector. Using current techniques, the majority of this time (about 1 hour) is spent stripping the ribbons and assembling them in the fiber organizers. Fiber-end preparation using the multiribbon cutting tool described in the Appendix requires about 15 minutes to prepare both ends of the cable. After the 144 fibers have been cut, the organizer is removed from the cutting tool and clamped to a micropositioner stage in preparation for insertion into the substrate of the splice connector. As shown in Fig. 5, tapered prealignment combs allow the ribbons to be lowered into the prealignment slots and grooves of the substrate. A mechanical wiper is attached to each organizer and is used to massage the fibers to assure that they are seated properly in their grooves. After the wiping process is completed, epoxy is used to permanently fix the wipers in place. The splice is closed by means of an assembly that enables the coverplate to be tacked in place with extra-fast-setting epoxy. An epoxy index-matching material is then injected through the slot in the coverplate to complete the splice. To assemble the connector itself requires only 30

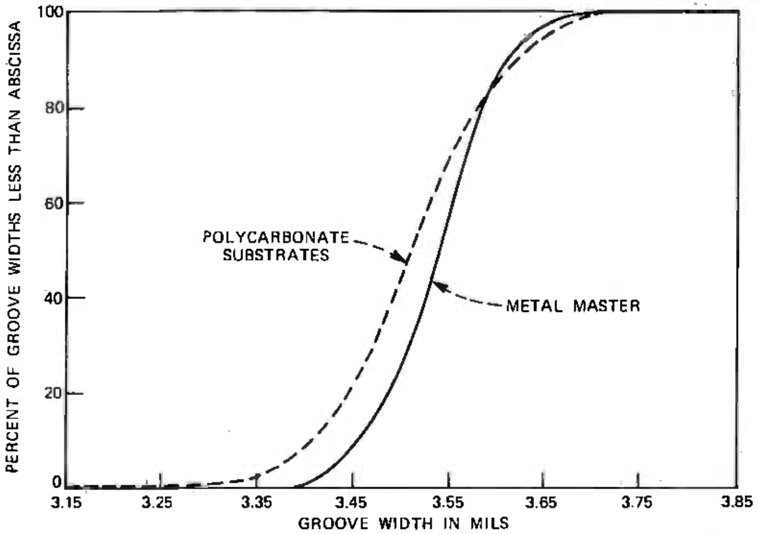

Fig. 4—Cumulative distribution function of groove widths.

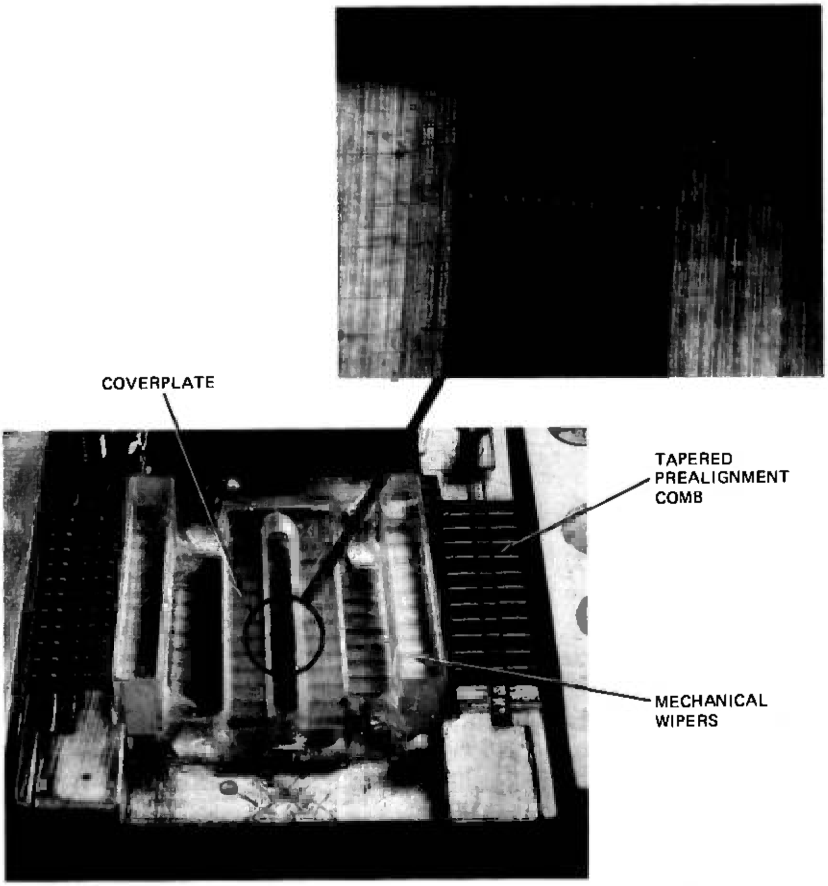

Fig. 5—Splice with coverplate epoxied in place showing expanded view of one ribbon joint.

minutes. Since splicing is a parallel operation, all twelve ribbons are spliced simultaneously.

IV. EVALUATION OF SPLICE CONNECTOR

Using Corning Glass Works graded-profile 90-μm OD fibers with 55-μm core diameters, adhesive sandwich ribbons[6] were made and formed into short prototype cables for the splicing studies. Following the procedures outlined in the previous section, five different cable splices were assembled and measured. Included in the statistics quoted were all ribbon-to-ribbon splices with twelve fibers present at the splice joint. When fiber breakage occurred, ribbon-to-ribbon splices with less than twelve fibers present were included in the statistics if proper alignment was maintained. Figures 6 and 7 show, for the 425

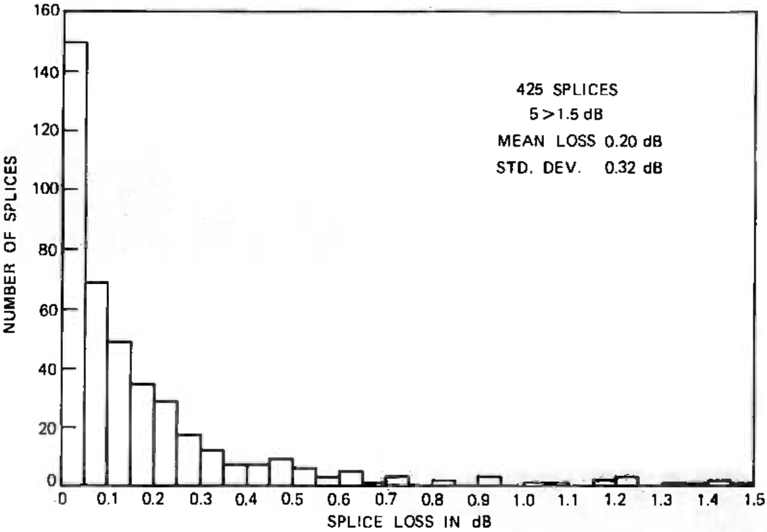

Fig. 6—Histogram of total splice loss data.

splice joints measured, the histogram and derived cumulative distribution function of the total splice loss data taken. The average splice loss was 0.20 dB with a standard deviation of 0.32 dB. Fifty percent of the total losses measured were less than 0.1 dB and 95 percent of the splice joints had losses less than 0.8 dB. Five additional outliers, not shown in the histogram but included in the statistics, had losses of 1.60, 1.64, 1.79, 2.03, and 2.66 dB. Four of these high-loss splices occurred in one of the cable splices.

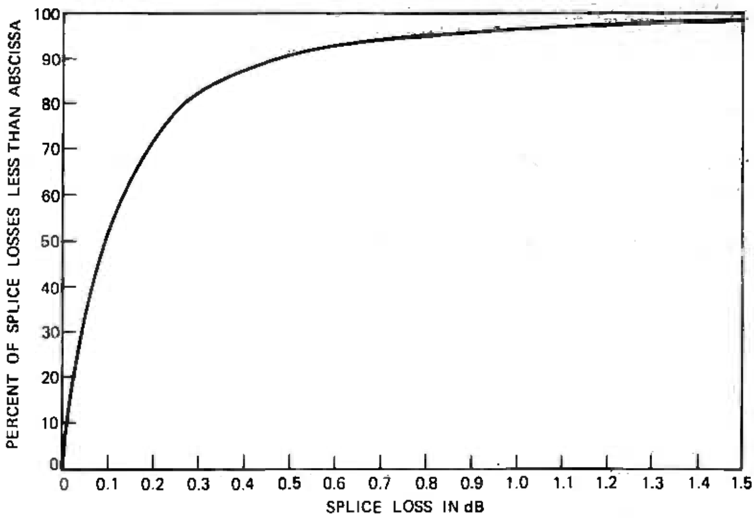

Fig. 7—Derived cumulative distribution of total splice loss data.

To determine the loss in a splice joint, an input beam with a numerical aperture approximately equal to that of the fiber was used and the input and output power to the splice joint was measured. This technique for measuring the loss in a splice joint has been described in detail in a previous paper.[1] The detector used in this study consisted of a United Detector Technology PIN long-line photodiode housed in a special glycerin-immersed fixture built to accommodate a ribbon organizer. To maintain accuracy in the splice loss measurements when measuring large groups of fibers (144 fibers in a linear array), it is necessary to establish accurate positioning of individual fibers on the surface of the detector. Variations in the sensitivity, as a function of position on the active surface of a large area detector, can cause errors in the measurements which are greater than 0.1 dB.

V. REQUIRED IMPROVEMENTS AND DISCUSSION

To maintain a high splice yield with this method of parallel splicing of large groups of optical fibers, 12 contiguous fibers must be present. If fibers are broken in the ribbons during ribbon stripping, fiber organizing, or end-preparation processes, gross misalignment (>10-μm transverse misalignment) can occur at the splice joint. The small alignment grooves shown in Fig. 8 do not provide adequate guidance unless the 12 contiguous fibers are present to force partial alignment of the fibers in the connector.

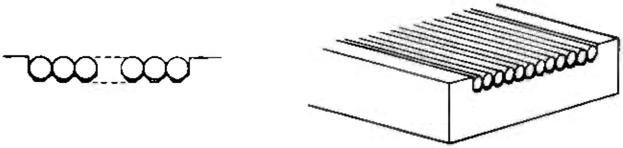

CURRENT DESIGN

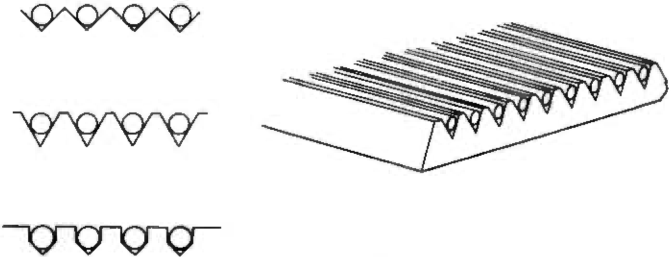

ALTERNATE DESIGNS

Fig. 8—Alternate groove depths.

Typically, two fibers per cable end are broken in the ribbon stripping, cleaning, and organizing processes. The fiber-end preparation process yields about 99.7 percent efficiency. Thus, three to five ribbons within the group of twenty-four ribbons being spliced in a connector have less than twelve surviving fibers and have the potential for being badly misaligned.

The development of automated ribbon-stripping techniques and better fiber-handling methods will improve the yield of this process. It is very probable, however, that some fibers will break. To prevent high splice losses in an entire ribbon, if breakage occurs, requires a redesign of the molded connector. Increasing the alignment groove depth as shown in the connector designs of Fig. 8 will tend to provide guidance for individual fibers independent of the ribbon structure. When guidance of this type is achieved, the breaking of an individual fiber will not affect the alignment of the remaining fibers in a ribbon, and splicing performance will be greatly improved.

APPENDIX

A Multiribbon Optical-Fiber Cutting Tool

The production of low-loss splices between optical fibers or the splicing of groups of optical fibers in the form of fiber ribbons and cables requires a reliable and convenient method of fiber-end preparation. Two basic techniques of end preparation have been developed and are described in the literature. The first, a conventional grinding and polishing technique, has been used by Miller[3] and Cherin[1] in the splicing of optical-fiber cables and ribbons. This technique of end preparation could be utilized in a controlled environment to prepare the ends of factory-installed cable connectors.[3] The second method of fiber-end preparation requires the controlled fracturing or breaking of fibers as developed by Gloge et al.[7] A simple cutting tool for preparing the ends of individual fiber ribbons has been used by Chinnock et al.[4] and Cherin and Rich[1,2] with excellent results. A properly engineered tool of this type seems well-adapted for use under field conditions.

In this Appendix, we briefly describe the design of a cutting tool that, operating on the principle described by Gloge et al.,[7] is capable of cutting 12 fiber ribbons (144 fibers) simultaneously. The cutting tool has been designed to be compatible with the injection-molded splice connector described in this paper.

A.1 Cutting tool and ribbon organizer

The fiber-cutting tool, shown in Fig. 9, consists of four basic parts.

(*i*) A precision diamond-tip-stylus scoring assembly used to create a crack or origin of fracture on the outer surface of the fibers.

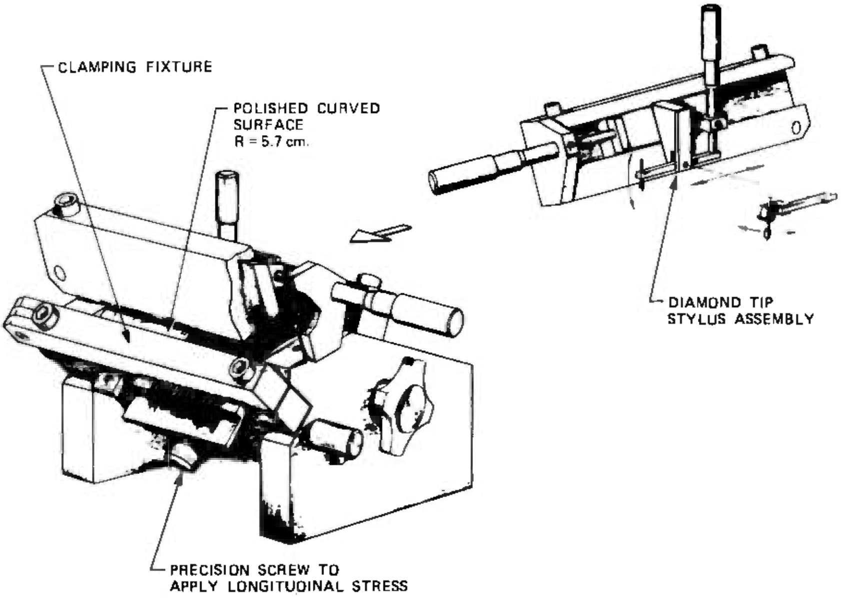

Fig. 9—Fiber ribbon cutting tool.

(*ii*) A polished curved surface over which sets of fiber ribbons are securely clamped. When the fiber ribbons are stressed over this surface, the stress distribution necessary to form flat hackle-free ends on the fibers is created.
(*iii*) Clamps to secure the fiber ribbons during the scoring and stress-application portions of the cutting process.
(*iv*) A precision screw, which displaces a clamp and causes the application of a longitudinal stress within the fibers.

A ribbon organizer is used to hold 12 ribbons in the form of a linear array. The organizer is clamped to the cutting tool and holds the fibers securely in place during the cutting process. After the 144 fibers have been cut, the organizer is removed from the cutting tool and is ready for insertion into the cable-repair splicing fixture.

A.2 Cutting experience

To date 52 cable ends have been prepared using the cutting tool. The nominal cable consisted of 12 ribbons each containing 12 fibers. Planar ends have been made on 99.67 percent of all the fibers that have been cut, 7328 out of 7352 (a few of the ribbons had less than 12 fibers within them). Typical fiber ends that were prepared using the tool are shown in Fig. 10. The total cutting efficiency of the tool was determined by the number of fibers surviving the entire process

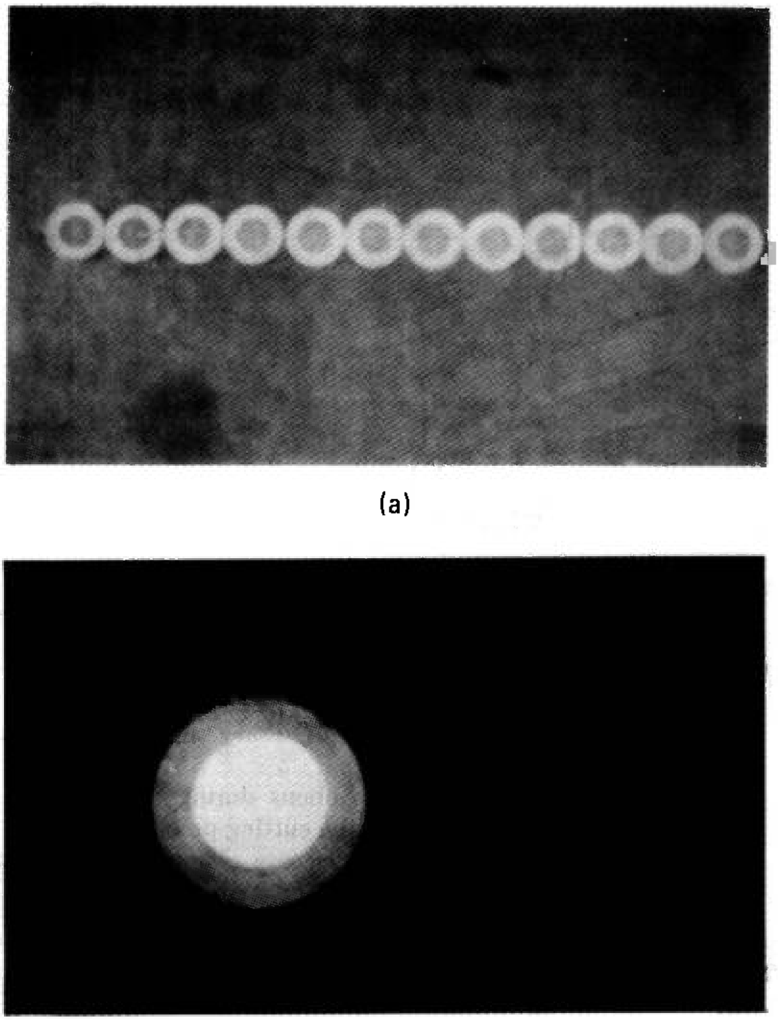

(a)

(b)

Fig. 10(a)—Optical ribbon with prepared fiber ends. (b) Typical fiber end.

of clamping, scoring, and tensioning. A total of 7283 fibers successfully survived the entire process, yielding a cutting efficiency of 99.06 percent.

REFERENCES

1. A. H. Cherin and P. J. Rich, "A Multi-Groove Embossed Plastic Splice Connector for Joining Groups of Optical Fibers," Appl. Opt., *14*, No. 12 (December 1975), pp. 3026–3030.

2. A. H. Cherin and P. J. Rich, "A Splice Connector for Joining Linear Arrays of Optical Fibers," *Optical Fiber Transmission* (digest of technical papers presented at the topical meeting on optical fiber transmission, January 7–9, 1975, Williamsburg, Va.), Optical Society of America, pp. WB3–1 to WB3–4.
3. C. M. Miller, "A Fiber Optic Cable Connector," B.S.T.J., *54*, No. 9 (November 1975), pp. 1547–1555.
4. E. L. Chinnock, D. Gloge, P. W. Smith, and D. L. Bisbee, "Preparation of Optical Fiber End for Low-Loss Tape Splices," B.S.T.J., *54*, No. 3 (March 1975), pp. 471–477.
5. P. W. Smith, D. L. Bisbee, D. Gloge, and E. L. Chinnock, "A Molded-Plastic Technique for Connecting and Splicing Optical-Fiber Tapes and Cables," B.S.T.J., *54*, No. 6 (July-August 1975), pp. 971–984.
6. M. J. Saunders, unpublished work.
7. D. Gloge, P. W. Smith, D. L. Bisbee, and E. L. Chinnock, "Optical Fiber End Preparation for Low-Loss Splices," B.S.T.J., *52*, No. 9 (November 1973), pp. 1579–1588.

Copyright © 1976 American Telephone and Telegraph Company
THE BELL SYSTEM TECHNICAL JOURNAL
Vol. 55, No. 8, October 1976
Printed in U.S.A.

Digital Coding of Speech in Sub-bands

By R. E. CROCHIERE, S. A. WEBBER, and J. L. FLANAGAN

(Manuscript received March 26, 1976)

A rationale is advanced for digitally coding speech signals in terms of sub-bands of the total spectrum. The approach provides a means for controlling and reducing quantizing noise in the coding. Each sub-band is quantized with an accuracy (bit allocation) based upon perceptual criteria. As a result, the quality of the coded signal is improved over that obtained from a single full-band coding of the total spectrum. In one implementation, the individual sub-bands are low-pass translated before coding. In another, "integer-band" sampling is employed to alias the signal in an advantageous way before coding. Other possibilities extend to complex demodulation of the sub-bands, and to representing the sub-band signals in terms of envelopes and phase-derivatives. In all techniques, adaptive quantization is used for the coding, and a parsimonious allocation of bits is made across the bands. Computer simulations are made to demonstrate the signal qualities obtained for codings at 16 and 9.6 kb/s.

I. DIVISION OF SPEECH SPECTRUM INTO SUB-BANDS

For digital transmission a signal must be sampled and quantized. Quantization is a nonlinear operation and produces distortion products that are typically broad in spectrum. Because of the characteristics of the speech spectrum, quantizing distortion is not equally detectable at all frequencies. Coding the signal in narrower sub-bands offers one possibility for controlling the distribution of quantizing noise across the signal spectrum and, hence, for realizing an improvement in signal quality. In earlier work, splitting of the spectrum by high-pass and low-pass filtering has been used advantageously for video and speech transmission.[1,2]

A question, then, is what design of sub-bands makes sense for speech coding? A choice based upon perceptual criteria is suggested, namely, band-partitioning such that each sub-band contributes equally to the so-called articulation index (AI).[3] The AI concept is based upon a nonuniform division of the frequency scale for the speech spectrum. Twenty nonuniform contiguous bands are derived in which each elemental band contributes 5 percent to the total AI.

Appealing to this notion, one partitioning of the frequency range 200 to 3200 Hz into four "equal-contribution" bands is given below and shown in Fig. 1.

Sub-band Number	Frequency Range (Hz)
1	200–700
2	700–1310
3	1310–2020
4	2020–3200

Each sub-band in its original analog form contributes 20 percent to AI. The total AI, therefore, is 80 percent, which corresponds to a word intelligibility of approximately 93 percent.[4]

II. LOW-PASS TRANSLATION OF SUB-BANDS

A straightforward approach to processing the sub-bands is to make a low-pass translation before coding. This facilitates sampling-rate reduction and realizes any benefits which might accrue from coding the low-pass signal.

The low-pass translation can be accomplished in a variety of ways. One method is shown in Fig. 2. The input speech signal is filtered with a bandpass filter of width W_n for the nth band. W_{1n} is the lower edge of the band and W_{2n} is the upper edge of the band. The resulting signal $s_n(t)$ is modulated by a cosine wave, cos $(W_{1n}t)$, and filtered

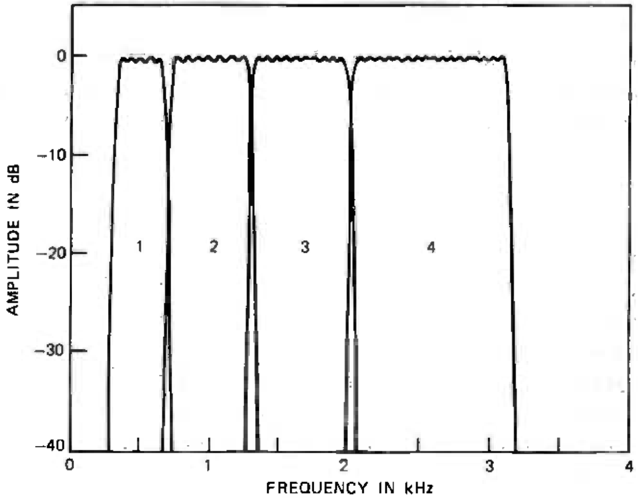

Fig. 1—Partitioning of the speech spectrum into four contiguous bands that contribute equally to articulation index. The frequency range is 200 to 3200 Hz.

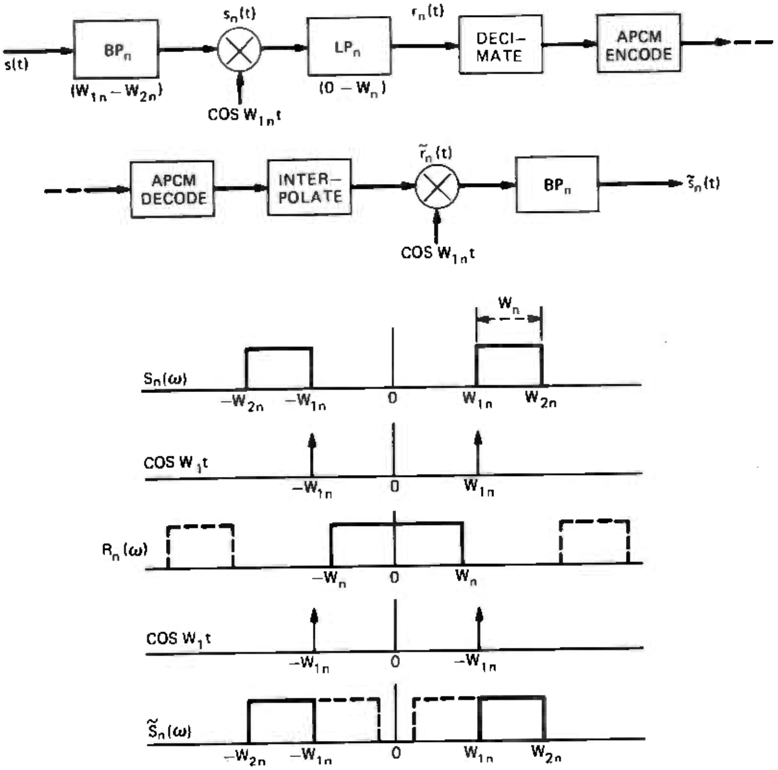

Fig. 2—Sequence of operations for low-pass translation of speech sub-bands, adaptive PCM encoding, transmission, decoding, and band restoration.

by a low-pass filter $h_n(t)$ with bandwidth $(0 - W_n)$. This filter is necessary to remove the unwanted signal images above $2W_{1n}$, as shown in Fig. 2. The resulting signal $r_n(t)$ corresponds to the low-pass translated version of $s_n(t)$ and can be expressed in the form:

$$r_n(t) = [s_n(t) \cos (W_{1n}t)]^* h_n(t). \tag{1}$$

Notice, in this instance, that a constraint is implied by the convolution, namely, that the passband width $W_n \leqq 2W_{1n}$, or that $W_{2n} \leqq 3W_{1n}$. Practically this poses no problem.*

The signal $r_n(t)$ is sampled at rate $2W_n$. If it is already in digital form, the sampling rate is decimated (reduced) to the rate $2W_n$. This signal is digitally encoded and multiplexed with encoded signals from other channels as shown in Fig. 3. At the receiver the data is demulti-

---

* For example, this constraint requires that W be increased slightly, from 200 to 233 Hz, for $n = 1$ in Fig. 1.

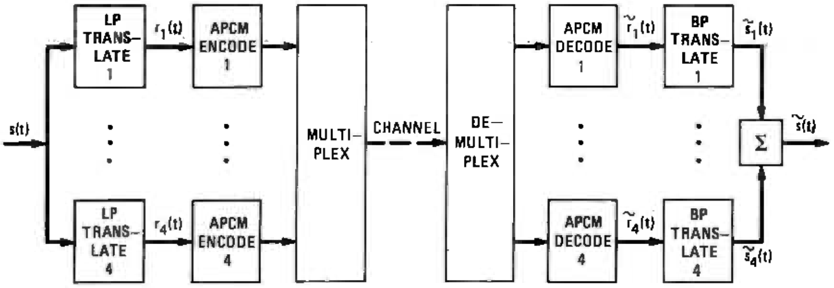

Fig. 3—Four-band encoder using low-pass translation and APCM encoding in each band.

plexed into separate channels, decoded, and interpolated to give the estimate $\tilde{r}_n(t)$ for the nth channel. Reconstruction of the detected signal is simply done by the reverse band translation. That is, it is modulated by cos $(W_{1n}t)$ and bandpass filtered to the original passband, as shown in Fig. 2. The sub-band signal $\tilde{s}_n(t)$ is then summed with the other bands to give the full-band signal $\tilde{s}(t)$.

An alternate implementation of the low-pass translation method, which avoids the above-mentioned restriction on W_n, follows from a modification of the complex demodulation process. In this approach, $s(t)$ is complex modulated by $e^{j\omega_n t}[\omega_n = (W_{1n} + W_{2n})/2 =$ center frequency of band $n]$ and filtered by a low-pass filter $h_n'(t)$ with bandwidth $(0 - W_n/2)$. The resulting complex signal $a_n(t) + jb_n(t)$,

$$a_n(t) = [s(t)\cos\omega_n t]^* h_n'(t) \tag{2a}$$

$$b_n(t) = [s(t)\sin\omega_n t]^* h_n'(t) \tag{2b}$$

corresponds exactly to the output of the phase vocoder.[5] The conjugate of this signal $a_n(t) - jb_n(t)$ corresponds to a modulation of $s(t)$ by $e^{-j\omega_n t}$. If the complex signal $a_n(t) + jb_n(t)$ is complex modulated by $e^{-j(W_n/2)t}$ and its conjugate complex modulated by $e^{j(W_n/2)t}$, the two resulting complex signals correspond to the negative and positive frequency components of the low-pass translated signal $r_n(t)$, as shown in Fig. 4. The sum of these two signals gives a real signal corresponding to the desired low-pass translated signal $r_n(t)$; i.e.,

$$r_n(t) = [a_n(t) + jb_n(t)]e^{-j(W_n/2)t} + [a_n(t) - jb_n(t)]e^{+j(W_n/2)t}, \tag{3}$$

or

$$r_n(t) = 2\left[a_n(t)\cos\left(\frac{W_n}{2}t\right) + b_n(t)\sin\left(\frac{W_n}{2}t\right)\right]. \tag{4}$$

For reconstruction, it can be shown that $a_n(t)$ and $b_n(t)$ can be recovered from the low-pass translated signal $r_n(t)$ by the following relations

$$a_n(t) = [r_n(t) \cos (W_n t/2)]^* h_n'(t) \tag{5a}$$

$$b_n(t) = [r_n(t) \sin (W_n t/2)]^* h_n'(t). \tag{5b}$$

Equations (4) and (5) suggest a method of implementation of the low-pass translation and reconstruction with a phase vocoder. For a digital implementation of the low-pass translation, this approach is particularly appealing. For example, at the sampling rate $f_s = 2W_n/2\pi$, the sequences corresponding to $\cos (W_n t/2)$ and $\sin (W_n t/2)$ are 1, 0, −1, 0, 1, ⋯, and 0, 1, 0, −1, 0, ⋯, respectively. Therefore, an efficient way to generate $r_n(t)$ is to sample a_n and b_n (or decimate if they are in digital form) to one half of this sampling rate (i.e., $W_n/2\pi$) and form $r_n(t)$ by interleaving samples of a_n and b_n (with appropriate sign changes). A similar approach can be used in the reconstruction process by recognizing that alternate samples of $r_n(t) \cos (W_n t/2)$ and

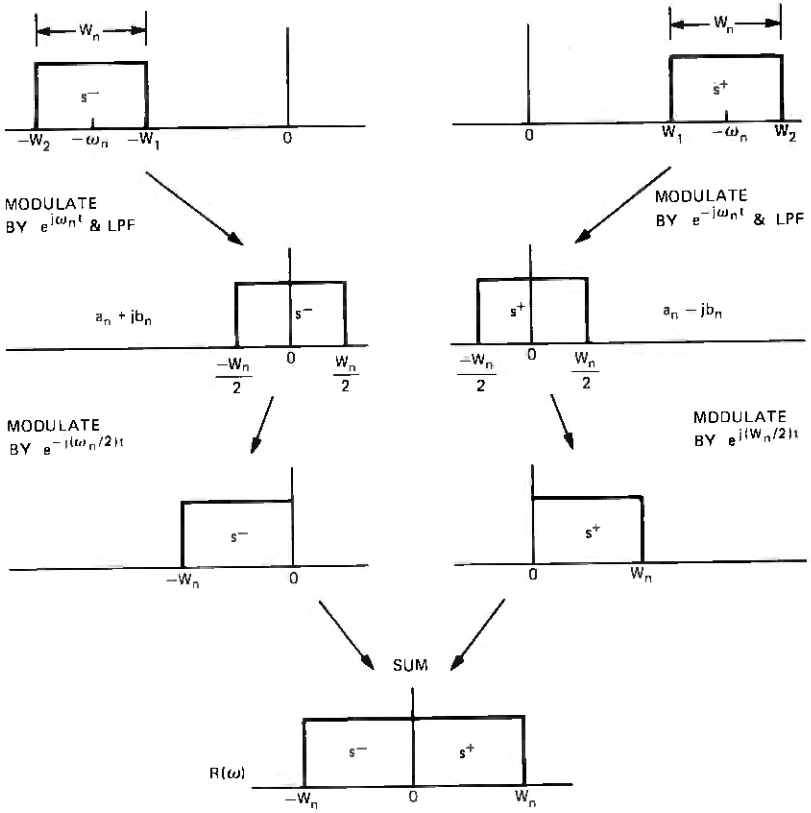

Fig. 4—Frequency-domain interpretation of complex demodulation method for low-pass translation.

$r_n(t) \sin (W_n t/2)$ (at sampling rate $2W_n/2\pi$) are zero valued. Thus, the two input sequences to the interpolators (which can be sampled at half of this rate or $W_n/2\pi$) can be generated by selecting alternate samples of $r_n(t)$ (with appropriate sign changes).

A further modification on this approach can be made by noting that, since adaptive coding is used to encode $r_n(t)$, the sign changes in the construction and separation of $r_n(t)$ are not necessary. That is, an alternate sequence $r_n'(t)$ can be generated by interleaving samples of a_n and b_n without sign changes. This sequence can be encoded and decoded and inputs to the interpolators can be formed from alternate samples of $\tilde{r}_n'(t)$ (without sign changes). Figure 5 shows an implementation of this method. The signal $s(t)$ is modulated by $\cos \omega_n t$ and $\sin \omega_n t$, where ω_n is the center frequency of band n. These signals are filtered with low-pass filters $h_n'(t)$ with bandwidth $(0 - W_n/2)$. The outputs are decimated (if they are in digital form) or sampled (if analog) at a sampling rate W_n. The low-pass translated signal $r_n'(t)$ is obtained (at sampling rate $2W_n$) by interleaving samples of a_n and b_n. $r_n'(t)$ is encoded, transmitted, and decoded as in Fig. 3. On reconstruction a_n and b_n are recovered by selecting alternate samples of $\tilde{r}_n'(t)$. These signals are then interpolated, filtered, modulated, and

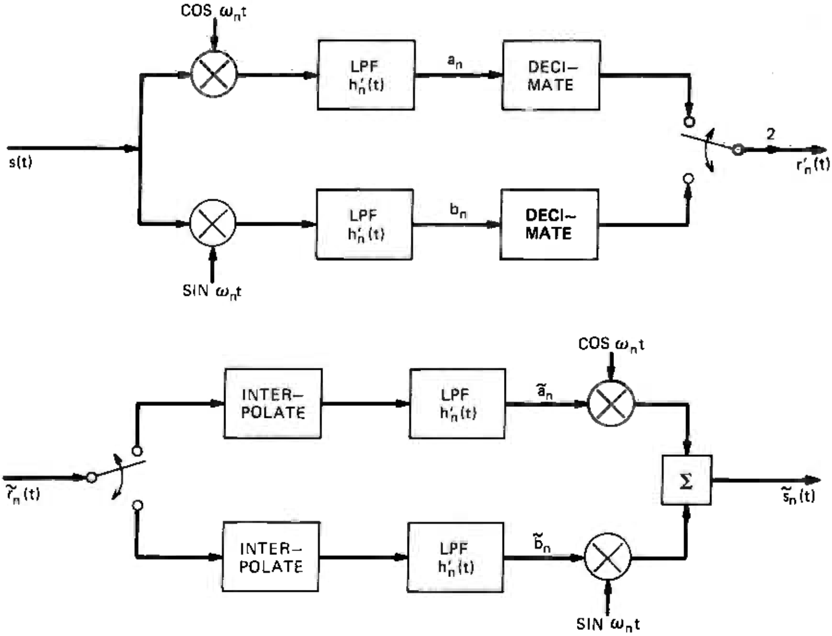

Fig. 5—Implementation of complex demodulation for low-pass translation with interleaving of samples of a_n and b_n.

summed as shown in Fig. 5 to give the reconstructed sub-band signal $\tilde{s}_n(t)$.

For digital implementation h_n' can be realized with a digital filter. Decimation, or sampling-rate reduction by an integer factor M, can be achieved by retaining only one out of every M samples of the output of the filter. The filter is necessary to avoid aliasing. Interpolation by an integer factor M is accomplished by increasing the sampling rate by filling in $M - 1$ zero-valued samples between each pair of input samples. The filter h_n' then removes the unwanted harmonic images of the base-band signal and smooths (i.e., interpolates) these samples to appropriate values of the base-band waveform. Efficient methods for implementing digital decimators and interpolators are discussed in Ref. (6).

III. ENCODING OF THE SUB-BAND SIGNALS

Digital encoding of the low-pass translated signal $r_n(t)$ is best accomplished using adaptive-PCM (APCM).[7,8] APCM encoding is preferred over adaptive-differential PCM (ADPCM) methods in this case due to the low sample-to-sample correlation of the low-pass-translated, Nyquist-rated, sampled signals.

For computer simulations, APCM coders based on a one-word step-size memory were used according to methods proposed by Jayant, Flanagan, and Cummiskey.[7–9] Step-size adaption is achieved according to the relation

$$\Delta_r = \Delta_{r-1} \times M, \tag{6}$$

where Δ_r is the quantizer step-size used for the rth sample and Δ_{r-1} is the step-size of the $(r - 1)$th sample. M is a multiplication factor whose value depends on the quantizer level at the $(r - 1)$th sample. For example, in a two-bit quantizer, two magnitude levels and the sign can be represented. If the smaller magnitude level is used at time $r - 1$, M is chosen to have a value $M = M_1 < 1$, and if the larger magnitude level is chosen, $M = M_2 > 1$ is used. For a three-bit quantizer, four magnitude levels and the sign can be represented. In this case, there are four choices for M. Through simulations, appropriate values of M for a two-bit quantizer were found to be $M_1 = 0.845$ and $M_2 = 1.96$. For a three-bit quantizer, they are $M_1 = 0.845$, $M_2 = 1.0$, $M_3 = 1.0$, and $M_4 = 1.4$. Note that the three-bit quantizer does not change its step-size at time r unless the largest or smallest quantizer level is encountered at time $r - 1$. The above values of M are in approximate agreement with values proposed by Jayant[7] for full-band APCM encoding.

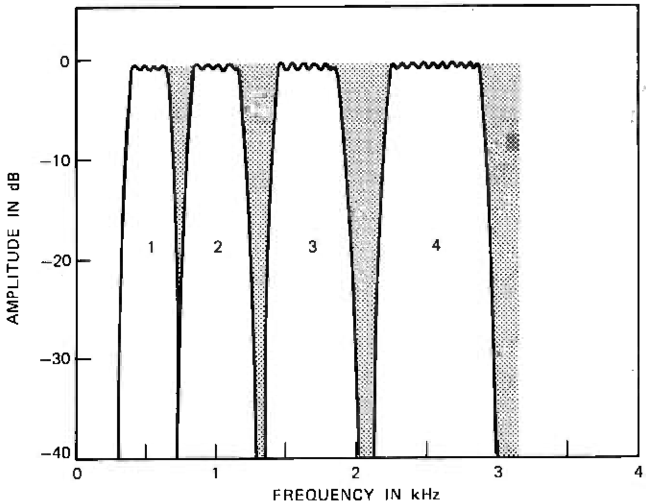

Fig. 6—Partitioning of the speech spectrum into four noncontiguous bands to achieve reduced bit-rate coding.

IV. SUB-BAND CODING FOR TRANSMISSION AT DATA RATES

The transmission bit rate of the sub-band coder can be reduced into the range of conventional data speeds by further limiting the sub-bands in width and tolerating some spectral gaps as shown in Fig. 6. Carried to excess, the noncontiguous bands produce a reverberant quality in the signal, such as one gets from comb filtering. In moderation, however, some highly useful compromises can be achieved between transmission bit rate and quality. The coded bands still cover a respectable range of the speech spectrum, and provide a quality considerably better than coding a single full-band signal.

V. INTEGER-BAND SAMPLING AND HARDWARE CONSIDERATIONS

Another attractive alternate implementation of these ideas is to use "integer-band" sampling to code a signal that is aliased in an advantageous way. The technique is illustrated in Fig. 7.

The signal sub-bands $s_n(t)$ are chosen to have a lower cutoff frequency of mf_n and an upper cutoff frequency of $(m + 1)f_n$, where m is an integer and f_n is the bandwidth of the nth band. This bandpassed signal is sampled at $2f_n$ to produce the sampled spectrum shown in Fig. 7 (for $m = 2$). The received signal is recovered by decoding and bandpassing to the original signal band. Typically, values of m from 1 to 3 are most useful for coder applications with lower bands using values of $m = 1$ and upper bands using $m = 2$ or $m = 3$. This integer-band sampling technique achieves the theoretical maximum efficiency in sampling.[10]

A very attractive advantage of the integer-band sampling approach is that it does not require the use of modulators. A slight disadvantage is that the above restrictions prevent the choice of bands strictly on the basis of equal contribution to AI. However, little loss in performance is observed if this equal contribution to AI condition is only approximate (within a factor of 2). This implementation was used for perceptual comparisons, which will be discussed later.

This approach is especially attractive for implementing the bandpass filters as charge-coupled-device (CCD) transversal filters. The analog to discrete-time conversion is inherently accomplished by the CCD filter with little or no analog prefiltering or post filtering required for the prevention of aliasing. The initial signal sampling can be conveniently high, say 15 kHz, to realize the CCD filter, and the filter output can be decimated to the $2f_n$ rate for coding. After transmission and decoding, the $2f_n$ rate can be interpolated to the 15-kHz rate for the final bandpass filtering, again by the analog CCD filter.

Another advantage of CCD filters (and also digital filters) is that the filter cutoff frequencies are inherently normalized to the initial sampling frequency. Therefore, the sampling frequency and, consequently, the bit rate of the coder, can be varied over a limited range by

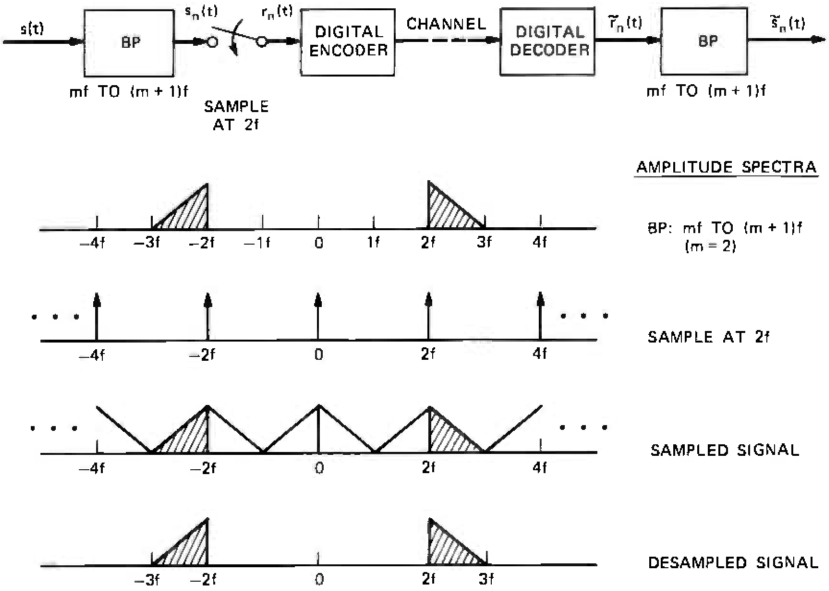

Fig. 7—Integer-band sampling technique for digital encoding of speech sub-bands.

Table I — Frequencies and sampling rates for the 16-kb/s coder

Sub-band No.	ω_n Center Freq (Hz)	$r_n'(t)$ Sampling Rate (s^{-1})	Decimation (From 10 kHz)	Quantization (Bits)
1	448	1250	16	3
2	967	1429	14	3
3	1591	1667	12	2
4	2482	2500	8	2

varying the master clock frequency. This cannot be achieved with analog filters.

Present technology is able to provide four 100-tap CCD transversal filters on a single integrated-circuit chip or one 200-tap filter on a chip with all necessary drivers and control logic.

VI. COMPUTER SIMULATIONS OF SUB-BAND ENCODERS

The sub-band coder has been implemented by computer simulation for transmission bit rates of approximately 16 kb/s and 9.6 kb/s. The complex demodulation approach in Fig. 5 was used for low-pass translation of the bands. An initial sampling rate of 10 kHz was employed in both cases.

The 16-kb/s coder was implemented with the band center frequencies and sub-band sampling rates shown in Table I. Bandwidths are equal to one half of the sampling rates and correspond to those shown in Fig. 1. Three-bit coders were used in the two lower bands, and two-bit coders were used for the upper bands. The filters were 125-tap FIR filters. As can be observed in Fig. 1, the filters overlap in their transition bands and give an overall flat frequency response from 200 Hz to 3100 Hz.

The 9.6-kb/s coder was implemented with the bands given in Table II and illustrated in Fig. 6. In this case gaps were allowed between bands. Larger filter orders, 175-tap (FIR), were used to reduce transition bands and conserve bandwidth. Only the lower band used a three-bit coder. Upper bands used 2-bit coders.

Table II — Frequencies and sampling rates for the 9.6-kb/s coder

Sub-band No.	ω_n Center Freq (Hz)	$r_n'(t)$ Sampling Rate (s^{-1})	Decimation (From 10 kHz)	Quantization (Bits)
1	448	800	25	3
2	967	952	21	2
3	1591	1111	18	2
4	2482	1538	13	2

Illustrations of the signal coded for 16 kb/s and 9.6 kb/s by the above-band-translation technique are given by the spectrograms of Figs. 8 and 9, respectively. In each figure, the upper spectrogram corresponds to the original sentence. The middle spectrogram corresponds to the signal played through the filters, decimators, and interpolators—but without coders. The bottom spectrogram illustrates the sub-band encoded speech at the designated bit rate.

Other simulations have also been made for encoding the signals $a_n(t)$ and $b_n(t)$ directly and also for encoding the magnitude and phase derivative (as in the phase vocoder). Similar quality results were found in these simulations.

VII. SUBJECTIVE COMPARISONS WITH OTHER ENCODING METHODS

Informal listening tests were made to compare the quality of the sub-band coder simulations with that of full-band encoding. For the 16-kb/s coder, comparisons were made with 2- and 3-bit ADPCM. For the 9.6-kb/s coder, comparisons were made with adaptive delta modulation (ADM) (i.e., 1-bit ADPCM). Results for the 16-kb/s coder comparisons are given in Table III.

Twelve listeners were asked to compare pairs of sentences for signal quality and indicate which was better. Two speakers were used in the experiments and sentence pairs were played in a randomly selected order. Each listener made a total of 16 comparisons in each of the experiments.

In comparing 16-kb/s sub-band encoding to 16-kb/s (2 bits/sample) ADPCM, listeners rated the sub-band encoded sentence as having higher quality in 94 percent of the sentence pairs. When the bit rate of the ADPCM coder was increased to 24 kb/s (3 bits/sample), they rated the sub-band encoded sentence as having higher quality in 34 percent of the sentence pairs. Experiment I demonstrates that the quality of the 16-kb/s sub-band coder is clearly preferred over that of ADPCM at the same bit rate. In Experiment II listeners exhibited much greater indecision, indicating that the quality of the 16-kb/s sub-band coder is close to that of 24-kb/s ADPCM, but that preference leans slightly in favor of the ADPCM.

Also included in Table III are signal-to-quantizing-noise ratios (s/n) measured on the speech signals, averaged for the two speakers for each of the coding methods. s/n data is not found to be a reliable indicator of listener preference. This observation is not surprising and has been previously recognized in the speech coding literature.[7,8]

A second series of listening experiments compared 9.6-kb/s sub-band coding with ADM. The sub-band encoder in this case is implemented with the integer-band method described earlier. The ADM coder is a

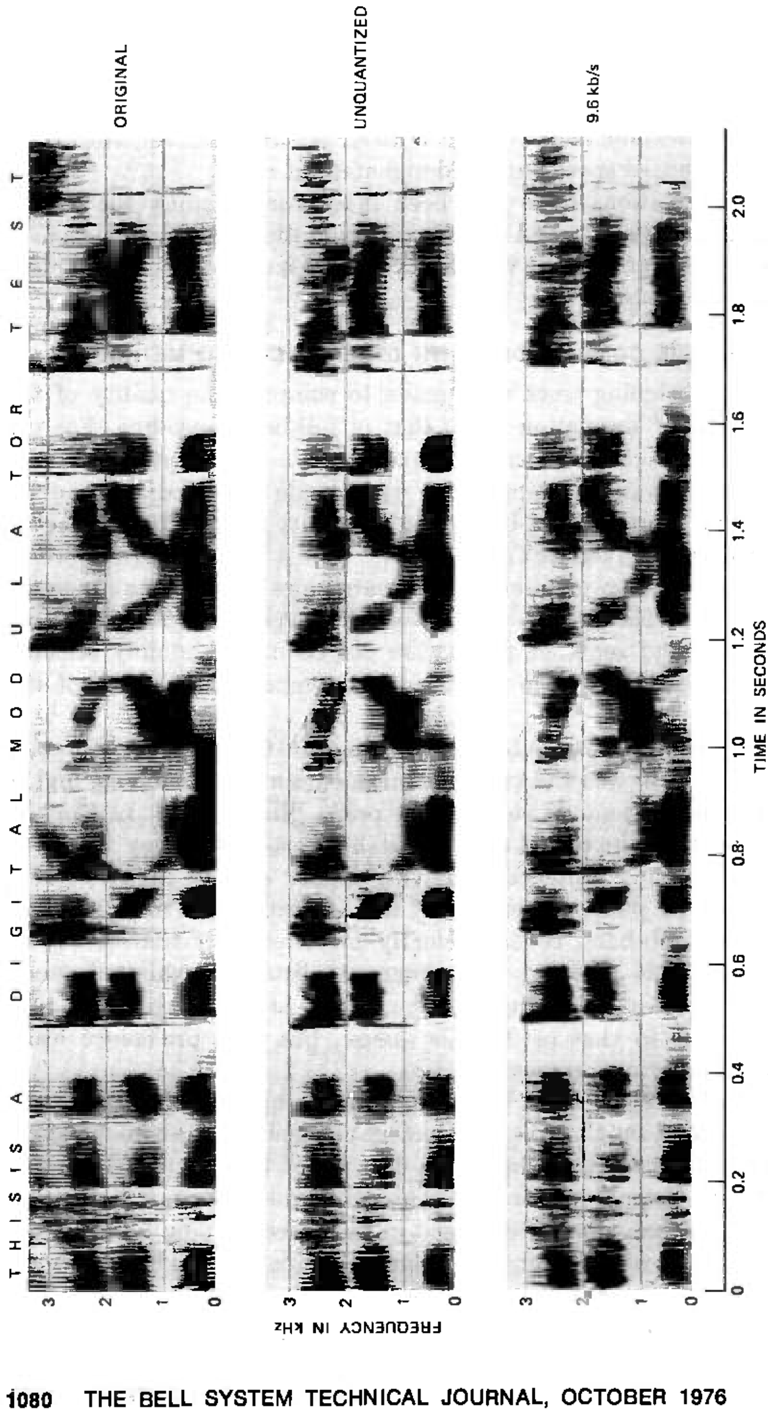

Fig. 8—Sound spectrograms comparing original, unquantized speech output and the 16-kb/s output from the sub-band coder.

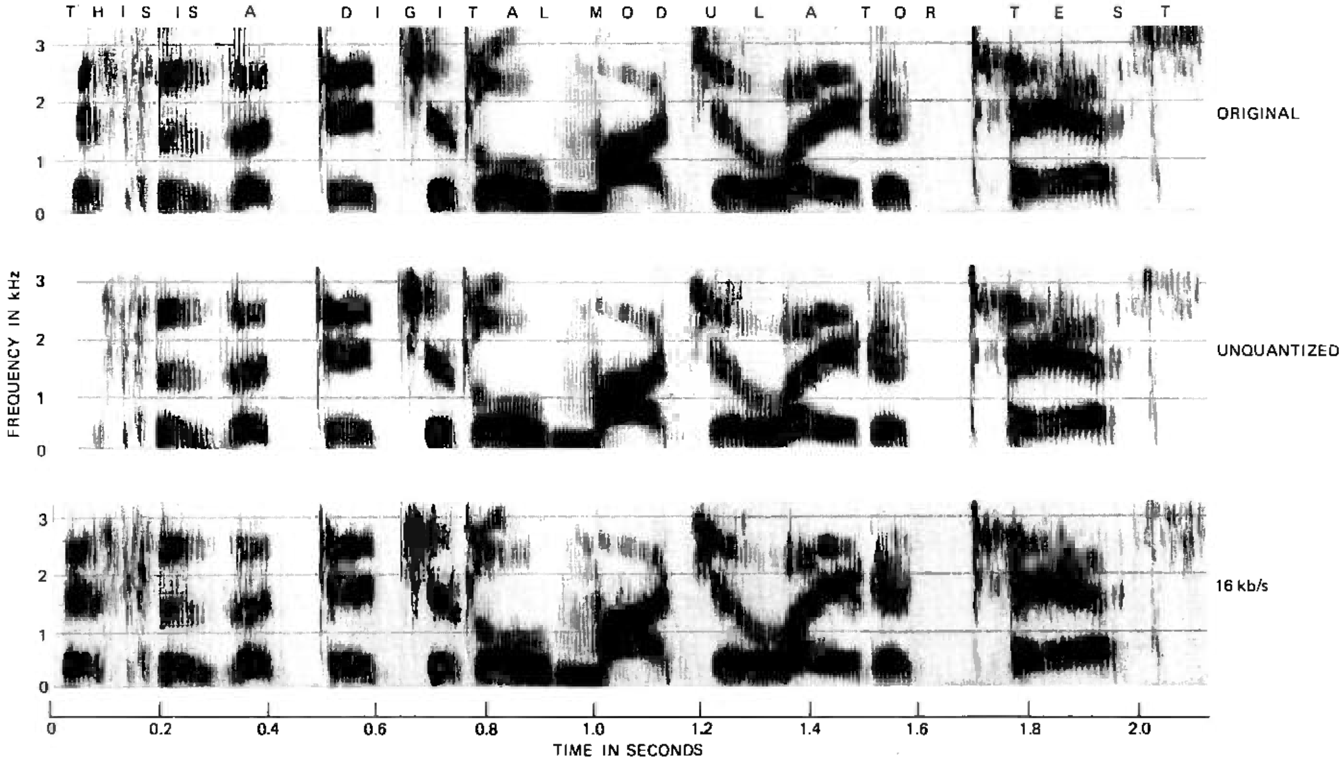

Fig. 9—Sound spectrograms comparing original, unquantized speech output and the 9.6-kb/s output from the sub-band coder.

Table III — Comparison of 16-kb/s sub-band coder with ADPCM

Experiment 1: 16-kb/s Sub-band vs 16-kb/s ADPCM

	Listener Preference (%)	S/N (dB)
16-kb/s Sub-band	94	11.1
16-kb/s ADPCM (2 Bits)	6	10.9

Experiment 2: 16-kb/s Sub-band vs 24-kb/s ADPCM

	Listener Preference (%)	S/N (dB)
16-kb/s Sub-band	34	11.1
24-kb/s ADPCM	66	14.5

forward step-size transmitting coder shown by Jayant[11] to have improved performance over conventional ADM. Table IV shows the results of these experiments. Three different bit rates, 10.3, 12.9, and 17.2 kb/s, were used for the ADM coder. In the first two experiments, the 9.6-kb/s sub-band coder was clearly preferred. In the third experiment, there was greater indecision with preference leaning slightly in favor of the sub-band coder. Note that this is true despite the opposite ordering of the s/n values! In other words, the perceptual palatability is not well reflected in the s/Ds as has been observed previously.[8]

Table IV — Comparison of 9.6-kb/s sub-band coder with ADM

Experiment 1: 9.6-kb/s Sub-band vs 10.2-kb/s ADM

	Listener Preference (%)	S/N (dB)
9.6-kb/s Sub-band	96	9.9
10.3-kb/s ADM	4	8.2

Experiment 2: 9.6-kb/s Sub-band vs 12.9-kb/s ADM

	Listener Preference (%)	S/N (dB)
9.6-kb/s Sub-band	82	9.9
12.9-kb/s ADM	18	9.7

Experiment 3: 9.6-kb/s Sub-band vs 17.2-kb/s ADM

	Listener Preference (%)	S/N (dB)
9.6-kb/s Sub-band	61	9.9
17.2-kb/s ADM	39	11

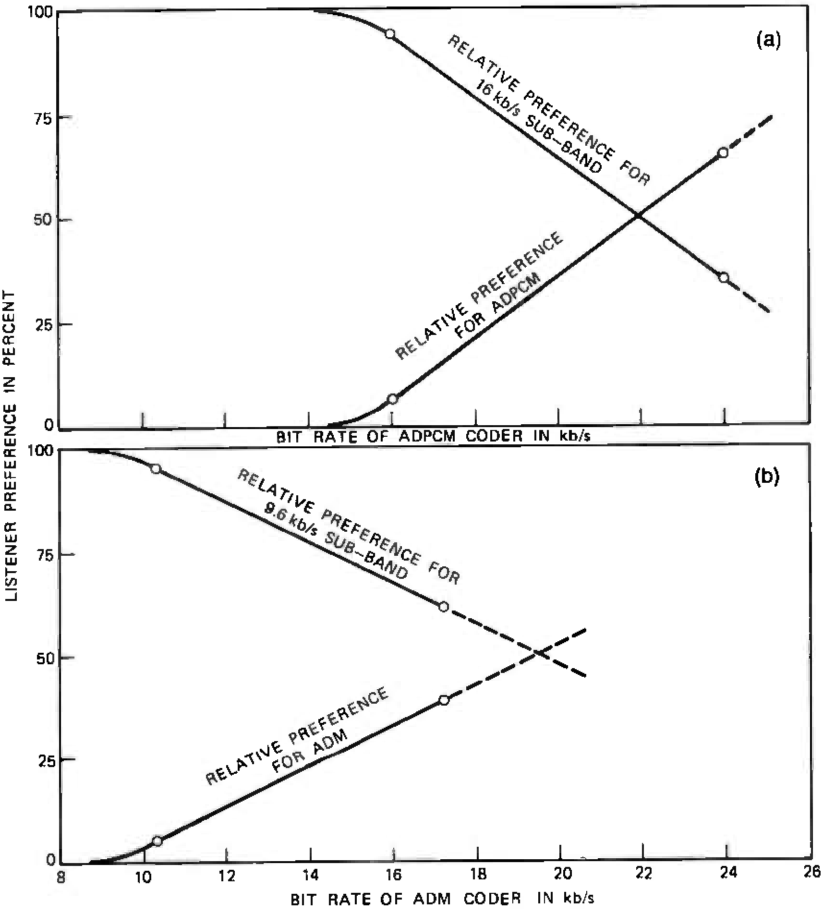

Fig. 10—(a) Relative comparison of quality of 16-kb/s sub-band coding against ADPCM coding (based on listener preference) for different ADPCM coder bit rates. (b) Relative comparison of quality of 9.6-kb/s sub-band coding against ADM coding for different ADM coder bit rates.

Figure 10 summarizes the results of the listener preference tests in Tables III and IV. Listener preference is plotted against the ADPCM and ADM coder bit rates. The crossover points of the curves in the two comparisons determine the point at which the two types of coders have approximately equal subjective quality. In the first comparison, the quality of the 16-kb/s sub-band coder is seen to be comparable to that of 22-kb/s ADPCM; i.e., it has a 6-kb/s advantage over the ADPCM coder. In the second comparison, the 9.6-kb/s coder has a subjective quality that is comparable to the 19-kb/s ADM and, therefore, has a 9.4-kb/s advantage over ADM.

It is clear from the listener preference tests that the sub-band coding technique is considerably better in quality than full-band ADPCM or ADM coding methods. We have carried this coding down to 7.2 kb/s and find that the quality is only slightly poorer than that at 9.6 kb/s. We have also pressed the coding rate down to 4.8 kb/s and find that the quality becomes considerably poorer owing to the increased band limiting and gaps between bands.

VIII. CONCLUSION

We have described a method for digitally coding speech in sub-bands of the total signal spectrum. Partitioning into sub-bands has several distinct advantages. Bit allocations for quantization of each band can be made on a perceptually palatable basis. Quantization products in a given band are confined to that band and do not "spill over" into adjacent frequency ranges. Selection of sub-band widths can also be made according to perceptual criteria, namely, for equal contributions to AI (and hence to signal intelligibility). As a result, the sub-band coding produces a quality signal that is better than a single full-band coding at the same total bit rate. The price paid is the band-filtering and the individual coding.

"Integer-band" sampling is demonstrated to be an economical and effective method for implementing the sub-band coder. Emerging technologies in device fabrication (such as CCDs) suggest economical implementations of the band filtering in terms of analog transversal filters.

The sub-band coder, implemented by integer band sampling, is demonstrated for speech transmission at rates of 16, 9.6, and 7.2 kb/s. The latter two transmission rates push down into the data range and are attractive for "voice-coordination" over data channels.

Informal perceptual experiments demonstrate that the signal quality of speech coded at 9.6 kb/s by the sub-band method is approximately equivalent to a 19-kb/s coding of the full-band signal. For a given transmission bit rate, therefore, the sub-band technique provides a significant improvement in signal quality. Or alternatively, for a given signal quality, the sub-band system can provide the transmission at a significantly reduced bit rate.

REFERENCES

1. E. R. Kretzmer, "Reduced-Alphabet Representation of Television Signals," IRE Convention Record, *4* (1956), pp. 140–147.
2. E. E. David and H. S. McDonald, "A Bit-Squeezing Technique Applied to Speech Signals," IRE Convention Record, *4* (1956), pp. 148–153.
3. L. L. Beranek, "The Design of Communications Systems," Proc. IRE, *35* (September 1947), pp. 880–890.

4. K. D. Kryter, "Methods for the Calculation and Use of the Articulation Index," J. Acoust. Soc. Amer., *34* (1962), pp. 1689–1697.
5. J. L. Flanagan and R. M. Golden, "Phase Vocoder," B.S.T.J., *45* (November 1966), pp. 1493–1509.
6. R. E. Crochiere and L. R. Rabiner, "Optimum FIR Digital Filter Implementations for Decimation, Interpolation, and Narrowband Filtering," IEEE Trans. Acoust., Speech, and Signal Proc., *ASSP-23*, No. 5, October 1975, pp. 444–456.
7. N. S. Jayant, "Digital Coding of Speech Waveforms: PCM, DPCM, and DM Quantizers," Proc. IEEE, *62* (May 1974), pp. 611–632.
8. P. Cummiskey, N. S. Jayant, and J. L. Flanagan, "Adaptive Quantization in Differential PCM Coding of Speech," B.S.T.J., *52* (September 1973), pp. 1105–1118.
9. N. S. Jayant, "Adaptive Quantization With a One-Word Memory," B.S.T.J., *52* (September 1973), pp. 1119–1144.
10. C. B. Feldman and W. R. Bennett, "Band Width and Transmission Performance," B.S.T.J., *28* (July 1949), pp. 490–595.
11. N. S. Jayant, "Step-Size Transmitting Differential Coders for Mobile Telephony," B.S.T.J., *54* (November 1975), pp. 1557–1581.

Copyright © 1976 American Telephone and Telegraph Company
THE BELL SYSTEM TECHNICAL JOURNAL
Vol. 55, No. 8, October 1976
Printed in U.S.A.

Subjective Evaluation of PCM Coded Speech

By D. J. GOODMAN, B. J. McDERMOTT, and L. H. NAKATANI

(Manuscript received February 3, 1976)

Subjective quality ratings of PCM coded speech were obtained with the aims of (i) determining the effects of certain coder parameters and their interactions on speech quality, (ii) finding objective measures for predicting perceived distortions, and (iii) providing guidelines for optimizing coder design. Coders with various combinations of four clipping levels, seven step sizes, four bandwidths, and three logarithmic companding laws were simulated. The coders were rated for quality on a 10-point scale by 48 listeners who heard male and female speech processed by the coders.

The ratings depended strongly on clipping level and step size, but only weakly on bandwidth. None of the coder parameters interacted strongly with another. Clipping noise power grossly overestimated the extent of perceived overload distortion; instead, clipping percentage is proposed as a much more realistic predictor. Signal-to-granular-noise ratio was a good predictor of perceived granular noise. For a given bit rate, the coder with the highest quality rating was not the coder with minimum total clipping and granular noise power, contrary to traditional wisdom.

I. INTRODUCTION

"How does it sound?" This is a fundamental but elusive question for the engineer designing or evaluating a system for transmitting, recording, or processing speech signals. If the system is analog, the engineer has as a guide a substantial body of information about the interrelated effects on speech quality of such factors as attenuation, noise, linear and nonlinear distortion, echo, and cross-talk.[1] With respect to digital systems, however, the subjective effects of characteristic distortions have been documented to a much smaller extent and, as a consequence, the quality of an existing system and the merits of proposed designs are much harder to predict.

One approach to the evaluaton of digital systems is to relate a digital signal distortion to one of the analog distortions, and to define digital speech quality as the subjective correlate of the equivalent analog distortion.[2] Although expedient and reasonably accurate for certain individual distortions, the value of this approach seems quite limited in the important situations where several distortions occur simultaneously.

While the engineering literature contains many reports of subjective tests of digitally coded speech, most of the tests were undertaken to provide performance data on the overall distortions produced by specific coders. Among the exceptions to this approach and more aligned with the spirit of our work are the experiments reported by Donaldson and Chan,[3] O'Neal and Stroh,[4] and Yan and Donaldson[5] in which individual sources of distortion were identified and the manner of their interaction investigated. In these studies, the effects of bandwidth, predictor network, number of bits per sample and transmission error rate in PCM (pulse code modulation) and differential PCM systems were studied. Another design variable, quantizer overload point, was held fixed although Ref. 5 ends with the suggestion, "A careful study of the dependence of subjective quality on . . . [overload point] . . . seems necessary." Our experiment contains a thorough study of the role of this parameter in PCM.

II. AN OVERVIEW OF THE EXPERIMENT

We used a digital computer to process speech with 208 different PCM coding schemes whose characteristics span an important range of bandwidths, number of bits per sample, overload levels, and compression characteristics. Our aims included the study of: (*i*) the influence on speech quality of the above design parameters, (*ii*) objective measurements that are good predictors of speech quality, and (*iii*) optimum combinations of code parameters.

In the experiment, 48 listeners used a 10-point opinion scale to provide quality ratings of speech processed by each of the coders. The speech material consisted of 10 sentences, each spoken by two females and two males. Our principal conclusions from the analyses of the data are:

(*i*) Overload level and quantizing step size were primary determiners of listeners' ratings. Bandwidth was, by comparison, a secondary determiner of speech quality.

(*ii*) The traditional objective measurement, overall signal-to-noise ratio, was not a useful predictor of speech quality. On the other hand, the percent of samples clipped, P and the signal-to-noise ratio, Q of the granular quantizing noise were useful and independent predictors of speech quality. A simple linear equation

$$R = aP + bQ + c,$$

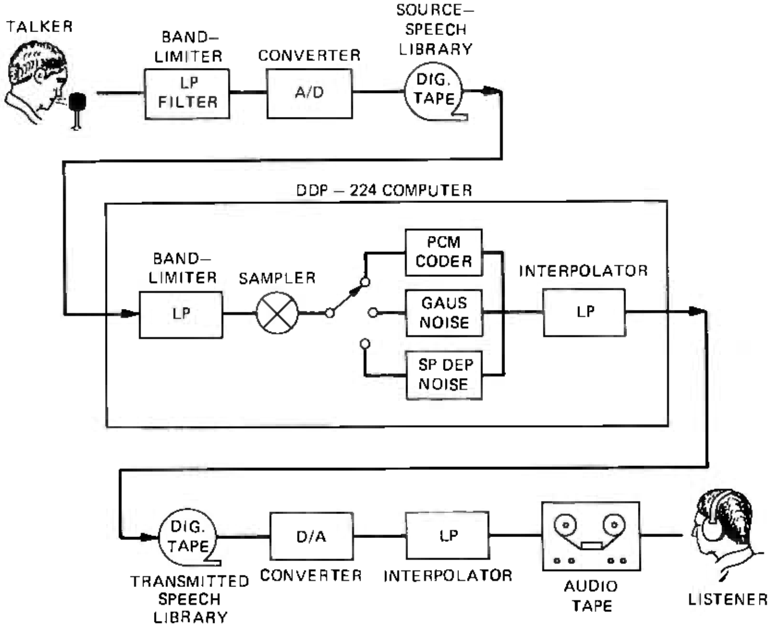

Fig. 1—Block diagram of major steps in the experiment.

where *a*, *b*, and *c* are empirically derived constants, was a good predictor of the quality rating *R*.

(*iii*) For a fixed number of bits per sample, the coder with the highest quality rating was not the coder with the highest signal-to-noise ratio.

The experiment involved three major steps, as shown in Fig. 1. The first step was to compile a source speech library consisting of high-quality recordings of sentences. The second step was to simulate a variety of coders and noise processes on a computer. The final step was to process the source speech with the simulated coders and noise processes in accordance with an overall experimental design and to obtain subjective quality ratings from listeners.

III. SOURCE-SPEECH LIBRARY

Digital recordings were made of the ten phonetically balanced sentences listed in Table I as spoken by two females and two males. The talkers were seated in a sound-proof booth and spoke into a Sony ECM 22p microphone. The amplified microphone signal was low-pass filtered at 9.6 kHz, sampled 24,000 times per second, uniformly quantized to 12 bits per sample, and written onto digital tape. Each sample was represented by an integer between -2047 and $+2048$. For each talker, the quantizer step size was adjusted manually to use the full quantizer range without clipping. Once a step size was established for a talker, the same step size was used for all ten sentences. This procedure approximately equalized the peak power level of the four talkers over all sentences. The source-speech library thus consisted of digital recordings of 40 sentences containing all the speech sounds spoken by four talkers and approximately equalized for peak power over talkers.

IV. SIMULATION OF CODERS AND NOISE PROCESSES

A PCM system contains a low-pass presampling filter of bandwidth W, a sampler that generates $2W$ equally spaced signal samples per second, a quantizer operating independently on each sample, and a low-pass desampling filter of bandwidth W which generates a continuous waveform from the quantized sequence. In the experiment, each of these components—presampling filter, quantizer, desampling filter—was simulated on a DDP-224 digital computer. Within the computer, "analog speech" appeared in the 24,000-samples/second, 12-bits/sample format of the recording scheme, while sampled and quantized speech appeared with fewer bits and fewer samples.

4.1 Bandlimiting and sampling

The four sampling rates used in the experiment were all integer submultiples of 24 kilosamples/second: 12, 8, 6, and 4.8 kilosamples/second and the nominal cutoff frequencies of the associated low-pass filters were 6, 4, 3, and 2.4 kHz, respectively. The filters, all realized as finite impulse-response digital filters with integer coefficients, were designed to meet the requirements listed in Table II, which conform to

Table I — The ten sentences spoken by each of four talkers *

1. A lathe is a big tool.
2. Grab every dish of sugar.
3. An icy wind raked the beach.
4. Her father failed many tests.
5. Joe brought a young girl.
6. The chairman cast three votes.
7. The boy was mute about his task.
8. Beige woodwork never clashes.
9. Both teams started from zero.
10. My cap is off for the judge.

* Each is a simple declarative sentence that can be spoken in approximately two seconds. The list includes all the phonemes of English in initial, final, and intervocalic position.

Table II — Bandlimiting filter specifications

Sampling rate (kilosamples/s)	12	8	6	4.8
Nominal cutoff W kHz (Attenuation at least 15 dB at $f = W$)	6	4	3	2.4
Passband edge attenuation within ±0.125 dB	4.5	3	2.25	1.8
Stopband edge attenuation at least 30 dB	7.125	4.75	3.562	2.85
Filter order	21	33	41	51
Oversampling ratio	2	3	4	5

the requirements imposed on channel banks of digital multiplex systems.

4.2 Interpolation

The digital interpolating filter simulates the desampling filter of a PCM coder. The latter transforms a sampled signal to a continuous waveform. In the computer, "continuous waveforms" appear as samples occurring at the rate of 24,000 per second; to produce them, an interpolating filter inserts 1, 2, 3, or 4 new samples between each pair of PCM samples, depending on whether the sampling rate of the simulated coder is 12, 8, 6, or 4.8 kHz, respectively.

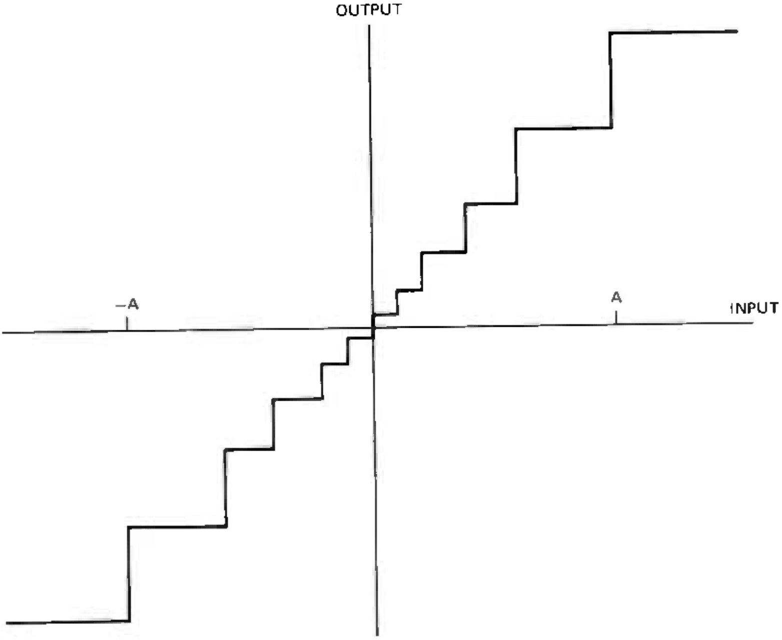

Fig. 2—Input/output diagram of a quantizer.

While, in practice, specifications of desampling filters are often identical to those of presampling filters, we found for our purposes that a 30-dB stopband attenuation was insufficient at certain frequencies. Some speech sounds, particularly nasals, with strong low-frequency components produced audible output tones in the vicinity of the sampling frequency in desampling. For example, the spectrum of sound with considerable energy around 200 Hz has images at 5800 Hz and 6200 Hz when sampled 6000 times per second. Even attenuated 40 dB, these images produced an audible "whistle," which was very distracting to listeners. In the design of interpolating filters, therefore, we specified an attenuation of at least 65 dB near the sampling frequency.

4.3 Quantization

A quantizer is defined by an input/output diagram such as Fig. 2. To study the subjective effects of quantization, it is appropriate to formulate this operation as a sequence of four processes as in Fig. 3: clipping, compression, uniform quantization, and expansion.

Clipping is an inherent part of the quantizing operation. Figure 2

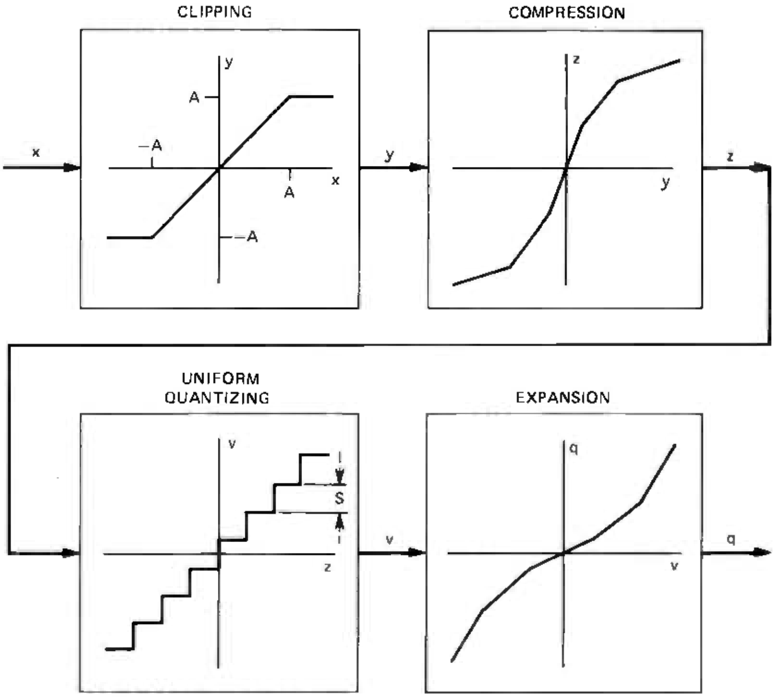

Fig. 3—Four processes included in quantization.

shows that the largest magnitude that can be represented by the quantizer is A. All samples greater than A result in the same output, as do all samples less than $-A$. Hence, the quantizer operates as a device that first clips the input and then represents with finite resolution all signal samples in the range $-A$ to A.

Compression and expansion (each the inverse of the other) are nonlinear transformations of the uniform quantizer's analog input samples and quantized output samples, respectively. Current trends in communication technology favor the use of segment-compression characteristics, which are piecewise linear approximations to logarithmic input/output relationships. In the experiment, we simulated segmented μ-law quantizers* in which the length of each linear segment is double, and the slope one-half, that of the previous segment.[6] The compression curve in Fig. 3 contains five segments. There are three segments for positive inputs and three for negative inputs, with the innermost positive and negative segments colinear. In the input/output characteristic, the quantization step size is constant over a segment and double that of the previous segment. Hence, high-level samples are quantized more coarsely than low-level samples.

In practice, the number of positive (or negative) segments is a power of 2 so that the total number of distinct segments can be written as $2^{(c+1)} - 1$. In the experiment, we studied quantizers with $c = 0$ (uniform quantization), $c = 2$, and $c = 3$, which are 1, 7, and 15 segment quantizers with parameter $\mu = 0$, 15, and 255, respectively.

We describe the uniform quantizer in Fig. 3 by its step size S which is equal to the minimum step size of the nonuniform quantizer of Fig. 2.

The entire quantizer is now defined by three parameters: the overload level A, the companding number μ, and the step size S. For engineering purposes, the most important quantizer parameter is the number of bits per sample B. Table III shows the dependence of B on A, μ, and S over the range of parameters appearing in the experiment. While, in engineering studies, quantizers are usually specified by μ, B, and S or by μ, B, and A, the design and analysis of experiments such as this one are greatly facilitated by viewing μ, A, and S as the independent variables of a quantizer. The advantages of this point of view derive from the fact that quality varies monotonically with both A and S. The relationship of quality to B is considerably more complicated (see Section VIII) and is more readily derived as a combination of two relatively simple functions than measured directly.

Because the source speech appears in the computer encoded in

---

* The compressor characteristics are piecewise linear approximations to

$$z = sgn(y)[\log(1 + \mu|y|)]/\log(1 + \mu).$$

Table III — Number of bits as a function of step size and clipping level

	$\mu = 0$ Clipping level						
Step size	2048	1024	512	256	128	64	32
1	12*	11	10	9*	8*	7*	6
2	11*	10	9	8*	7*	6*	5
4	10*	9	8	7*	6*	5*	4
8	9*	8	7	6*	5*	4*	3
16	8*	7	6	5*	4*	3*	2
32	7*	6	5	4*	3*	2*	1
64	6*	5	4	3*	2*	1*	
128	5	4	3	2	1		
256	4	3	2	1			
512	3	2	1				
1024	2	1					
2048	1						

	$\mu = 15$ Clipping level						
Step size	1920	960	480	240	120	60	30
1	10*	9	8	7*	6*	5*	4
2	9*	8	7	6*	5*	4*	3
4	8*	7	6	5*	4*	3*	
8	7*	6	5	4*	3*		
16	6*	5	4	3*			
32	5*	4	3				
64	4*	3					
128	3						

	$\mu = 255$ Clipping level			
Step size	2040	1020	510	255
1	7*	6	5	4*
2	6*	5	4	
4	5*	4		
8	4*			

* Indicates quantizers used in experiment.

steps of 1 from -2047 to 2048, A cannot exceed 2048 and S cannot be less than 1. Hence, for each c, there is an upper limit on the number of bits per sample that can be simulated. The limit is 12 bits for $c = 0$, 10 bits for $c = 2$, and 7 bits for $c = 3$. Conversely, there is a lower limit on B because there must be at least one output level for each positive segment and one for each negative segment in the compression curve. This implies that the $c = 2$ quantizer must have at least 3 bits/sample and the $c = 3$ quantizer at least 4 bits.

After a pilot experiment, we decided to vary S in octave steps. Table III shows for each companding law the values of S, A, and B that can be simulated by our procedure. An asterisk indicates a quantizer used in the experiment. The first column of each matrix contains quantizers with no clipping. We omitted quantizers in the second and third column because the pilot study suggested that the deterioration in quality associated with the transition from the first to the fourth column was approximately the same as the deteriorations in the transition from fourth to fifth, and fifth to sixth columns.

4.4 Noise processes

In addition to speech degraded by the PCM coding process, the experiment included speech distorted by two types of additive noise. There were four levels of simulated white gaussian noise added to speech samples; the noise levels were chosen to provide signal-to-noise ratios around 30, 20, 10, and 0 dB. It was felt that gaussian noise is similar in character to the granular quantizing noise of a uniform quantizer ($c = 0$).

In addition, we included four levels of speech-dependent noise.[7] To each sample x_n was added $\pm \rho x_n$, where ρ is the noise-to-signal ratio and the + or − sign is determined by a simulated coin-toss. Thus, the noise magnitude added to each sample is proportional to the magnitude of the sample. This type of distortion is similar in character to the quantizing noise of a companded quantizer in which the noise magnitude increases in a probabilistic sense with signal magnitude. The four speech-dependent noise levels provide the signal-to-noise ratios 30, 20, 10, and 0 dB, where $s/n = 20 \log (1/\rho)$ dB.

V. SUBJECTIVE EVALUATION OF TRANSMITTED SPEECH

After all simulations were completed, the source speech was processed by the coders and noise processes and the processed speech written onto digital tape to form a transmitted speech library, as shown in Fig. 1. When the library was complete, the transmitted speech was converted from digital to analog and recorded onto audio tape for subjective evaluation.

Four analog tapes were prepared, each containing one example of each of the 240 experimental conditions: (52 coders + 8 noise conditions) × 4 bandwidths. The assignment of talkers to conditions followed a latin square design in a bandwidth by tape-number matrix. Thus, for a given coder or noise condition, a different talker was associated with each of the bandwidths on a single tape. Over the four tapes all 16 talker-bandwidth combinations appeared with each coder and noise condition. For a given bandwidth, each sentence occurred 6 times and each talker 15 times over the 60 noise and coder conditions.

The 240 conditions on each tape were presented in random order to 48 students at a local university, who listened to the stimuli on TDH-39 earphones. Twelve subjects judged the stimuli of each tape. They were asked to "rate each sentence on a scale of 1 to 10 according to its acceptability as a communication link, using 1 to represent the least acceptable, 10 the most acceptable, and the other numbers between 1 and 10 for intermediate ratings." Before the test began, 20 representative conditions were presented to familiarize the listeners with the range of speech quality.

VI. OBJECTIVE MEASURES OF SPEECH QUALITY

Because signal-to-noise ratio (s/n) is the most frequently cited measure of speech quality, the relationship of s/n to subjective appraisal of processed speech is a matter of substantial interest in an experiment such as ours. A very strong inference of our data is that a single s/n statistic—the ratio of the power in the original speech to the power in the difference between processed speech and original speech—is a poor predictor of subjective quality. Instead, we find that the effects of clipping and granular quantization must be considered separately if we are to arrive at a correct prediction of perceived quality. Therefore, we define two noise components: NC, the clipping noise, defined as $y - x$ in Fig. 3, and the granular quantizing noise NG, defined as $q - y$. The total quantizing noise is

$$NQ = q - x = NC + NG.$$

To facilitate measurement of these and other quantities for each quantizer, we produced a digital data tape which, for each utterance passed through each presampling filter, recorded the number of times each possible sample amplitude (from -2047 to 2048) occurred. We used this tape to calculate the power in each filtered utterance, the mean square values of NG, NC, and NQ for each quantizer, and additionally, the percentage of samples clipped by each quantizer. This last statistic, P, proved a better correlate of listener opinions than the mean square value of NC.

VII. RESULTS

7.1 Overview of data analyses

Statistical procedures were applied to evaluate the relative influence of each of the experimental variables on the listeners' ratings. Analyses of variance showed that two variables, clipping level A and step size S, were the major sources of variability influencing the ratings. Multiple regression procedures provided linear estimates of ratings as functions of two objective distortion measures, one related to A, the other to S.

7.2 Determiners of speech quality

7.2.1 Listeners and tapes

An analysis of variance was computed to study the variability of the ratings of the 12 listeners who judged a single tape, and the variability among the four listener groups, each of which judged a different tape. The analysis showed that the listeners within each group were not significantly different in their ratings and that the ratings among the four groups of listeners were not significantly different. In each case, the F ratios were less than 1.0. Therefore, the mean of the listeners' ratings for each condition was used for all further analyses.

7.2.2 Coder parameters

A second analysis of variance was computed, using the means of the listeners' ratings, to study the effects of the experimental variables. In this analysis, the differences in the ratings due to step size, clipping, and companding were statistically significant, as expected, and in combination accounted for 84 percent of the total variance. While the variability in the ratings due to the different talkers, the different bandwidths, and their interaction were all statistically significant, each of these effects accounted for only 2 to 3 percent of the total variance.

7.2.3 Talkers

Figure 4 shows the mean rating across clipping and step size as a function of bandwidth for each talker at the three companding values

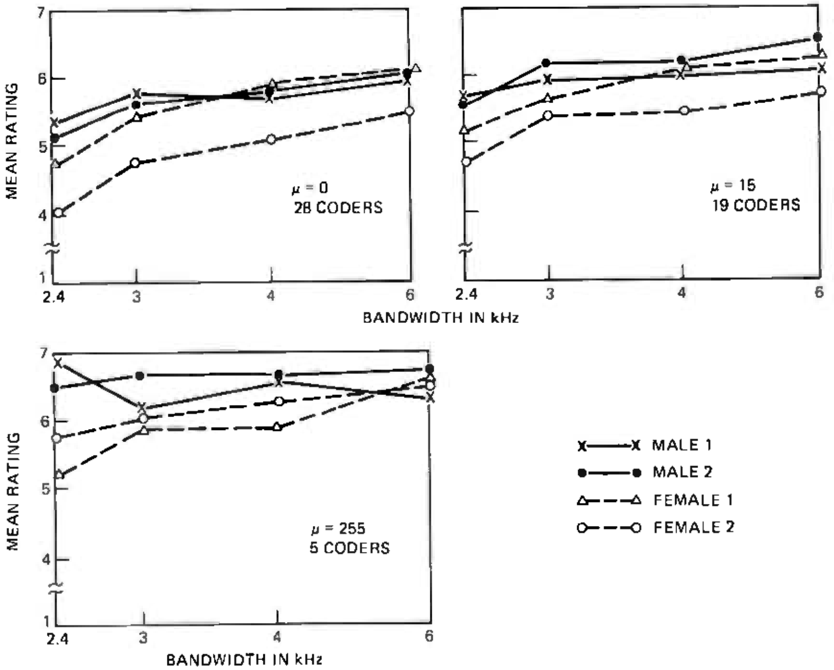

Fig. 4—Mean rating across clipping level and step size as a function of bandwidth for each talker and each companding law.

Table IV — Mean ratings across talkers and listeners

Companding			$\mu = 0$				$\mu = 15$				$\mu = 255$	
Clipping Level			2048	256	128	64	1920	240	120	60	2040	255
6 kHz Bandwidth	Step size	1	9.2	8.8	7.0	4.7	9.1	7.6	6.9	4.7	9.2	5.0
		2	9.2	8.5	6.3	4.4	9.1	7.4	5.3	3.4	7.8	
		4	9.1	8.3	6.1	4.1	8.3	6.2	5.2	3.3	6.5	
		8	8.1	7.1	5.8	4.0	8.7	4.8	3.8		4.6	
		16	8.1	6.3	4.8	3.8	7.6	3.9				
		32	6.3	5.1	4.0	2.4	5.9					
		64	5.0	3.8	3.2	1.3	4.3					
4 kHz Bandwidth	Step size	1	9.0	7.6	6.3	3.6	8.7	7.2	5.3	3.8	7.7	4.8
		2	8.3	7.6	6.4	4.2	8.6	6.7	4.7	3.8	7.3	
		4	8.3	6.8	5.7	4.2	8.2	6.3	5.1	3.2	6.0	
		8	7.2	6.2	4.9	4.3	7.5	5.3	3.7		5.2	
		16	6.7	5.7	4.7	3.6	6.9	3.9				
		32	5.9	4.8	3.6	2.5	5.6					
		64	5.3	3.6	3.1	1.2	4.7					
3 kHz Bandwidth	Step size	1	7.9	6.7	5.3	3.9	8.1	6.4	5.1	3.6	8.2	4.5
		2	7.9	6.6	5.2	3.7	8.7	6.2	4.3	3.4	6.9	
		4	7.2	6.4	4.5	4.1	7.8	6.3	4.4	2.7	5.7	
		8	6.6	5.6	5.3	3.3	6.6	4.6	3.3		5.0	
		16	5.8	4.9	4.4	2.7	5.7	4.1				
		32	4.7	3.9	3.6	2.1	4.5					
		64	3.8	2.9	2.6	1.3	3.6					
2.4 kHz Bandwidth	Step size	1	9.4	7.7	6.0	4.7	8.9	8.0	5.5	3.9	8.4	4.6
		2	9.1	6.9	6.2	4.4	8.4	7.2	5.1	4.0	7.5	
		4	8.2	7.3	6.1	4.3	8.1	6.1	4.1	3.3	6.0	
		8	8.0	6.7	5.6	4.2	8.1	5.7	3.5		5.2	
		16	7.1	5.7	5.1	3.2	6.7	4.3				
		32	5.6	4.5	4.2	3.0	5.8					
		64	4.9	4.4	2.8	1.3	5.0					

$\mu = 0$, 15, 255. Although there was some evidence that the coded speech of female talkers was rated somewhat lower than that of male talkers, the major source of the statistically significant differences among the talkers and the talker-bandwidth interaction was the consistently lower ratings assigned to one female voice. The mean power of her speech was approximately 3 dB greater than that of the other three talkers and the standard deviation of the power about 0.2 dB less, making her speech more sensitive to clipping and filtering. Since the effect of the talkers was minimal, the mean rating across talkers was used for further analyses, thus reducing the variability in the data to that due to the influence of only the physical variables of the coders. The mean ratings across talkers and listeners are shown in Table IV.

7.2.4 Bandwidth

Figure 4 also shows the effect of the four different bandwidths on the ratings. Although the ratings tended to decrease as the bandwidth narrowed, the differences between 6, 4, and 3 kHz were very small. Indeed, the source of the significant differences due to bandwidth was the much lower ratings that resulted from reducing the bandwidth from 3 to 2.4 kHz. The ratings pertaining to three of the talkers contained no significant interactions between bandwidth and the other coder design variables. Only in the data for the female talker with the low ratings were these interactions statistically significant. The most salient of these interactions was between bandwidth and clipping.

7.2.5 Clipping, step size, and companding

Figure 5 shows the mean rating across listeners, talkers, and bandwidth at each step size as a function of clipping level, A, for each of the three companding conditions. The horizontal axes show A decreasing (i.e., the amount of clipping increasing) from left to right.

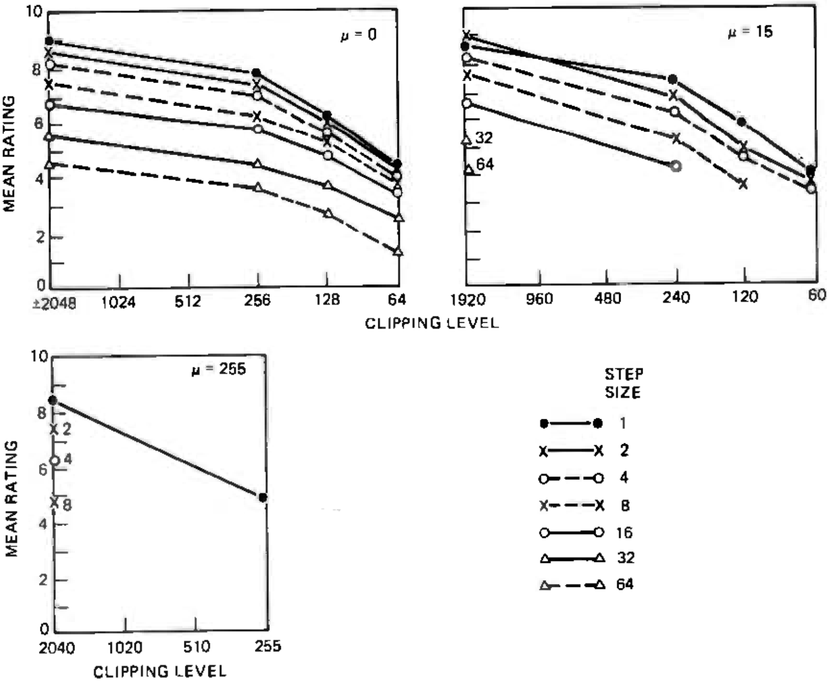

Fig. 5—Mean rating across listeners, talkers, and bandwidth at each step size as a function of clipping level for each companding law.

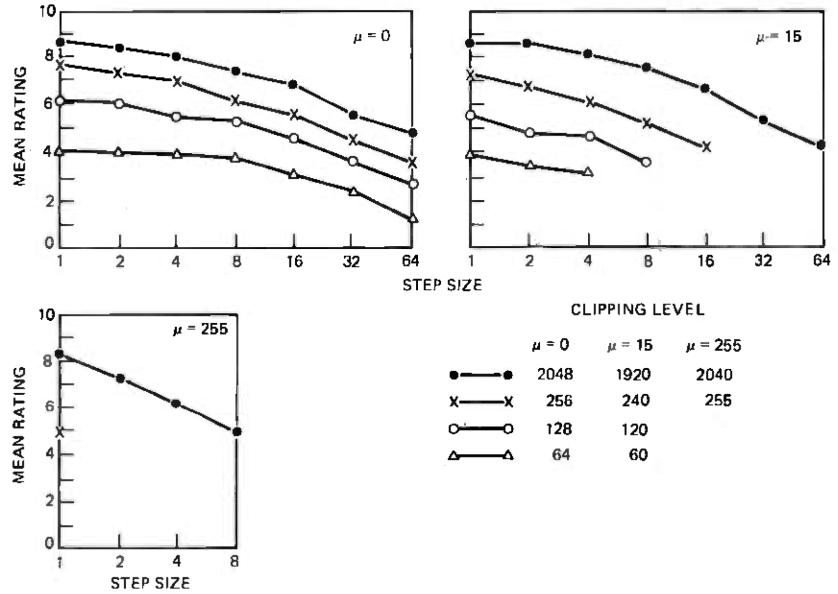

Fig. 6—Mean rating across listeners, talkers, and bandwidth at each clipping level as a function of step size for each companding law.

For each step size S the mean rating decreases as the amount of clipping increases. With $\mu = 0$ or $\mu = 15$, an octave decrease in A results in a relatively small decline in rating when $A > 256$ and a relatively large decrease when $A \leqq 256$. The data for $\mu = 255$, though limited, suggest that relative to the other compression laws, ratings are more sensitive to small amounts of clipping ($A > 256$).

Figure 6 shows the same data points plotted as a function of step size at each clipping level. While, for each A, the ratings are inversely related to S, equal incremental differences in S tend to result in larger differences in the ratings as S increases. That is, the curves generally have a steeper slope when $S > 8$ for $\mu = 0$, and $S > 4$ for $\mu = 15$. The steeper slope of the curve for $\mu = 255$ suggests that quality may be influenced by an interaction between μ and S. An analysis of the ratings of unclipped speech with $S = 1$, 2, 4, and 8 confirms this observation. While the ratings for $\mu = 0$ and $\mu = 15$ were not significantly different, those at $\mu = 255$ were significantly different from the ratings for the other two companding laws.

7.3 Prediction of quality ratings

7.3.1 Signal-to-noise ratio

Figure 7 is a scatter plot of average rating vs measured s/n for the 28 uniform quantizers and the 4 white-gaussian-noise processes. Here, s/n is the usual engineering measure: the ratio of signal power to mean-square difference between quantizer input and output ($x - q$ in Fig. 3). The s/n coordinate of a point in Fig. 7 is the average of the 16 s/n's of the individual utterances (4 bandwidths by 4 talkers) processed by a coder or noise condition. The most important feature of Fig. 7 is the horizontal clustering of the seven points associated with a given value of A, when $A \leqq 256$. In all of these quantizers, the clipping noise, NC, substantially dominates the granular noise, NG, in the total noise, $NC + NG$. This dominance implies that s/n is virtually independent of S with $A \leqq 256$, while, by contrast, perceived distortion depends strongly on S, as evidenced by the vertical spread of the points pertaining to each A. Clearly, in the presence of clipping, s/n is a poor guide to ratings of speech quality: coders with the same s/n elicit widely divergent ratings.

7.3.2 Noise references

In Fig. 7, ratings and s/n are well correlated for one set of coders: those with no clipping, $A = 2048$. Here, the relationship of rating to s/n is similar to that observed for the gaussian noise processes. Figure 7 suggests, therefore, that for uniform quantizing, white gaussian noise is a good noise reference when there is no clipping; it is a poor noise reference when clipping is significant.

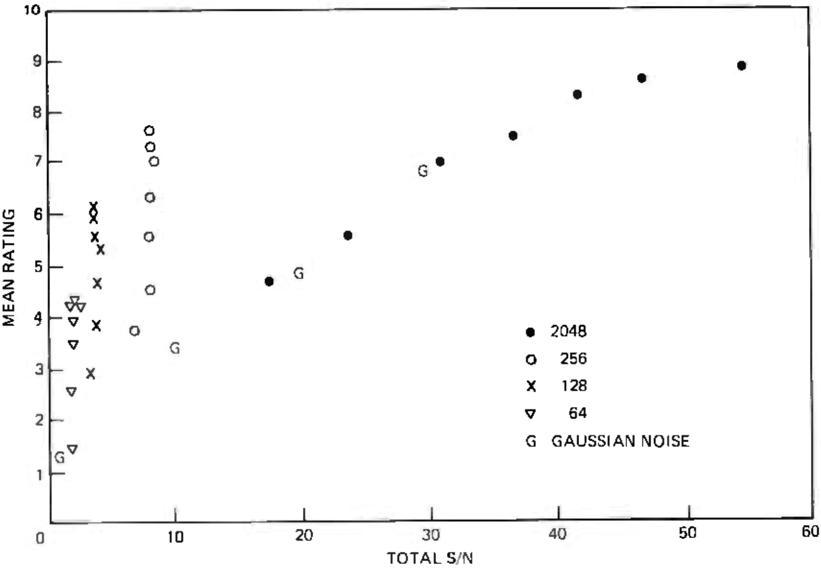

Fig. 7—Relationship between mean rating and total s/n for the 28 linear conditions and the 4 gaussian-noise conditions.

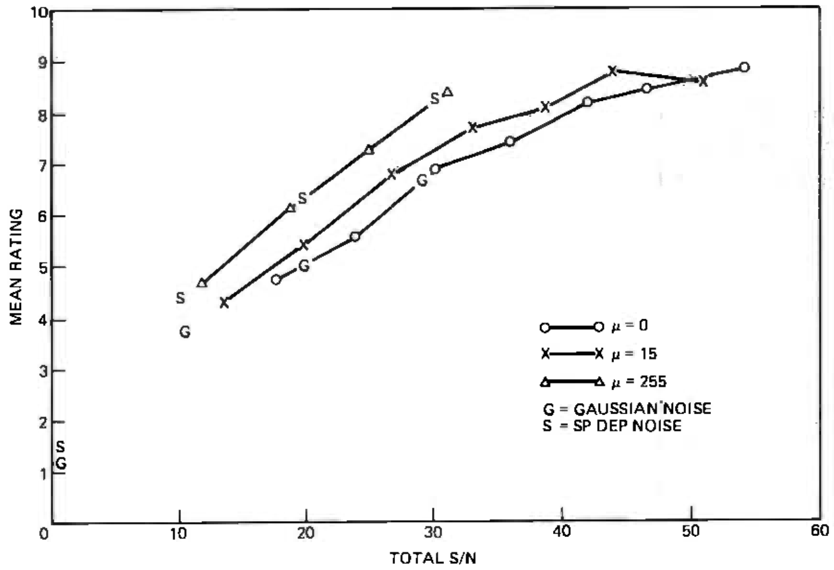

Fig. 8—Mean ratings of unclipped speech for each companding law and the added noise conditions as a function of the total s/n.

Because the amount of granular distortion produced by a coder with companding depends on signal amplitude, one may suppose that speech-dependent noise would provide a better noise reference than white gaussian noise for companded coders.[2,7] Figure 8 lends support to this conjecture by showing, for all of the coders with no clipping and all of the noise processes, the relationship of average rating to s/n. For $\mu = 255$, the relationship is similar to that observed with speech-dependent noise; for $\mu = 0$, it is similar to that observed with white gaussian noise. $\mu = 15$ is an intermediate case.

7.3.3 Regression analysis

Because total s/n proved a poor correlate of listener ratings, we turned to multiple regression procedures to find an objective predictor of the ratings. The analyses of variance indicated that the ratings were primarily influenced by S and A, which have nearly independent effects.* Consequently, we used as independent variables of the regression one distortion measure related to S and one related to A. Appropriate measures proved to be Q, the granular s/n (ratio of signal power to power in NG) measured in dB, and P, the clipping probability (the proportion of speech samples $> A$), expressed as a percentage.

---

* In the analyses of the linear conditions, S accounted for 35 percent of the total variance, A for 45 percent, and the interaction of S and A for only 1 percent.

The regression was computed at each companding level with the original values for each talker at each bandwidth included as repeated observations. For example, each of the 28 coders with $\mu = 0$ was represented by 16 measurements (4 talkers × 4 bandwidths). Table V lists the coefficients obtained by the regression procedure at each companding level and also by combining the three companding levels. While the values of the coefficients change with μ, the correlations and the rms values of the residuals do not change radically. The regression procedure was applied to the data for the coders with $\mu = 255$ for completeness, but the computation was based on information for only five coders at the smaller step sizes and only one clipping condition. When the ratings of the three companding laws were also included as repeated observations, the ratings predicted by appropriate weighting of only the Q and P correlate highly with the obtained ratings.

VIII. DISCUSSION

8.1 Effects of design variables

Among the PCM design variables, system bandwidth W had the smallest effect on the ratings, a finding consistent with that of O'Neal and Stroh[4] who state that "over the range of 2.4–4.3 kHz changes in the bandwidth W of the speech signal are inconsequential in terms of the resultant user ratings." (To describe our data, we would substitute "of minor importance" for "inconsequential.") In considering the practical application of this conclusion, a caveat is necessary. In a recent experiment, Goodman, Goodman, and Chen[8] found that band-limiting, although less important than clipping and quantizing in determining listener ratings, had a very strong effect on consonant intelligibility. This suggests that the impact of band-limiting on the quality of communication may be more substantial than the results of rating tests imply.

The significance of the dependence of ratings on the quantizer variables, μ (compression law), S (step size), and A (clipping level),

Table V — Coefficients obtained by regression level
($\hat{R} = aP + bQ + c$)

	a	b	c	Correlations	RMS Residual
$\mu = 0$	−0.08	0.09	3.87	0.87	1.005
$\mu = 15$	−0.11	0.11	3.09	0.87	0.957
$\mu = 255$	−0.27	0.16	2.96	0.84	0.825
Combined	−0.10	0.09	3.99	0.85	1.038

P = Percent clipped.
Q = s/n granular quantizing noise.

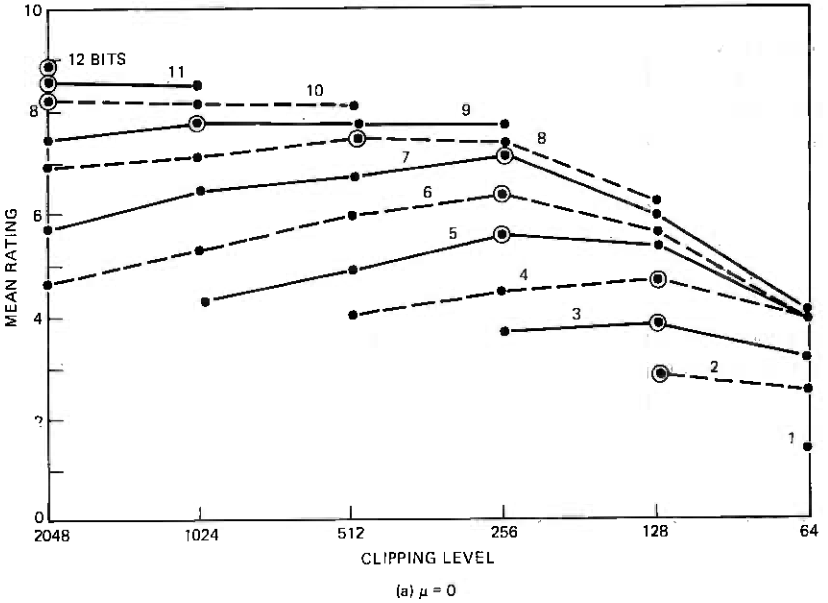

(a) $\mu = 0$

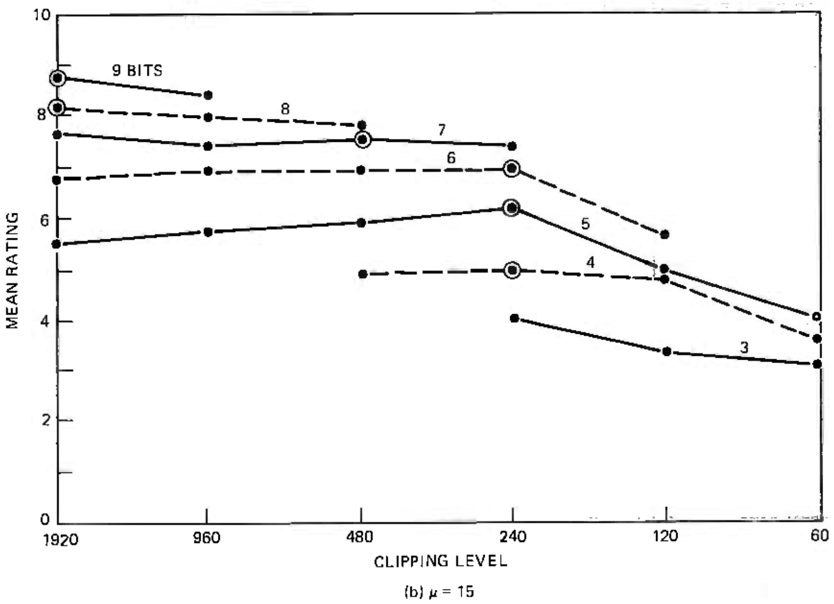

(b) $\mu = 15$

Fig. 9—Mean ratings at a constant number of bits as a function of clipping level for (a) $\mu = 0$ and (b) $\mu = 15$. A circle indicates the highest-rated quantizer of a certain number of bits.

will be more apparent if we return to the usual engineering description of a quantizer which includes the number of bits per sample, B, as an independent variable. Thus, in Fig. 9, we have plotted the same points that appear in Fig. 5, but in this case, we have drawn lines showing contours of constant B rather than constant S. Here we see the effect on subjective ratings of the well-known compromise between clipping and quantizing in coder design. At the left of each curve, we have the quantizers that cause little or no overload but have high step sizes and, therefore, substantial granular quantizing noise. At the right, clipping distortion predominates over granular noise.

Figure 10 demonstrates the effect of companding on ratings by displaying on the same graph rating vs clipping level curves for 5-bit and 6-bit encoders with $\mu = 0$ and $\mu = 15$. For a given clipping level, even this small amount of companding (practical values of μ are 100 and 255) produces substantially higher ratings than those given the uniform quantizer. The companding advantage is well known and accounts for the presence of compandors in all PCM transmission systems. In terms of statistical signal theory, we may explain the advantage by saying that a nonuniform quantizer provides a better match to the probability distribution of speech amplitudes than a uniform quantizer. A perceptual explanation is that the low-level portions of a speech signal carry the most information. With A and B

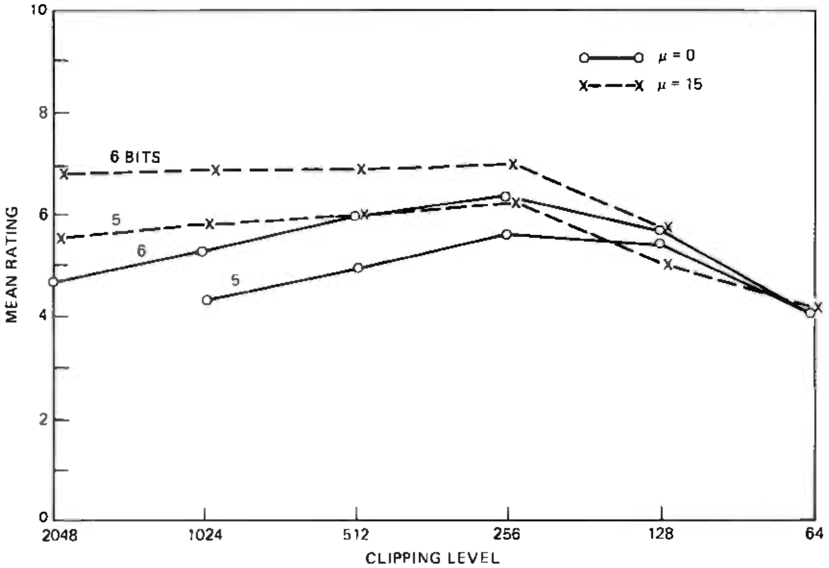

Fig. 10—Mean rating as a function of clipping level for 5 and 6 bits at $\mu = 0$ and $\mu = 15$, demonstrating the effect of companding.

given, a nonuniform quantizer codes low-amplitude samples with a smaller step size (and, therefore, lower NG) than the corresponding uniform quantizer.

8.2 Objective measures of distortion

Figure 11 shows, for coders with uniform quantizers, total s/n as a function of A. There are striking differences between these curves and Fig. 9. The most important differences are in the locations of the maximum points on corresponding curves and the substantially steeper slopes to the right of the maxima in Fig. 11. Both of these differences reflect the fact that NC increases very rapidly from zero as the clipping level decreases from $A = 2048$, while, by contrast, listener opinions are relatively insensitive to clipping until $A < 512$.

The disparity between Figs. 9 and 11 suggests that even with B constant, s/n, the usual engineering measure of quantizer quality, is a poor guide to subjective ratings, mainly because the mean-square clipping is a poor predictor of listener ratings. A more useful measure of clipping distortion is clipping probability, which we have measured as the percentage of samples clipped in an utterance. P varies with A in the manner shown in Fig. 12. Observe that, like the ratings, P changes slowly as A decreases from 2048 and that it is most sensitive to changes in A when $A < 512$. These similarities account for the accuracy of the regression formulas in Table V, which have as in-

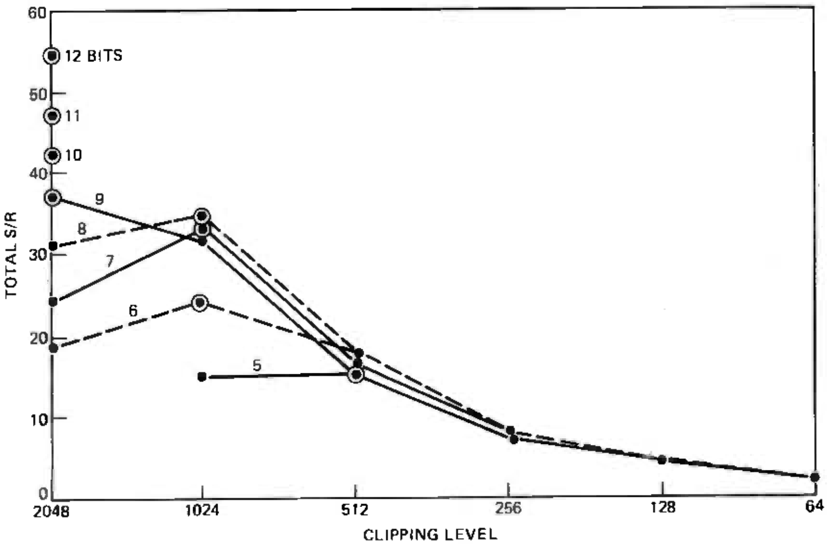

Fig. 11—Total s/n as a function of clipping level at a constant number of bits. Circles indicate the maximum s/n at each bit rate.

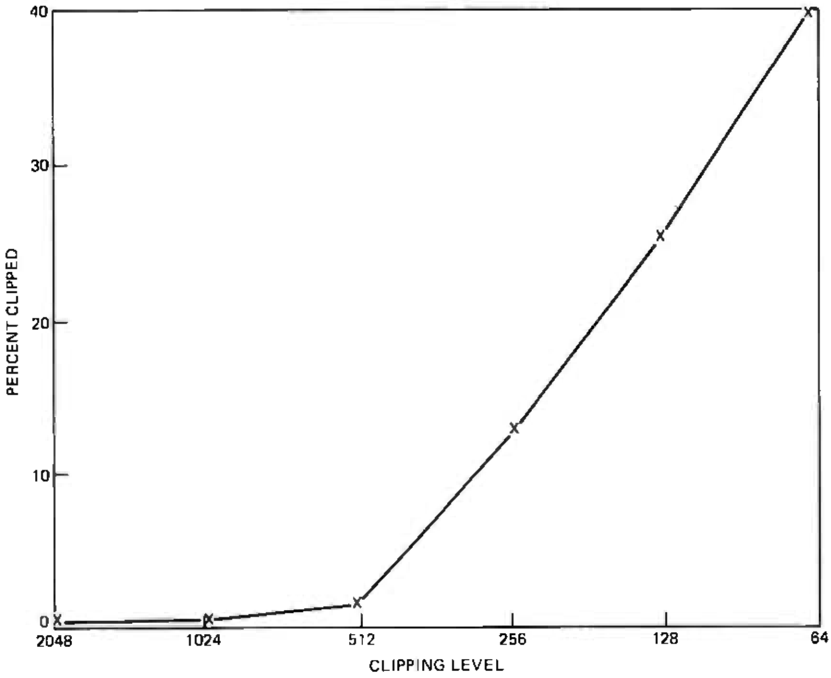

Fig. 12—Percent clipped as a function of clipping level.

dependent variables P and the signal-to-noise ratio Q of the granular quantizing noise NG. These formulas, based on the notion of two perceptually distinct distortions, are more useful predictors of subjective quality than is total s/n, which is based on the fallacious assumption that listeners attend only to the difference between quantizer input and output with no regard to the components of this difference.

8.3 Optimum quantizers

Given a companding law and a fixed number of bits per sample, there is an optimum quantizer with overload point A^* that provides the best mixture of clipping distortion and granular noise. For $A < A^*$, clipping is the predominant type of distortion; for $A > A^*$ granular noise predominates. A circle in Fig. 9 indicates the subjectively optimum overload point for a given bit rate. As the number of bits per sample increases, so does A^*. In high-resolution quantizers, it is possible to have low granular noise and very little clipping simultaneously. Notice that the optimum points in Fig. 9 are all one or two octaves to the right of the corresponding points in Fig. 11. The experiment demonstrates that listeners are more tolerant of clipping than s/n measurements suggest. In addition, the curves in Fig. 9 are considerably broader than those in Fig. 11, which indicates that listeners are relatively insensitive to changes in A in the region of A^*.

This observation relates directly to the quantizer dynamic range problem. While in the experiment we have held the speech power fixed and varied A, we would have obtained the same distortions by holding A fixed and changing the speech signal level. It follows that the horizontal axes that we have labeled "clipping level" can, for a single quantizer, be renamed "speech level," which increases from left to right. Figure 11 shows that a uniform quantizer has near-optimum signal-to-noise performance for only a narrow range of speech levels. By contrast, we see in Fig. 9 that listeners give nearly optimum ratings over a much wider range of input powers.

IX. CONCLUSIONS

Our results lead to several general observations regarding the subjective evaluation of speech degraded by digital coding. First, our data indicate that when the degraded speech includes certain types of digital signal distortions, such as peak clipping, then total s/n is a poor objective indicator of subjective speech quality. For the coders we studied, a simple linear combination of two objective measures was a good predictor of the subjective quality of speech with quantizing and clipping distortions; however, we do not know of any single objective measure which would be a good composite indicator of subjective speech quality for all types and combinations of digital signal distortions. Second, because some types of digital signal distortions seem to be perceptually distinct, it seems unlikely that the subjective quality of digital speech can be evaluated by reference to a single type of analog or digital signal distortion, such as speech-dependent noise. And third, because coders are optimized by trading off different types of distortions, it follows that the important cases to study are those where distortions occur in combination rather than singly. This implies that knowing the relationships between subjective speech quality and various types of reference-signal distortions occurring singly—be they digital or analog—may be of limited value for predicting the subjective quality of coded speech if most practical coders produce speech degraded by combinations of distortions. These observations should be kept in mind by designers who must struggle with the problem of how various parameters of their coders affect the subjective quality of the speech.

REFERENCES

1. D. L. Richards, *Telecommunication by Speech*, London: Butterworths, 1973, Ch. 4.
2. H. B. Law and R. A. Seymour, "A Reference Distortion System Using Modulated

Noise," Proc. Inst. Elec. Eng. London, Part-B, Electron., *109*, No. 48 (November 1962), pp. 484–487.

3. R. W. Donaldson and D. Chan, "Analysis and Subjective Evaluation of Differential Pulse-Code Modulation Voice Communication Systems," *IEEE Trans. Commun. Technol.*, *COM-17*, No. 1 (February 1969), pp. 10–19.
4. J. B. O'Neal, Jr. and R. W. Stroh, "A Speech Encoder-Multiplexer Feasibility Study," Air Force Office of Scientific Research, Report No. AD 739965, March 8, 1972, Ch. 4.
5. J. Yan and R. W. Donaldson, "Subjective Effects of Channel Transmission Errors on PCM and DPCM Voice Communication Systems," *IEEE Trans. Commun.*, *COM-20*, No. 3 (June 1972), pp. 281–290.
6. H. Kaneko, "A Unified Formulation of Segment Companding Laws and Synthesis of Codecs and Digital Compandors," B.S.T.J., *49*, No. 7 (September 1970), pp. 1555–1588.
7. M. R. Schroeder, "Reference Signal for Signal Quality Studies," *J. Acoust. Soc. Amer.*, *44* (1968), pp. 1735–1736.
8. D. J. Goodman, J. S. Goodman, and M. Chen, "Relationship of Intelligibility and Subjective Quality in Digitally Coded Speech," Talk given at the 90th Meeting of the Acoustical Society of America, Abstract in *J. Acoust. Soc. Amer.*, *58*, Supplement No. 1 (Fall 1975), p. S130.

Copyright © 1976 American Telephone and Telegraph Company
THE BELL SYSTEM TECHNICAL JOURNAL
Vol. 55, No. 8, October 1976
Printed in U.S.A.

Rain-Rate Distributions and Extreme-Value Statistics

By S. H. LIN

(Manuscript received March 17, 1976)

An extension of a method of Chen and Lahlum[1] *for estimating the distributions of high rain rates is described. Through application of the statistical theory of extremes to available yearly maximum rain-rate data, a reasonably accurate distribution is obtained. The calculated results agree well with previously obtained 20-year data. Application of this method to Weather Bureau Rainfall Intensity-Duration-Frequency Curves has yielded 50-year distributions of 5-minute rain rates for 36 locations in the western United States; others can be similarly obtained. Such long-term rain-rate distributions are valuable for microwave radio-path engineering, especially in the western United States where shorter-term data sources are inadequate.*

I. INTRODUCTION

References 2 and 3 describe a procedure for obtaining long-term ($\geqq 20$ years) distributions of 5-minute rain rates from data published by the National Climatic Center.[4] Such distributions have been obtained for 202 locations in the eastern and midwestern United States and applied to path engineering of 11-GHz radio links.

However, the excessive short duration rainfall data[4] on which these distributions are based contain only rainfalls that exceed an excessive rainfall threshold defined by the National Climatic Center.[2,3] For example, the threshold is 75 mm/hr for 5-minute intervals. In low rain-rate areas, such as Oregon and Washington, almost all rainfalls do not exceed the threshold and, hence, are not included in the excessive short-duration rainfall data. For example, at Spokane, Washington, the 5-minute rain rate exceeded the 75 mm/hr threshold only once in the 20-year period from 1953 to 1972. This data source, therefore, is an unsatisfactory basis for radio-path engineering in such areas. On the other hand, processing other longer-term data—say 50 years—is tedious and costly. This has motivated the search for an alternative method. Fortunately, the statistical behavior of the extremes of a random variable has been extensively investigated.[5–10] This paper describes a method for obtaining distributions of high rain rates by applying this theory to the yearly maximum rain-rate data published by the National Climatic Center.

In an unpublished work, Chen and Lahlum[1] have applied the theoretical distribution of yearly maximum 5-minute rain rates and an empirical extrapolation to obtain the rain-rate distribution in the range of interest to radio-path engineering. In this paper, we extend Chen and Lahlum's method by incorporating the theoretical distributions of yearly kth largest 5-minute rain rates for k ranging from 1 to 12. The application of the higher-order statistics of extremes eliminates the need for empirical extrapolation.

In this paper, a 5-minute rain rate corresponds to the average value of the randomly varying rain rate in a 5-minute interval and is calculated as $\Delta H/\tau$, where ΔH is the 5-minute accumulated depth of rainfall and $\tau = 1/12$ hour $= 5$ minutes. For illustration, only the statistics of 5-minute rain rates are discussed in this report. The method is also applicable to other integration times.

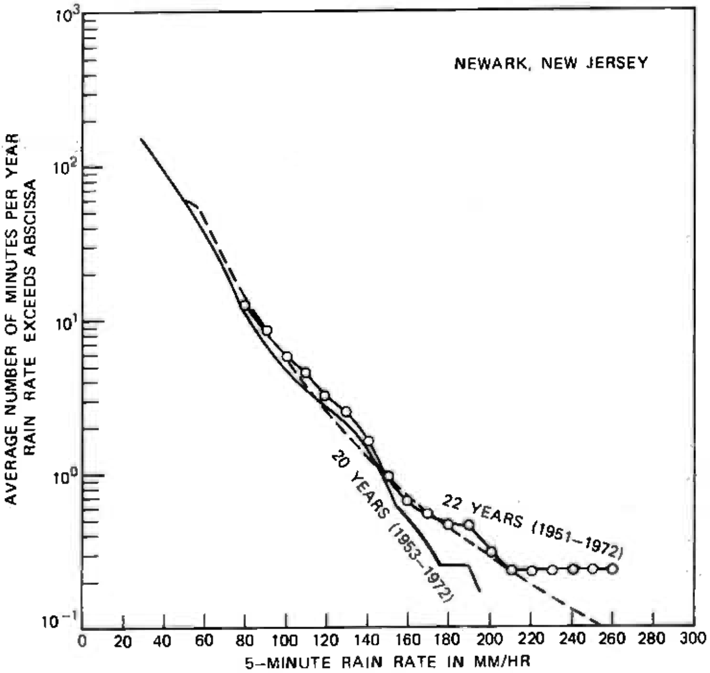

Fig. 1—Comparison of 20-year rain-rate distribution calculated by extreme statistics method (dashed line) with 20- and 22-year data (solid lines) for Newark, New Jersey. The difference between the 20- and 22-year data also indicates the instability of high rain-rate statistics.

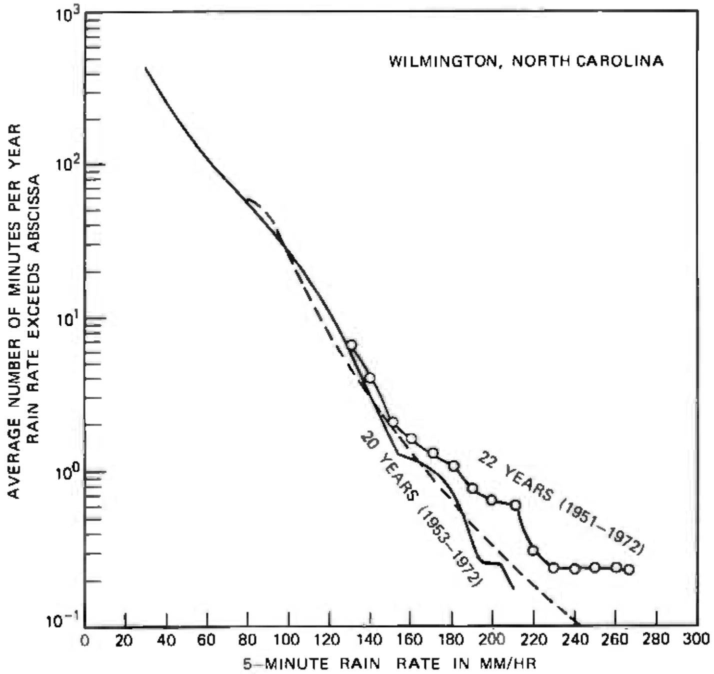

Fig. 2—Comparison of 20-year rain-rate distribution calculated by extreme statistics method (dashed line) with 20- and 22-year data (solid lines) for Wilmington, North Carolina. The difference between the 20- and 22-year data also indicates the instability of high rain-rate statistics.

II. THE STATISTICS OF EXTREMES

Let R be the randomly varying 5-minute rain rate and R_k be the kth largest 5-minute rain rate in a given year. In other words, R_1 is the yearly maximum 5-minute rain rate, R_2 is the yearly second largest 5-minute rain rate, etc. The value of R_k varies from year to year, and the probability distribution of R_k is the subject of the statistics of the kth extreme.

Many sets of rain-rate data[11–15] indicate that rain-rate distributions in the moderate and low rain-rate region can be closely approximated by the lognormal distribution. In the tail region, the time bases are usually insufficient to yield stable results for testing the lognormal hypothesis. Figures 1 and 2 show instability at extreme values occurring in 20-year time bases. We will assume that the rain-rate distributions are lognormal and proceed to show that the calculated distributions of extreme rain rates agree well with the data as displayed in Figs. 1 through 9.

Let

$$x = \ln R, \tag{1}$$

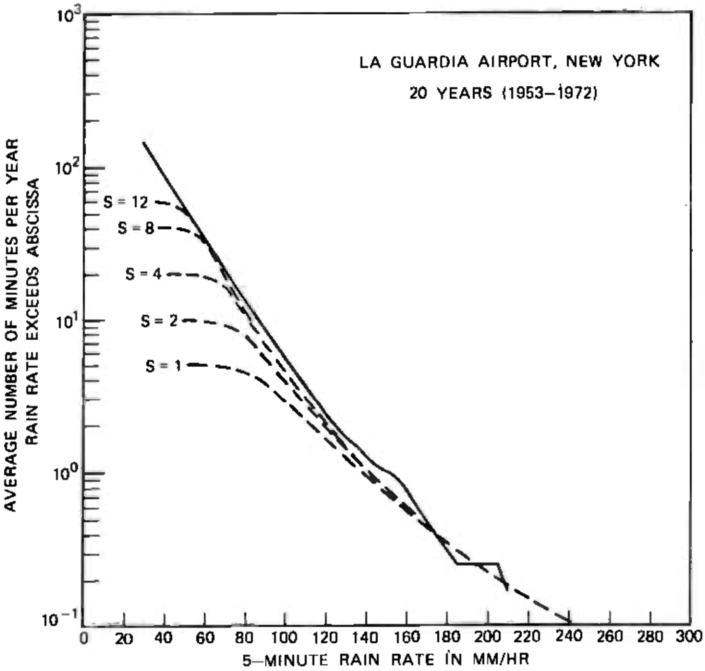

Fig. 3—Comparison of 20-year rain-rate distribution calculated by extreme statistics method (dashed lines) with the 20-year data (solid line) at La Guardia Airport, New York, New York.

and

$$x_k = \ln R_k. \tag{2}$$

The lognormal hypothesis for R is equivalent to the statement that x is (approximately) normal. The distribution of the kth extreme, x_k, as derived by Cramer[8] is

$$P(x_k \geqq X) = 1 - e^{-e^{-y}} \sum_{N=0}^{k-1} \frac{e^{-Ny}}{N!}, \tag{3}^*$$

where

$$y = \alpha(X - U) \tag{4}$$

and is called the reduced variate. In this expression, α and U are scale and location parameters, respectively, and are related to the sample mean and sample standard deviation of x_1. Notice that the distribution, $P(x_k \geqq X)$, for any k, is completely determined by the two parameters α and U. These two parameters can be calculated from the measured

---

* The cumulative distribution function (3) is obtained by integrating the probability-density function derived by Cramer in Ref. 8.

yearly maximum rain-rate data. Let

$$R_1(j),\ j = 1, 2, 3, \cdots, M \tag{5}$$

be the measured yearly maximum 5-minute rain rate in M years of measurements. For example, $R_1(7)$ represents the yearly maximum 5-minute rain rate observed in the seventh year of an M year experiment. Let

$$x_1(j) = \ln\left[R_1(j)\right] \tag{6}$$

be the yearly maximum value of x in the jth year. From the measured data of $x_1(j)$, $j = 1, 2, 3, \cdots, M$, we can obtain an approximate distribution of x_1. The parameters α and U can be estimated by fitting the theoretical $P(x_1 \geqq X)$ to the measured data. Gumbel[6] has shown that a least-square fit of $P(x_1 \geqq X)$ to the data leads to the following formulas for calculating α and U:

$$\alpha = \frac{\sigma_z}{\sigma_x}, \tag{7}$$

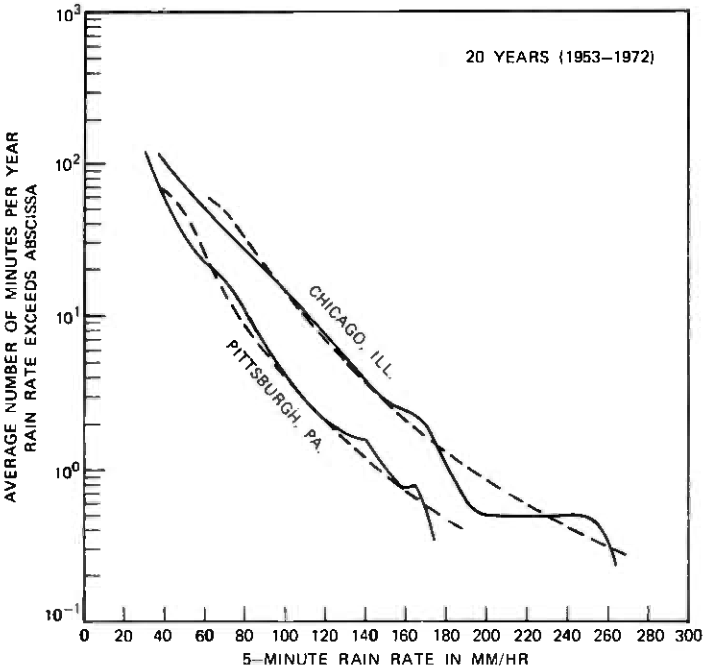

Fig. 4—Comparison of 20-year rain-rate distribution calculated by extreme statistics method (dashed line) with 20-year data (solid line) for Pittsburgh, Pennsylvania, and Chicago, Illinois.

and

$$U = \bar{x}_1 - \frac{\bar{z}}{\alpha}, \tag{8}$$

where

$$\bar{x}_1 = \frac{1}{M} \sum_{j=1}^{M} x_1(j) \tag{9}$$

is the sample mean of x_1,

$$\overline{x_1^2} = \frac{1}{M} \sum_{j=1}^{M} [x_1(j)]^2, \tag{10}$$

$$\sigma_x = \sqrt{\overline{x_1^2} - \bar{x}_1^2} \tag{11}$$

is the sample standard deviation of x_1,

$$Z(j) = -\ln\left(-\ln \frac{j}{M+1}\right), \tag{12}$$

$$\bar{Z} = \frac{1}{M} \sum_{j=1}^{M} Z(j), \tag{13}$$

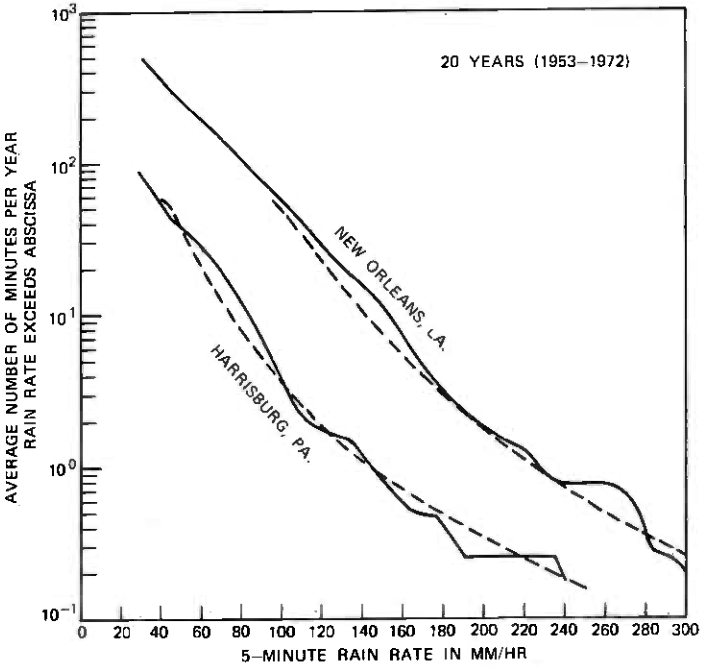

Fig. 5—Comparison of 20-year rain-rate distribution calculated by extreme statistics method (dashed line) with 20-year data (solid line) for Harrisburg, Pennsylvania, and New Orleans, Louisiana.

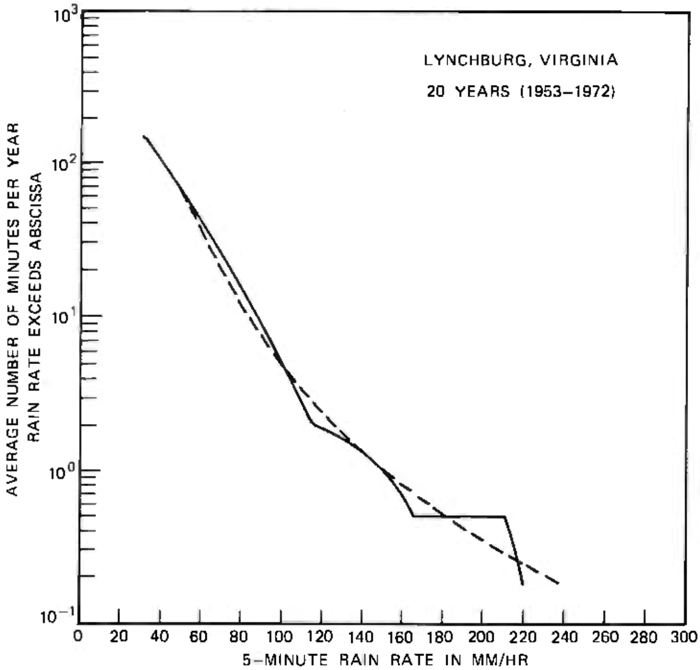

Fig. 6—Comparison of 20-year rain-rate distribution calculated by extreme statistics method (dashed line) with 20-year data (solid line) for Lynchburg, Virginia.

$$\overline{Z^2} = \frac{1}{M} \sum_{j=1}^{M} [Z(j)]^2, \tag{14}$$

and

$$\sigma_z = \sqrt{\overline{Z^2} - \bar{Z}^2}. \tag{15}$$

Thus, we have all the necessary formulas for calculating $P(x_k \geqq x)$. To obtain the rain-rate distribution, we substitute (2) into (3) to yield

$$P(R_k \geqq r) = 1 - e^{-e^{-y}} \sum_{N=0}^{k-1} \frac{e^{-Ny}}{N!}, \tag{16}$$

where

$$y = \alpha[(\ln r) - U]. \tag{17}$$

Therefore, the time that R_k will exceed the threshold r, on long-term average, is

$$\begin{aligned} T(R_k > r) &= \tau \times P(R_k \geqq r) \\ &= \tau \times \left\{ 1 - e^{-e^{-y}} \sum_{N=0}^{k-1} \frac{e^{-Ny}}{N!} \right\}, \end{aligned} \tag{18}$$

where $\tau = 5$ minutes is the rain-gauge integration time. Furthermore, in any given year, R_k and R_l will never occur in the same 5-minute

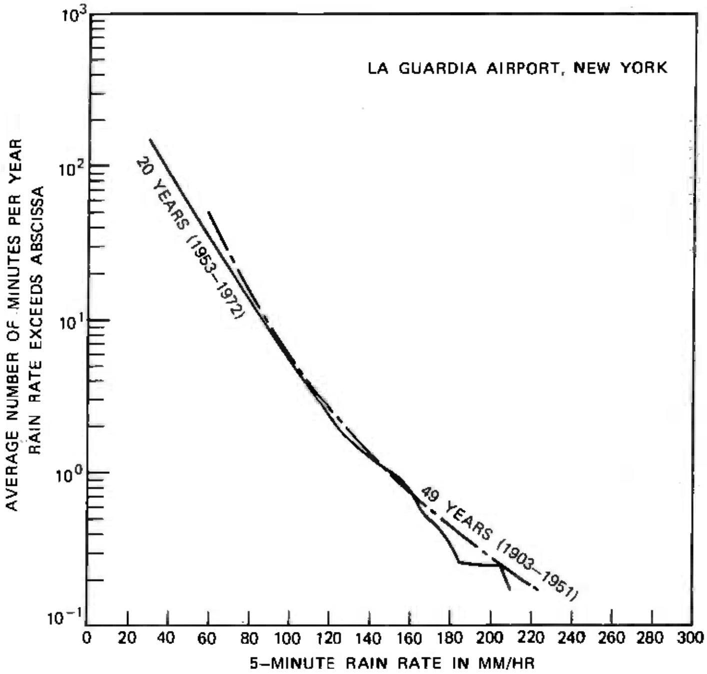

Fig. 7—Comparison of 49-year (1903–1951) distribution of 5-minute rain rates calculated by extreme statistics method with measured 20-year (1953–1972) data at La Guardia Airport, New York, New York.

interval if $k \neq l$. This means $T(R_k \geqq r)$ for various order k can be summed to yield an approximation to the original rain-rate distribution in the extremal region; i.e.,

$$T(R \geqq r) \simeq \sum_{k=1}^{S} T(R_k \geqq r) \tag{19}$$

for high rain rates.

The only input required for the calculation is the yearly maximum 5-minute rain rates,

$$R_1(j),\ j = 1, 2, 3, \cdots, M,$$

which can be obtained from National Climatic Center publications.[4]

III. COMPARISON OF CALCULATED AND MEASURED RESULTS

Figures 1 through 6 display the comparison of the distributions of high rain rates calculated via statistics of extremes from the data for eight locations. The number of years M is 20 (from 1953 to 1972). In these figures, the solid lines represent the data obtained by the method described in Refs. 2 and 3, whereas the dashed lines are the distribution calculated by the theory of extremes.

In Fig. 3, the value of S in eq. (19) is varied from 1 to 12. For $S = 1$, $T(R_1 \geqq r)$ is the distribution of yearly maximum 5-minute rain rate and is approximately equal to $T(R \geqq r)$ *only* in the extremal region (beyond 160 mm/hr). As r decreases, $T(R_1 \geqq r)$ deviates significantly from $T(R \geqq r)$, limiting at the 5-minute-per-year level as r approaches zero. The basis for this saturation is that there is only *one* yearly maximum 5-minute rain rate (with 5-minute duration by definition) in any given year. It is obvious that the yearly maximum 5-minute rain rate can exceed any threshold by no more than 5 minutes per year. Similarly, for $S = 2$, $T(R_1 \geqq r)$ plus $T(R_2 \geqq r)$ is limited to a 10-minute-per-year level as r approaches zero. However, Fig. 3 shows that the applicable range of approximation (19) increases rapidly with S.

For engineering terrestrial radio paths, we are interested in the range of rain-rate distributions below 50 minutes per year, because a single radio hop outage exceeding 50 minutes per year is considered

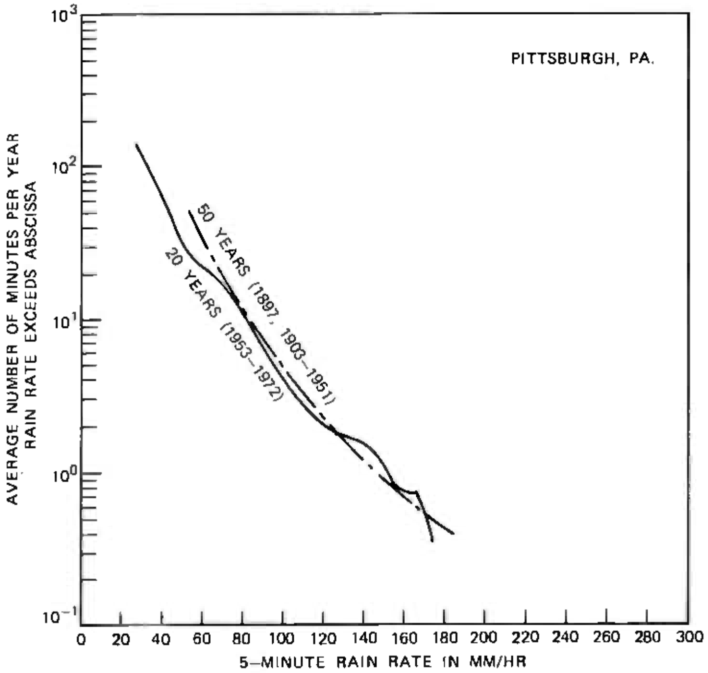

Fig. 8—Comparison of 50-year (1897, 1903–1951) distribution of 5-minute rain rates calculated by extreme statistics method with measured 20-year (1953–1972) data for Pittsburgh, Pennsylvania.

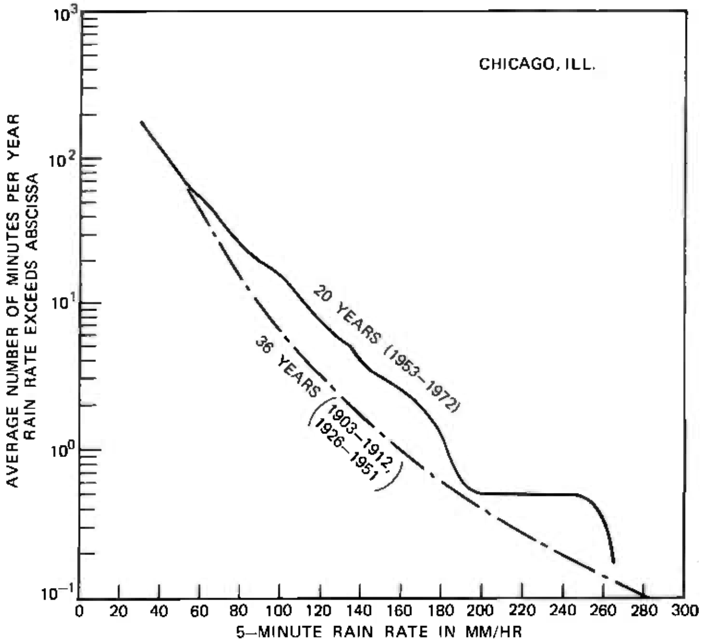

Fig. 9—Comparison of 36-year (1903–1912, 1926–1951) distribution of 5-minute rain rates calculated by extreme statistics method with measured 20-year (1953–1972) data at Midway Airport, Chicago, Illinois.

undesirable. Figure 3 shows that using $S = 12$ in eq. (19) includes the range of interest to terrestrial radio-path engineering.

Figures 1 to 6 show similar close agreement between the calculated results and the data.

The advantage of using the extreme statistics method is its simplicity; i.e., it is much easier to obtain the extreme-statistics results from the set of 20 maximum yearly rain rates than to obtain the other displayed results which require analyzing all heavy rainfalls in each year.

IV. FIFTY-YEAR DISTRIBUTIONS OBTAINED FROM RAINFALL INTENSITY-DURATION-FREQUENCY CURVES

Rainfall intensity-duration-frequency curves published by the Weather Bureau[16] were obtained from approximately 50 years (1900–1950) of rain-rate data processed in accordance with the statistical theory for distribution of yearly maximum rain rate by the Gumbel method.[6] In other words, these curves represent $P(R_1 \geqq r)$, where R_1 is the yearly maximum rain rate. The return period $Q(R_1 \geqq r)$, which is the reciprocal of $P(R_1 \geqq r)$, is labeled on each curve; i.e.,

$$Q(R_1 \geqq r) = \frac{1}{P(R_1 \geqq r)} \text{ years.} \tag{20}$$

These curves cover the range-of-return period from 2 to 100 years and rain-gauge integration time τ (i.e., the duration) from 5 minutes to 24 hours. We considered only the 5-minute rain-rate statistics in this report.

Since these curves represent $P(R_1 \geqq r)$, the two parameters α and U in eq. (17) can be estimated by fitting the theoretical $P(R_1 \geqq r)$ to two points on the intensity-duration-frequency curves. Once α and U are obtained, we can calculate a distribution of high rain rates by eqs. (18) and (19). However, one adjustment is needed in this process. Gumbel[6] has shown that as the number of years M approaches infinity, $\bar{Z}$ and σ_z in eqs. (13) and (15) approach the following asymptotic values

$$\begin{aligned}\lim_{M\to\infty} \bar{Z} = \gamma &= \text{Euler's Constant}\\ &\simeq 0.5772\end{aligned} \tag{21}$$

$$\lim_{M\to\infty} \sigma_z = \frac{\pi}{\sqrt{6}}. \tag{22}$$

The corresponding asymptotic forms for α and U are

$$\lim_{M\to\infty} \alpha = \alpha_\infty = \frac{\pi}{\sqrt{6}\cdot\sigma_x}, \tag{23}$$

and

$$\lim_{M\to\infty} U = U_\infty = \bar{x}_1 - \frac{\gamma}{\alpha_\infty}. \tag{24}$$

The rainfall intensity-duration-frequency curves were obtained using the asymptotic values, α_∞ and U_∞, even though the number of years M are 50 or less. Such approximations introduce slight errors and can be corrected by the following relationships among α_∞, U_∞, α, and U:

$$\alpha = \alpha_\infty \cdot \sigma_z \cdot \frac{\sqrt{6}}{\pi} \tag{25}$$

$$U = U_\infty + \frac{1}{\alpha_\infty}\left[\gamma - \frac{\bar{Z}}{\sigma_z}\cdot\frac{\pi}{\sqrt{6}}\right]. \tag{26}$$

To relate theoretical $P(R_1 \geqq r)$ with the intensity-duration-frequency data, we combine eq. (16) and (20) to give

$$Q(R_1 \geqq r) = \frac{1}{1 - e^{-e^{-y}}}, \tag{27}$$

where

$$y = \alpha_\infty[(\ln r) - U_\infty]. \tag{28}$$

The two parameters, α_∞ and U_∞, can be determined by equating (27) to two sets of data, say (r_a, Q_a) and (r_b, Q_b), read from the intensity-duration-frequency curves. It is easily shown that the relationships are

$$\alpha_\infty = \frac{A_a - A_b}{\ln r_a - \ln r_b}, \tag{29}$$

and

$$U_\infty = \frac{A_a \ln r_b - A_b \ln r_a}{A_a - A_b}, \tag{30}$$

where

$$A_a = -\ln\left[\ln \frac{Q_a}{Q_a - 1}\right], \tag{31}$$

and

$$A_b = -\ln\left[\ln \frac{Q_b}{Q_b - 1}\right]. \tag{32}$$

By substituting α_∞ and U_∞ into (25) and (26), we obtain α and U for the 50-year data. Substituting α and U into (18) and (19) gives the 50-year distribution of 5-minute rain rates.

The time bases (i.e., M) in the intensity-duration-frequency curves are mostly 50 years or less. However, several locations have time bases much shorter than 50 years. For example, the time bases are 18, 16, and 17 years for Mt. Tamalpais, California; Tonopah, Nevada; and Yakima, Washington, respectively. Due to this limitation, we have chosen $Q_a = 2$ years and $Q_b = 10$ years for calculations of α and U. Since Q_a and Q_b are fixed, we then need only three numbers: M, r_a, and r_b for each location, read from the intensity-duration-frequency curves to calculate the rain-rate distribution.

For example, for New York City, the three numbers are:

$$M = 49 \text{ years } (1903\text{–}1951)$$
$$r_a = 4.4 \text{ inches/hr} = 111.8 \text{ mm/hr}$$
$$r_b = 6.5 \text{ inches/hr} = 165 \text{ mm/hr}.$$

Substituting r_a and r_b into eqs. (29) and (30) yields

$$\alpha_\infty = 4.828$$
$$U_\infty = 4.64.$$

Substituting M into eqs. (12) through (15) and α_∞ and U_∞ into (25) and (26) gives

$$\alpha = 4.363$$
$$U = 4.63.$$

The 49-year (1903–1951) distribution of 5-minute rain rate calculated from this α, U pair for New York City is very close to the 20-year

(1953–1972) data, as shown in Fig. 7. Figure 8 shows similar close agreement between 50-year and 20-year distributions in Pittsburgh, Pennsylvania.

However, Fig. 9 shows an appreciable difference between 36-year and 20-year distributions for Chicago, Illinois. This appreciable difference, the irregular shape of the 20-year distribution in Fig. 9 and the instability noted in Figs. 1 and 2 indicate that a 20-year time base with a single rain-gauge measurement may not be sufficient to guarantee a stable distribution for extremely high rain rates. If more stable results are required, the 20- and 50-year data may be combined to give a 70-year distribution.

The calculated curves (dashed lines) in Figs. 1 through 6 are based on 20-year data from 1953 to 1972 in Ref. 4, whereas the calculated curves (dash-dot lines) in Figs. 7 through 9 are based on approximately 50 years of data in Ref. 16.

V. CONCLUSION

A method has been described for calculating the distribution of high rain rates by applying the statistical theory of extremes to the available yearly maximum 5-minute rain-rate data. Figures 1 through 9 show that the calculated distributions agree closely with the data in the heavy-rain region of interest to radio-path engineering. The virtue of this method is that only yearly maximum rain-rate data are required to generate satisfactory results for radio-path engineering. The rainfall intensity-duration-frequency curves[16] provide approximately 50 years (1900–1950) of such data for 203 locations in the United States. Furthermore, a new publication on "Maximum Short-Duration Precipitation,"[17] for approximately 300 U. S. locations issued annually by the National Climatic Center since 1973, provides additional yearly maximum rain-rate data. Therefore, long-term ($\geqq 50$ years) distributions of high rain rates for 203 U. S. locations can easily be obtained by this method.

VI. ACKNOWLEDGMENTS

The author is grateful to W. Y. S. Chen and R. L. Lahlum for valuable discussion on the application of statistics of extremes.

REFERENCES

1. W. Y. S. Chen and R. L. Lahlum, unpublished work.
2. W. Y. S. Chen, "A Simple Method for Estimating 5-Minute Rain Rate Distributions Based on Available Climatological Data," B.S.T.J., *55*, No. 1 (January 1976), pp. 129–134.
3. S. H. Lin, "Dependence of Rain Rate Distribution on Rain Gauge Integration Time," B.S.T.J., *55*, No. 1 (January 1976), pp. 135–141.

4. "Climatological Data, National Summary," annual issues since 1950, U. S. Department of Commerce, National Oceanic and Atmospheric Administration, National Climatic Center, Asheville, North Carolina.
The Excessive Short Duration Rainfall Data prior to 1950 are published in the Monthly Weather Review, the U. S. Meteorological Yearbook (last published for the period 1943–1949), and the Report of the Chief of the Weather Bureau (last published for 1931).
5. R. A. Fisher and L. H. C. Tippett, "Limiting Forms of the Frequency Distribution of the Largest or Smallest Member of a Sample," Proc. Cambridge Phil. Soc., *24* (1928), pp. 180–190.
6. E. J. Gumbel, *Statistical Theory of Extreme Values and Some Practical Applications*, National Bureau of Standards, Applied Mathematics series No. 33 (February 12, 1954), pp. 15, 16, and 28.
7. E. J. Gumbel, *Statistics of Extremes*, New York: Columbia University Press, 1958.
8. H. Cramer, *Mathematical Methods of Statistics*, Princeton University Press, 1957, Section 28.6, pp. 370–378.
9. H. Cramer and M. R. Leadbetter, *Stationary and Related Stochastic Processes*, New York: John Wiley, 1967, Section 12.3, pp. 271–272.
10. G. S. Watson, "Extreme Values in Samples From M-Dependent Stationary Stochastic Processes," Ann. Math. Stat., *25* (1954).
11. S. H. Lin, "A Method for Calculating Rain Attenuation Distributions on Microwave Paths," B.S.T.J., *54*, No. 6 (July-August 1975), pp. 1051–1086, Figs. 10–13.
12. L. Hansson, "General Characteristics of Rain Intensity Statistics in the Stockholm Area" (Sweden), TELE, No. 1 (1975), pp. 43–48.
13. L. Hansson, "General Characteristics of Rain Intensity Statistics in the Gothenburg Area," Report USR 75 012, Central Administration of Swedish Telecommunications, January 1975, S-12386, Farsta, Sweden.
14. S. H. Lin, "Statistical Behavior of Rain Attenuation," B.S.T.J., *52*, No. 4 (April 1973), pp. 557–581.
15. P. T. Schickedanz, "Theoretical Frequency Distributions for Rainfall Data," International Symposium on Probability and Statistics in the Atmospheric Sciences, June 1–4, 1971, Honolulu, Hawaii, Sponsored by American Meteorological Society and Co-sponsored by the World Meteorological Organization, Boston, Massachusetts. Preprints of Symposium Papers, pp. 131–136.
16. "Rainfall Intensity-Duration-Frequency Curves," U. S. Department of Commerce, Weather Bureau, Technical Paper No. 25, Washington, D. C. (December 1955).
17. "Maximum Short Duration Precipitation," contained in "Climatological Data, National Summary," annual issues since 1973, National Climatic Center, Asheville, North Carolina.

Copyright © 1976 American Telephone and Telegraph Company
THE BELL SYSTEM TECHNICAL JOURNAL
Vol. 55, No. 8, October 1976
Printed in U.S.A.

Distinguishing Stable Probability Measures
Part I: Discrete Time

By B. W. STUCK

(Manuscript received April 1, 1976)

A sequence of N, independent, identically distributed, random variables is observed from one of two stable distributions with known parameters. The likelihood-ratio test for discriminating between these two distributions is found explicitly and performance limitations are determined.

When the two distributions differ only in location, the likelihood-ratio test is sensitive to whether the distribution is nongaussian stable ($0 < \alpha < 2$) when nonlinear soft limiting of large deviations is used, or gaussian stable ($\alpha = 2$) when linear processing is used.

When the two distributions differ only in scale, the likelihood-ratio test is sensitive to whether $0 < \alpha < 2$ when nonlinear soft limiting of large deviations is used, or gaussian ($\alpha = 2$) when a chi-squared test is used.

The analysis of the two remaining cases, distinguishing between one of two characteristic indices, and between one of two skewness parameters, parallels the analysis of distinguishing between one of two scale parameters and is only touched upon briefly.

I. INTRODUCTION

The problem of classifying a series of observations as coming from one of two or more possible classes or hypotheses has received a great deal of attention in the statistical and engineering literature. In many physical situations, a variety of disturbances corrupt the observations; rather than model each disturbance separately, it is often argued on physical grounds that the disturbances add and are independent, and the central limit theorem is invoked to model this sum using a gaussian distribution. This approach is adequate as long as the sum is not dominated by one or a few of the summands; if one or a few of the summands does dominate the sum, the disturbances can possibly be modeled as a stable distribution, one member of a family of probability distributions which includes the gaussian, by invoking a frequently overlooked generalization of the central limit theorem.

The gaussian distribution has enjoyed great popularity in hypothesis testing because it is analytically tractable and because it is the only stable distribution with finite variance. Although it may be argued that mathematical models with infinite variance are physically inappropriate, this view conveniently overlooks the fact that the gaussian distribution is unbounded, which is also a physically inappropriate mathematical model. The gaussian model may adequately model disturbances over a narrow range of amplitudes; an infinite-variance, stable-distribution model may adequately model disturbances over a larger range of amplitudes. Both distributions may be physically inappropriate mathematical models, but the infinite-variance distribution may, in this sense, be the better model. This paper examines several stable-distribution hypothesis-testing problems.

The primary motivation for this work on stable probability measures is drawn from a recent statistical analysis[1] of noise on various telephone lines. This analysis indicated telephone noise may be adequately modeled (on the lines examined) by a sum of sinusoids at various frequencies plus a purely nondeterministic random process that is well characterized by a stable distribution (either gaussian or nongaussian stable). Since only a small number of lines were examined, this analysis is preliminary, awaiting other independent investigations.*

Indirect motivation for this work is drawn from detecting electromagnetic signals at frequencies of 100 kHz or less. Noise at these frequencies is claimed to be nongaussian; unfortunately, adequate statistical evidence to substantiate this claim is lacking, with one exception.[2]

A final source of motivation is found in financial problems. Over the last decade, a large body of statistical evidence has been amassed which indicates that the differences of logarithms of successive equally spaced prices of common stocks can be adequately modeled using stable distributions.[3, 4]

II. OUTLINE OF DISCUSSION †

A sequence of N random variables is observed; for simplicity, it is assumed they are independent and identically distributed—drawn from one of two stable distributions with known parameters (characteristic index $0 < \alpha^j \leqq 2$, skewness parameter $-1 \leqq \beta^j \leqq 1$, scale parameter $\gamma^j > 0$, location parameter $-\infty < \delta^j < \infty$; $j = 0, 1$).‡ It

---

* Applications of this work to removing telephone noise will be presented elsewhere.

† These results were first presented at the Eighth Annual Princeton Conference on Information Sciences and Systems, March 28–29, 1974, p. 405, and at the 1975 Johns Hopkins Conference on Information Sciences and Systems, April 2–4, 1975, pp. 49–51.

‡ Both subscripts and superscripts will be used to denote the stable-distribution parameters under hypothesis $H_j (j = 0, 1)$; these parameters will be discussed more fully in Section III.

is well known that the likelihood-ratio test is a decision rule that is optimum with respect to either a Neyman-Pearson or Bayes criterion.[5] Here, the likelihood ratio is found explicitly and performance limitations of the test are determined. The extension of these results from two to M stable distributions is well known and will not be dealt with here.[5]

The (log) likelihood decision rule, because of the independence assumption, takes the following simple form:

$$\Lambda' = \sum_{i=1}^{N} l(r_i) \underset{H_0}{\overset{H_1}{\gtrless}} L'$$

$$l(r_i) = \ln \frac{p(r_i;\alpha^1,\beta^1,\gamma^1,\delta^1)}{p(r_i;\alpha^0,\beta^0,\gamma^0,\delta^0)},$$

where $\{r_i\}_1^N$ are the N observed random variables, drawn from a distribution with probability density $p(x;\alpha^j,\beta^j,\gamma^j,\delta^j)$, and L' is a threshold. Since $l(r_i)$ can be rewritten as the sum of four functions,

$$l(r_i) = \ln \frac{p(r_i;\alpha^1,\beta^1,\gamma^1,\delta^1)}{p(r_i;\alpha^0,\beta^1,\gamma^1,\delta^1)} + \ln \frac{p(r_i;\alpha^0,\beta^1,\gamma^1,\delta^1)}{p(r_i;\alpha^0,\beta^0,\gamma^1,\delta^1)}$$
$$+ \ln \frac{p(r_i;\alpha^0,\beta^0,\gamma^1,\delta^1)}{p(r_i;\alpha^0,\beta^0,\gamma^0,\delta^1)} + \ln \frac{p(r_i;\alpha^0,\beta^0,\gamma^0,\delta^1)}{p(r_i;\alpha^0,\beta^0,\gamma^0,\delta^0)},$$

each of which tests for only one different parameter, this suggests studying each of these four situations separately.

Two special cases are examined in detail: when the distributions differ only in location and when they differ only in scale. The probabilities of error of the first and second kind are found for three analytically tractable cases (gaussian, Cauchy, and Pearson V) by calculating the characteristic function of the log likelihood probability measure induced under each hypothesis; the general case is apparently analytically intractable, and quite expensive to tackle numerically at present. Exponentially sharp upper and lower bounds on both types of probabilities of error, and also the total probability of error, can be simply derived from the Laplace transform of the log likelihood probability measure induced under each hypothesis. These bounds are found analytically in three cases, and relatively inexpensive numerical results are presented for selected other cases.

When the two distributions differ only in location, the likelihood-ratio test is shown to be extremely sensitive to whether the distribution is nongaussian stable ($0 < \alpha < 2$), when nonlinear soft limiting of large deviations is employed, or gaussian ($\alpha = 2$), when linear processing is used. When the distribution is nongaussian stable, performance is found analytically to be quite sensitive to whether a linear (suboptimum) or likelihood (optimum) decision rule is used: the total probability of error for the linear test behaves asymptotically ($N \gg 1$) as $O(AN^{1-\alpha})$, while the total probability of error for the likelihood-ratio test is upper bounded by $\exp(-BN + C)$, where (A, $B > 0$, C) depend on parameters of the two distributions and are independent of N. (For related work that complements the results in our discussion, see the list of references and particularly Refs. 6, 7, and 8.)

When the two distributions differ only in scale, the likelihood-ratio test is extremely sensitive to whether the distribution is nongaussian stable when nonlinear soft limiting of large deviations is used, or gaussian when a chi-squared test is used. Performance for nongaussian stable distributions is extremely sensitive to whether a suboptimum (chi-squared) or optimum (likelihood-ratio) test is used: the total probability of error for the chi-squared test behaves asymptotically ($N \gg 1$) as $O(FN^{-(\alpha/2-1)})$, while the total probability of error for the likelihood-ratio test is upper bounded by $\exp(-GN + H)$, where (F, $G > 0$, H) depend on parameters of the two distributions and are independent of N.

The analysis of the two remaining cases, distinguishing between one of two characteristic indices and between one of two skewness parameters, closely parallels the analysis that distinguishes between two scale factors and is only touched upon here.

The continuous time analogs of these discrete-time problems are studied, where a sample function from one of two stable, stationary, independent-increment processes is observed for a finite time interval in the second part of this work. In contrast with this work, the analysis is simpler, and it is possible to obtain many results analytically in closed form.

Section III deals with various mathematical preliminaries. A brief, selective, tutorial overview of the central limit theorem, infinitely divisible distributions, and independent-increment processes is presented to place this work in perspective (as well as to fix notation). No attempt is made to be exhaustive in the discussion.

The length of the discussion is due to the many special sets of parameter values that must be taken into account to be thorough. The main reason for this completeness is to adequately cover all cases where uncertainty is modeled using a distribution arising from a central-limit-theorem type of argument. The main contribution here is the results per se, many of which are presented here for the first time, which unfortunately often involve either tedious algebraic manipulation or machine calculations. It is hoped this will not obscure the surprising (at first glance) nature of the results: the quite singular behavior of both the log-likelihood-ratio test and (perhaps more importantly) its performance, for the gaussian vs nongaussian stable distribution, in distinguishing either location or scale. The generalization of these two results to a wide class of infinitely divisible distributions (which include the family of stable distributions) is immediate, and is sketched at the end of Section IV.

III. MATHEMATICAL PRELIMINARIES

The reader is assumed to be familiar with the fundamentals of measure theory and probability theory, as found in standard references.[9–12]

Underlying the discussion to follow are:

(*i*) The notion of a probability space: a triple $\{\Omega, A, P\}$, where Ω is the set of elementary events, A is a σ-algebra of Borel measurable subsets of Ω, and P is a probability measure on A.

(*ii*) The definition of a stochastic process $x(t, \omega)$ defined on a parameter set E (henceforth called time), with $t \in E$, $\omega \in \Omega$, which is a function mapping the direct product $E \times \Omega$ into the real line, and the associated probability measure induced by $x(t, \omega)$.

(*iii*) The measure theoretic concept of absolute continuity of one measure with respect to another, and the measure theoretic Lebesgue decomposition theorem.

3.1 Infinitely divisible distributions and independent-increment processes

In this section, various properties of infinitely divisible distributions and independent-increment processes are briefly reviewed. The interested reader is referred to the literature for much more information.[12–15]

This tutorial section serves several purposes:

(*i*) It gathers together for convenient reference all material on stable distributions to be used in Part II.

(*ii*) It fixes notation.

(*iii*) It emphasizes the central role played by stable distributions in understanding both the central limit theorem and the Lévy decomposition of the infinitely divisible distributions.

(*iv*) Finally, it alerts the reader to the rich structure and variety of infinitely divisible distributions, in general, and stable distributions, in particular, in the hope that they will find greater use in modeling uncertainty.

The characteristic function of a (first-order) probability distribution $P(x)$[*] is defined as

$$C_x(v) = \int e^{ivx} dP(x) = E(e^{ivx}) \qquad \text{a.s.}$$

---

[*] Upper case $P(\cdot)$ will denote a probability distribution, while lower case $p(\cdot)$ will denote the associated probability density function; all probability distributions examined here in any detail are absolutely continuous with respect to Lebesgue measure.

It can be shown that two probability distributions are identical if and only if their characteristic functions are identical (Ref. 14, page 28); thus, there is a one-to-one correspondence between characteristic functions and probability distribution functions. A random variable is said to be infinitely divisible if, for every natural number n, the random variable can be represented as the sum of n independent identically distributed (i.i.d.) random variables, or equivalently if its characteristic function can be written as

$$C_x(v) = [\tilde{C}_x(v, n)]^n \qquad n = 1, 2, \cdots,$$

where $\tilde{C}_x$ is the characteristic function of some probability distribution which may depend on n. Two well-known examples of infinitely divisible random variables are the gaussian [taking values on $(-\infty, \infty)$] and the Poisson (taking values at nonnegative integer multiples of h):

$$\text{Gaussian:} \quad C_x(v) = \int_{-\infty}^{\infty} e^{ixv} \frac{1}{\sqrt{2\pi\sigma^2}} \exp\{-(x-m)^2/2\sigma^2\} dx$$

$$= \exp(imv - \tfrac{1}{2}\sigma^2 v^2)$$

$$\text{Poisson:} \quad C_x(v) = \sum_{k=0}^{\infty} \frac{\lambda^k e^{-\lambda}}{k!} (e^{ivh})^k = \exp[\lambda(e^{ivh} - 1)].$$

De Finetti conjectured that any infinitely divisible distribution could be written as the convolution of a gaussian and a generalization of the Poisson; the resulting characteristic function can be written as

$$\ln C_x(v) = imv - \tfrac{1}{2}\sigma^2 v^2 + \int (e^{ivu} - 1) dF(u),$$

where the measure $F(u)$ specifies at what points the Poisson variable takes on nontrivial values. However, this conjecture was shown to hold only for a subset of the infinitely divisible distributions by Lévy; if one desires a canonical form of the characteristic function of an infinitely divisible distribution, then the following remarkable theorem can be proved (Ref. 13, page 76).

Theorem (Lévy): Any infinitely divisible characteristic function can be uniquely written in the canonical form

$$\ln C_x(v) = i\delta v - \tfrac{1}{2}\sigma^2 v^2 + \int_{-\infty}^{0-} \left(e^{ivu} - 1 - \frac{ivu}{1+u^2}\right) d\nu_-(u) + \int_{0+}^{\infty} \left(e^{ivu} - 1 - \frac{ivu}{1+u^2}\right) d\nu_+(u),$$

where δ is a location parameter $(-\infty < \delta < \infty)$, $\sigma^2 > 0$ is the variance of the gaussian component, and (ν_-, ν_+) are called the Lévy measure of the *generalized Poisson distribution. The conditions the Lévy measure must satisfy are (i)* ν_- *and* ν_+ *are nondecreasing on the intervals* $(-\infty, 0)$ *and* $(0, \infty)$*, respectively, (ii)* $\nu_-(-\infty) = \nu_+(\infty) = 0$*, and (iii) for every finite* $\epsilon > 0$*,*

$$\int_{-\epsilon}^{0-} u^2 d\nu_-(u) < \infty \qquad \int_{0+}^{\epsilon} u^2 d\nu_+(u) < \infty.$$

Some examples now follow:

Example 1 (Poisson): $\delta = iv h\lambda/(1 + h^2)$, $\sigma^2 = 0$, $\nu_- = 0$, $-\infty < u < 0$

$$\nu_+ = \begin{cases} -\lambda & 0 < u < h \\ 0 & h \leqq u < \infty \end{cases};$$

$$\therefore \quad \ln C_x(v) = \lambda(e^{ivh} - 1).$$

Example 2 (Cauchy): $\sigma^2 = 0$, $\delta = 0$,

$$\nu_- = \frac{c}{\pi|u|} \qquad -\infty < u < 0$$

$$\nu_+ = \frac{-c}{\pi u} \qquad 0 < u < \infty;$$

$$\therefore \quad \ln C_x(v) = i\delta v - c|v|.$$

Example 3 (Gamma): $\sigma^2 = 0$, $\nu_- = 0$, $-\infty < u < 0$

$$\delta = p \int_0^\infty \frac{e^{-qu}}{1 + u^2} du < \infty$$

$$d\nu_+(u) = pe^{-qu} d(\ln u);$$

$$\therefore \quad C_x(v) = \left(1 - \frac{iv}{p}\right)^{-q}.$$

Most of the attention here will be focused on one particular class of infinitely divisible distributions, the stable distributions.

Definition: A probability distribution is said to be stable if, for all $a_1 > 0$, $a_2 > 0$, b_1, b_2, there exist constants $a > 0$, b such that

$$P(a_1 x + b_1) * P(a_2 x + b_2) = P(ax + b),$$

where $*$ denotes convolution. In other words, stable distributions are closed under the action of the group of linear affine transformations on the real line.

An important reason for examining stable distributions is found in the central limit theorem (Ref. 13, page 162; Ref. 15, page 168):

Theorem: *$P(x)$ is a limiting distribution for a sum of suitably scaled and translated, independent, identically distributed, random variables if and only if $P(x)$ is stable.*

In many practical problems, a large number of independent disturbances add and introduce uncertainty in a measurement. To analyze the effects of uncertainty, it is often convenient to replace this sum by its limiting distribution, which must be a stable distribution. The reader is referred to the bibliography for references on exactly what conditions govern the limiting distribution being gaussian vs nongaussian stable (Ref. 12, pages 171–190; Ref. 15, pages 165–169).

Stable distributions are infinitely divisible; the associated Lévy measures can be shown to be $\nu_-(u) = c_-|u|^{-\alpha}$, $\nu_+(u) = -c_+u^{-\alpha}$ (Ref. 13, pages 164–168; Ref. 14, pages 128–133). Requirement (*i*) that the measure be nondecreasing leads to $\alpha > 0$, while the final requirement (*iii*) forces $\alpha < 2$. Substituting this into the canonical representation of the characteristic function of an infinitely divisible distribution and explicitly evaluating the integral over the Lévy measure results in the following theorem:

Theorem (Ref. 13, page 164; Ref. 14, page 136): The characteristic function of a stable distribution can be expressed as

$$\ln E(e^{ixv}) = \begin{cases} -\gamma|v|^{\alpha}\left[1 + i\beta\dfrac{v}{|v|}\tan\left(\dfrac{\pi\alpha}{2}\right)\right] + i\delta v & \alpha \neq 1, \\ -\gamma|v|\left[1 + i\beta\dfrac{v}{|v|}\dfrac{2}{\pi}\ln|\gamma v|\right] + i\delta v & \alpha = 1, \end{cases}$$

where $0 < \alpha \leqq 2$, $-1 \leqq \beta \leqq 1$, $\gamma > 0$ $(\gamma \doteq c^{\alpha})$, $-\infty < \delta < \infty$. *For* $0 < \alpha < 1$, $\beta = c_- - c_+/c_- + c_+$; *for* $1 \leqq \alpha \leqq 2$, $\beta = c_+ - c_-/c_+ + c_-$. Note that for $\alpha = 2$, the characteristic function, as a complex-valued function of v, is C^{∞}, but for $1 < \alpha < 2$, it is only C^1, and for $0 < \alpha \leqq 1$ is only C^0.

For fixed β $(\beta \neq 0)$, the characteristic function is discontinuous (as a function of α) in the neighborhood of $\alpha = 1$. One approach to this problem is to rewrite the characteristic function $(\alpha \neq 1)$ as

$$\begin{aligned} \ln E(e^{ixv}) &= -\gamma|v|^{\alpha}\left[1 + i\beta\frac{v}{|v|}\tan\left(\frac{\pi\alpha}{2}\right)\right] \\ &\qquad + iv\left(\delta + \gamma\beta\tan\frac{\pi\alpha}{2} - \gamma\beta\tan\frac{\pi\alpha}{2}\right) \\ &= -\gamma|v|^{\alpha} + i\gamma\beta v\tan\frac{\pi\alpha}{2}\left[1 - |v|^{\alpha-1}\right] \\ &\qquad + iv\left(\delta + \gamma\beta\tan\frac{\pi\alpha}{2}\right). \end{aligned}$$

If a new parameter $\delta' \doteq \delta + \gamma\beta\tan(\pi\alpha/2)$ is defined, then for β fixed

$$\lim_{\alpha\to1}\tan\frac{\pi\alpha}{2}\left[1 - |v|^{\alpha-1}\right] = \frac{2}{\pi}\ln|v|.$$

By inspection, this form of the characteristic function is not discontinuous in the neighborhood of $\alpha = 1$.

Since the characteristic function is in $L_1(-\infty, \infty)$, all stable distributions are absolutely continuous with respect to Lebesgue measure, and have analytic probability density functions. Four parameters completely specify a stable distribution:

(*i*) α, the characteristic index of the stable distribution $P(X; \alpha, \beta)$ is associated with the asymptotic behavior of $P(X; \alpha, \beta)$. For $-1 < \beta < 1, 0 < \alpha < 2$,

$$\lim_{X \to -\infty} |X|^\alpha P(-X) = k_- > 0, \qquad \lim_{X \to \infty} X^\alpha [1 - P(X)] = k_+ > 0.$$

For $\beta = -1$ (a similar argument holds for $\beta = +1$), Lipschutz[16] and Ibragimov and Linnik (Ref. 17, pages 62 to 66)[*] have shown that for $1 < \alpha < 2$,

$$P(X) = 0\{k(\alpha)|X|^{\alpha/2(1-\alpha)} \exp[-c(\alpha)|X|^{\alpha/\alpha-1}]\} \quad \text{as} \quad X \to -\infty$$
$$\lim_{X \to \infty} X^\alpha [1 - P(X)] = k_+ > 0,$$

while for $0 < \alpha < 1$,

$$P(X) = 0\{k(\alpha)X^{\alpha/2(1-\alpha)} \exp[-c(\alpha)X^{-\alpha/1-\alpha}]\} \quad \text{as} \quad X \downarrow 0+$$
$$\lim_{X \to \infty} X^\alpha [1 - P(X)] = k_+ > 0,$$

where $k(\alpha)$, $c(\alpha)$ are constants which depend only on α. For the asymmetric Cauchy probability density function, it can be shown (Ref. 17, pages 57 to 60) that

$$p(X; \alpha = 1, \beta = -1) = 0\left[\exp\left(\frac{\pi}{4}|X| - \frac{2}{\pi e}\exp(\pi|X|/2)\right)\right] X \to -\infty$$
$$\lim_{X \to \infty} p(X; \alpha = 1, \beta = -1)X^2 = k_+ > 0.$$

(*ii*) β characterizes skewness of the distribution: if $\beta = 0$ the distribution is symmetric about $x = \delta$. Otherwise,

$$\lim_{X \to \infty} \frac{1 - P(X; \alpha, \beta) - P(-X; \alpha, \beta)}{1 - P(X; \alpha, \beta) + P(-X; \alpha, \beta)} = -\beta$$
$$\lim_{X \to \infty} \frac{P(-X; \alpha, \beta)}{1 - P(X; \alpha, \beta)} = \frac{1 + \beta}{1 - \beta}.$$

For $1 < \alpha < 2$, the distribution is skewed to the left for $-1 \leqq \beta < 0$, since $P(\delta) < 1 - P(\delta)$, with the degree of skewness increasing as β

---

[*] Note typographical errors in eqs. (2.4.30) and Theorem (2.4.7), of Ref. 17.

decreases. It suffices to consider varying β over one half its range because from the characteristic function it follows that the probability density $p(x)$ obeys the relation

$$p(x;\alpha,\beta,\gamma,\delta=0)=p(-x;\alpha,-\beta,\gamma,\delta=0).$$

(*iii*) γ(or $c \triangleq \gamma^{1/\alpha}$) is a measure of the dispersion or spread of the distribution.

(*iv*) δ is a location parameter, and for $1<\alpha\leqq 2$, δ is the mean.

Only three analytic closed-form expressions for stable probability density functions are known at present:

Gaussian ($\alpha=2, -1\leqq\beta\leqq 1$):

$$p(x)=\frac{1}{\sqrt{4\pi c^2}}\exp\left[-\left(\frac{x-\delta}{2c}\right)^2\right]\qquad -\infty<x<\infty;$$

Cauchy ($\alpha=1, \beta=0$):

$$p(x)=\frac{c}{\pi}[(x-\delta)^2+c^2]^{-1}\qquad -\infty<x<\infty;$$

Pearson V ($\alpha=\frac{1}{2}, \beta=-1$):

$$p(x)=\begin{cases} c\dfrac{1}{\sqrt{2\pi}}\left(\dfrac{x-\delta}{c}\right)^{-\frac{3}{2}}\exp\left[-\dfrac{c}{2(x-\delta)}\right] & x\geqq\delta\\ 0 & x<\delta\end{cases}$$

and its conjugate density

$$p(x;\alpha=\tfrac{1}{2},\beta=1,\gamma,\delta=0)=p(-x;\alpha=\tfrac{1}{2},\beta=-1,\gamma,\delta=0).$$

Series expansions are known for the remaining stable density functions (Ref. 14, pages 138–148):

$$p(x;\alpha,\beta,\gamma=1,\delta=0)$$
$$=\frac{1}{\pi}\sum_{k=1}^{\infty}\frac{(-1)^k\Gamma\left(\dfrac{k}{\alpha}+1\right)}{k!}x^{k-1}\sin\frac{k\pi}{2\alpha}(\theta-\alpha)\qquad 1<\alpha\leqq 2,$$

$$p(x;\alpha,\beta,\gamma=1,\delta=0)$$
$$=\frac{1}{\pi}\sum_{k=1}^{\infty}\frac{(-1)^k\Gamma(k\alpha+1)}{k!}x^{-\alpha k-1}\sin\frac{k\pi}{2}(\theta-\alpha)\qquad 0<\alpha<1,$$

$$p(x;\alpha,\beta,\gamma=1,\delta=0)$$
$$=\frac{1}{\pi}\sum_{k=0}^{\infty}\frac{(-1)^k}{k!}x^k\left[\int_0^{\infty}t^k\{\sin(1+\beta)t\}e^{-(2\beta/\pi)t\ln t}dt\right]^{*}\qquad \alpha=1,$$

where

$$\tan(\theta\pi/2)=\beta\tan(\pi\alpha/2),\qquad\text{and}\qquad x>0.$$

---

* For asymptotic expansions for $\alpha=1$, see Ref. 17, Theorem 2.4.3 and Ref. 18.

The reader can check that the series for $\alpha = 2$ reduces to the series for the gaussian, and the series for $0 < \alpha < 1$ and $|\beta| = 1$ are zero on a half line (cf. Pearson V). For $(0 < \alpha < 1,\ -1 < \beta < 1)$ and $(1 \leqq \alpha \leqq 2,\ -1 \leqq \beta \leqq 1)$, stable probability densities have support on $(-\infty, \infty)$. The series expansion for the density for $0 < \alpha < 1$ can be used as an asymptotic expansion for the density for $1 < \alpha < 2$ for $|\beta| \neq 1$. It can be shown from the characteristic function directly that all stable distributions are unimodal (Ref. 13, pages 158 to 161; Ref. 17, pages 66 to 76).

Figure 1 is a plot of various stable probability density functions for fixed α $(1 < \alpha < 2)$ and several β; for α near two, it is quite difficult to distinguish symmetric $(\beta = 0)$ and asymmetric stable distributions. Figure 2 shows that around the mode, all stable distributions appear roughly gaussian, for $1 < \alpha < 2$ (note the logarithmic scale).

For α in the neighborhood of two, the gaussian and nongaussian stable distributions are virtually identical around their mode, and it is only in the tails of these distributions that the differences are pronounced. One crude measure of the point at which the gaussian and nongaussian stable distributions diverge is the point at which the first term in the asymptotic series $(\alpha < 2)$ equals the gaussian density: for $\alpha = 1.90$, 1.95, 1.99, this occurs at 3.342, 3.635, 4.158 gaussian standard deviations, respectively.

One reason stable distributions have attracted little attention in the mathematical modeling of uncertainty is found in the theorem from Ref. 14, page 169: *A stable distribution with characteristic index α has all absolute moments of order p, $0 < p < \alpha < 2$: $E(|x|^p) < \infty$. Conversely, $E(|x|^p)$ does not exist, i.e., it diverges, for $p \geqq \alpha$, $\alpha < 2$.*

This suggests (albeit heuristically) that stable distributions may find application in modeling uncertainty when, as the number of observations increases, for $0 < \alpha < 1$, both the sample mean and sample variance "wander erratically," being dominated by one or a few observations, while for $1 < \alpha < 2$, the sample mean stabilizes but the sample variance does not [cf. Refs. 1, 2, 3, 4].

The generalization of these ideas from discrete time sequences of independent, identically distributed, random variables drawn from an infinitely divisible distribution to continuous time sample functions of an independent increment process is clear. The characteristic functional of a stationary independent increment process can be uniquely written as

$$\begin{aligned}\ln E\left[e^{iv[x(t)-x(s)]}\right] &= (t-s)\left[i\delta v - \tfrac{1}{2}\sigma^2 v^2 + \int_{-\infty}^{0-}\left(e^{ivu} - 1 - \frac{ivu}{1+u^2}\right)d\nu_-(u)\right.\\ &\qquad\left. + \int_{0+}^{\infty}\left(e^{ivu} - 1 - \frac{ivu}{1+u^2}\right)d\nu_+(u)\right]\end{aligned}$$

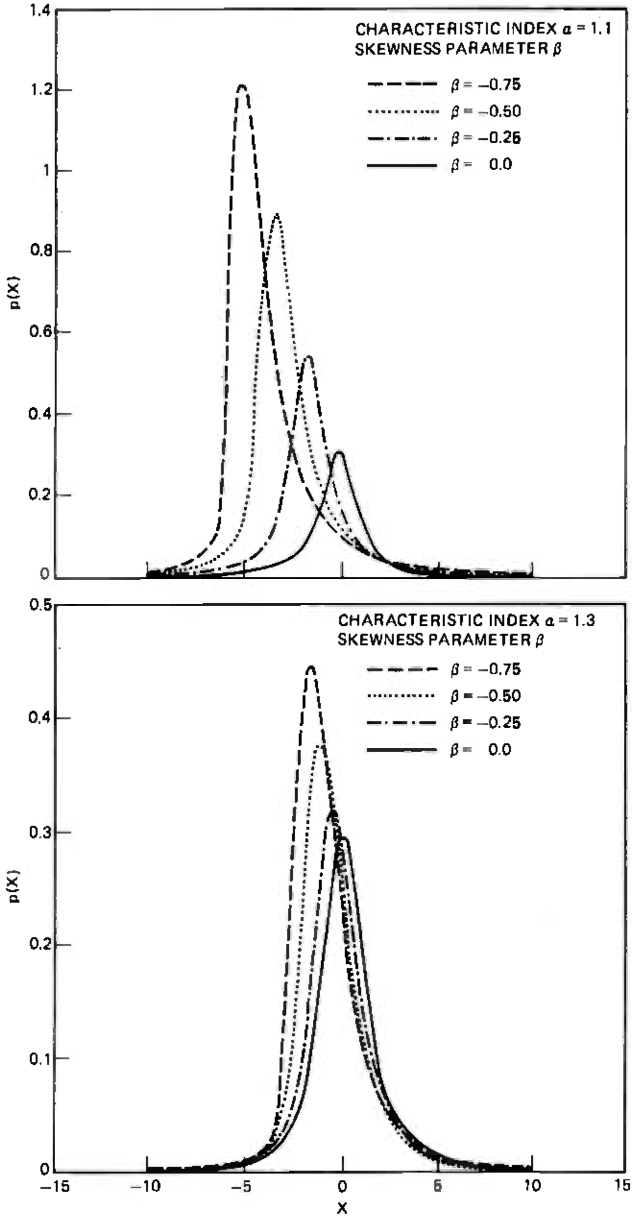

Fig. 1—Stable probability density functions [$\alpha = 1.1(0.2)1.7, \beta = -0.75(0.25)0.0$]; scale factor $c = 1.0$; location parameter $\delta = 0.0$.

for $0 \leqq s < t < T$. The parameters δ, σ^2, and (ν_-, ν_+) have been defined already. In words, any independent increment process can be decomposed into

(*i*) A singular piece, called the drift, specified by δ.

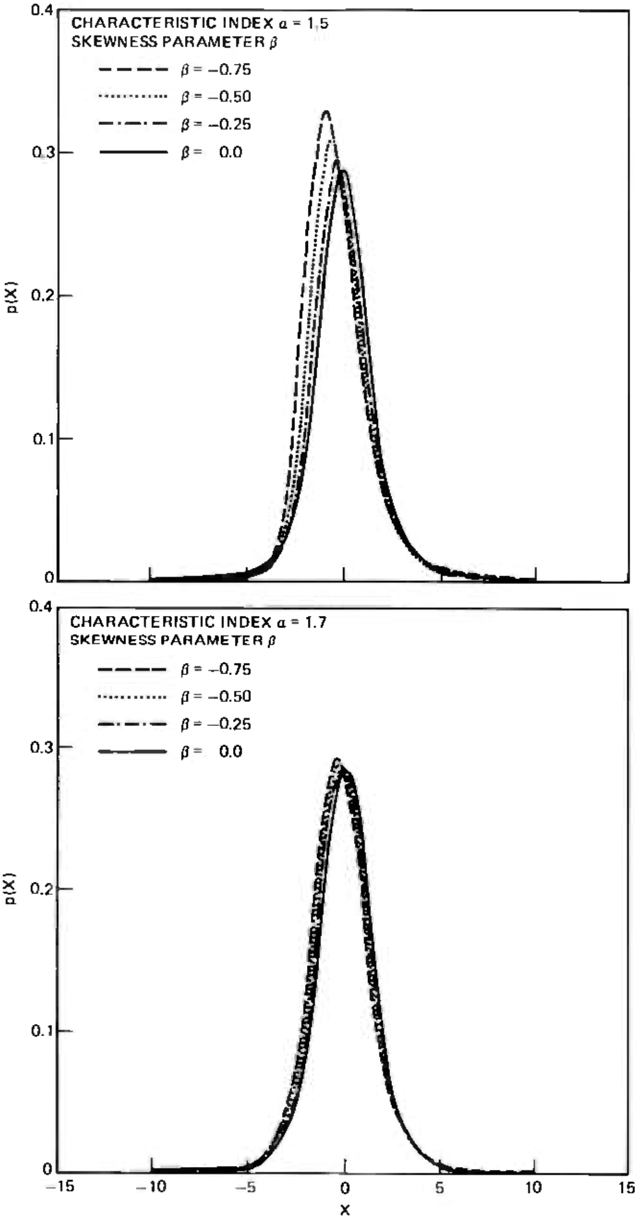

Fig. 1—(continued)

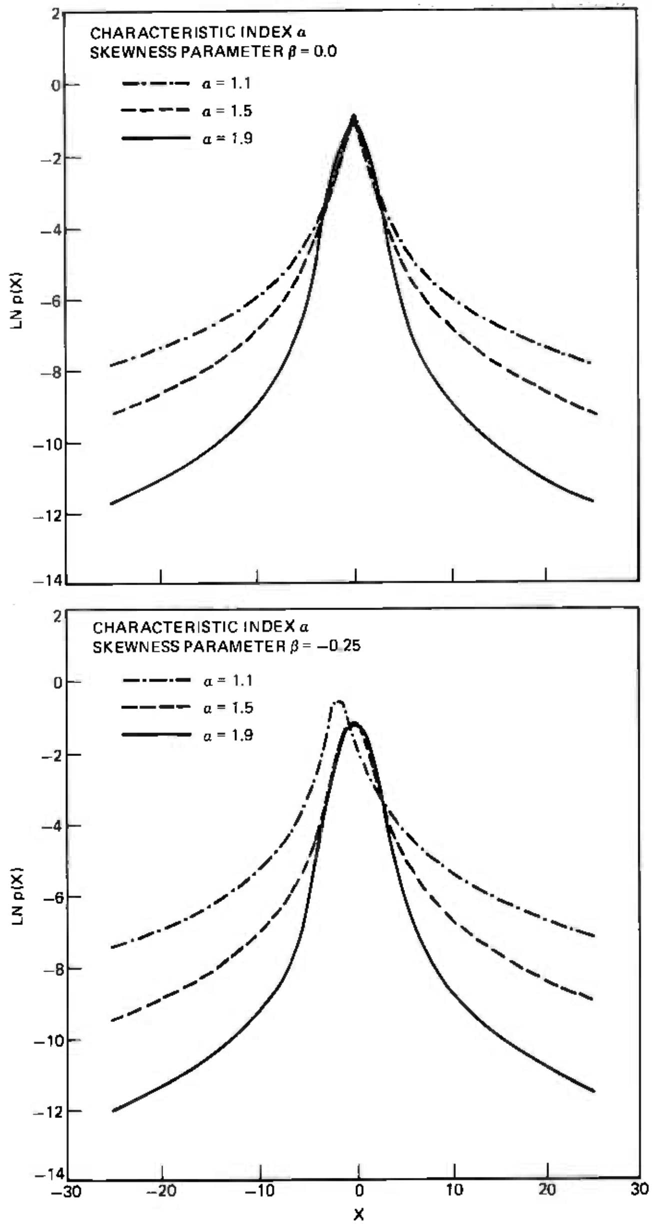

Fig. 2—Stable probability density functions (semilogarithmic) [$\alpha = 1.1(0.4)1.9$, $\beta = -0.5(0.5)0.5$]; scale factor $c = 1.0$; location parameter $\delta = 0.0$.

(*ii*) A gaussian component, a component with continuous sample paths that have unbounded variation with probability one (w.p.1), specified by σ^2.

(*iii*) A generalization of the Poisson process called a jump process,

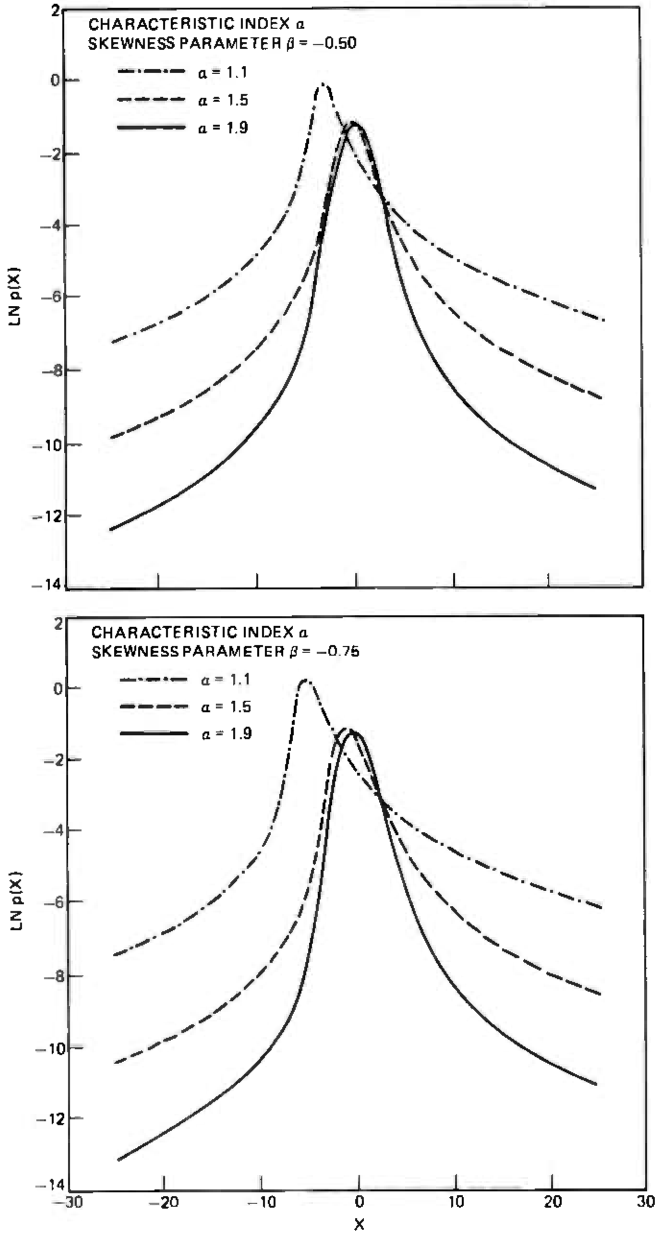

Fig. 2—(continued)

with sample paths that are constant except for simple jump discontinuities at random times with random amplitudes, specified by the Lévy measure (ν_-, ν_+).

A (separable) pure jump process, a stationary independent increment process with no gaussian component, has sample functions that are of bounded variation* with probability one if and only if

$$\int_{-1}^{0-} |u| d\nu_-(u) + \int_{0+}^{1} u d\nu_+(u) < \infty .$$

An example of an independent increment process with bounded variation (w.p.1) is a stable independent increment process $(0 < \alpha < 1)$ while stable independent increment processes $(1 \leqq \alpha \leqq 2)$ have unbounded variation (w.p.1). The intuitive meaning of the Lévy measure is that first proposed by De Finetti: the Lévy measure specifies the density of the amplitudes of the jumps of the Poisson process, provided the process sample paths are of bounded variation (w.p.1).

By allowing δ, σ^2, and (ν_-, ν_+) to depend upon time, a time-varying generalization of infinitely divisible distributions or nonstationary independent increment processes is obtained. By examining nonanticipative functionals of either a discrete time sequence of i.i.d. random variables drawn from an infinitely divisible distribution, or a continuous time independent increment process, a wide variety of Markov processes are derived. Thus, the generalizations of the results presented here to many other situations may sometimes be immediate. The richness of this class of random processes suggests these results may find wide application.

Historically, the mathematical study of independent increment processes concentrated first on the gaussian case, then on the stable case, and finally on the general case. To date, most of the engineering literature has concentrated on the gaussian case or the purely Poisson case, with the notable exception of Frost.[19] It is hoped this work will suggest promising avenues of constructive research by studying the stable case, as well as shedding light on some of the quirks of the gaussian case.

IV. DISCRETE TIME DETECTION OF TRANSLATES OF STABLE MEASURES

One of two sequences of independent, identically distributed (i.i.d.), stable, random variables is observed, under one of two hypotheses (H_0, H_1):

$$\begin{array}{lll} H_1 & r_k = s^1 + n_k & \\ & & 1 \leqq k \leqq N. \\ H_0 & r_k = s^0 + n_k & \end{array}$$

---

* The variation of a function $f(t), 0 < t < T$, is defined as $\sup \sum_{i=0}^{N-1} |f(t_{i+1}) - f(t_i)|$ where the supremum is over all possible partitions of the interval $[0, T]: 0 = t_0 < t_1 < \cdots < t_N = T$.

The observed or received sequence is denoted $\{r_k\}_1^N$, while $\{n_k\}_1^N$ is a sequence of i.i.d. stable random variables with known parameters $(\alpha, \beta, \gamma, \delta = 0)$; both s^1 and s^0 are known. The *a priori* probability of H_j is denoted π_j $(j = 0, 1)$. (The extension of allowing s^1, s^0 to depend on k is immediate and is not dealt with here.)

The measures induced by $\{r_k\}_1^N$ under H_0 and H_1 are clearly *not* mutually orthogonal. Two cases occur: for $(0 < \alpha < 1, -1 < \beta < 1)$ and $(1 \leqq \alpha \leqq 2, -1 \leqq \beta \leqq 1)$, the stable measures have support on the whole real line, and hence are equivalent. For $(0 < \alpha < 1, \beta = 1$ or $-1)$, the stable measures have support on a half line, and hence one measure is absolutely continuous with respect to the other but *not* vice versa: the supports of the two measures overlap except for the interval $[s^0, s^1)$. In either case, since the measures are not mutually orthogonal, the decision rule, which as is well known minimizes both a Bayes criterion as well as a Neyman-Pearson criterion, is the likelihood-ratio test.[5] The goal is to find the exact form of this test, and characterize its performance.* Performance here means calculating the probability that H_1 is chosen given that H_0 is true, and the probability that H_0 is chosen given that H_1 is true; these are called probabilities of error of the first and second kind, and are denoted P_{10} and P_{01}, respectively. A quantity which is also of interest is the total probability of error, defined as $(\pi_0 P_{10} + \pi_1 P_{01}) \doteq P_E$.

4.1 The likelihood-ratio test

The structure of the optimum detector is handled in two separate cases. First, when $(0 < \alpha < 1, \; -1 < \beta < 1)$ or $(1 \leqq \alpha \leqq 2, -1 \leqq \beta \leqq 1)$, the likelihood ratio is always strictly positive and finite, and is

$$\Lambda = \Lambda(r_1, \cdots, r_N) = \prod_{i=1}^{N} \frac{p_n(r_i - s^1)}{p_n(r_i - s^0)} \underset{H_0}{\overset{H_1}{\gtrless}} L,$$

where $p_n(\cdot)$ is the probability density of n_k. An equivalent test is to compute the log likelihood ratio,

$$\Lambda' = \ln \Lambda = \sum_{i=1}^{N} l(r_i) \underset{H_0}{\overset{H_1}{\gtrless}} \ln L = L',$$

where

$$l(r_i) = \ln \frac{p_n(r_i - s^1)}{p_n(r_i - s^0)},$$

and this can be explicitly calculated using the series expansions described earlier. Before doing so, it is worthwhile to examine two

---

* A discussion of the power of this test (or any other test) is deliberately omitted.

analytically tractable cases:

Gaussian ($\alpha = 2, -1 \leqq \beta \leqq 1$):

$$p_n(x) = \frac{1}{\sqrt{4\pi c}} e^{-x^2/4c^2} \qquad -\infty < x < \infty;$$

$$\therefore \quad l(r_i) = -\frac{1}{4c^2}[(r_i - s^1)^2 - (r_i - s^0)^2]$$

$$= \frac{1}{4c^2}[2r_i(s^1 - s^0) - (s^1)^2 + (s^0)^2];$$

$$\therefore \quad \Lambda' = \ln \Lambda = \frac{s^1 - s^0}{2c^2} \sum_{i=1}^{N} r_i - \left(\frac{N}{4c^2}\right)[(s^1)^2 - (s^0)^2] \underset{H_0}{\overset{H_1}{\gtrless}} \ln L \equiv L'.$$

The log likelihood test can be implemented using only linear processing. The rule has the interpretation of comparing an energy-like quantity, the received signal suitably translated and squared, with a threshold. Equivalently, the test defines a hyperplane in R^N, and depending upon which side of the hyperplane $(r_1, \cdots, r_N)$ lies, H_1 or H_0 is chosen. All of this is well known (see Ref. 5, pages 94–97 and 163–173).

Cauchy ($\alpha = 1, \beta = 0$):

$$p_n(x) = \frac{c}{\pi}(x^2 + c^2)^{-1} \qquad -\infty < x < \infty;$$

$$\therefore \quad l(r_i) = \ln \frac{(r_i - s^0)^2 + c^2}{(r_i - s^1)^2 + c^2};$$

$$\therefore \quad \Lambda' = \sum_{i=1}^{N} \ln \frac{(r_i - s^0)^2 + c^2}{(r_i - s^1)^2 + c^2} \underset{H_0}{\overset{H_1}{\gtrless}} \ln L \equiv L'.$$

Unlike the gaussian case, the Cauchy log likelihood detector operates nonlinearly on the observation. A straightforward Taylor series expansion of the log likelihood about $r_i = \frac{1}{2}(s^1 + s^0)$ shows that for small perturbations about this point the log likelihood is linear in the perturbing quantity. On the other hand, for large excursions in any one observation,

$$\left|\frac{r_i - s^1}{c}\right| \gg 1, \qquad \left|\frac{r_i - s^0}{c}\right| \gg 1,$$

this one term in the sum behaves as $O(r_i^{-1})$ or, in other words, very large excursions in the received signal are essentially (but not entirely) discarded; this type of behavior will be called soft limiting. Only for $N = 1$ does this test reduce to finding a hyperplane and determining on which side of the hyperplane the observation lies in order to choose H_1 or H_0.

The cases ($0 < \alpha < 1, -1 < \beta < 1$) and ($1 \leqq \alpha \leqq 2, -1 < \beta < 1$), can now be examined; it is a straightforward exercise to substitute into the log likelihood the series expansions for stable probability density

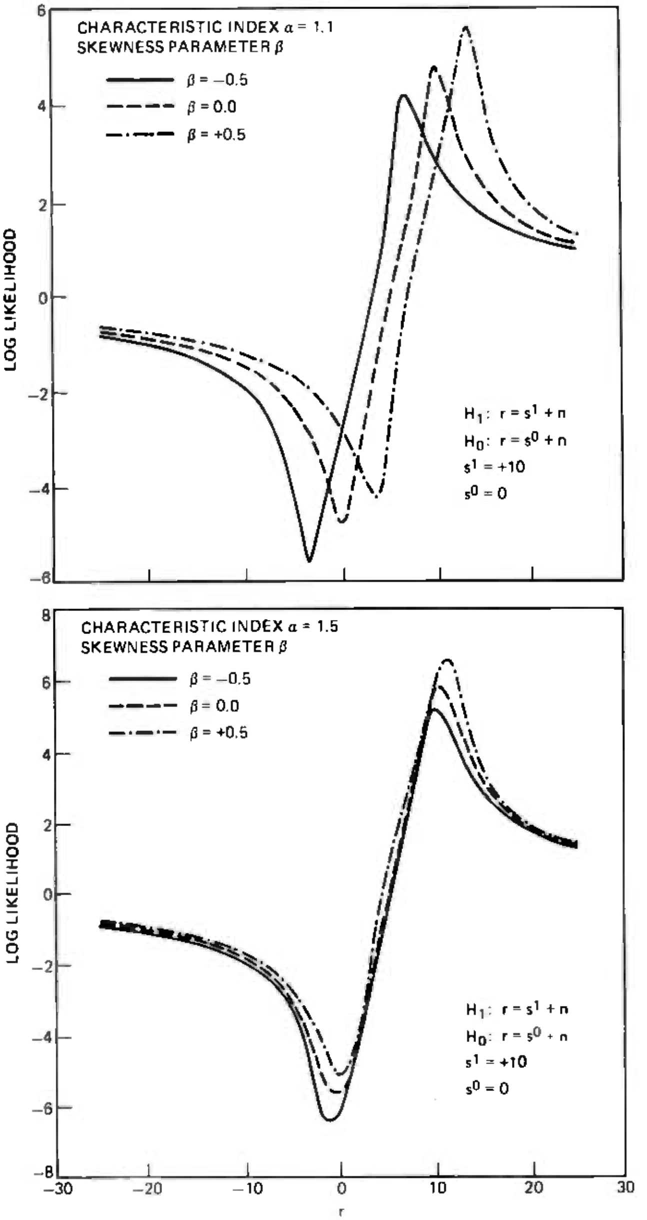

Fig. 3—Representative log likelihood functions ($s^1 = +10$, $s^0 = 0$) (α fixed, β varying); scale factor $c = 1.0$; location parameter $\delta = 0$.

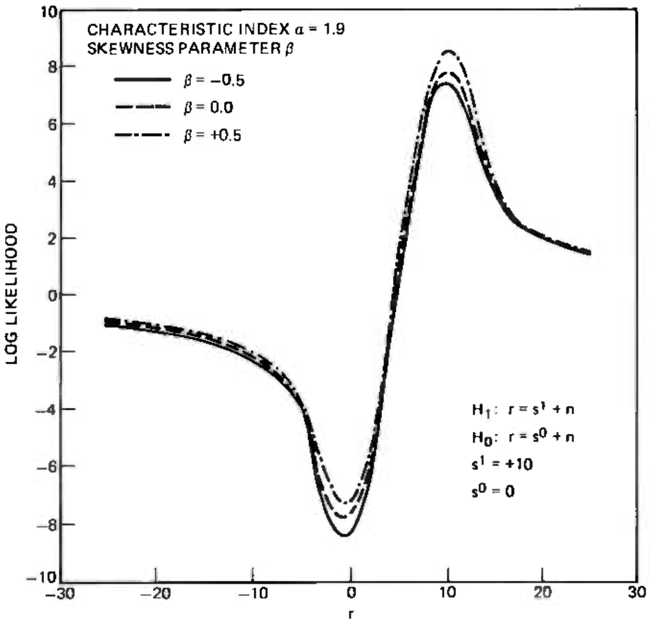

Fig. 3—(continued)

functions. Figures 3 and 4 show various representative log likelihood ratios $[l(r_i)]$ for $(1 < \alpha < 2,\ -1 < \beta < 1)$ with a fixed α and β varying; Fig. 5 shows the same log likelihood ratios as in Fig. 4 with β fixed and α varying. Similar results hold in the remaining cases $(0 < \alpha < 1,\ -1 < \beta < 1)$.

Three points are emphasized here. First, the structure of the optimum (log likelihood) detector is very sensitive to whether the underlying distribution is gaussian or nongaussian stable; this is not surprising, because small perturbations away from $\alpha = 2$ result in a singular perturbation in the probability density function.* Second, when the observation is in a neighborhood of $\frac{1}{2}(s^0 + s^1)$, an identical Taylor series argument, as used in the Cauchy example, is applicable, and small perturbations about this midway point result in linear perturbations about the corresponding log likelihood point. Third, when large excursions occur,

$$\left|\frac{r_i - s^0}{c}\right| \gg 1, \qquad \left|\frac{r_i - s^1}{c}\right| \gg 1,$$

the (log) likelihood for this term behaves as $O(r_i^{-1})$, which follows from asymptotic expansions.

---

* However, stable distributions in the neighborhood of $\alpha = 2$ are all close with respect to the topology induced by any reasonable metric, e.g., Prokhorov's metric.

The first two points in the preceding discussion hold for $(1 \leqq \alpha < 2, |\beta| = 1)$. The third point must be slightly modified (assume now $\beta = -1$, since a similar argument follows immediately for $\beta = 1$): $l(r_i) \sim O(r_i^{-1})$ for $r_i > 0$, but for $r_i < 0$, $l(r_i) \sim O(-|r_i|^{1/\alpha - 1})$ (cf. gaussian case) $(1 < \alpha < 2)$, while for $r_i < 0$, $\alpha = 1$,

$$l(r_i) \sim O[-\exp(\pi |r_i|/2)].$$

It remains to consider $\{n_k\}_1^N$, a sequence of i.i.d. stable random variables with $(0 < \alpha < 1, |\beta| = 1)$. Assume from here on $\beta = -1$, $s^1 > s^0$. The likelihood ratio is thus zero or strictly positive and finite, and the log likelihood is either minus infinity or finite. First, consider the Pearson V distribution as an example:

Pearson V $(\alpha = \frac{1}{2}, \beta = -1)$:

$$p_n(x) = \begin{cases} c\dfrac{1}{\sqrt{2\pi}}\left(\dfrac{x}{c}\right)^{-\frac{3}{2}} \exp[-c/2x] & x \geqq 0 \\ 0 & x < 0; \end{cases}$$

$$\therefore \quad l(r_i) = \begin{cases} -\dfrac{3}{2}\ln\left(\dfrac{r_i - s^1}{r_i - s^0}\right) - \dfrac{c}{2}\left[\dfrac{1}{r_i - s^1} - \dfrac{1}{r_i - s^0}\right] & r_i \geqq s^1 > s^0 \\ -\infty & s^1 > r_i \geqq s^0; \end{cases}$$

$$\therefore \quad \Lambda' = \sum_{i=1}^{N}\left[-\frac{3}{2}\ln\left(\frac{r_i - s^1}{r_i - s^0}\right) - \frac{c}{2}\left[\frac{1}{r_i - s^1} - \frac{1}{r_i - s^0}\right]\right] \underset{H_0}{\overset{H_1}{\gtrless}} L' \qquad \begin{aligned} &r_i \geqq s^1 > s^0 \\ \text{for all } i, \quad &1 \leqq i \leqq N, \end{aligned}$$

$$\Lambda' = -\infty \ (\text{choose } H_0) \text{ if } s^1 > r_i \geqq s^0 \qquad \text{for some } i, \quad 1 \leqq i \leqq N.$$

If all the received signal samples are greater than s^1, the optimum test is to compute the log likelihood and compare it with a threshold to choose H_1 or H_0. Note that for $(r_i - s^1)/c \gg 1$, $l(r_i)$ decays asymptotically as $O(r_i^{-1})$, and thus large deviations are weighted lightly. For $r_i > s^1$, $(r_i - s^1) \ll c$, $l(r_i) \sim (r_i - s^1)^{-1}$. If one or more observations fall in the interval $[s^0, s^1)$, the optimum rule is to choose H_0.

The remaining cases $(0 < \alpha < 1$ and $\beta = -1)$ can be treated in an identical manner, using the series expansion for the densities. The important points are (*i*) the optimum detector is fundamentally nonlinear; for $(r_i - s^1)/c \gg 1$, $l(r_i)$ decays as $O(r_i^{-1})$, (*ii*) if any observation falls in the interval $[s^0, s^1)$, the optimum strategy is to choose H_0, (*iii*) for $r_i > s^1$, $|r_i - s^1| \ll c$, $l(r_i) \sim O[(r_i - s^1)^{-(1/1-\alpha)}]$.

4.2 Performance limitations

To complete the solution of the problem, the probabilities of error of the first and second kind must be calculated. This appears to be quite difficult in the general case of an arbitrary stable distribution and bounds are developed in Section 4.3. In this section the performance of the optimum (log likelihood) detector is found explicitly for the three analytically tractable stable distributions to illustrate the

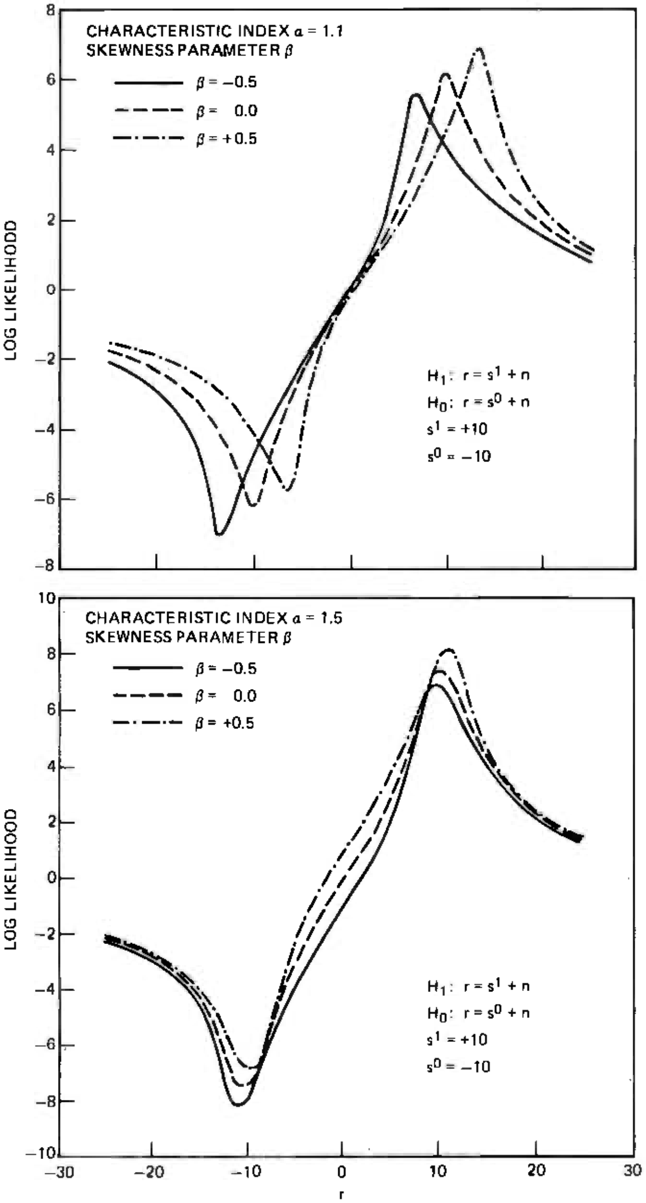

Fig. 4—Representative log likelihood functions ($s^1 = +10$, $s^0 = -10$) (α fixed, β varying); scale factor $c = 1.0$; location parameter $\delta = 0.0$.

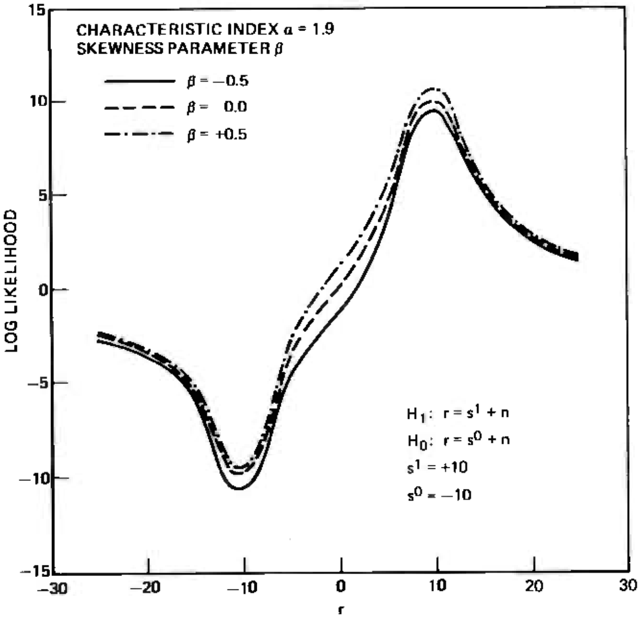

Fig. 4—(continued)

problems that must be addressed in the general case. The approach adopted is to calculate the characteristic function of the log likelihood probability measure induced under either H_1 or H_0.

Gaussian ($\alpha = 2, -1 \leqq \beta \leqq 1$)

Section 4.1 showed that the log likelihood ratio is

$$\Lambda' = -\frac{1}{4c^2}\left\{\sum_{i=1}^{N}\left[(r_i - s^1)^2 - (r_i - s^0)^2\right]\right\},$$

and since the log likelihood is a sum of i.i.d. random variables, its characteristic function can be found by using elementary Fourier techniques. The results are:

$$\ln E(e^{iv\Lambda'}|H_1) = \frac{N(s^1 - s^0)^2}{4c^2}\left[iv - v^2\right]$$

$$\ln E(e^{iv\Lambda'}|H_0) = \frac{N(s^1 - s^0)^2}{4c^2}\left[-iv - v^2\right].$$

Using the Fourier inversion lemma, the density of the log likelihood under either hypothesis can be found in closed form to be

$$p(\Lambda'|H_j) = \frac{1}{\sqrt{4\pi c'}}\exp\left[-(\Lambda' - \delta_j')^2/4c'^2\right] \qquad -\infty < \Lambda' < \infty \qquad j = 0, 1,$$

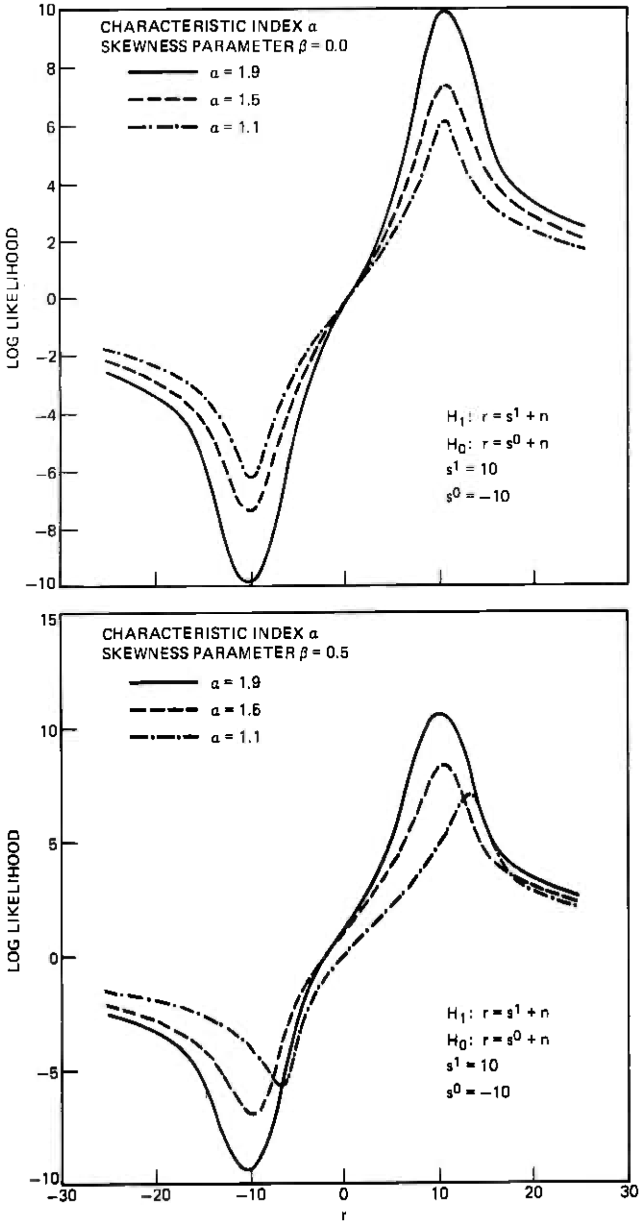

Fig. 5—Representative log likelihood functions ($s^1 = +10$, $s^0 = -10$) (α varying, β fixed).

where

$$\delta_1' = -\delta_0' = \frac{N}{4c^2}(s^1 - s^0)^2, \qquad c' = \frac{|s^1 - s^0|\sqrt{N}}{2c}.$$

The probabilities of an error of the first and second kind are

$$\begin{aligned} P_{10} = \Pr[\text{choose } H_1|H_0 \text{ true}] &= \int_{L'}^{\infty} p(\Lambda'|H_0)d\Lambda' \\ &= \frac{1}{2}\operatorname{erfc}\left(\frac{L' - \delta_0'}{2c'}\right) = \frac{1}{2}\left\{1 - \left(\frac{L' - \delta_0'}{c'\sqrt{\pi}}\right)\right. \\ &\qquad \cdot \exp\left[-\left(\frac{L' - \delta_0'}{2c'}\right)^2\right] {}_1F_1\left[1; \frac{3}{2}; \left(\frac{L' - \delta_0'}{2c'}\right)^2\right]\left.\vphantom{\frac{1}{2}}\right\}. \\ P_{01} = \Pr[\text{choose } H_0|H_1 \text{ true}] &= 1 - \frac{1}{2}\operatorname{erfc}\left(\frac{L' - \delta_1'}{2c'}\right) \\ &= \frac{1}{2}\left\{1 + \left(\frac{L' - \delta_1'}{c'\sqrt{\pi}}\right)\exp\left[-\left(\frac{L' - \delta_1'}{2c'}\right)^2\right]\right. \\ &\qquad \cdot {}_1F_1\left[1; \frac{3}{2}; \left(\frac{L' - \delta_1'}{2c'}\right)^2\right]\left.\vphantom{\frac{1}{2}}\right\}, \end{aligned}$$

where erfc $(\cdot)$ is the complementary error function (Ref. 20, eq. 7.1.2) and ${}_1F_1$ is a hypergeometric function (Ref. 20, eq. 7.1.21; see also Slater, Ref. 21).

Cauchy $(\alpha = 1, \beta = 0)$*

It was noted previously that the log likelihood ratio can be written as

$$\Lambda' = \sum_{i=1}^{N} \ln \frac{(r_i - s^0)^2 + c^2}{(r_i - s^1)^2 + c^2}.$$

The characteristic function for the log likelihood can be found just as for the gaussian case:

$$\begin{aligned} &E(e^{iv\Lambda'}|H_1) \\ &= \int_{-\infty}^{\infty} \cdots \int_{-\infty}^{\infty} \exp\left(iv \sum_{j=1}^{N} \ln \frac{(r_j - s^0)^2 + c^2}{(r_j - s^1)^2 + c^2}\right) \prod_{j=1}^{N} \frac{c\,dr_j/\pi}{(r_j - s^1)^2 + c^2} \\ &= \prod_{j=1}^{N} \int_{-\infty}^{\infty} [(r_j - s^0)^2 + c^2]^{iv}[(r_j - s^1)^2 + c^2]^{-iv-1}\left(\frac{c}{\pi}\right) dr_j \\ &= \left\{\int_{-\infty}^{\infty} [(x + \Delta)^2 + c^2]^{iv}[(x - \Delta)^2 + c^2]^{-iv-1}\left(\frac{c}{\pi}\right) dx\right\}^N, \end{aligned}$$

where

$$\Delta = \tfrac{1}{2}(s^1 - s^0), \qquad x = r_j - \tfrac{1}{2}(s^1 + s^0).$$

---

* The following analysis was suggested to the author by S. O. Rice; any errors in the development here are the responsibility of the author alone.

It now helps to realize

$$(x \pm \Delta)^2 + c^2 = (x^2 + \Delta^2 + c^2)\left(1 \pm \frac{2\Delta x}{x^2 + \Delta^2 + c^2}\right)$$

so that the characteristic function can be written as

$$\begin{aligned} E(e^{iv\Lambda'}|H_1) &= \left[\int_{-\infty}^{\infty}\left(1 + \frac{2\Delta x}{x^2 + \Delta^2 + c^2}\right)^{iv}\left(1 - \frac{2\Delta x}{x^2 + \Delta^2 + c^2}\right)^{-iv-1}\right. \\ &\qquad \left.\cdot\left(\frac{c}{\pi}\right)\frac{dx}{x^2 + \Delta^2 + c^2}\right]^N \\ &= \left[\int_{-\infty}^{\infty}\sum_{m=0}^{\infty}\sum_{n=0}^{\infty}\binom{iv}{m}\binom{-iv-1}{n}\left(\frac{2\Delta x}{x^2 + \Delta^2 + c^2}\right)^{m+n}\right. \\ &\qquad \left.\cdot\left(\frac{c}{\pi}\right)(-1)^n\frac{dx}{x^2 + \Delta^2 + c^2}\right]^N. \end{aligned}$$

Only even powers of $(m + n)$ contribute to the integral. This observation can be combined with the definition of the beta function (Ref. 20, eq. 6.2.1.) to show that

$$\begin{aligned} E(e^{iv\Lambda'}|H_1) &= \left[\sqrt{\frac{c^2}{\Delta^2 + c^2}}\sum_{m=0}^{\infty}\sum_{n=0}^{\infty}\binom{iv}{m}\binom{-iv-1}{n}\right. \\ &\qquad \left.\cdot\left(\frac{4\Delta^2}{\Delta^2 + c^2}\right)^{(m+n)/2}\frac{(-1)^n}{\pi}\,\frac{\Gamma^2\left(\frac{m+n+1}{2}\right)}{\Gamma(m+n+1)}\right]^N. \end{aligned}$$

Substituting $(m + n) = 2l$, and using the identity (Ref. 20, eq. 6.1.18)

$$\frac{\Gamma(l + \frac{1}{2})}{\Gamma(2l)} = \frac{2\sqrt{\pi}}{4^l\Gamma(l)},$$

results in the final form of the log likelihood characteristic function assuming H_1 is true,

$$\begin{aligned} E(e^{iv\Lambda'}|H_1) &= \left[-\sqrt{\frac{c^2}{c^2 + \Delta^2}}\sum_{l=0}^{\infty}\left(\frac{(\Delta/2)^2}{\Delta^2 + c^2}\right)^l\right. \\ &\qquad \left.\cdot\frac{(-iv)_{2l}}{(l!)^2}\,{}_2F_1(-2l, iv + 1; iv - 2l + 1; -1)\right]^N. \end{aligned}$$

The term

$$(-iv)_{2l} = \frac{\Gamma(-iv + 2l)}{\Gamma(-iv)}$$

is standard notation for Pochhammer's symbol (Ref. 20, eq. 6.1.22). A similar expression results for the characteristic function of the log likelihood, assuming the other hypothesis is true:

$$E(e^{iv\Lambda'}|H_0) = \left[-\sqrt{\frac{c^2}{c^2+\Delta^2}} \sum_{l=0}^{\infty} \frac{(1+iv)_{2l}}{(l!)^2} \cdot \left(\frac{(\Delta/2)^2}{\Delta^2+c^2} \right)^l {}_2F_1(-2l, iv; -iv-2l; -1) \right]^N \cdot$$

Since these series converge for all v $(-\infty < v < \infty)$, as well as for all (finite) values of Δ and c, the Fourier inversion lemma guarantees that a unique inverse to these transforms exists, and thus in principle the density of the log likelihood under either hypothesis is known and the probabilities of error of the first and second kind can be calculated. Numerical results are presented in a later section that were arrived at in exactly this manner.

Several additional observations can be made. For $N = 1$ the log likelihood is a random variable whose distribution has compact support on the interval

$$\ln \frac{\sqrt{\Delta^2+c^2}-\Delta}{\sqrt{\Delta^2+c^2}+\Delta} \leqq \Lambda' - \left(\frac{s^1+s^0}{2} \right) \leqq \ln \frac{\sqrt{\Delta^2+c^2}+\Delta}{\sqrt{\Delta^2+c^2}-\Delta}$$

and thus the support of the log likelihood distribution for any finite number of samples, say N, is on the closed interval

$$N \ln \frac{\sqrt{\Delta^2+c^2}-\Delta}{\sqrt{\Delta^2+c^2}+\Delta} \leqq \Lambda' - N \left(\frac{s^1+s^0}{2} \right) \leqq N \ln \frac{\sqrt{\Delta^2+c^2}+\Delta}{\sqrt{\Delta^2+c^2}-\Delta}.$$

Since the log likelihood distribution has compact support, it is well known (Ref. 22, p. 121) that its Fourier transform has support on the entire real axis. The second observation concerns the asymptotic $(v \gg 1)$ behavior of the characteristic function of the log likelihood. Since the saddle points of the log likelihood characteristic function are at $\pm\sqrt{\Delta^2+c^2}$, stationary phase arguments[23] show that asymptotically $(v \gg 1)$:

$$\begin{aligned} E(e^{iv\Lambda'}|H_1) &= \left[\int_{-\infty}^{\infty} \exp\left(iv \ln \frac{(x+\Delta)^2+c^2}{(x-\Delta)^2+c^2} \right) \left(\frac{c}{\pi} \right) \frac{dx}{(x-\Delta)^2+c^2} \right] \\ &\sim \left[\frac{c^2}{\sqrt{\pi\Delta v}} (\Delta^2+c^2)^{\frac{1}{4}} \left\{ \exp\left(iv \ln \frac{\sqrt{\Delta^2+c^2}+\Delta}{\sqrt{\Delta^2+c^2}-\Delta} + i\frac{\pi}{4} \right) \right. \right. \\ &\qquad \left. \left. + \exp\left(iv \ln \frac{\sqrt{\Delta^2+c^2}-\Delta}{\sqrt{\Delta^2+c^2}+\Delta} - i\frac{\pi}{4} \right) \right\} + O\left(\frac{i}{v} \right) \right]^N, \end{aligned}$$

so that asymptotically the characteristic function decays as $|v|^{-N/2}$. A similar result holds for the log likelihood characteristic function assuming H_0 is true.

An alternate approach is to calculate the Mellin transform of the likelihood probability density (for $N = 1$), then raise it to the Nth power and find the inverse transform; this was investigated without success. A direct approach, convolving the probability density of the log likelihood with itself N times, was also attempted; the resulting integrals were intractable.

Pearson V $(\alpha = \frac{1}{2}, \beta = -1)$

Assuming H_1 is true, the characteristic function of the log likelihood is

$$\begin{aligned} E(e^{iv\Lambda'}|H_1) &= \int_{s^1}^{\infty} \cdots \int_{s^1}^{\infty} \exp\left\{ iv \sum_{j=1}^{N} \left[-\frac{3}{2} \ln\left(\frac{r_j - s^1}{r_j - s^0}\right) \right.\right. \\ &\quad \left. - \frac{c}{2}\left(\frac{1}{r_j - s^1} - \frac{1}{r_j - s^0}\right)\right] \prod_{j=1}^{N} \frac{1}{c\sqrt{2\pi}} \left(\frac{r_j - s^1}{c}\right)^{-\frac{3}{2}} \\ &\qquad \left. \cdot \exp\left(-\frac{c}{2(r_j - s^1)}\right) dr_j \right\} \\ &= \prod_{j=1}^{N} \left\{ \int_{s'}^{\infty} \exp\left[-\frac{3}{2} iv \ln\left(\frac{r_j - s^1}{r_j - s^0}\right) - \frac{ivc}{2}\left(\frac{1}{r_j - s^1} - \frac{1}{r_j - s^0}\right)\right] \right. \\ &\qquad \left. \cdot \frac{1}{c\sqrt{2\pi}} \left(\frac{r_j - s^1}{c}\right)^{-\frac{3}{2}} \exp\left(-\frac{c}{2(r_j - c)}\right) dr_j \right\} \\ &= \left\{ \int_{\Delta}^{\infty} \exp\left[-\frac{3}{2} iv \ln\left(\frac{x - \Delta}{x + \Delta}\right) - \frac{ivc}{2}\left(\frac{1}{x - \Delta} - \frac{1}{x + \Delta}\right)\right] \right. \\ &\qquad \left. \cdot \frac{1}{c\sqrt{2\pi}} \left(\frac{x - \Delta}{c}\right)^{-\frac{3}{2}} \exp\left(-\frac{c}{2(x - \Delta)}\right) dx \right\}^{N}, \end{aligned}$$

where $\Delta = \frac{1}{2}(s^1 - s^0)$, $x = r_j - \frac{1}{2}(s^1 + s^0)$. All attempts to simplify this expression were unsuccessful. Stationary phase arguments show that asymptotically $(v \gg 1)$

$$E(e^{iv\Lambda'}|H_1) \sim \left\{ \left[\sqrt{\frac{\pi}{k_1 v}}\, k_2 \exp\left(ivk_3 + i\frac{\pi}{4} \right) \right] + O\left(\frac{1}{v}\right) \right\}^{N},$$

where (k_1, k_2, k_3) are complicated functions of (c, Δ).

An attempt was made to find $E(e^{iv\Lambda'}|H_0)$, assuming no observation occurred in the interval (s^0, s^1); this approach encountered the same problems as finding $E(e^{iv\Lambda'}|H_1)$, and was unsuccessful.

It is worth noting that the log likelihood has only one maximum on the interval (s^1, ∞), for $E(e^{iv\Lambda'}|H_j)(j = 0, 1)$, and hence only one stationary point enters into the stationary phase asymptotic expression for $E(e^{iv\Lambda'}|H_j)$. It can be shown this behavior is typical of any asymmetric $(|\beta| = 1)$ stable distribution. In contrast, the log likelihood has two maxima for any stable distribution ($-1 < \beta < 1$), and hence two stationary points (cf. Cauchy).

Neither the use of Mellin transforms (instead of Fourier transforms) nor convolving the log likelihood density with itself N times made the problem any more tractable.

In the case of an arbitrary stable distribution, it appears quite difficult to find the density of the log likelihood by calculating the characteristic function of the log likelihood probability measure induced under either H_1 or H_0, because only series expansions are known at present for stable probability density functions (except for the three cases covered here). Even resorting to numerical approximation techniques poses some quite difficult problems: for $0 < \alpha < 2$, $-1 \leqq \beta \leqq 1$ (as for the Cauchy and Pearson V distributions) the log likelihood characteristic function has its support on the entire axis, and oscillates and decays asymptotically as $O[(e^{ivw_0}/\sqrt{v})^N]$ from stationary phase arguments.* To accurately approximate numerically the probabilities of error of the first and second kind from the log likelihood characteristic function, the characteristic function must be approximated and stored at a great many frequencies, and the total cost (especially due to storage) can be quite high. Furthermore, one would like to carry out calculations for many different values of (α, β, γ, δ). The storage cost plus the large number of parameter variations often desired can make this program quite expensive at present.

4.3 Analytic performance bounds

Because of analytical and numerical problems encountered in explicitly calculating the probabilities of errors of the first and second kind, as well as the total probability of error, bounds on these quantities were investigated.

Let P_1 and P_0 be probability measures defined on the same measure space (Ω, A). For $0 < q < 1$, define

$$h_q(P_1, P_0) = \left(\frac{dP_1}{d\mu}\right)^q \left(\frac{dP_0}{d\mu}\right)^{1-q} \mu,$$

where μ is any measure defined on (Ω, A) such that $\mu \gg P_1$, $\mu \gg P_0$. (An example of such a μ is $\mu = P_0 + P_1$.) This definition of h_q is seen by inspection to be independent of μ. Define

$$H_q(P_1, P_0) = \int_\Omega dh_q(P_1, P_0)$$

---

* Different contours of integration (e.g., path of steepest descent) were investigated without success.

as the Kakutani inner product of P_0 with P_1 (Ref. 24); the classical Hellinger integral is a special case of the Kakutani inner product, and is defined as $H_{\frac{1}{2}}(P_1, P_0)$. It is known that

$$0 \leqq H_q(P_1, P_0) \leqq 1,$$

with $H_q = 1$ iff $P_1 \equiv P_0$ a.e. The Kakutani inner product can be thought of intuitively as the amount of "colinearity" or "overlap" of two probability measures, with the larger the Kakutani inner product, the larger the "overlap." A number of useful properties of the Kakutani inner product are summarized in the following easily proven lemma[24,25]:

Lemma: *(1)* *P_0 and P_1 are mutually orthogonal (denoted $P_0 \perp P_1$), $\Leftrightarrow H_q(P_0, P_1) = 0 \Leftrightarrow h_q(P_0, P_1) = 0$*

(2) *If $0 < q < 1$, $H_q(P_0, P_1)$ is continuous in q. Four cases determine the behavior of $H_q(P_0, P_1)$ at $q = 0, 1$:*

(2a) *If P_0 and P_1 are equivalent, then $H_q(P_0, P_1)$ is continuous at $q = 0$ and $q = 1$.*

(2b) *If P_0 is absolutely continuous with respect to P_1 but not vice versa, then $H_q(P_0, P_1)$ is continuous at $q = 1$ but not at $q = 0$.*

(2c) *If P_1 is absolutely continuous with respect to P_0 but not vice versa, then $H_q(P_0, P_1)$ is continuous at $q = 0$ but not at $q = 1$.*

(2d) *If P_0 and P_1 are neither mutually orthogonal nor equivalent, then $H_q(P_0, P_1)$ is discontinuous at $q = 0$, $q = 1$.*

(3) *$H_q(P_0, P_1)$ and its logarithm are convex functions, $0 < q < 1$. The convexity is strict iff $(dP_1/dP_0)(x)$ is not constant for all $x \in \operatorname{supp}(P_0) \cap \operatorname{supp}(P_1)$.*

It is instructive to rewrite $H_q(P_0, P_1)$ in two different ways to explicitly show the relationship between the log likelihood functional and the Kakutani inner product:

$$\begin{aligned}(i)\ H_q(P_0, P_1) &= \int \exp\{q \ln (dP_1/dP_0)\} dP_0 \\ &= E\{\exp [q \ln (dP_1/dP_0)] | H_0\}, \\ (ii)\ H_q(P_0, P_1) &= \int \exp\{(q-1) \ln (dP_1/dP_0)\} dP_1 \\ &= E\{\exp [(q-1) \ln (dP_1/dP_0)] | H_1\}.\end{aligned}$$

(i) and *(ii)* are the Laplace transforms of the log likelihood probability density (also called the moment generating function of Λ), evaluated at q and $(q-1)$, and assuming H_0 and H_1 are true, respectively. It is

196–197). Using Hölder's inequality, it is straightforward to show that the logarithm of H_q and, hence, H_q itself, are convex functions of q, $0 < q < 1$.

Chernoff[26] was apparently first to use $H_q(P_0, P_1)$ (where $P_0 \ll \mu$, $P_1 \ll \mu$, $\mu \doteq$ Lebesgue measure) to upper bound the probabilities of error of the first and second kind, and his work has found widespread application in the engineering and statistical literature (see also, Ref. 14, pages 517–520 and the references therein).

In the notation used here, Chernoff showed

$$P_{01} \leqq \inf_{0<q} H_q(P_0, P_1)e^{-qL'}$$

$$P_{10} \leqq \inf_{q<1} H_q(P_0, P_1)e^{-(q-1)L'},$$

where L' is the threshold in the log likelihood ratio test.

Chernoff's original ideas have been generalized in several directions. Kraft[27] obtained upper and lower bounds on the total probability of error. For some choice of L' (see also Ref. 28):

$$\tfrac{1}{2} \min (\pi_0, \pi_1)H_{\frac{1}{2}}^2(P_0, P_1) \leqq P_E \leqq (\pi_0\pi_1)^{\frac{1}{2}}H_{\frac{1}{2}}(P_0, P_1).$$

Hellman and Raviv[29] have also worked on this problem. Shannon, Gallager, and Berlekamp[25] obtained lower bounds on the probabilities of error of the first and second kind in terms of the logarithm of $H_q(P_0, P_1)$, and the first and second derivatives of the logarithm.

Here the Kakutani inner product plays two key roles, providing a check on whether or not singular or perfect detection is possible [iff $H_q(P_0, P_1) \equiv 0$], as well as giving exponentially sharp bounds on the performance of the log likelihood ratio test if detection is not singular. Since the Kakutani inner product need only be calculated at a small number of values of q to accurately numerically approximate upper and lower bounds on error probabilities, unlike calculating the probabilities of error of the first and second kind from the log likelihood characteristic function, this approach may be useful as a practical design tool because it is relatively inexpensive.

The following observations are strightforward exercises:

(*i*) When a sequence of N i.i.d. random variables is observed, $H_q(P_0, P_1) = e^{-AN}$, where A is independent of N, depending solely on P_0, P_1, and q.

(*ii*) When P_0 and P_1 are absolutely continuous with respect to Lebesgue measure, and the corresponding densities are unimodal translates of one another, then for fixed q, the larger the separation the smaller the inner product $H_q(P_0, P_1)$.

The Kakutani inner product $H_q(P_0, P_1)$ can be explicitly calculated for the three analytic cases discussed earlier:

Gaussian ($\alpha = 2, -1 \leqq \beta \leqq 1$):

$$p_n(x) = 1/\sqrt{4\pi c}\exp(-x^2/4c^2) \qquad -\infty < x < \infty$$

$$H_q(P_0, P_1) = e^{N\mu(q)},\ \mu(q) \doteq \ln \int_{-\infty}^{\infty} p_n^q(x - s^1)p_n^{1-q}(x - s^0)dx$$

$$\mu(q) = -q(1 - q)(s^1 - s^0)^2/4c^2;$$

$$\therefore\ \mu\left(\frac{1}{2}\right) = -\left(\frac{s^1 - s^0}{4c}\right)^2.$$

Cauchy ($\alpha = 1, \beta = 0$):

$$p_n(x) = \frac{c}{\pi}(x^2 + c^2)^{-1} \qquad -\infty < x < \infty$$

$$H_q(P_0, P_1) = \left[\int_{-\infty}^{\infty} p_n^q(x - s^1)p_n^{1-q}(x - s^0)dx\right]^N$$

$$\int_{-\infty}^{\infty} p_n^q(x - s^1)p_n^{1-q}(x - s^0)dx = \sum_{j=0}^{\infty} - \sqrt{\frac{c^2}{c^2 + \Delta^2}}\left[\frac{(\Delta/2)^2}{\Delta^2 + c^2}\right]^j \cdot \frac{(1 - q)_{2j}}{(j!)^2}\,{}_2F_1(q, -2j; q - 2j; -1),$$

where $\Delta = (s^1 - s^0)/2$.

From tables (Ref. 30, 263.00) for elliptic integrals:

$$H_{\frac{1}{2}}(P_0, P_1) = \left\{\frac{1}{\pi}\left[\left(\frac{s^1 - s^0}{2c}\right)^2 + 1\right]^{-\frac{1}{2}} cn^{-1}\left[-1, \left[\left(\frac{s^1 - s^0}{2c}\right)^2 + 1\right]^{-\frac{1}{2}}\right]\right\}^N,$$

where $cn^{-1}(\cdot, \cdot)$ is an inverse Jacobian elliptic function.

Pearson V ($\alpha = \frac{1}{2}, \beta = -1$):

$$p_n(x) = \begin{cases} \dfrac{1}{c\sqrt{2\pi}}\left(\dfrac{x}{c}\right)^{-\frac{3}{2}} e^{-c/2x} & x \geqq 0 \\ 0 & x < 0 \end{cases}$$

$$H_q(P_0, P_1) = \left[\int_{-\infty}^{\infty} p_n^q(x - s^1)p_n^{1-q}(x - s^0)dx\right]^N.$$

The integral could not be expressed in any other analytic form. Since P_1 is absolutely continuous with respect to P_0, but not vice versa, $H_q(P_0, P_1)$ is continuous for $q \in (0, 1]$, and is discontinuous at $q = 0$. Apparently only in the gaussian case does the Kakutani inner product or the Hellinger integral reduce to a simple form, and for general stable distributions the problem appears to be analytically intractable at present. Thus, it seemed worthwhile to investigate numerical methods for approximating the desired integrals. Again it seems important to emphasize that an accurate approximation of the log likelihood probability density Laplace transform under H_1 or H_0 is needed at only a small number of choices of q, so the calculations can be quite inexpensive. In the previous section, the log likelihood characteristic function had to be approximated at a great many frequencies, and the resulting computation effort and storage made that program relatively more expensive.

4.4 Numerical approximation of performance bounds

At present, three approaches have been investigated for calculating stable probability density functions. The first involves summing power series and asymptotic series,[31] the second involves quadrature of an integral representation of the density,[32] and the third uses a discrete fast Fourier transform of the characteristic function (Ref. 33, pages 35–42; and Ref. 34).

The approach used here was a combination of the first and third methods. The stable probability density function was approximated over its central region via a discrete fast Fourier transform, while asymptotic expansions were used outside this region. This approach avoids the difficulty of knowing how to merge the power series and asymptotic series (see Ref. 31).

The Kakutani inner product was broken into two integrals. The first integral was approximated by a fixed step size Romberg integration

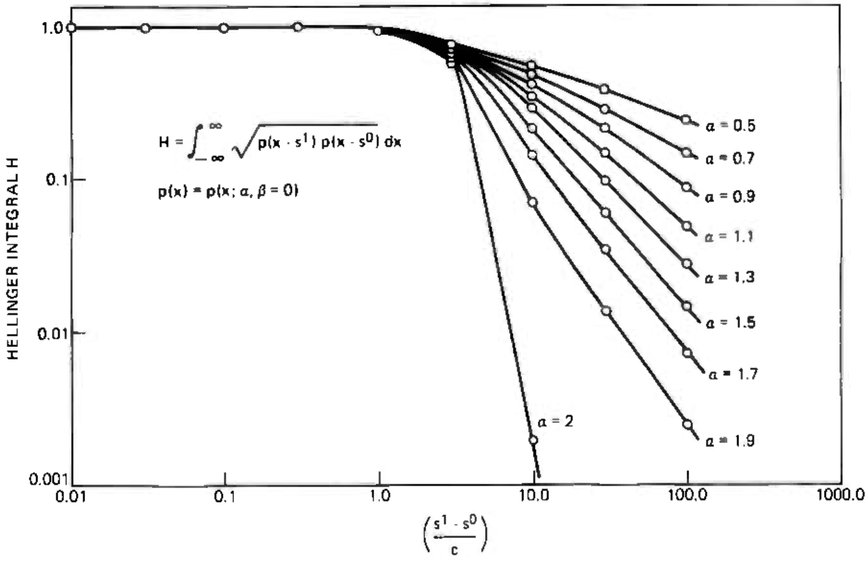

Fig. 6—Hellinger integral vs $(s^1 - s^0)/c$ $[\alpha = 0.5(0.2)1.9, \beta = 0]$.

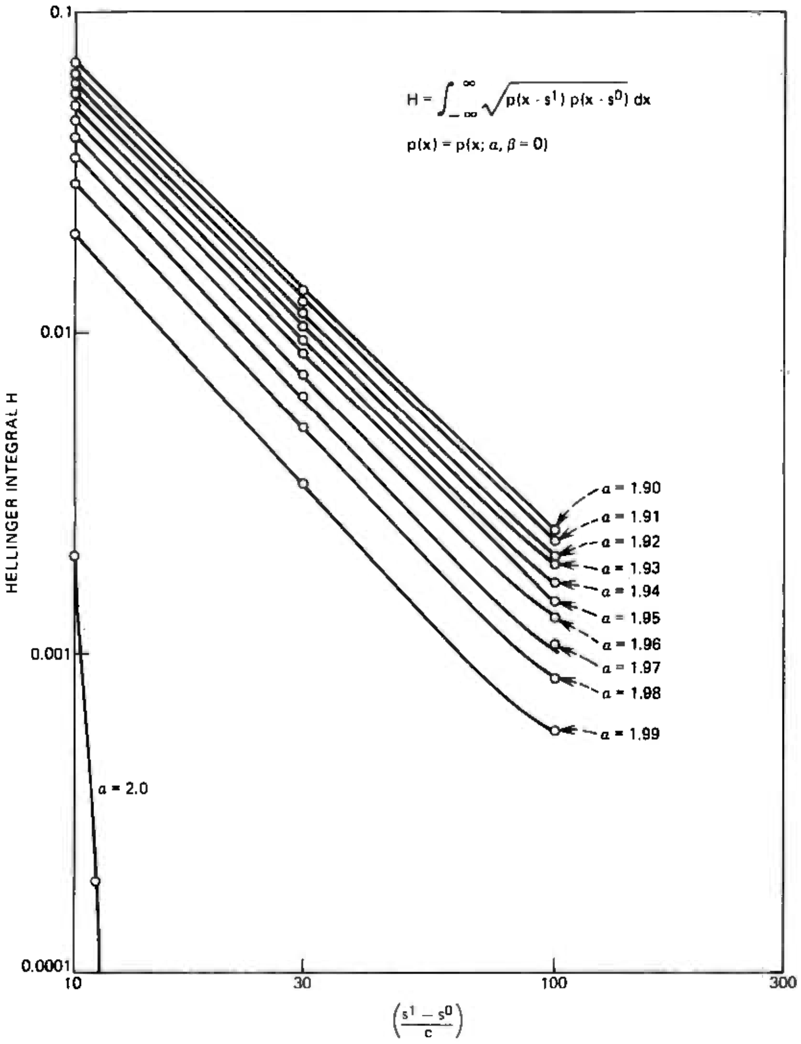

Fig. 7—Hellinger integral vs $(s^1 - s^0)/c$ $[\alpha = 1.90(0.01)2.00, \beta = 0]$.

routine[35] using the discrete fast Fourier transform approximation to the density (typically, 4096 points were used). The second integral was approximated by a variable step size Romberg integration algorithm using the asymptotic expansion for the density.

While this approach is adequate for finite mean stable distributions ($1 < \alpha \leqq 2$), and with care works for $0.5 \leqq \alpha \leqq 1$, it is inadequate for $0 < \alpha < 0.5$, because the expense is too great at present. The reason is that for $0 < \alpha < 1$, a great many evenly spaced points must be used to adequately approximate the characteristic function in the neighborhood of the origin (where its derivative is unbounded), as well as at other frequencies, and the expense of storing these values (to carry out the discrete fast Fourier transform) is prohibitive. One possible approach around this problem is to simply use only the series expansion (see Ref. 33).

All results presented here were calculated on a Honeywell 6070 computer using double-precision arithmetic (14 significant figures); the estimated relative error in all cases was less than a tenth of one percent.

Figure 6 shows the Hellinger integral for various parameters $[\alpha = 0.5(0.2)1.9,\ \beta = 0]$ as a function of $[(s^1 - s^0)/c]$, for $N = 1$. This figure suggests an interesting conjecture, that the Hellinger integral is smaller the closer the characteristic index α is to two, all other factors being the same. No proof of this is known, at present.

Figure 7 depicts results of numerically calculating the Hellinger integral for various characteristic indices close to two $[\alpha = 1.90(0.01)1.99,\ \beta = 0]$, for $N = 1$. The singular nature of the gaussian distribution $(\alpha = 2)$ is quite evident when compared with that of $\alpha = 1.99$ or $\alpha = 1.98$.

Figure 8 shows $\mu(q)$ vs q for fixed $[(s^1 - s^0)/c]$. Again, the closer the index is to two, the smaller the inner product.

Figure 9 presents $\mu(q)$ vs q for various choices of $[(s^1 - s^0)/c]$, and fixed characteristic index α and skewness parameter β; the larger $(s^1 - s^0)/c$, the smaller $H_q(P_0, P_1)$.

4.5 Comparison of the performance of the log likelihood decision rule ($\alpha = 1.95$) with a linear decision rule

It is interesting to compare the performance of the log likelihood decision rule with a linear decision rule, when the observations are drawn from a nongaussian stable distribution with characteristic index near two. To be explicit, it is assumed the observations are i.i.d. stable random variables ($\alpha = 1.95$, $\beta = 0$), with $\pi_0 = \pi_1 = \frac{1}{2}$ and $s^1 = -s^0 = S$ chosen for simplicity. The linear decision rule is simply

$$\sum_{i=1}^{N} r_i \underset{H_0}{\overset{H_1}{\gtrless}} 0.$$

This sum is a stable random variable, with parameters ($\alpha = 1.95$ $\beta = 0$, $N\gamma$, Ns^j), assuming $H_j (j = 0, 1)$ is true. The total probability of error is equal to the probability of either an error of the first or second kind,

$$P_E = P_{10} = P_{01},$$

and can be computed from the series described earlier, or from pub-

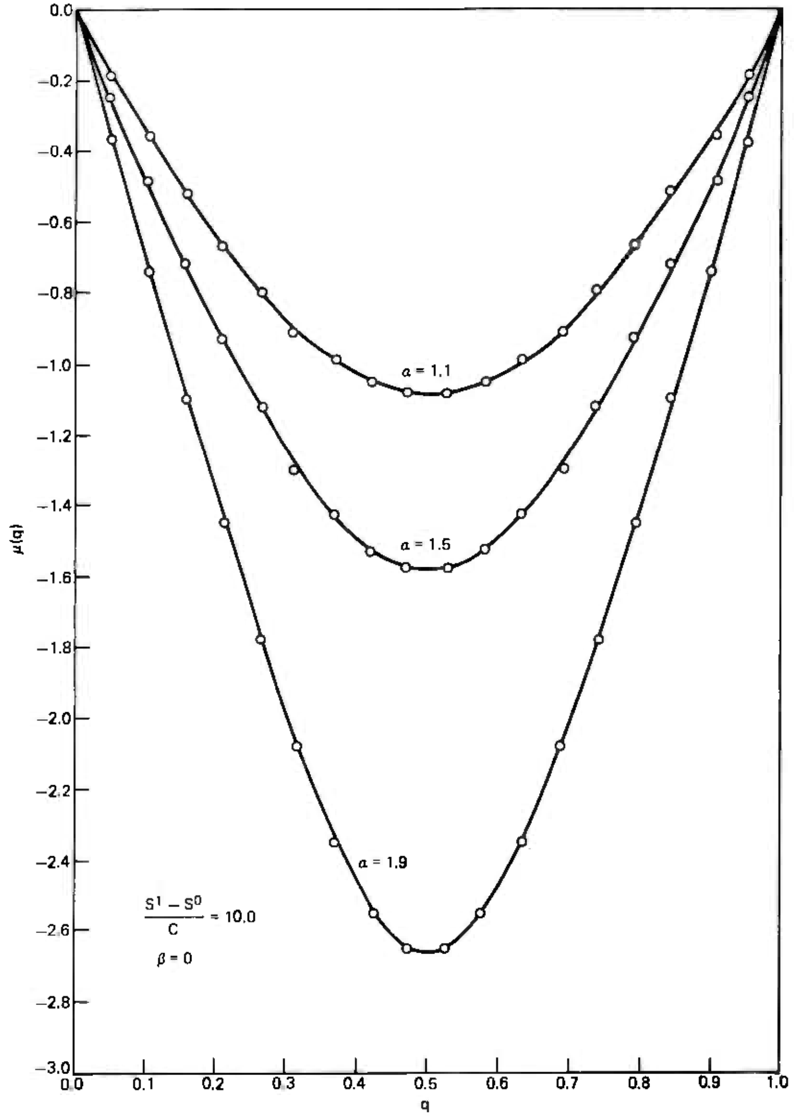

Fig. 8—Logarithm of Kakutani inner product H_q vs q [$\alpha = 1.1(0.4)1.9$, $\beta = 0$] [$(s^1 - s^0)/c = 10$].

lished tables.[31] This is plotted in Fig. 10 as a function of [$(s^1 - s^0)/c$] for various N. The same figure includes plots of the Hellinger integral upper bound on the total probability of error using the log likelihood decision rule. The figure makes it quite clear that the log likelihood decision rule, for many cases of interest, has a much much smaller probability of error than the linear decision rule.

Asymptotically, the total probability of error for the linear detection strategy behaves as

$$P_E \sim O\left(\left[\frac{NS}{(N\gamma)^{1/\alpha}}\right]^{-\alpha}\right), \qquad \gamma \doteq c^{\alpha};$$

$$\therefore \quad P_E \sim O[(S/c)^{-\alpha}N^{1-\alpha}],$$

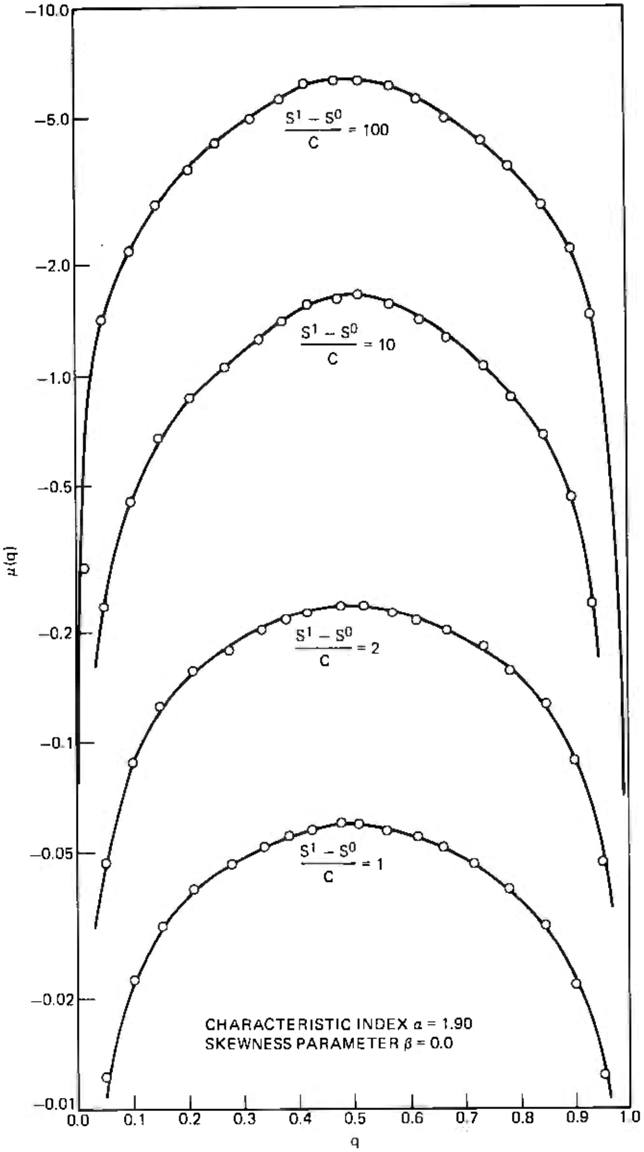

Fig. 9—Logarithm of Kakutani inner product H_q vs q $[(s^1 - s^0)/c = 1, 2, 10, 100]$ $(\alpha = 1.90, \beta = 0)$.

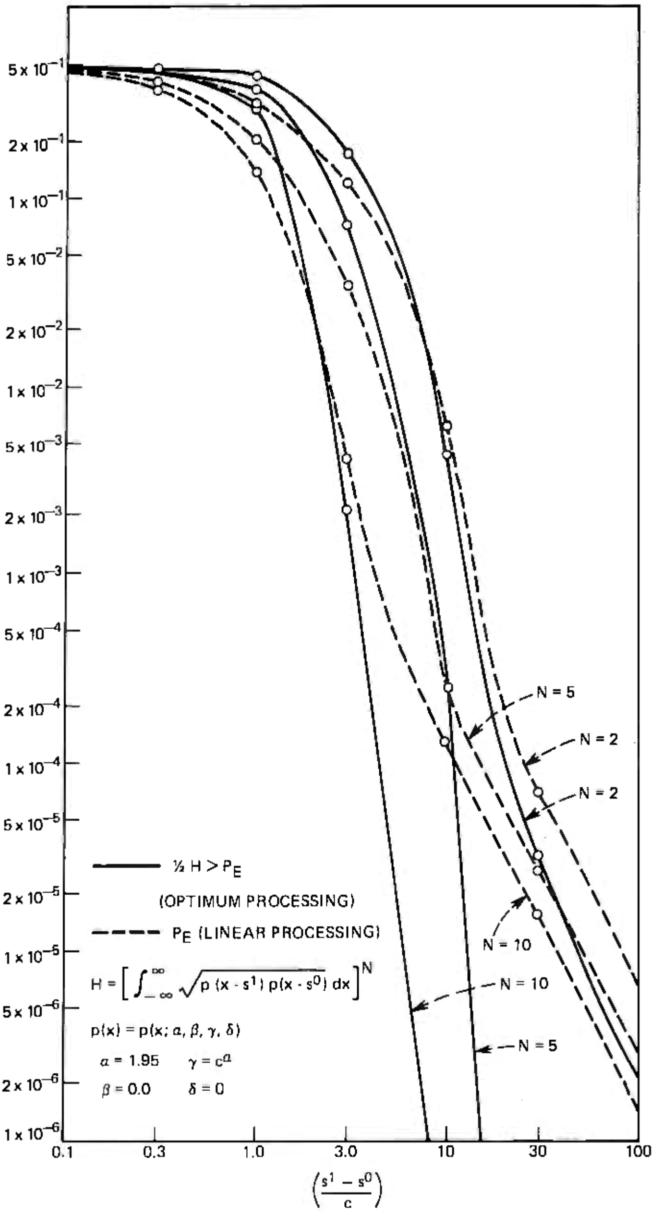

Fig. 10—Linear processing probability of error and Hellinger integral upper bound on nonlinear processing probability of error vs $(s^1 - s^0)/c$ ($\alpha = 1.95$, $\beta = 0$).

while the probability of error for the log likelihood detection strategy asymptotically behaves at

$$P_E = O(e^{-AN}),$$

where $A = A(\alpha, \beta, \gamma, S) > 0$, independent of N. This simple asymptotic analysis suggests that the log likelihood decision rule has a much smaller probability of error than the linear decision rule, for large N, which is borne out in Fig. 10.

4.6 Comparison of the upper and lower bounds and P_E

It remains to compare the bounds on total probability of error, and probabilities of errors of the first and second kind, with the actual quantities. None of the bounds employed here are tight, because the upper and lower bounds have different exponents. This program is quite difficult, and has only been carried out analytically for the gaussian case, and numerically for the Cauchy case. The remaining cases can be handled numerically following Shannon et al.[25] For simplicity, from this point on it is assumed that $\pi_0 = \pi_1 = \frac{1}{2}$, $s^1 = -s^0 = s$.

Gaussian $(\alpha = 2,\ -1 \leqq \beta \leqq 1)$

Earlier it was shown that

$$P_E = P_{10} = P_{01} = \frac{1}{2} \operatorname{erfc}\left(\frac{\sqrt{N}s}{2c}\right).$$

This can be upper and lower bounded tightly by (see Ref. 20, eq. 7.1.13)

$$K_L e^{-Ns^2/4c^2} < P_E < K_u e^{-Ns^2/4c^2},$$

where

$$K_L = \frac{1}{2} \cdot \left(\frac{\sqrt{N}s}{c} + \sqrt{\frac{Ns^2}{c^2} + 8}\right)^{-1} \cdot \pi^{-\frac{1}{2}}$$

$$K_u = \frac{1}{2} \cdot \left(\frac{\sqrt{N}s}{c} + \sqrt{\frac{Ns^2}{c^2} + \frac{16}{\pi}}\right)^{-1} \cdot \pi^{-\frac{1}{2}}.$$

Since both K_L and K_u behave as $O(N^{-\frac{1}{2}})$, $P_E \sim e^{-Ns^2/4c^2 - 0[LN(N)]}$, where K_u and K_L introduce factors of log (N) in the exponent. The Hellinger integral bounds are [27]

$$\frac{1}{4} \exp\left(-N \frac{s^2}{2c^2}\right) < P_E < \frac{1}{2} \exp\left(-\frac{Ns^2}{4c^2}\right).$$

By inspection, the exponent in the upper bound agrees with the tight lower and upper bound exponent [to within a factor of $LN(N)$]. The Chernoff upper bounds[26] on P_{10}, P_{01} are

$$\begin{aligned} &P_{01} \leqq \exp[-Nq^2(s/c)^2] \\ \text{or} \quad &P_{10} \leqq \exp[-N(1-q)^2(s/c)^2], \end{aligned} \qquad \text{for some } q \in [0, 1]$$

and for $q = \frac{1}{2}$ these exponents agree with the tight upper and lower bound exponents to within a factor on $LN(N)$. The lower bounds[25] are

$$P_{01} > \tfrac{1}{4}\exp[-Nq^2(s/c)^2 - q(s/c)\sqrt{2N}] \qquad \text{for some } q \in [0, 1]$$

$$\text{or} \quad P_{10} > \tfrac{1}{4}\exp[-N(1-q)^2(s/c)^2 - (1-q)(s/c)\sqrt{2N}],$$

and for N sufficiently large, the upper and lower bound exponents are identical within a factor of $O(N^{-\frac{1}{2}})$.

Cauchy ($\alpha = 1, \beta = 0$)

The real and imaginary parts of the characteristic function of the Cauchy log likelihood were calculated numerically at 513 evenly spaced frequencies starting at $v = 0$ from a direct numerical quadrature of the (complex) integral

$$\varphi(v) = \int_{-\infty}^{\infty} \exp\left(iv \ln \frac{(x+s)^2 + c^2}{(x-s)^2 + c^2}\right)\left(\frac{c}{\pi}\right)\frac{dx}{(x-s)^2 + c^2}, \qquad v = k\Delta v, \qquad k = 0, \cdots, 512$$

using an adaptive, step-size, Romberg, numerical integration algorithm, with an estimated error of 10^{-10} (all arithmetic was performed in double precision). One representative characteristic function is plotted in Fig. 11. The stationary-phase asymptotic expression was used for frequencies outside of this range. The resulting approximation to the characteristic function was multiplied by itself N times, and a numerical approximation of the inverse transform of this resulting characteristic function was calculated, using a fixed, step-size, Romberg algorithm for the first 513 frequencies; an adaptive, step-size, Romberg algorithm was used for the tail of the inverse transform. The final results are felt to be accurate to three significant figures. The results are plotted in Fig. 12, along with the Hellinger integral upper bound. Clearly, the Hellinger integral upper bound is quite conservative; it is straightforward to check that the Hellinger integral (squared) lower bound is too optimistic, from the curves in Fig. 12.

4.7 Generalizations

The extensions of the results in this section (as well as the following section) to a much wider class of infinitely divisible distributions is immediate. Here these extensions are sketched. Elementary arguments (Ref. 15, page 540) show that if the Lévy measure of an infinitely divisible distribution behaves asymptotically as a power, i.e., $\nu(X, \infty) \sim O(X^{-p})$, $\nu(-\infty, -X) \sim O(X^{-q})$, then $\Pr[x > X] \sim O(X^{-p})$, $\Pr[x < -X] \sim 0(X^{-q})$, where $p, q > 0$. Given a sequence of i.i.d. random variables drawn from such a distribution with one of two location parameters, it is straightforward to check that results analo-

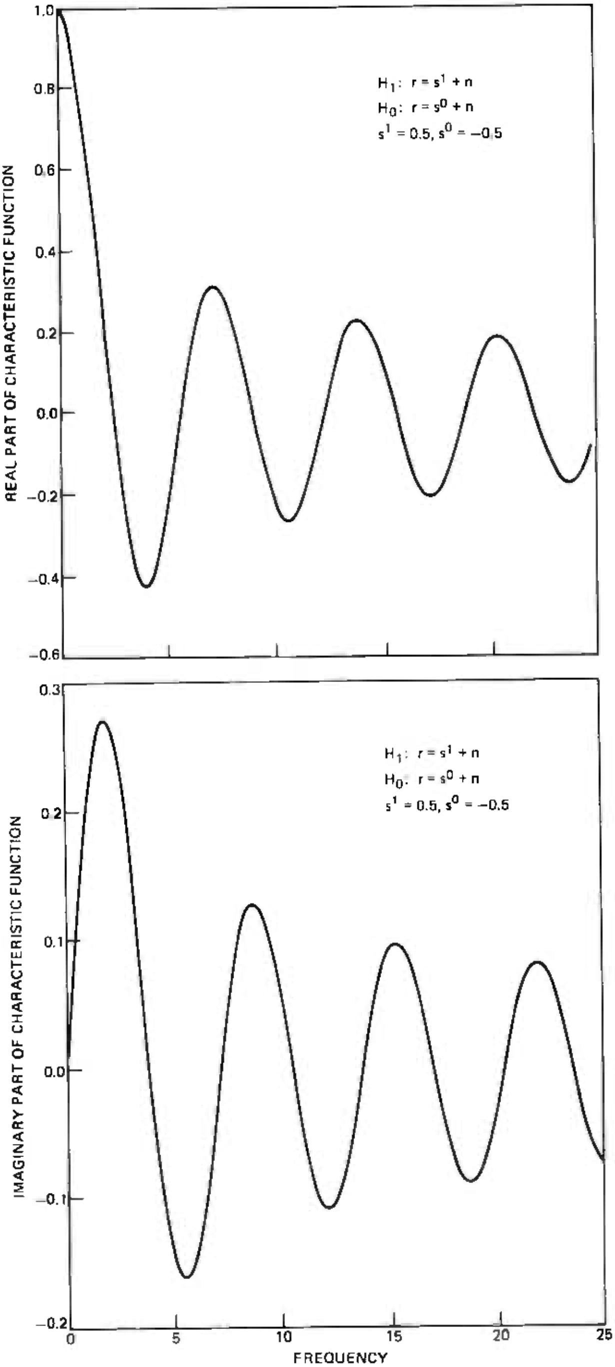

Fig. 11—Cauchy log likelihood characteristic function.

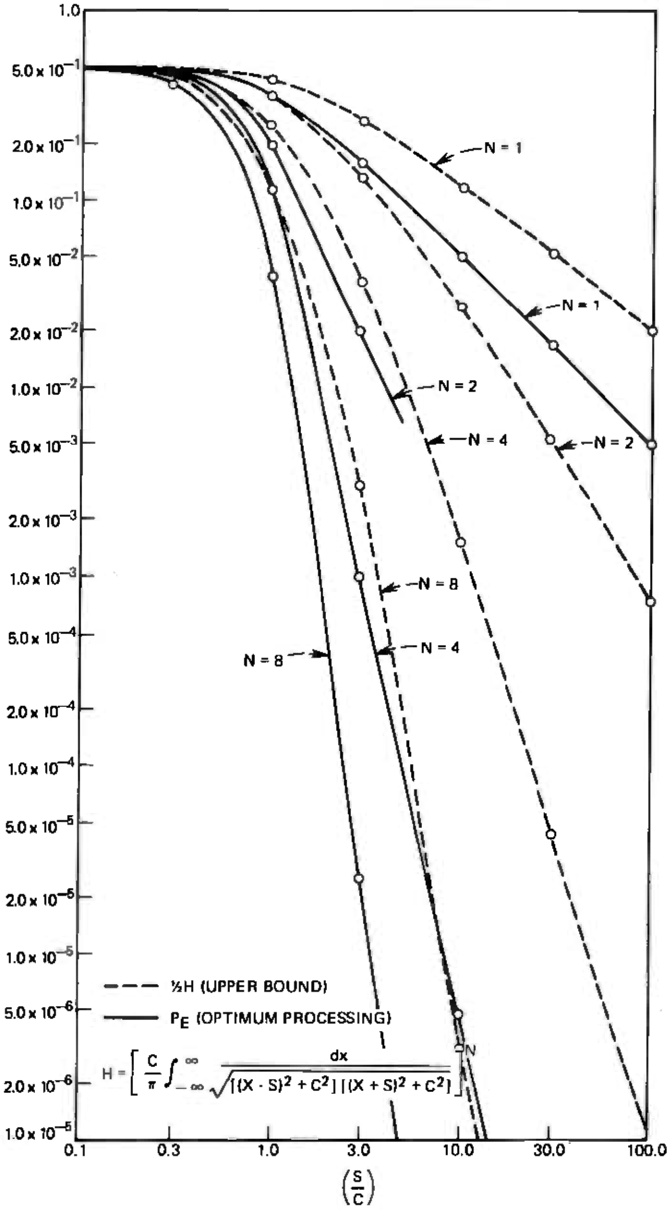

Fig. 12—Log likelihood probability of error and Hellinger integral upper bound for Cauchy ($\alpha = 1$, $\beta = 0$) samples vs (s/c).

gous to those in this section hold: (*i*) $l(r_i) \sim 0(r_i^{-1})$, (*ii*) the probability of an error of the first and second kind, using a log likelihood ratio test, is upper bounded by $\exp(-AN)$, (*iii*) using a simple linear test to discriminate between hypotheses, i.e., adding up the observations and comparing the sum with a threshold, results in the probability of an error of the first or second kind behaving as $0(NL'^{-p})$, $0(NL'^{-q})$, and choosing L' directly proportional to N (as in the gaussian case) gives $P_{01}, P_{10} \sim 0(N^{1-p}), 0(N^{1-q})$, which is much worse than the performance of the log likelihood test in this asymptotic sense.

V. DISCRETE TIME DETECTION OF STABLE MEASURES WITH DIFFERENT SCALES

In this section, one approach is studied for hypothesis testing of different scale parameters; since the ideas are quite similar to that just developed, the treatment is much shorter.

One of two sequences of i.i.d. stable random variables is observed (under one of two hypotheses, H_0 and H_1):

$$\begin{matrix} H_1 & r_k = s^1 n_k \\ H_0 & r_k = s^0 n_k \end{matrix} \qquad 1 \leqq k \leqq N.$$

The observed or received sequence is denoted $\{n_k\}_1^N$, where the $\{n_k\}_1^N$ are i.i.d. stable random variables with known parameters (α, β, $\gamma = 1$, $\delta = 0$); both s^1 and s^0 are known. The *a priori* probability of H_j is π_j ($j = 0, 1$). The measures induced by $\{n_k\}_1^N$ under H_0 and H_1 are equivalent for ($0 < \alpha \leqq 2$, $-1 \leqq \beta \leqq 1$); it remains to find the optimum decision rule, the log likelihood ratio, and characterize its performance.

5.1 *Likelihood ratio test*

Before discussing the general case, the three special analytically tractable cases are treated.

Gaussian ($\alpha = 2$, $-1 \leqq \beta \leqq 1$):

$$p_n(x) = \frac{1}{\sqrt{4\pi}} e^{-x^2/4} \qquad -\infty < x < \infty;$$

$$\therefore \quad l(r_i) = \ln \frac{p_n(r_i/s^1)/s^1}{p_n(r_i/s^0)/s^0} = \ln \frac{s^0}{s^1} - \frac{r_i^2}{4}\left[\left(\frac{1}{s^1}\right)^2 - \left(\frac{1}{s^0}\right)^2\right];$$

$$\therefore \quad \Lambda' = \sum_{i=1}^{N} l(r_i) = N \ln\left(\frac{s^0}{s^1}\right) - \left[\left(\frac{1}{2s^1}\right)^2 - \left(\frac{1}{2s^0}\right)^2\right] \cdot \sum_{i=1}^{N} r_i^2 \underset{H_0}{\overset{H_1}{\gtrless}} L'.$$

The test involves squaring the observations and comparing with a threshold; this test is the well-known chi-squared test (see Ref. 5, pages 163–173).

Cauchy ($\alpha = 1, \beta = 0$):

$$p_n(x) = \frac{1}{\pi}(x^2 + 1)^{-1} \qquad -\infty < x < \infty;$$

$$\therefore \quad l(r_i) = \ln \frac{p_n(r_i/s^1)/s^1}{p_n(r_i/s^0)/s^0} = \ln\left(\frac{s^0}{s^1}\right) - \ln \frac{r_i^2 + (s^0)^2}{r_i^2 + (s^1)^2};$$

$$\therefore \quad \Lambda' = N \ln\left(\frac{s^0}{s^1}\right) - \sum_{i=1}^{N} \ln \frac{r_i^2 + (s^0)^2}{r_i^2 + (s^1)^2} \underset{H_0}{\overset{H_1}{\gtrless}} L'.$$

For $|r_i| \ll s^0, s^1$, Taylor series arguments show $l(r_i)$ behaves as r_i^2, just as in the gaussian case. However, unlike the gaussian case, where $l(r_i)$ behaves asymptotically ($|r_i| \gg s^1, s^0$) as $0(r_i^2)$, here $l(r_i) \sim \ln(s^1/s^0) + 0(r_i^{-2})$; again, large excursions are soft limited, or essentially discarded.

Pearson V ($\alpha = \frac{1}{2}, \beta = -1$):

$$p_n(x) = \begin{cases} \frac{1}{\sqrt{2\pi}} x^{-\frac{3}{2}} e^{-\frac{1}{2}x} & x > 0 \\ 0 & x < 0; \end{cases}$$

$$\therefore \quad l(r_i) = \ln \frac{p_n(r_i/s^1)/s^1}{p_n(r_i/s^0)/s^0}$$

$$= \begin{cases} -\frac{1}{2}\ln\left(\frac{s^0}{s^1}\right) - \frac{1}{2r_i}[s_1 - s_0] & (r_i > 0); \\ 0 & (r_i < 0) \end{cases}$$

$$\therefore \quad \Lambda' = -\frac{N}{2}\ln\left(\frac{s^0}{s^1}\right) - \frac{1}{2}(s^1 - s^0)\sum_{i=1}^{N}\left(\frac{1}{r_i}\right) \underset{H_0}{\overset{H_1}{\gtrless}} L'.$$

Again, large deviations in r_i are soft limited or weighted lightly, since asymptotically ($r_i \gg s^1, s^0$)$l(r_i)$ behaves as $0(r_i^{-1})$.

The remaining cases can be treated in identical manner using the power series and asymptotic series expansions for the stable probability density function. For ($0 < \alpha < 2, -1 < \beta < 1; \alpha \neq 1$), the important points are: (*i*) for $|r_i| \ll s^0, s^1$, the *i*th term ($\beta \neq 0$) in the log likelihood behaves as r_i, unlike in the gaussian case, while for $\beta = 0$, $l(r_i) \sim r_i^2$, (*ii*) for $|r_i| \gg s^0, s^1$, soft limiting of large deviations is used, and the log likelihood's *i*th term behaves as $\alpha \ln(s^1/s^0) + 0(|r_i|^{-\alpha})$. Figures 13 and 14 show representative log likelihood ratios for fixed α and varying β, and fixed β with α varying, respectively, computed from power series and asymptotic series.[31]

The final case ($0 < \alpha < 2$, $\beta = 1$, or $\beta = -1$) must be handled with a little more care. Only the case $\beta = -1$ is discussed, since the other follows immediately. For ($1 < \alpha < 2$), the first point made above is still valid, while the second point is valid only for $r_i > 0$, $r_i \gg s^0, s^1$.

For $r_i < 0$, $|r_i| \gg s^0, s^1$, $l(r_i)$ behaves as $\alpha \ln (s^1/s^0) + 0(-|r_i|^{1/1-\alpha})$, i.e., decreasing with $|r_i|$. For $(0 < \alpha < 1)$, for $r_i > 0$, $r_i \ll s^0, s^1$, the ith term in the log likelihood behaves as $0(r_i^{-(1/1-\alpha)})$. Finally, for $\alpha = 1$, $l(r_i) = 0\{-\exp[(\pi/2)|r_i|]\}$ as $r_i \to -\infty$.

5.2 Performance limitations

The general problem of finding P_E, P_{01}, and P_{10} for arbitrary stable distributions is still open, both analytically and numerically (because of expense). The three special analytic cases are treated here, to point out the problems that must be overcome in the general case, if one attempts to find the log likelihood probability density by transform methods.

Gaussian $(\alpha = 2,\ -1 \leqq \beta \leqq 1)$: assuming hypothesis $H_j (j = 0, 1)$ true, the Fourier transform of the log likelihood probability density is

$$E(e^{iv\Lambda'}|H_1) = \left(\frac{s^0}{s^1}\right)^{ivN} \left\{1 - iv\left[\left(\frac{s^1}{s^0}\right)^2 - 1\right]\right\}^{-N/2}$$

$$E(e^{iv\Lambda'}|H_0) = \left(\frac{s^0}{s^1}\right)^{ivN} \left\{1 + iv\left[\left(\frac{s^0}{s^1}\right)^2 - 1\right]\right\}^{-N/2}.$$

These Fourier transforms can be inverted:

$$\left.\begin{aligned} p(x|H_1) &= \left(\frac{(s^0)^2}{(s^1)^2 - (s^0)^2}\right)^{N/2} x^{(N/2)-1} \\ &\quad \cdot \exp\left(-\frac{(s^0)^2}{(s^1)^2 - (s^0)^2}\, x\right) \Big/ \Gamma(N/2) \\ p(x|H_0) &= \left(\frac{(s^1)^2}{(s^1)^2 - (s^0)^2}\right)^{N/2} x^{(N/2)-1} \\ &\quad \cdot \exp\left(-\frac{(s^1)^2}{(s^1)^2 - (s^0)^2}\, x\right) \Big/ \Gamma(N/2) \end{aligned}\right\} x = \Lambda' - N \ln\left(\frac{s^0}{s^1}\right) > 0$$

$$p(x|H_1) = p(x|H_0) = 0 \qquad x = \Lambda' - N \ln\left(\frac{s^0}{s^1}\right) < 0.$$

Finally, the probabilities of errors of the first and second kind are:

$$\begin{aligned} P_{10} &= 1 - \frac{2}{N}\left(\frac{L'[(s^1)^2 - (s^0)^2]}{(s^0)^2}\right)^{N/2} \\ &\quad \cdot {}_1F_1\left(\frac{N}{2}; 1 + \frac{N}{2}; \frac{L'[(s^0)^2 - (s^1)^2]}{(s^0)^2}\right) \Big/ \Gamma(N/2) \\ P_{01} &= \frac{2}{N}\left(\frac{L'[(s^0)^2 - (s^1)^2]}{(s^1)^2}\right)^{N/2} \\ &\quad \cdot {}_1F_1\left(\frac{N}{2}; 1 + \frac{N}{2}; \frac{L'[(s^0)^2 - (s^1)^2]}{(s^1)^2}\right) \Big/ \Gamma(N/2) \\ &\qquad\qquad L' > N \ln (s^0/s^1) \end{aligned}$$

$$P_{10} = 1,\ P_{01} = 0 \qquad L' < N \ln (s^0/s^1).$$

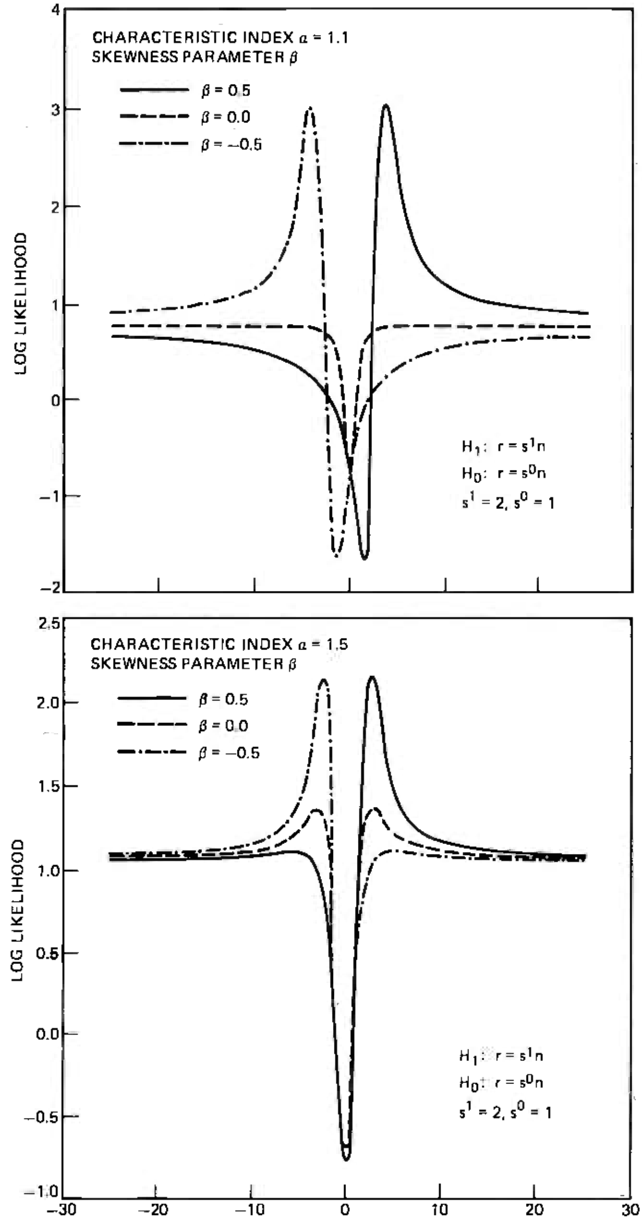

Fig. 13—Representative log likelihood functions (α fixed, β varying).

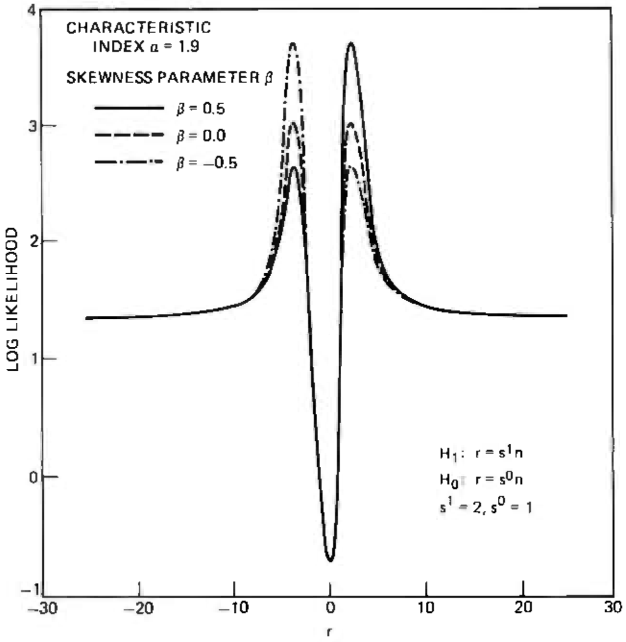

Fig. 13—(continued)

Cauchy ($\alpha = 1, \beta = 0$): the log likelihood characteristic function under H_1 is

$$E(e^{iv\Lambda'}|H_1) = \left\{\int_{-\infty}^{\infty} \frac{s^1}{\pi}\left(\frac{s^1}{s^0}\right)^{iv}[x^2+(s^0)^2]^{iv}[x^2+(s^1)^2]^{-iv-1}dx\right\}^N$$
$$= \left\{(s^1/s^0)^{iv+1}{}_2F_1\left[iv+1,\frac{1}{2};1;-1+\left(\frac{s^1}{s^0}\right)^2\right]\right\}^N,$$

where $s^1 > s^0$ was assumed. Stationary phase arguments show that the characteristic function decays asymptotically as $0(|v|^{-N/2})$. Again, the Fourier inversion lemma guarantees that the problem of finding P_{01} is solved. A similar analysis holds assuming H_0 is true.

An alternate approach is to compute the Mellin transform of the likelihood probability density function; the results are

$$E(\Lambda^{s-1}|H_1) = \left\{\left(\frac{s^1}{s^0}\right)^{s}{}_2F_1\left[s,\frac{1}{2};1;-1+\left(\frac{s^1}{s^0}\right)^2\right]\right\}^N$$
$$E(\Lambda^{s-1}|H_0) = \left\{\left(\frac{s^1}{s^0}\right)^{s-1}\cdot{}_2F_1\left[s-1,\frac{1}{2};1;-1+\left(\frac{s^1}{s^0}\right)^2\right]\right\}^N.$$

Unfortunately, it is not clear how to invert this transform to find P_{01} and P_{10}.

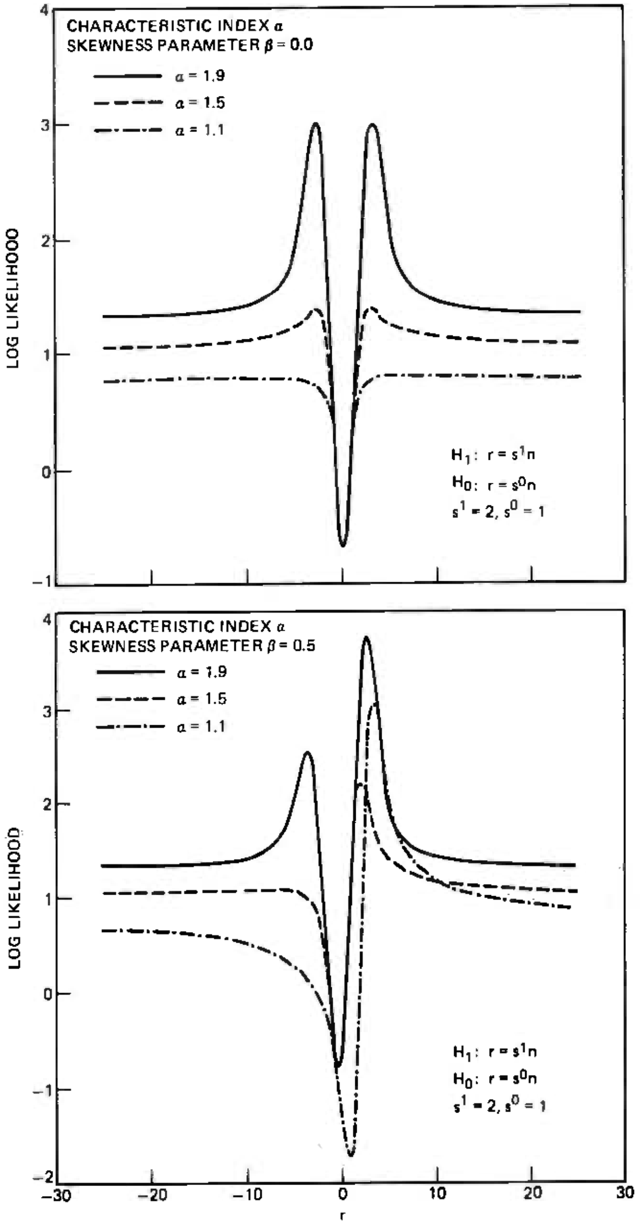

Fig. 14—Representative log likelihood functions (α varying, β fixed).

A third approach is to convolve the probability density of the log likelihood with itself N times; for $N = 2$, the convolution involves elliptic integrals; successive convolutions are quite formidable. This was not investigated further.

Pearson V $(\alpha = \frac{1}{2}, \beta = -1)$: the log likelihood characteristic function is (assuming now $s^0 > s^1$)

$$E(e^{iv\Lambda'} | H_1) = \left\{(s^1)^{iv}(s^0)^{-iv} \Big/ \left[1 - iv\left(\frac{s^0}{s^1} - 1\right)\right]\right\}^{N/2}$$

$$E(e^{iv\Lambda'} | H_0) = \left\{(s^1)^{iv}(s^0)^{-iv} \Big/ \left[1 - iv\left(1 - \frac{s^1}{s^0}\right)\right]\right\}^{N/2}.$$

The log likelihood probability density is

$$p(\Lambda' | H_1) = \left(\frac{s^1}{s^0 - s^1}\right)^{N/2} x^{(N/2)-1} e^{-(s^0 - s^1/s^1)x} \Big/ \Gamma\left(\frac{N}{2}\right)$$

$$x = \Lambda' - \frac{N}{2} \ln (s^1/s^0) > 0$$

$$p(\Lambda' | H_0) = \left(\frac{s^0}{s^0 - s^1}\right)^{N/2} x^{(N/2)-1} e^{-(s^0 - s^1/s^0)} \Big/ \Gamma\left(\frac{N}{2}\right)$$

$$p(\Lambda' | H_1) = p(\Lambda' | H_0) = 0 \qquad \Lambda' < \frac{N}{2} \ln (s^1/s^0).$$

The probabilities of errors of the first and second kind are

$$P_{10} = 1 - \frac{2}{N}\left(\frac{L'(s^0 - s^1)}{s^1}\right)^{N/2} {}_1F_1\left(\frac{N}{2}; \frac{N}{2} + 1; \frac{L'(s^1 - s^0)}{s^1}\right) \Big/ \Gamma\left(\frac{N}{2}\right)$$

$$L' > \frac{N}{2} \ln (s^1/s^0)$$

$$P_{01} = \frac{2}{N}\left(\frac{L'(s^0 - s^1)}{s^0}\right)^{N/2} {}_1F_1\left(\frac{N}{2}; \frac{N}{2} + 1; \frac{L'(s^1 - s^0)}{s^0}\right) \Big/ \Gamma\left(\frac{N}{2}\right)$$

$$P_{10} = 1, \qquad P_{01} = 0 \qquad L' < \frac{N}{2} \ln (s^1/s^0).$$

Again, the general problem is still open analytically, because closed-form expressions for stable probability density function are unknown at present (except for the three cases covered here). The general problem is expensive to tackle numerically at present, because of the expense of both calculating and storing the characteristic function of the log likelihood probability density, and because of the expense of repeating these calculations for many different parameter choices.

5.3 Analytic performance bounds

Apparently only in the three special cases does the Kakutani inner product reduce to simple expressions. These results are recorded here, while Section 5.4 discusses numerical approximations of these integrals for various cases of interest.

Gaussian ($\alpha = 2,\ -1 \leqq \beta \leqq 1$):

$$p_n(x) = \frac{1}{\sqrt{4\pi}} e^{-x^2/4} \qquad -\infty < x < \infty$$

$$H_q(P_0, P_1) = \left\{ \int_{-\infty}^{\infty} \left[\frac{1}{s^1} p_n\left(\frac{x}{s^1}\right) \right]^q \left[\frac{1}{s^0} p_n\left(\frac{x}{s^0}\right) \right]^{1-q} dx \right\}^N ;$$

$$\therefore \quad H_q(P_0, P_1) = (s^1)^{-qN} (s^0)^{-(1-q)N} \left(\frac{q}{(s^1)^2} + \frac{1-q}{(s^0)^2} \right)^{-N/2} ;$$

$$\therefore \quad H_{\frac{1}{2}}(P_0, P_1) = \left[\frac{1}{2} \left(\frac{s^0}{s^1} + \frac{s^1}{s^0} \right) \right]^{-N/2} .$$

Cauchy ($\alpha = 1,\ \beta = 0$):

$$p_n(x) = \frac{1}{\pi} (x^2 + 1)^{-1} \qquad -\infty < x < \infty$$

$$H_q(P_0, P_1) = \left\{ \int_{-\infty}^{\infty} \left[\frac{1}{s^1} p_n\left(\frac{x}{s^1}\right) \right]^q \left[\frac{1}{s^0} p_n\left(\frac{x}{s^0}\right) \right]^{1-q} dx \right\}^N ,$$

where

$$\int_{-\infty}^{\infty} \left[\frac{1}{s^1} p_n\left(\frac{x}{s^1}\right) \right]^q \left[\frac{1}{s^0} p_n\left(\frac{x}{s^0}\right) \right]^{1-q} dx = \left(\frac{s^1}{s^0} \right)^q {}_2F_1\left(\frac{1}{2}, q; 1; -1 + \frac{(s^1)^2}{(s^0)^2} \right) .$$

The Hellinger integral can be evaluated from the tables in Ref. 30 263.00:

$$H_{\frac{1}{2}}(P_0, P_1) = \left[\frac{1}{\pi} cn^{-1} \left(-1, \frac{i(s^1 - s^0)}{2\sqrt{s^1 s^0}} \right)^2 \right]^N .$$

Pearson V ($\alpha = \frac{1}{2},\ \beta = 1$):

$$p_n(x) = \begin{cases} \dfrac{1}{\sqrt{2\pi}} x^{-3/2} e^{-1/2x} & x \geqq 0 \\ 0 & x < 0 ; \end{cases}$$

$$\therefore \quad H_q(P_0, P_1) = \left(\frac{(s^1)^q (s^0)^{1-q}}{q s^1 + (1-q) s^0} \right)^{N/2} ;$$

$$\therefore \quad H_{\frac{1}{2}}(P_0, P_1) = \left(\frac{2\sqrt{s^1 s^0}}{s^1 + s^0} \right)^{N/2} .$$

5.4 Numerical approximation of performance bounds

The methods and checks employed were identical with those used in the detection of location for accurately calculating the inner product of the two stable probability measures.

Figure 15 shows $\mu(q)$ vs q for fixed (s^1/s^0) and $[\alpha = 1.1\ (0.4)\ 1.9, \beta = 0]$. This raises the conjecture that the closer the characteristic index is to 2, the smaller the Kakutani inner product.

Figure 16 shows $\mu(q)$ vs q for fixed (α, β) and various values of (s^1/s^0): the smaller the (s^1/s^0), the smaller the $H_q(P_0, P_1)$.

Figure 17 shows $H_{\frac{1}{2}}(P_0, P_1)$ for various (α, β) as a function of (s^1/s^0); note that the case $\alpha = 2$ does not appear to be singular here.

5.5 Comparison of performance of log likelihood decision rule with a chi-squared test

How does the performance of the log likelihood test compare with that of a chi-squared test, in particular for characteristic index α near 2?

The chi-squared test involves

$$\sum_{i=1}^{N} r_i^2 \underset{H_0}{\overset{H_1}{\gtrless}} L'.$$

The distribution of any one of the r_i^2 can be found from the series described earlier:

$$p(r_i^2 | H_j) = \begin{cases} \dfrac{1}{2s^j\sqrt{r_i}}\, p_n[x = \sqrt{r_i}; \alpha, \beta, (s^j)^\alpha, \delta = 0] & r_i > 0 \\ 0 & r_i < 0. \end{cases}$$

The discussion now follows from that in Section 4.6, but is not as detailed. Using elementary arguments (Ref. 15, pages 268–272), it can be shown that if $0 < \alpha < 2$, $-1 < \beta < 1$, then

$$\Pr\left(\sum_{i=1}^{N} r_i^2 > L' | H_j\right) \sim 0(NL'^{-(\alpha/2)}).$$

If L' is set at a threshold which is a fraction of N, then

$$P_E \sim 0(N^{1-(\alpha/2)});$$

i.e., the probability of error grows with N, the number of observations. For comparison, the upper bounds on P_{01}, P_{10}, and P_E for log likelihood detection all behave as $0(e^{-AN})$, where A depends on (α, β, s^1, and s^0). Thus, the log likelihood test is asymptotically far superior to the chi-squared by the above argument.

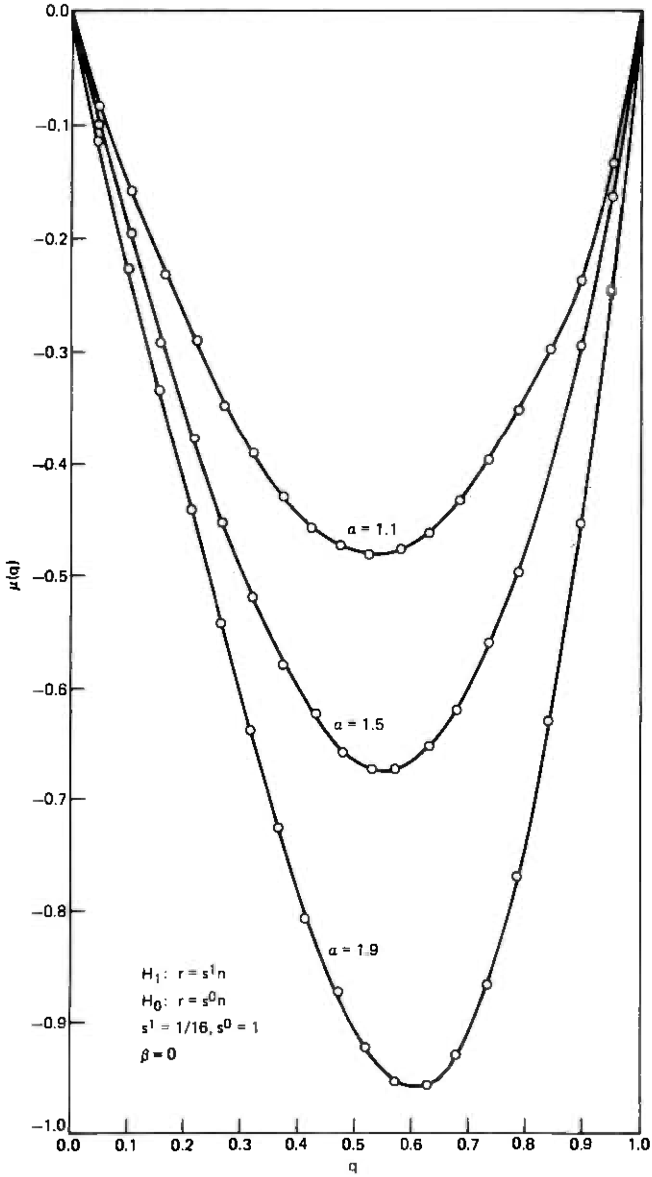

Fig. 15—Logarithm of Kakutani inner product H_q vs q [$\alpha = 1.1(0.4)1.9, \beta = 0$] $(s^0/s^1) = 16$.

VI. DISTINGUISHING STABLE PROBABILITY MEASURES WITH DIFFERENT CHARACTERISTIC INDICES AND SKEWNESS PARAMETERS

For completeness, this section touches on the form the log likelihood test takes for discriminating between stable distributions with different characteristic indices and with different skewness parameters. Performance of this test will not be covered here; much of the earlier discussion on performance is applicable here. A table in the Appendix summarizes the behavior of $l(r_i)$ both asymptotically and for

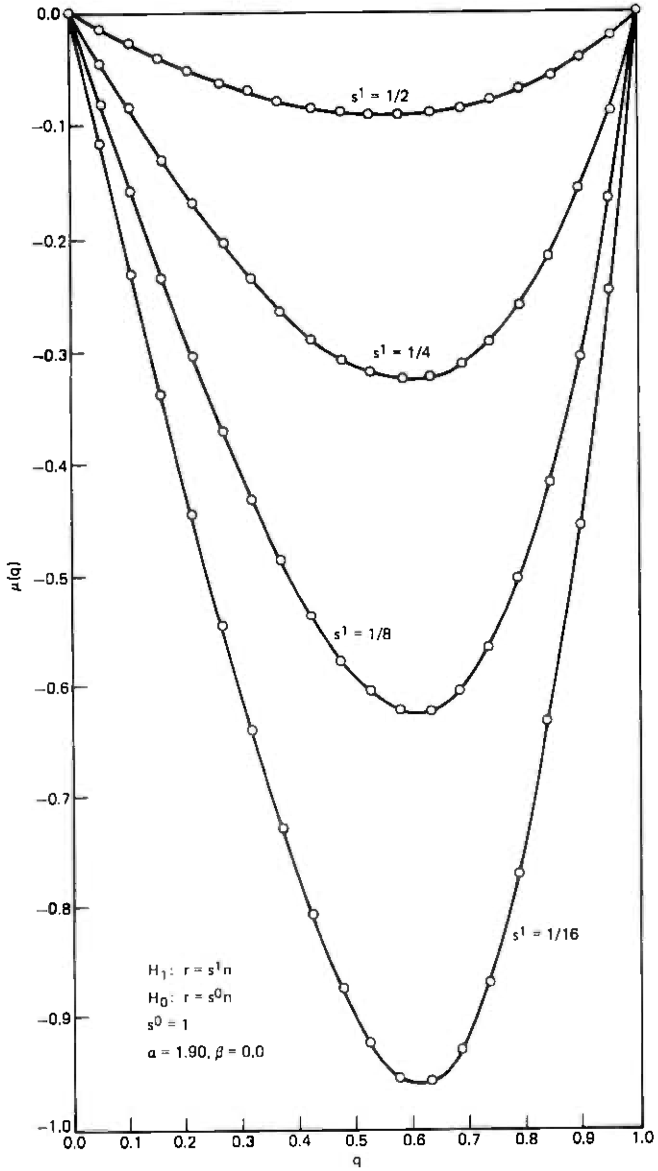

Fig. 16—Logarithm of Kakutani inner product H_q vs q [($\alpha = 1.90$, $\beta = 0$), $(s^0/s^1) = 1, 4, 8, 16$].

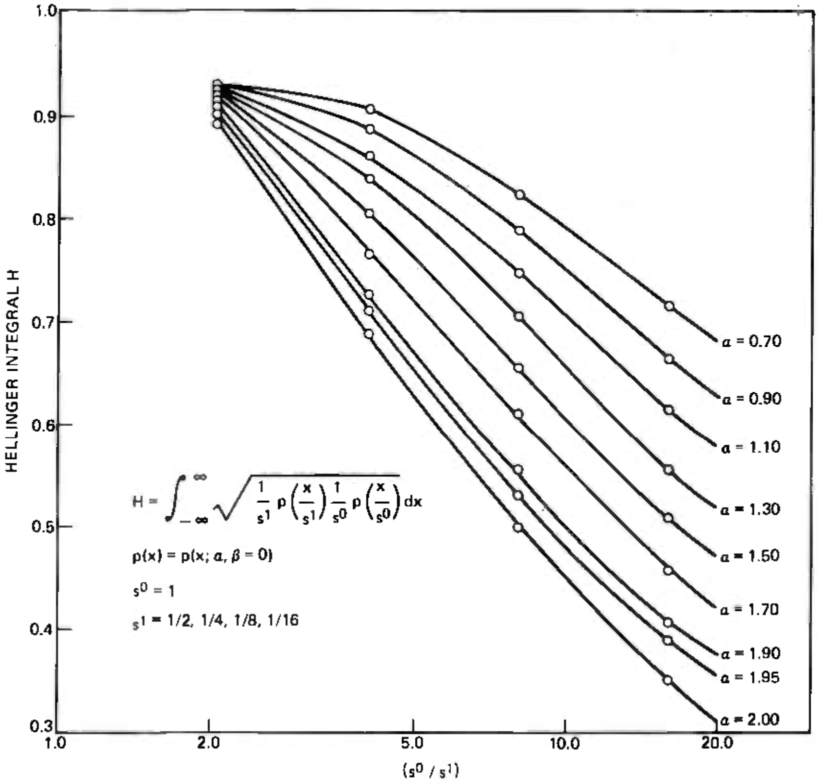

Fig. 17—Hellinger integral vs (s^1/s^0) $[\alpha = 0.7(0.2)1.90, \beta = 0]$.

$|r_i| \ll 1$, and includes both the results in the Sections 5.4 and 5.5 as well as the results of this section.

One of two sequences of i.i.d. stable random variables with known parameters is observed. In Section 6.1, the parameters are $(\alpha^j, \beta, \gamma = 1, \delta = 0)$, where $0 < \alpha^0 < \alpha^1 \leqq 2$; in Section 6.2, the parameters are $(\alpha, \beta^j, \gamma = 1, \delta = 0)$, where $-1 < \beta^0 < \beta^1 \leqq 1$ (recall $j = 0, 1$). The special case $(\alpha = 1, |\beta| = 1)$ is covered in the table in the Appendix but not in the discussion here.

6.1 Distinguishing different characteristic indices

For $-1 < \beta < 1$, the measures P_0 and P_1 are equivalent, so the log likelihood ratio is always finite. The log likelihood test is

$$\Lambda' = \sum_{i=1}^{N} l(r_i) \underset{H_0}{\overset{H_1}{\gtrless}} L',$$

where

$$l(r_i) = \ln \frac{p_n(r_i; \alpha^1, \beta, \gamma = 1, \delta = 0)}{p_n(r_i; \alpha^0, \beta, \gamma = 1, \delta = 0)}.$$

Two cases arise: symmetric ($\beta = 0$) and asymmetric ($\beta \neq 0$, $-1 < \beta < 1$) stable distributions. For the symmetric case, the distributions are symmetric about their unique mode, and thus $l(r_i) \sim |r_i^2|$ for $|r_i| \ll 1$. For the asymmetric case, the modes no longer coincide, and $l(r_i) \sim r_i$ for $|r_i| \ll 1$. Recall that for $1 < \alpha < 2$, for fixed skewness β ($\beta < 0$) the mode decreases as α decreases; for $0 < \alpha < 1$, the opposite is true. Thus, $l(r_i)$ is the difference of two unimodal functions and, in general, should have two points of zero slope. For $|r_i| \gg 1$, $l(r_i) = 0(-\ln |r_i|)$, so large deviations are weighted quite strongly. Note the log likelihood distribution has its support on whole line, unlike the two previous sections, except for $(0 < \alpha_0 < 1 \leqq \alpha_1 \leqq 2$, $|\beta| = 1)$.

For $\beta = -1$, and $1 < \alpha^0 < \alpha^1 < 2$, the measures P_0 and P_1 are equivalent, and the above discussion follows immediately with one exception: for $r_i \gg 1$, $l(r_i) = 0(-\ln r_i)$, while for $|r_i| \gg 1$, $r_i < 0$, $l(r_i) = 0(|r_i|^{\alpha_0/\alpha_0 - 1})$.

For $\beta = -1$, $0 < \alpha^0 < \alpha^1 < 1$, the measures P_0 and P_1 are equivalent. For $r_i > 0$, $|r_i| \ll 1$, $l(r_i) \sim r_i^{\alpha_0/1-\alpha_0}$, while for $r_i \gg 1$, $l(r_i) = 0(-\ln r_i)$.

Finally, for $\beta = -1$, $0 < \alpha^0 < 1 < \alpha^1 < 2$, the measures P_0 and P_1 are neither equivalent nor mutually orthogonal. For $r_i \gg 1$, $l(r_i) = 0(-\ln r_i)$, while for $r_i < 0$, $l(r_i) = \infty$. For $r_i > 0$, $r_i \ll 1$, $l(r_i) = 0(r_i^{\alpha_0/\alpha_0 - 1})$.

6.2 Distinguishing different skewness parameters

For $-1 < \beta^0 < \beta^1 < 1$, the measures P_0 and P_1 are equivalent, so the log likelihood ratio is finite. The discussion follows that of Section 6.1 exactly, with the difference that if $r_i \gg 1$, $l(r_i) = \ln (R_1/R_0) + 0(r_i^{-\alpha})$, while if $|r_i| \gg 1$, $r_i < 0$, $l(r_i) = \ln (L_1/L_0) + 0(|r_i|^{-\alpha})$.*

For $-1 = \beta^0 < \beta^1 < 1$, $1 \leqq \alpha < 2$, the measures P_0 and P_1 are equivalent. For $|r_i| \gg 1$, $r_i < 0$, $l(r_i) = 0(|r_i|^{\alpha/\alpha - 1})$, while for $r_i \gg 1$, $l(r_i) = \ln (R_1/R_0) + 0(r_i^{-\alpha})$.

For $-1 = \beta^0 < \beta^1 < 1$, $0 < \alpha < 1$, the measures P_0 and P_1 are neither equivalent nor mutually orthogonal. For $r_i \gg 1$, $l(r_i) = \ln (R_1/R_0) + 0(r_i^{-\alpha})$, while for $0 < r_i \ll 1$, $l(r_i) = 0(r_i^{\alpha/\alpha - 1})$. For $0 > r_i$, $l(r_i) = \infty$.

VII. ACKNOWLEDGMENTS

S. O. Rice and J. A. Morrison were quite helpful in evaluating the performance limitations of the likelihood ratio test for distinguishing between one of two location parameters. J. L. Blue had many suggestions concerning the numerical analysis. M.-L. Thomson provided a useful computer program for calculating hypergeometric functions.

---

* See the Appendix for definition of constants R_j, $L_j (j = 0, 1)$.

APPENDIX

Asymptotic Behavior of Log Likelihood Ratio

A.1 Location (δ)

$$l(x) = \ln \frac{p(x;\alpha,\beta,\gamma,\delta_1)}{p(x;\alpha,\beta,\gamma,\delta_0)} \qquad \delta_0 < \delta_1$$

	$x \to +\infty$	$x \to -\infty$
$\alpha = 2$	$0(x)$	$0(x)$
$0 < \alpha < 2,\ -1 < \beta < 1$	$0(x^{-1})$	$0(x^{-1})$
$1 < \alpha < 2,\ \beta = -1$	$0(x^{-1})$	$0(-\lvert x\rvert^{1/\alpha-1})$
$\alpha = 1,\ \beta = -1$	$0(x^{-1})$	$0(-e^{(\pi/2)\lvert x-\delta_1\rvert})$
	$x \to +\infty$	$x \downarrow \delta_1$
$0 < \alpha < 1,\ \beta = -1$	$0(x^{-1})$	$0(-(x-\delta_1)^{\alpha/\alpha-1})$.

A.2 Scale (c)

$$l(x) = \ln \frac{p(x;\alpha,\beta,\gamma_1 = c_1^\alpha,\delta = 0)}{p(x;\alpha,\beta,\gamma_0 = c_0^\alpha,\delta = 0)} \qquad c_0 < c_1$$

	$x \to +\infty$	$x \to -\infty$
$\alpha = 2$	$0(x^2)$	$0(x^2)$
$0 < \alpha < 2,\ -1 < \beta < 1$*	$\alpha \ln (c_1/c_0) + 0(x^{-\alpha})$	$\alpha \ln (c_1/c_0) + 0(\lvert x\rvert^{-\alpha})$
$1 < \alpha < 2,\ \beta = -1$	$\alpha \ln (c_1/c_0) + 0(x^{-\alpha})$	$0(-\lvert x\rvert^{\alpha/\alpha-1})$
$\alpha = 1,\ \beta = -1$	$\alpha \ln (c_1/c_0) + 0(x^{-\alpha})$	$0(-e^{(\pi/2)\lvert x/c_1\rvert})$
	$x \to +\infty$	$x \downarrow 0$
$0 < \alpha < 1,\ \beta = -1$	$\alpha \ln (c_1/c_0) + 0(x^{-\alpha})$	$0(-x^{\alpha/\alpha-1})$.

A.3 Characteristic index (α)

$$l(x) = \ln \frac{p(x;\alpha_1,\beta,\gamma = 1,\delta = 0)}{p(x;\alpha_0,\beta,\gamma = 1,\delta = 0)}, \qquad 0 < \alpha_0 < \alpha_1 \leqq 2$$

	$x \to +\infty$	$x \to -\infty$
$0 < \alpha_0 < \alpha_1 = 2,\ -1 < \beta < 1$	$0(-x^2)$	$0(-x^2)$
$0 < \alpha_0 < \alpha_1 < 2,\ -1 < \beta < 1$	$0(-\ln x)$	$0(-\ln \lvert x\rvert)$
$1 < \alpha_0 < \alpha_1 = 2,\ \beta = -1$	$0(-x^2)$	$0(\lvert x\rvert^{\alpha_0/\alpha_0-1})$
$1 < \alpha_0 < \alpha_1 < 2,\ \beta = -1$	$0(-\ln x)$	$0(\lvert x\rvert^{\alpha_0/\alpha_0-1})$
$1 = \alpha_0 < \alpha_1 = 2,\ \beta = -1$	$0(-x^2)$	$0(e^{(\pi/2)\lvert x\rvert})$
$1 = \alpha_0 < \alpha_1 < 2,\ \beta = -1$	$0(-\ln x)$	$0(e^{(\pi/2)\lvert x\rvert})$
	$x \to +\infty$	$x \downarrow 0$
$0 < \alpha_0 < 1 < \alpha_1 < 2,\ \beta = -1$	$0(-\ln x)$	$0(x^{\alpha_0/\alpha_0-1})$
$0 < \alpha_0 < \alpha_1 = 1,\ \beta = -1$	$0(-\ln x)$	$0(x^{\alpha_0/\alpha_0-1})$
$0 < \alpha_0 < \alpha_1 < 1,\ \beta = -1$	$0(-\ln x)$	$0(x^{\alpha_0/\alpha_0-1})$.

---

[*] This excludes the Cauchy ($\alpha = 1$, $\beta = 0$), which was examined in the text as a special case.

A.4 Skewness (β)

$$l(x) = \ln \frac{p(x;\alpha,\beta_1,\gamma=1,\delta=0)}{p(x;\alpha,\beta_0,\gamma=1,\delta=0)} \qquad -1 \leqq \beta_0 < \beta_1 \leqq 1$$

	$x \to +\infty$	$x \to -\infty$
$0 < \alpha < 2, -1 < \beta_0 < \beta_1 < 1$	$\ln (R_1/R_0) + 0(x^{-\alpha})$	$\ln (L_1/L_0) + 0(\lvert x\rvert^{-\alpha})$
$1 < \alpha < 2, -1 = \beta_0 < \beta_1 < 1$	$\ln (R_1/R_0) + 0(x^{-\alpha})$	$0(\lvert x\rvert^{\alpha/\alpha-1})$
$\alpha = 1, -1 = \beta_0 < \beta_1 < 1$	$\ln (R_1/R_0) + 0(x^{-\alpha})$	$0(e^{(\pi/2)\lvert x\rvert})$
$1 < \alpha < 2, -1 = \beta_0, 1 = \beta_1$	$0(-x^{\alpha/\alpha-1})$	$0(\lvert x\rvert^{\alpha/\alpha-1})$
$\alpha = 1, -1 = \beta_0, 1 = \beta_1$	$0(-e^{(\pi/2)\lvert x\rvert})$	$0(e^{(\pi/2)\lvert x\rvert})$

	$x \to +\infty$	$x \downarrow 0$
$0 < \alpha < 1, -1 = \beta_0 < \beta_1 < 1$	$\ln (R_1/R_0) + 0(x^{-\alpha})$	$0(x^{\alpha/\alpha-1})$

$$R_j = \sin \frac{\pi}{2} (\theta_j - \alpha),\ \tan (\pi\theta_j/2) = \beta_j \tan (\pi\alpha/2)$$

$$j = 0, 1$$

$$L_j = \sin \frac{\pi}{2} (\theta_j - \alpha),\ \tan (\pi\theta_j/2) = -\beta_j \tan (\pi\alpha/2).$$

REFERENCES

1. B. W. Stuck and B. Kleiner, "A Statistical Analysis of Telephone Noise," B.S.T.J., *53* (September 1974), pp. 1263–1320.
2. J. E. Evans, "Preliminary Analysis of ELF Noise," M.I.T. Lincoln Laboratory Tech. Note 1969-18 (26 March 1969), DDC AD691814.
3. P. Cootner ed., *The Random Character of Stock Market Prices*, Cambridge, Mass.: M.I.T. Press, 1964.
4. E. F. Fama, "The Behavior of Stock Market Prices," J. Bus., *38* (January 1965), pp. 34–105.
5. E. H. Lehmann, *Testing Statistical Hypotheses*, New York: Wiley, 1959.
6. P. Huber, "A Robust Version of the Probability Ratio Test," Ann. Math. Statist., *36* (December 1965), pp. 1753–1758.
7. R. M. Lerner and V. R. Algazi, "Binary Detection in White Non-Gaussian Noise," Available from University of Calif. (Davis) Elec. Eng. Dept.
8. J. E. Evans and A. S. Griffiths, "Design of a Sanguine Noise Processor Based Upon World-Wide Extremely Low Frequency (ELF) Recordings," IEEE Trans. Commun. Theory, *22* (April 1974), pp. 528–539.
9. J. Neveu, *Mathematical Foundations of the Calculus of Probability*, San Francisco; Holden-Day, 1965.
10. J. F. C. Kingman and S. J. Taylor, *Introduction to Measure and Probability*, Cambridge University Press, 1965.
11. J. L. Doob, *Stochastic Processes*, New York: Wiley, 1953.
12. L. Breiman, *Probability*, Reading, Mass.: Addison-Wesley, 1968.
13. B. V. Gnedenko and A. N. Kolmogorov, *Limit Distributions for Sums of Independent Random Variables*, Revised, Reading, Mass.: Addison-Wesley, 1968.
14. E. Lukacs, *Characteristic Functions*, 2nd ed., N. Y.: Hafner, 1968.
15. W. Feller, *An Introduction to Probability Theory and Its Applications*, Vol. II, N. Y.: Wiley, 1966.
16. M. Lipschutz, "On Strong Bounds for Sums of Independent Random Variables Which Tend to a Stable Distribution," Trans. Amer. Math. Soc., *81* (January–April, 1956), pp. 135–154.
17. I. A. Ibragimov and Yu. V. Linnik, *Independent and Stationary Sequences of Random Variables*, Groningen, Netherlands: Wolters-Nordhoff, 1971, pp. 47–76.

18. A. V. Skorokhod, "Asymptotic Formulas for Stable Distribution Laws," Transl. Math. Statist. Probl., *1*, Providence, R. I.: American Mathematical Society, 1961, pp. 157–161.
19. P. A. Frost, "Some Singular Estimation and Detection Problems for Conditionally Independent Increment Processes," p. 232, Proc. Ninth Annual Allerton Conf., 1971, University of Illinois.
20. M. Abramowitz and I. A. Stegun, *Handbook of Mathematical Functions*, New York: Dover, 1958.
21. L. J. Slater, *Confluent Hypergeometric Functions*, Cambridge University Press, 1965.
22. H. Dym and H. P. McKean, *Fourier Series and Integrals*, New York: Academic, 1972.
23. E. T. Copson, *Asymptotic Expansions*, Cambridge University Press, 1965.
24. E. J. Brody, "An Elementary Proof of the Gaussian Dichotomy Theorem," Z. Wahrschein. Verwandte Geb., *20* (November 1971), pp. 217–226.
25. C. E. Shannon, R. G. Gallager, and E. R. Berlekamp, "Lower Bounds to Error Probabilities for Coding on Discrete Memoryless Channels, I," Inform. Contr., *10* (January 1967), pp. 65–103.
26. H. Chernoff, "A Measure of Asymptotic Efficiency for Tests of a Hypothesis Based on a Sum of Observations," Ann. Math. Statist., *23* (December 1952), pp. 493–507.
27. C. H. Kraft, "Some Conditions for Consistency and Uniform Consistency of Statistical Procedures," University of Calif. (Berkeley), Publ. Statistics *2*, No. 6 (1955), pp. 125–142.
28. T. T. Kadota and L. A. Shepp, "On the Best Set of Linear Observables for Discriminating Two Gaussian Signals," IEEE Trans. Inform. Theory, *13* (April 1967), pp. 278–284.
29. M. E. Hellman and J. Raviv, "Probability of Error, Equivocation, and the Chernoff Bound," IEEE Trans. Inform. Theory, *16* (July 1970), pp. 368–372.
30. P. F. Byrd and M. D. Friedman, *Handbook of Elliptic Integrals for Engineers and Physicists*, 2nd ed., New York: Springer, 1971.
31. M.-J. Cross, "Tables of Finite Mean Nonsymmetric Stable Distributions as Computed From Their Convergent and Asymptotic Series," J. Statist. Computat. Simul., *3* (January 1974), pp. 1–27.
32. V. M. Zolotarev, "On Representation of Stable Laws by Integrals," Transl. Math. Statist. Prob., *6*, Providence, R. I.: American Mathematical Society, 1966, pp. 84–88.
33. W. H. DuMouchel, "Stable Distributions in Statistical Inference," Yale University, Ph.D. dissertation, 1971.
34. J. Cooley, P. Lewis, and P. Welch, "The Fast Fourier Transform Algorithm and Its Applications," IBM Research Paper RC-1743, 9 Feb. 1967.
35. F. L. Bauer, H. Rutishauser, and E. Stiefel, "New Aspects in Numerical Quadrature," pp. 199–218, Proc. Symp. App. Math., *15*, Am. Math. Soc., Providence, R. I., 1963.

Copyright © 1976 American Telephone and Telegraph Company
THE BELL SYSTEM TECHNICAL JOURNAL
Vol. 55, No. 8, October 1976
Printed in U.S.A.

Distinguishing Stable Probability Measures
Part II: Continuous Time

By B. W. STUCK

(Manuscript received April 1, 1976)

A sample function from one of two stable, stationary, independent-increment processes is observed for a finite time interval. For differing location, characteristic index, skewness, or scale, the probabilities measures induced by the process under either hypothesis are found to be mutually orthogonal. By suitably modifying the Lévy measure associated with each probability measure, continuous-time tests for differing characteristic indices, skewness, or scale parameters can be posed as nonsingular detection problems; distinguishing location remains a singular detection problem. For the nonsingular problems, the likelihood functional is found explicitly, and performance limitations are determined. As an alternative approach, the observed sample function is sampled at discrete time instants over a finite time interval, and the performance of log likelihood test is studied as a function of sample spacing with a fixed, total number of observations.

I. INTRODUCTION

In this paper, the work begun in Part I[1] on discrete-time hypothesis testing of stable probability measures is extended to continuous time. In contrast to the earlier work, analytic closed-form expressions are found for both the log likelihood functional and Chernoff-type upper and lower bounds on various error probabilities for the log likelihood test. As in Part I, the singular role played by the gaussian probability measure within the family of stable probability measures is emphasized, both in terms of the form of the log likelihood functional and the expressions for Chernoff-type bounds on error probabilities. The earlier work dealt with observing N samples from a stable process with one of two sets of parameters at time instants Δt apart; here, we fix the observation interval at duration T, and allow the number of observations to become infinite while the spacing between samples shrinks to zero ($N \to \infty$, $\Delta t \to 0$, such that $N \cdot \Delta t = T$).

Section II briefly reviews some properties of independent-increment processes and infinitely divisible distributions that were touched on in Part I. Section III draws on this tutorial material by considering an elementary hypothesis-testing problem for discriminating between two Poisson distributions with differing parameters.* Section IV briefly reviews some work by Newman[2,3] and Newman and the author[4,5] on calculating log likelihood functionals and Chernoff-type bounds on error probabilities for the path-space probability measures induced by independent-increment processes. These results are used in Section V to show if one or more of the parameters of the two stable-probability measures ($0 < \alpha < 2$) differs, then the two path-space measures are mutually orthogonal. Section VI develops one remedy to this so-called singular detection by modifying the Lévy measure of the two distributions to account for the real physical limitation that the process can only be observed to within an accuracy intrinsic in all measurement apparatus. Section VII considers a different but related issue, where the observed sample function is sampled at discrete time instants over a finite time interval, and the performance of the log likelihood test is studied as the sample spacing shrinks to zero; this allows one to trade off the sample spacing, or the rate at which samples are observed, for the total duration of the observation interval, or the total number of samples.†

The results developed here are novel in that one can immediately ascertain explicit bounds on the performance of the likelihood ratio test, while it is *not* clear how to do this after reading the literature (e.g., see Refs. 6 through 10). The method of proof here relies on probabilistic semigroup tools or on the explicit nature of the sample paths of an independent-increment process, and this appears to be novel when contrasted with such approaches as those referenced above.

II. MATHEMATICAL PRELIMINARIES ‡

Let $r_j(t)$ ($j = 0, 1$) be a scalar real-valued random process, with right continuous sample paths with left-hand limits everywhere defined. More explicitly, let $r_j(t)$ be the sum of a deterministic drift process, $\delta_j t$, and N independent Poisson processes (labeled by k, $1 \leqq k \leqq N$), where each Poisson process has rate λ_{jk} and hops of height h_{jk}. In words, $r_j(t)$ has simple jump discontinuities of heights h_{jk}, $1 \leqq k \leqq N$, at random times. The characteristic functional of

---

* The results in Sections III through VI were first announced in Proceedings of the 13th Annual Allerton Conference, University of Illinois, Champaign-Urbana, Illinois, October 1–3, 1975, pp. 234–239.

† The results in Section VII were first announced in Proceedings of the 1976 Johns Hopkins Conference on Information Sciences and Systems, Baltimore, Maryland, March 30–April 2, 1976, pp. 151–154.

‡ See Ref. 1, Section 3.1 and its list of references for much more information.

$r_j(t)$ is easily seen to be $(t > s)$,

$$E[e^{iv[r_j(t)-r_j(s)]}] = \exp\left\{(t-s)\left[iv\delta_j + \sum_{k=1}^{N} \lambda_{jk}(e^{ivh_{jk}} - 1)\right]\right\}\cdot$$

If we now pass to the limit of an infinite sum of Poisson processes, then the jump amplitudes $\{h_{jk}\}$ take on a continuum of values, and the characteristic functional becomes $(t > s)$

$$E[e^{iv[r_j(t)-r_j(s)]}] = \exp\left\{(t-s)\left[iv\delta_j + \int_{u\neq 0} (e^{ivu} - 1)d\nu_j(u)\right]\right\},$$

where ν is called the *Lévy measure* associated with the path-space measure of r_j, and generalizes the rate parameter set $\{\lambda_{jk}\}$; $(t-s)\int_{u\in A} d\nu_j(u)$ is the expected number of jumps of r_j whose amplitude falls in the set A, in a time interval of duration $(t-s)$. Lévy and Khinchin showed the following remarkable generalization of this heuristic development:

Theorem (Ref. 11, p. 76): *Let $r_j(t)$ be an R^n valued random process with independent increments. Then*

$$E(\exp\{iv^{TR}[r_j(t) - r_j(s)]\}) = \exp\left\{(t-s)\left[iv^{TR}\delta_j - \tfrac{1}{2}v^{TR}S_jv \right.\right.$$
$$\left.\left. + \int_{u\neq 0}\left(\exp(iv^{TR}u) - 1 - \frac{iv^{TR}u}{1+u^{TR}u}\right)d\nu_j(u)\right]\right\},$$

where $\delta_j \in R^n$, S_j is an $n \times n$ positive semidefinite matrix, and

$$\int_{u\neq 0} \frac{u^{TR}u}{1+u^{TR}u}\, d\nu_j(u) < \infty.$$

In words, any independent increment is the sum of three independent processes: (*i*) a purely deterministic drift process, completely specified by δ_j, (*ii*) a purely nondeterministic gaussian process with zero drift and almost surely continuous sample paths, specified by S_j, and (*iii*) a purely nondeterministic jump process with zero drift, a sum of independent Poisson processes with different rates and jump amplitudes, specified by ν_j.

Historically, the mathematical study of independent increment processes concentrated first on the purely gaussian case $(\nu_j = 0)$; then on the purely stable case $(S_j = 0,\ d\nu_j = d\mu(\theta)dr/r^{\alpha+1},\ 0 < \alpha < 2$, where μ is a positive measure on the unit sphere in R^n and $[r, \theta]$ are polar coordinates in $R^n)$; and lastly on the general case, building on the insight gained in the first two cases.[12] A second reason for wishing to study the gaussian and stable $(0 < \alpha < 2)$ probability measures is that they arise naturally from studying limiting distributions of suitably scaled and translated sums of independent, identically distributed, random variables in the central limit theorem, and have found application in modeling noise in communication channels such as telephone lines.[13] These two reasons, as well as others, provide the major impetus for the study to follow. The richness of the structure of independent increment processes suggests they may find more and more application in model building as their properties become more widely known.

III. DISTINGUISHING POISSON PROCESSES

In this section, $r_j(t)$ $(j = 0, 1)$ is observed on the interval $[0, T)$, and is the sum of a purely deterministic drift process (specified by δ_j) and a purely nondeterministic Poisson process (specified by rate λ_j and jump amplitude h_j). What is the log likelihood functional, and what is its performance?

First, suppose the Poisson process has the same jump amplitude under either hypothesis, but the drifts differ. Then it is straightforward to show that the two probability measures P_0 and P_1, associated with r_j under hypothesis H_j, are mutually orthogonal, so (*i*) observing r over any finite interval, the log likelihood functional takes on the value $+\infty$ if H_1 is true, $-\infty$ if H_0 is true, and (*ii*) the probability of incorrectly choosing one hypothesis when the other is true is zero. The reason for this is clear on physical grounds: the Poisson component has constant sample functions with simple jump discontinuities at random times, while the drift process is continuous with constant slope. Thus, ignoring the jumps in the observation process, the slope of the continuous part of the sample path is δ_j, and to discriminate between the two hypotheses is now trivial. From this point on, therefore, it is assumed $\delta_1 = \delta_0$ and, without loss of generality, set $\delta_j = 0$ $(j = 0, 1)$.

What if the Poisson processes have different jump amplitudes? As soon as one or more jumps occur, it is possible to discriminate perfectly between the two processes, since the size of the jump h_j is associated with hypotheses H_j. To avoid this indeterminancy, it is assumed from this point on $h_1 = h_0 = 1$. Thus, P_0 and P_1, the probability measures associated with H_j, are mutually absolutely continuous.

Lemma 1: Let r_j be as just defined. Let

$$P_j'\left[r_j\left(\frac{k+1}{n}T\right)\middle| r_j\left(\frac{k}{n}T\right)\right], \qquad 0 \leqq k \leqq n-1;\ j = 0, 1$$

denote the conditional probability of r_j at time $[(k+1)/n]T$, given r_j

at time $(k/n)T$. *Then* $[r_j(0) = 0$ a.s.; $j = 0, 1]$,

$$(i)\ \Lambda = \ln \frac{dP_1}{dP_0}(r) = \lim_{n\to\infty} \sum_{k=0}^{n-1} \ln \frac{P_1'}{P_0'}(r).$$

$$(ii)\ H_q(P_0, P_1) = \lim_{n\to\infty} [H_q(P_0', P_1')]^n.$$

Proof: The proof follows from standard limit theorems (Ref. 7, Lemma 1.1), Q.E.D.

We now explicitly evaluate the limits in Lemma 1:

Proposition 2: Given the conditions of Lemma 1,

$$(i)\ \Lambda = \int_0^T \left\{ -(\lambda_1 - \lambda_0) + \sum_{k=0}^{N_r} \left[\ln\left(\frac{\lambda_1}{\lambda_0}\right) \right] \delta(t - t_k) \right\} dt$$

$$= \int_0^T \left[-(\lambda_1 - \lambda_0)dt + \ln\left(\frac{\lambda_1}{\lambda_0}\right) dr_t \right],$$

where N_r is the a.s. finite number of time instants $\{t_k\}$ where r_t changes state.

$$(ii)\ H_q(P_0, P_1) = \exp\{-T[q\lambda_1 + (1 - q)\lambda_0 - \lambda_1^q\lambda_0^{1-q}]\}.$$

Proof:

(*i*) Given r_j at time $(k/n)T$, it will remain in that state in the next time interval (T/n) with probability $1 - \lambda_j T/n + o(T/n)$, and will increase by one with probability $\lambda_j(T/n) + o(T/n)$. The desired result now follows Lemma 1.

(*ii*) If r_j changes its state in the next time interval of duration (T/n), then

$$H_q(P_0', P_1') = \frac{T}{n}\lambda_1^q\lambda_0^{1-q} + o(T/n);$$

while if r_j stays in its present state in the next (T/n) time units, then

$$H_q(P_0', P_1') = 1 - \frac{T}{n}[q\lambda_1 + (1 - q)\lambda_0] + o(T/n).$$

$$\therefore\quad H_q(P_0', P_1') = \exp\left[-\frac{T}{n}(q\lambda_1 + (1 - q)\lambda_0 - \lambda_1^q\lambda_0^{1-q})\right] + o(T/n),$$

$$\therefore\quad H_q(P_0, P_1) = \exp\{-T[q\lambda_1 + (1 - q)\lambda_0 - \lambda_1^q\lambda_0^{1-q}]\},$$

where the last step follows from Lemma 1.

Q.E.D.

Recall from Part I that a crude bound on the total probability of error P_E for a log likelihood ratio test is provided by

$$\tfrac{1}{4}\min(\pi_1, \pi_0)H_{\frac{1}{2}}^2 \leqq P_E \leqq \sqrt{\pi_1, \pi_0}H_{\frac{1}{2}},$$

where π_j is the *a priori* probability hypothesis that j is true. Here,

$$H_{\frac{1}{2}} = \exp\left[-T(\sqrt{\lambda_1} - \sqrt{\lambda_0})^2/2\right]$$

and hence for fixed T, one would like to have the difference in the square roots of the rates as large as possible.

To gain further insight into $H_q(P_0, P_1)$, we rewrite it as the expectation of a third Poisson process. Let $x_q(t)$ be a Poisson process with rate $\lambda_1^q\lambda_0^{1-q}$, hops of height $+1$, and $x_q(0) = 0$ a.s. (intuitively, the probability measure P_q associated with x_q has support on the common support of P_0 and P_1).

Proposition 3:

$$H_q(P_0, P_1) = \int dP_q \exp\left\{-\int_0^T D[x_q(t)]dt\right\}$$
$$= E_{x_q}\left(\exp\left\{-\int_0^T D[x_q(t)]dt\right\}\right),$$
$$D(x_q) = q\lambda_1 + (1-q)\lambda_0 - \lambda_1^q\lambda_0^{1-q}.$$

Proof: The proof follows from the definition of D, P_q, and x_q.

Q.E.D.

To the best of our knowledge, this result is new, and will be generalized in the following section and elsewhere.[4,5] Its significance lies in the fact that there exists a large body of results in both the mathematics and physics literature for studying properties of expectations of multiplicative functionals of random processes, so called Feynman-Kac functionals; now we can immediately draw on this body of knowledge.

IV. DISTINGUISHING INDEPENDENT INCREMENT PROCESSES

In this section, the results of Section III are extended to arbitrary independent increment processes. Here, $r_t \in R^n$ is observed over $[0, T)$, and has one of two sets of parameters (δ_j, S_j, ν_j) $(j = 0, 1)$. As before, define for $0 < q < 1$,

$$dh_q(P_0, P_1) = \left(\frac{dP_1}{d\mu}\right)^q\left(\frac{dP_0}{d\mu}\right)^{1-q} d\mu,\ P_1, P_0 \ll \mu$$
$$H_q(P_0, P_1) = \int dh_q(P_0, P_1),$$

where H_q is the Kakutani product associated with P_0, P_1. Next, it is useful to define a nonnegative measure $j_q(\nu_0, \nu_1)$ [the generalization of the point measure at +1 with mass $q\lambda_1 + (1-q)\lambda_0 - \lambda_1^q\lambda_0^{1-q}$ in Section III],

$$dj_q(\nu_0, \nu_1) = q\,d\nu_1 + (1-q)\,d\nu_0 - dh_q(\nu_0, \nu_1),$$
$$J_q(\nu_0, \nu_1) = \int dj_q(\nu_0, \nu_1),$$

and J_q is nonnegative and may be infinite, since ν_0 or ν_1 or both may not be finite measures. If $J_q < \infty$, it is convenient to define

$$\delta_j' = \delta_j - \int_{u\neq 0} \frac{u}{1+u^{TR}u}\, d\nu_j(u),$$
$$\delta_q = q\delta_1 + (1-q)\delta_0 - \int_{u\neq 0} \frac{u}{1+u^{TR}u}\, dj_q(\nu_0, \nu_1).$$

Finally, if $S_1 = S_0 = S$, and $J_q < \infty$, a third independent increment process $x_q(t)$ is defined with parameters $[\delta_q, S, h_q(\nu_0, \nu_1)]$.

Theorem 4: For P_0 and P_1 not to be mutually orthogonal, it is necessary and sufficient for the following three conditions to hold:

(*i*) $J_q(\nu_0, \nu_1) < \infty$
(*ii*) $S_1 = S_0 = S \geqq 0$
(*iii*) $\delta_q \in$ *range* (S).

If these three conditions are satisfied, then

$$\text{(a)}\quad \Lambda(r_t) = \int_0^T \left[\int_{u\neq 0} \ln \frac{d\nu_1}{d\nu_0}(u)\, d_u r_t - \int_{u\neq 0} (d\nu_1 - d\nu_0)\, dt \right] + \delta_q^{TR} S^{-1}[r_T - j_T - \tfrac{1}{2}(\delta_0' + \delta_1')],$$

where $d_u r_t$ assigns a point mass at time instants where $r_t - r_{t-} = u$, i.e., where r_t hops with amplitude u, and j_t is the jump process component of r_t.

$$\text{(b)}\quad H_q(P_0, P_1) = \exp\left[-TJ_q(\nu_0, \nu_1) - \frac{T}{2} q(1-q)\delta_q^{TR} S^{-1}\delta_q \right].$$

Proof (*sketched*)*: The proof is broken into two parts, one part dealing with the jump process, the other with the gaussian process (including drift). The part dealing with the gaussian component is classical,[6] and yields conditions (*ii*) and (*iii*), above. The main method employed in showing condition (*i*) for the jump-process component is to approximate the jump process by a sum of independent Poisson processes with different rates and jump amplitudes. As more and more Poisson processes are included in this sum, it can be shown that the approxi-

---

* From a detailed proof in Ref. 5.

mation converges weakly to the actual jump process. The Kakutani inner product of the probability measures of the approximations is simply the product of the Kakutani inner product associated with Poisson processes of the same jump amplitude (but possibly different rates); again, the delicate part of the proof is to show this approximation converges to the actual Kakutani inner product of the path-space probability measures of the two independent increment processes.

The program is to use this theorem in the remainder of this paper to exhibit the log likelihood functional and ascertain bounds on its performance in hypothesis testing for stable processes. Skorokhod[7–9] has obtained conditions (*ii*) and (*iii*) in Theorem 2, and instead of condition (*i*) obtained two conditions which must hold:

$$\int_{|g-1|>\frac{1}{2}} (g-1)d\nu_0 < \infty \quad \text{and} \quad \int_{|g-1|\leqq\frac{1}{2}} (g-1)^2 d\nu_0 < \infty,$$

where $g = (d\nu_1/d\nu_0)$; it is easy to show these two requirements are equivalent to $J_{\frac{1}{2}}(\nu_0, \nu_1) < \infty$. Hence, these conditions appear simpler than those of Skorokhod. Moreover, it is obvious how to use J_q to determine performance limitations, while it is not obvious at first glance how to apply Skorokhod's work. Also, the method of proof is different and may be easier to follow.

Finally, it is instructive to rewrite H_q as a Feynman-Kac type of functional of x_q:

Proposition 5: Let x_q be a stationary independent increment process with parameters (δ_q, S, h_q) as defined previously. Then,

$$\begin{aligned} H_q(P_0, P_1) &= E_{x_q}\left[\exp\left(-\int_0^T D(x_q)dt\right)\right] \\ &= \int dP_q \exp\left[-\int_0^T D(x_q)dt\right], \end{aligned}$$

where

$$D(x_q) = q(1-q)\delta_q^{TR}S^{-1}\delta_q/2 + \int_{u\neq 0} dj_q.$$

Proof: The proof follows immediately from the definitions of D, x_q, P_q. Q.E.D.

Again, note that

$$D(x_{\frac{1}{2}}) = \frac{1}{2}\left[(\delta_q^{TR}/2)S^{-1}(\delta_q/2) + \int_{u\neq 0}\left(\sqrt{\frac{d\nu_1}{d\mu}} - \sqrt{\frac{d\nu_0}{d\mu}}\right)^2 d\mu\right], \ \nu_1, \nu_0 \ll \mu$$

can be immediately used to provide a crude upper and lower bound on the total probability of error. As in the Poisson case, one desires the differences in the square roots of the Lévy measures (suitably defined) as large as possible, for good performance.

V. DISTINGUISHING STABLE PROCESSES

Let $x_j(t)$ $(j = 0, 1)$ be a scalar real-valued representation of a stable $(0 < \alpha < 2)$, stationary, independent increment process, $t \in [0, T)$, with characteristic functional $[x_j(0) = 0$ a.s.; $j = 0, 1]$.[*]

$$E(e^{ivx_j(t)}) = \exp\left\{t\left[i\delta_j v + \int_{u\neq 0}\left(e^{ivu} - 1 - \frac{ivu}{1+u^2}\right)d\nu_j(u)\right]\right\}$$

$$\nu_j(u) = \begin{cases} \nu_j^- = c_-^j |u|^{-\alpha_j} & u < 0 \\ \nu_j^+ = -c_+^j u^{-\alpha_j} & u > 0. \end{cases}$$

Following Section IV, it is clear that $J_q(\nu_0, \nu_1)$ diverges (to $+\infty$), from simply substituting in the explicit form for ν_j and carrying out the calculations. Hence, P_0 and P_1 are mutually orthogonal if one or more of the parameters differ, the log likelihood functional is either $+\infty$ or $-\infty$ on hypothesis one or zero, respectively, and the probability of incorrectly choosing one hypothesis when the other is true is zero.

Since $J_q(\nu_0, \nu_1)$ diverges because ν_j diverges as $|u| \to 0$, this suggests that being able to observe the process perfectly, down to jumps of vanishingly small amplitudes, may be the mathematical reason for singular detection; but therein lies the flaw: it may well be physically impossible (the mathematical model is inadequate) to achieve this. Frost[10] apparently first popularized this idea in the engineering literature; here we reach the same conclusions by entirely different methods. Sections VI and VII deal with two distinct methods for overcoming these flaws in the mathematical model.

VI. DISTINGUISHING PSEUDO-STABLE PROCESSES

Let $x_j(t)$ $(j = 0, 1)$ be a scalar real-valued representation of a stationary independent increment process just as in Section V, except that the Lévy measure is now written as

$$\nu_j(u) = \begin{cases} c_-^j |u|^{-\alpha_j} & u < -L \\ \lambda^j(u) & -L < u < 0 \\ \lambda_+^j(u) & 0 < u < R \\ -c_+^j u^{-\alpha_j} & R < u, \end{cases}$$

where

$$\int_{-L}^{0-} \frac{u}{1+u^2}\, d\lambda_-^j(u) < \infty, \quad \int_{0+}^{R} \frac{u}{1+u^2}\, d\lambda_+^j(u) < \infty,$$

and

$$\delta_j' = \delta_j - \int_{u\neq 0} \frac{u}{1+u^2}\, d\nu_j(u).$$

---

[*] The case $\alpha = 2$ is well known[6–10] and, for brevity, is not included here.

λ^j_-, λ^j_+ are absolutely continuous with respect to Lebesgue measure, and ν_j is nondecreasing on $(-\infty, 0-)$, nonincreasing on $(0+, \infty)$. The limit, as both R and L approach zero, of a sequence of such processes can be shown to converge weakly to a stable process, and hence these processes are christened pseudo stable processes. Here L and R quantify that the fact that no negative jumps can be observed with amplitude less than L, no positive jumps can be observed with amplitude less than R. Both the properties of the sample functions and the one-dimensional distributions are radically different here from stable processes: (*i*) pseudo-stable process sample functions are of bounded variation w.p.1, with only finitely many nonzero jumps in any finite time interval; stable process sample functions are of either unbounded $(1 < \alpha < 2)$ or bounded $(0 < \alpha < 1)$ variation w.p.1, with the set of time instants at which nonzero jumps occur being dense in any finite time interval, and (*ii*) the set of one-dimensional distributions of pseudo-stable processes is clearly not closed under convolution, which was the defining property of stable distributions, but the asymptotic tail behavior is the same, since

$$\Pr\left[x_j(t = 1) > x\right] \sim 0\left(\int_x^\infty d\nu_j(u)\right),$$

$$\Pr\left[x_j(t = 1) < -x\right] \sim 0\left(\int_{-\infty}^{-x} d\nu_j(u)\right).$$

For this special case, it is straightforward to show that $J_q(\nu_0, \nu_1) < \infty$, and hence condition (*i*) of Theorem 2 is satisfied. However, δ_q is not in general in the range of $S(=0)$, and again singular detection is possible. The reason is clear on physical grounds (cf. Section III, the Poisson case): the slope of the sample paths of $x_j(t)$ is δ_j', ignoring the jump discontinuities, and hence it is trivial to discriminate between two pseudo-stable processes with different drifts. Two approaches are available: either let S be nonzero, which we do not pursue here because this seems ad hoc, having introduced L, R, already, or make the drifts match, $\delta_1' = \delta_0'$, which we assume from this point on.

The log likelihood functional is thus

$$\Lambda(r_t) = \int_0^T dt\left[\int_{-\infty}^{-L} \ln\,(d\nu_1/d\nu_0)dr_t + \int_R^\infty \ln\,(d\nu_1/d\nu_0)dr_t\right] + \int_0^T dt\left[\int_{-\infty}^{-L}(-d\nu_1 + d\nu_0) + \int_R^\infty(-d\nu_1 + d\nu_0)\right],$$

where, for simplicity, it was assumed

$$\lambda^j_- = c^j_- L^{-\alpha_j}, \quad \lambda^j_+ = -c^j_+ R^{-\alpha_j}.$$

As expected, the form of the log likelihood functional is quite sensitive to whether $\alpha = 2$ or $0 < \alpha < 2$ (e.g., see Refs. 7–10 for $\alpha = 2$).

To obtain upper and lower bounds on the probabilities of an error of the first or second kind, and on the total probability of error, the Kakutani inner product H_q must be calculated. Assuming $\lambda_-^j = c_-^j L^{\alpha_j}$, $\lambda_+^j = -c_+^j R^{-\alpha_j}$, the result is

$$
\begin{aligned}
H_q(P_0, P_1) &= \exp\left[-TJ_q(\nu_0, \nu_1)\right], \\
J_q(\nu_0, \nu_1) &= q(c_-^1 L^{-\alpha_1} + c_+^1 R^{-\alpha_1}) + (1 - q)(c_-^0 L^{-\alpha_0} + c_+^0 R^{-\alpha_0}) \\
&\qquad - \frac{(\alpha_0 c_-^0)^{1-q}(\alpha_1 c_-^1)^q}{q\alpha_1 + (1 - q)\alpha_0} L^{-q\alpha_1 - (1-q)\alpha_0} \\
&\qquad\qquad - \frac{(\alpha_0 c_+^0)^{1-q}(\alpha_1 c_+^1)^q}{q\alpha_1 + (1 - q)\alpha_0} R^{-q\alpha_1 - (1-q)\alpha_0}, \\
H_q(P_0, P_1) &= E_{x_q}\left\{\exp\left[-\int_0^T D(x_q)dt\right]\right\}, \\
D(x_q) &= J_q.
\end{aligned}
$$

In summary, discriminating between Wiener processes ($\alpha = 2$) with different variances leads to singular detection, while if the variances are identical then the detection problem is nonsingular.[6–10] Discriminating between stable processes ($0 < \alpha < 2$) with one or more different parameters leads to singular detection. If the Lévy measure is modified to be a finite measure, then if the drifts differ, singular detection occurs, while if the drifts are identical, then the detection problem is nonsingular.

VII. DISTINGUISHING SAMPLED STABLE PROCESSES

The previous sections show that it is quite easy to find examples of continuous time singular-detection problems. In this section, it is assumed that N samples of a stable process with one of two sets of parameters are observed, and we wish to study the effect of choosing the sample spacing and the total length of the observation interval on the Kakutani inner product H_q; the goal is to make H_q as small as possible.

Attention is confined solely to scalar processes from this point on. The distribution of $x_j[(k + 1)\Delta t] - x_j(k\Delta t)$ is given by $P_j(\Delta t; \delta_j, S_j, \nu_j)$. The Kakutani inner product of the new two discrete time distributions is

$$
H_q(T, \Delta t) = \left[\int (dP_1/d\mu)^q (dP_0/d\mu)^{1-q} d\mu\right]^{T/\Delta t}.
$$

For $\Delta t \downarrow 0$ or $T \to \infty$, with $(T/\Delta t) \equiv N$ fixed in both cases, fixed, that H_q can approach one, some number between zero and one [say

e^{-kN}, where $k = k(\delta_1, \delta_0, S_1, S_0, \nu_1, \nu_0)]$, or zero. It is obvious that if the two continuous time independent increment process path-space measures are *not* mutually orthogonal, then the only approach to reducing H_q is to fix Δt and increase T. However, if the two continuous time independent increment processes have mutually orthogonal path-space measures, then it is possible to reduce H_q by decreasing Δt with $(T/\Delta t)$ fixed. To state the result, a lemma is needed:

Lemma 6. If μ *is an infinitely divisible probability measure, with* $\nu(u) \sim 0(|u|^{-\alpha})$ *as* $|u| \to 0$, $0 < \alpha < 2$, *then*

$$\int \exp\,(ivx)d\mu(x) = \exp\,[-S|v|^{\alpha} + D(v)], \qquad 0 < \alpha \leqq 2,$$

where if

$$\delta - \int_{u \neq 0} \frac{u}{1 + u^2}\, d\nu(u) = 0,$$

then

$$\lim_{|v| \to \infty} D(v)/|v|^{\alpha} = 0, \qquad 0 < \alpha \leqq 2;$$

otherwise,

$$D(v) = iv\delta + D'(v), \qquad \lim_{|v| \to \infty} D'(v)/|v|^{\alpha} = 0, \qquad 1 \leqq \alpha \leqq 2.$$

Proof: The proof follows from properties of ν, and is found in Ref. 5.
Q.E.D.

The main result can now be stated:

Proposition 7: For $0 < q < 1$, with a zero-drift gaussian component ($\alpha = 2$) present in either x_1, or x_0, or both, if $(T/\Delta t)$ is fixed

$$\lim_{\Delta t \downarrow 0} H_q(T, \Delta t) =$$

(a) 1 iff $S_1 = S_0 > 0$.
(b) Exp $(-kN)$ iff $S_1 \neq S_0$, $S_1 > 0$, and $S_0 > 0$,
$k = \ln\,[q(S_0/S_1)^{1-q} + (1 - q)(S_1/S_0)^q]^{\frac{1}{2}}$.
(c) 0 iff $S_1 \neq 0 = S_0$ or $S_1 = 0 \neq S_0$.

If a zero-drift nongaussian stable $(0 < \alpha < 2)$ component is present in either r_1 or r_0, then

$$\lim_{\Delta t \downarrow 0} H_q(T, \Delta t) =$$

(d) 1 iff $\alpha_1 = \alpha_0$, $S_1 = S_0$.
(e) Exp $(-kN)$ iff $\alpha_1 = \alpha_0$, $S_1 \neq S_0$, $S_1 > 0_1$, $S_0 > 0$.
(f) 0 iff $\alpha_1 \neq \alpha_0$.

Proof: The proof follows from scaling arguments, and is found in Ref. 5.

Q.E.D.

If a gaussian component is present in both processes, then decreasing the sampling interval has no effect on decreasing H_q, and T must be increased to decrease H_q. However, if no gaussian component is present in one or the other of the processes, or if $\alpha_1 \neq \alpha_0$, then it is possible to decrease H_q by decreasing Δt with $(T/\Delta t)$ fixed.

Analogous results for $T \rightarrow \infty$ with $(T/\Delta t)$ fixed are presented in Ref. 5, as well as some results on the rate at which H_q approaches its limiting value.

Related work on nonuniformly sampling a continuous time independent increment process with one of two drift parameters is available in the literature.[14] A typical result is that sampling two stable processes with identical characteristic index, skewness, and scale, but differing drifts, is a singular detection problem if

$$\sum_{j=0}^{\infty} (t_{j+1} - t_j)^{2[1-(1/\alpha)]}$$

diverges, where $\{t_j\}$ are the sampling epochs,

$$\sum_{j=0}^{\infty} (t_{j+1} - t_j) = T.$$

Thus, spacing the samples apart by $t_{j+1} - t_j \propto j^{-m} (m > 1)$ results in singular detection, but $(t_{j+1} - t_j) \propto e^{-mj} (m > 0)$ may not.

VIII. ACKNOWLEDGMENTS

The author gratefully acknowledges many enlightening conversations with P. A. Frost concerning continuous time detection problems.

REFERENCES

1. B. W. Stuck, "Distinguishing Stable Probability Measures, Part I: Discrete Time," B.S.T.J., this issue.
2. C. M. Newman, "The Inner Product of Path Space Measures Corresponding to Random Processes With Independent Increments," Bull. Amer. Math. Soc., *78*, No. 2 (March 1972), pp. 268–272.
3. C. M. Newman, "On the Orthogonality of Independent Increment Process," *Topics in Probability Theory*, ed. D. W. Stroock and S. R. S. Varadhan, Courant Institute of Mathematical Sciences, New York University, 1973, pp. 93–111.
4. C. M. Newman and B. W. Stuck, "Chernoff Bounds for Discriminating Between Two Markov Processes," unpublished paper.
5. C. M. Newman and B. W. Stuck, "On the Orthogonality of Path Space Measures of Infinitely Divisible Processes," unpublished paper.
6. R. H. Cameron and W. T. Martin, "The Behavior of Measure and Measurability Under Change of Seal in Wiener Space," Bull. Amer. Math. Soc., *53*, No. 3 (June 1947), pp. 130–137; "Transformations of Wiener Integrals Under Translations," Ann. Math., *45*, No. 3 (June 1944), pp. 386–396.

7. A. V. Skorokhod, "On the Differentiability of Measures Which Correspond to Stochastic Processes: I. Processes Independent Increments," Theory Probab. Appl., *2*, No. 2 (April 1957), pp. 407–432.
8. A. V. Skorokhod, *Studies in the Theory of Random Processes*, Reading, Mass.: Addison-Wesley, 1961.
9. I. I. Gikhman and A. V. Skorokhod, "On the Densities of Probability Measures in Function Space," Russ., Math. Surv., *21*, No. 1 (January 1966), pp. 83–156.
10. P. A. Frost, "Some Singular Estimation and Detection Problems for Conditionally Independent Increment Processes," Proceedings of the Ninth Annual Allerton Conference, University of Illinois, Champaign-Urbana, Illinois, 1971, p. 232.
11. B. V. Gnedenko and A. N. Kolmogorov, *Limit Distributions for Sums of Independent Random Variables* (revised), Reading, Mass.: Addison-Wesley, 1968.
12. S. J. Taylor, "Sample Path Properties of Processes With Stationary Independent Increments," in *Stochastic Analysis*, ed. D. G. Kendall and E. F. Harding, New York: Wiley, 1973, pp. 387–414.
13. B. W. Stuck and B. Kleiner, "A Statistical Analysis of Telephone Noise," B.S.T.J., *53*, No. 7 (September 1974), pp. 1263–1320.
14. L. A. Shepp, "Distinguishing a Sequence of Random Variables From a Translate of Itself," Ann. Math. Statist., *36*, No. 4 (August 1965), pp. 1107–1112.

THE BELL SYSTEM TECHNICAL JOURNAL
Vol. 55, No. 8, October 1976
Printed in U.S.A.

Alarm Statistics of the Violation Monitor and Remover

By G. S. FANG

(Manuscript received March 1, 1976)

Four of the Bell System digital transmission systems, T1 Outstate, T2, 3A-RDS (radio system at T3 rate), and T4M, have violation monitor and removers (VMRs) located at the receiving-end maintenance offices. Among other things, they monitor the lines, remove violations in the pulse transmission code, and generate alarms to initiate maintenance actions. This paper investigates the alarm statistics of the four types of VMR under the assumption that the information bits are statistically independent. It is found that all the VMRs have very sharp alarm thresholds. The results of the T4M VMR are presented in detail. Curves are given to show the various statistics obtained.

I. INTRODUCTION

Digital transmission systems serving large numbers of message channels should be continuously monitored to check the quality of service. This can be achieved by putting monitors at maintenance offices along the digital transmission route. An ideal monitor should provide the exact number of errors made in transmission. Since line errors cannot be directly measured in service, alternative criteria have to be used for performance monitoring. For instance, bipolar coding[1] can be employed so that the monitor can detect line errors from the violations of the coding sequence, and parity bits can be inserted into the transmitted digital stream so that the monitor can detect line errors if the received parity bits differ from those calculated from the received signal. The monitor generates alarms to initiate maintenance actions when the detected violation rates are greater than a predetermined threshold.

In some cases the digital stream has a periodic, identifiable pulse sequence called "frame format" to which the monitor must synchronize before it can detect violations. The monitor is said to be in-frame when it recognizes the location of the frame-pulse sequence. High line-error rates may alter the frame pulses such that they are unrecognizable by the monitor, which is then said to be out-of-frame. The in-frame condition is necessary to identify the various signal components that are multiplexed to form the digital stream. The monitor removes all violations detected so that violations do not propagate beyond the maintenance office; hence, the name "violation monitor and remover" (VMR) was designated. Removal of a violation is not an attempt to correct the line error. It is perfomed to guarantee that the VMR output is violation-free so that if an alarm condition exists, it will not propagate to the next maintenance office. The VMR performs other functions as well. If it is out-of-frame, a pseudorandom signal with proper frame format will replace the received digital stream at the VMR output in order to prevent alarm propagation.

Four of the Bell System digital transmission systems, T1 Outstate, T2, 3A-RDS (radio system at T3 rate), and T4M have VMRs located at the receiving-end maintenance offices. The T1 Outstate system uses bipolar coding. The T2 system utilizes B6ZS[1] (bipolar with six zeros extraction) coding. Both the 3A-RDS and the T4M systems employ added parity bits for performance monitoring. The VMR for each system has its own alarm rules. The durations of time for alarm generation and alarm release at various error rates are important system parameters. This paper investigates the alarm statistics of the four types of VMR under the assumption that the information bits are statistically independent; i.e., each bit is a Bernoulli trial. The derivations for the T4M VMR[2] are presented in detail in Section II. Those related to the other VMRs are discussed in Appendix A. Section III discusses some of the results obtained and their significance in digital transmission systems.

II. THE T4M VMR

2.1 Alarm strategy

The T4M digital transmission line[2] has a transmission rate of 274 megabits per second (Mb/s) with the information transmitted in a binary format. Its frame format[3] contains 196 bits of which 192 are information bits and 4 are housekeeping bits. One of the latter is a parity bit used to check the 192 information bits. The alarm strategy of the VMR at low-parity violation rates is implemented in the following manner. The first single parity violation that is observed triggers a 100-ms timer and a counter. If the counter accumulates more than 31 parity violations before the 100-ms measuring timer times out, a 3-ms waiting timer is immediately triggered. At the end of 3 ms, another 100-ms timer is triggered and the counter starts counting again. During this second 100-ms period, if the counter overflows; i.e., it accumulates more than 31 violations, a VMR alarm is generated immediately. The 3-ms waiting timer is employed so that a short burst of errors will not cause an alarm. Since the transmission rate is 274 Mb/s and violation is checked once every 196 bits, the alarm threshold violation rate is set at

$$\frac{31 \times 196}{2.74 \times 10^{8} \times 0.1} = 0.222 \times 10^{-3}.$$

It will be shown in the next section that this violation rate corresponds to an error rate of approximately 1.1×10^{-6}.

To avoid oscillatory alarms near the threshold violation rate, hysteresis is designed into the VMR alarm system. A 1-second release timer is used to measure the violation rate when the VMR is in the alarm state. The release timer is free-running and is not synchronized to the VMR alarm. The alarm is released only after a full duration of the release timer is passed and the 31-violation counter does not overflow. Thus, whenever an alarm is generated, it will last at least 1 second. This produces a release-error-rate threshold of about 1.1×10^{-7}.

When the VMR is out-of-frame for 0.5 ms, a pseudorandom signal with the proper frame format is switched in to provide a violation-free output. As soon as the VMR is back in-frame, the violation counter is reset and starts counting until the 1-second free-running release timer times out. If the counter does not overflow, the pseudorandom signal is then switched out. Thus, after a failure is restored, it takes anywhere from 0 to 1 second to switch out the pseudorandom signal.

2.2 Bit error rate versus parity violation rate

Since the digital transmission line performance objective is usually set in terms of the bit error rate, which cannot be directly measured in service, it is desirable to establish the relationship between the parity-violation rate and the bit-error rate. Let l be the number of information bits contained in each parity check. Then,

$$\begin{aligned} P\{\text{parity violation}\} = {} & P\{\text{odd number of bit errors in } l \text{ bits}\} \\ & \cdot P\{\text{the parity bit is correct}\} \\ & + P\{\text{even number of bit errors in } l \text{ bits}\} \\ & \cdot P\{\text{the parity bit is in error}\}. \end{aligned} \tag{1}$$

In what follows all random variables are in boldface type. Let the bit-error rate and the parity-violation rate be represented by $\boldsymbol{\varepsilon}$ and $\boldsymbol{v}$, respectively. For each realization of ϵ, (1) can be written as

$$v = (1 - b_l)(1 - \epsilon) + b_l \epsilon, \tag{2}$$

where b_l denotes the probability of having an even number of bit errors in l information bits. This event occurs if a correct first bit is followed by an even number of bit errors or if an incorrect first bit is followed by an odd number of bit errors. Therefore, for $l \geqq 1$,

$$b_l = (1 - \epsilon)b_{l-1} + \epsilon(1 - b_{l-1}), \qquad b_0 = 1. \tag{3}$$

Define the generating function[4]

$$B(S) = \sum_{l=0}^{\infty} b_l S^l \quad -1 < S < 1. \tag{4}$$

Multiplying (3) by S^l and adding over $l = 1, 2, \cdots$, we obtain

$$B(S) - 1 = (1 - \epsilon)SB(S) + \epsilon S(1 - S)^{-1} - \epsilon SB(S) \tag{5}$$

or

$$B(S) = \tfrac{1}{2}\{(1 - S)^{-1} + [1 - (1 - 2\epsilon)S]^{-1}\}. \tag{6}$$

Expanding into geometric series, we get

$$b_l = \frac{1 + (1 - 2\epsilon)^l}{2}, \tag{7}$$

which is equivalent but preferable to

$$b_l = \binom{l}{0}\epsilon^0(1 - \epsilon)^l + \binom{l}{2}\epsilon^2(1 - \epsilon)^{l-2} + \cdots.$$

Substituting (7) into (2)

$$v = \frac{1 - (1 - 2\epsilon)^l}{2} \times (1 - \epsilon) + \frac{1 + (1 - 2\epsilon)^l}{2} \times \epsilon. \tag{8}$$

Equation (8) establishes the relationship between the parity-violation rate and the bit-error rate. When $l\epsilon \ll 1$, it is easy to see that

$$v \approx (l + 1)\epsilon. \tag{9}$$

In the T4M frame format, $l = 192$. Therefore,

$$v \approx 193\epsilon. \tag{10}$$

Equation (10) is intuitively obvious because only errors occurring in the 192 information bits and the parity bit are counted by the VMR. Since a parity check is made every 196 bits, let $\epsilon' = v/196$, ϵ' can be considered as the measurable bit-error rate. It differs from ϵ by about 1.5 percent when (10) holds.

Figure 1 plots the parity violation rate versus the bit error rate based on (8) with $l = 192$, assuming the VMR stays in frame. We see that for bit-error rates below 10^{-3}, there is almost a one-to-one correspondence between a bit error and a parity violation. Above 10^{-3}, the VMR may go out of frame.

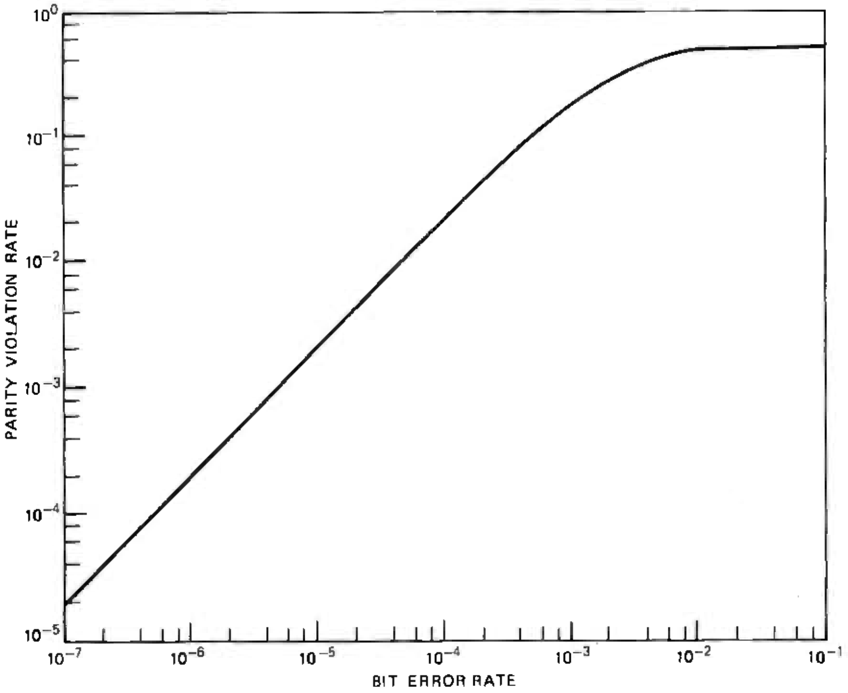

Fig. 1—Parity-violation rate vs bit-error rate.

In this paper, only low-parity-violation rates are being studied. Thus, ϵ will be used in place of ϵ' for simplicity.

2.3 Statistics of the alarm interval

Let γ represent the transmission rate, $\mathbf{N}$ the number of independent violations incurred, and $\mathbf{T}$ the time spent to count the violations. By the Bernoulli trial assumption,

$$P\{\mathbf{N} = n \mid \mathbf{T} = t, \boldsymbol{\varepsilon} = \epsilon\} = \binom{\gamma t}{n} \epsilon^{n}(1 - \epsilon)^{\gamma t - n}. \tag{11}$$

In this paper, only conditional distributions are discussed in most cases. For simplicity, conditions such as $\boldsymbol{\varepsilon} = \epsilon$, $\mathbf{N} = n$, and $\mathbf{T} = t$ are not expressed explicitly when they are understood.

Since γt is large, by De Moivre-Laplace limit theorem, a normal approximation to the binomial distribution is applicable.

$$P\{\mathbf{N} \geqq n\} \approx 1 - \Phi\left(\frac{n - \gamma t \epsilon}{\sqrt{\gamma t \epsilon(1 - \epsilon)}}\right), \tag{12}$$

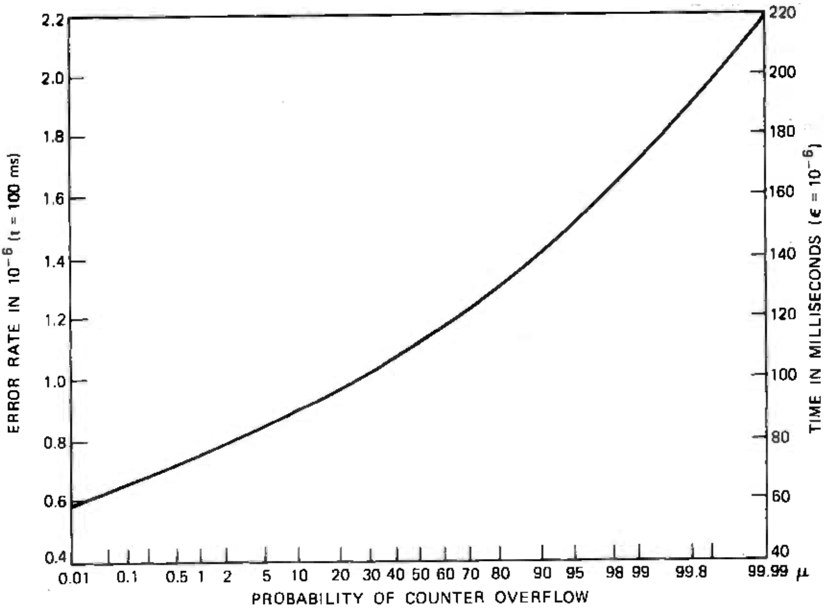

Fig. 2—Probability of counter overflow vs bit-error rate and time.

where

$$\Phi(x) = \int_{-\infty}^{x} \frac{1}{\sqrt{2\pi}} e^{-t^2/2} dt \tag{13}$$

is the cumulative normal distribution. Let

$$\mu = P\{\mathbf{N} \geqq n\}, \tag{14}$$

μ is the probability of counter overflow given an error rate and a fixed timer. Figure 2 shows, on a probability scale, this probability as a function of the bit-error rate for t_0 = 100 ms. The same curve with a different ordinate also shows the probability as a function of time for $\epsilon = 10^{-6}$. It can be seen that when the error rate varies from $\epsilon_0/2$ to $2\epsilon_0$, the probability of counter overflow varies from 0.0001 to 0.9999. Thus, the threshold is very "hard."

Let M be the random variable such that the VMR alarm is generated at the Mth measuring period. Each period is 100 ms if the counter does not overflow. It is desirable, then, to determine the probability p_m, $m = 0, 1, 2, \cdots$, that the VMR will generate an alarm at the mth measuring period, given $\mathbf{T} = t$ and $\boldsymbol{\varepsilon} = \epsilon$. If 1 represents the event that during a measuring interval the counter overflows and 0 represents the opposite, the m periods must be of the form

$$\underbrace{X\ X\ X \cdots X}_{m-3}\ 0\ 1\ 1,$$

where the sequence of $m - 3$ Xs does not have any 1 1 pair within it. Hence,

$$p_m = P\{\mathbf{M} = m\} \tag{15}$$

$$= P\{1\ 1 \text{ does not occur in a sequence of length } m - 3\} \cdot p\{011\}$$

$$= \left(1 - \sum_{i=0}^{m-3} p_i\right)(1 - \mu)\mu^2. \tag{16}$$

By definition, $p_0 = p_1 = 0$, $p_2 = \mu^2$, and $p_3 = (1 - \mu)\mu^2$. Denote

$$q_m = P\{\mathbf{M} > m\}$$

$$= 1 - \sum_{i=0}^{m} p_i, \tag{17}$$

then

$$p_m = q_{m-3}(1 - \mu)\mu^2. \tag{18}$$

Define the generating functions as

$$P(S) = \sum_{k=0}^{\infty} p_k S^k \qquad -1 \leqq S \leqq 1 \tag{19}$$

$$Q(S) = \sum_{k=0}^{\infty} q_k S^k \qquad -1 < S < 1. \tag{20}$$

Then,

$$(1 - S)Q(S) = 1 - P(S), \tag{21}$$

as can be seen by comparing the coefficients of any S^k terms on each side. From (19), (18), and (20)

$$P(S) = \mu^2 S^2 + (1 - \mu)\mu^2 S^3 Q(S). \tag{22}$$

Equations (21) and (22) give

$$P(S) = \frac{\mu^2 S^2 (1 - \mu S)}{1 - S + \mu^2 (1 - \mu) S^3}. \tag{23}$$

From (23), the statistics of **M** can be derived. For instance, the mean and the variance are

$$E\{\mathbf{M}\} = \sum_{m=0}^{\infty} m p_m$$

$$= \lim_{S \to 1} P'(S)$$

$$= \frac{1 + \mu}{\mu^2}. \tag{24}$$

$$\operatorname{Var}\{\mathbf{M}\} = \lim_{S\to 1}[P''(S) + P'(S) - P'^2(S)]$$

$$= \frac{(1-\mu)(1+3\mu+\mu^2)}{\mu^4}. \tag{25}$$

Higher-order statistics of **M** can be similarly obtained. At the threshold error rate, ϵ_0, $\mu = \frac{1}{2}$, $E\{\mathbf{M}\} = 6$. Thus, the expected alarm time is approximately 600 ms. The threshold variance is 22, which is quite large.

Two standard methods are available to evaluate the probability coefficients p_m, $m = 1, 2, \cdots$. The first one is

$$p_m = \lim_{S\to 0} \frac{P^{(m)}(S)}{m!} \qquad m = 0, 1, 2, \cdots.$$

The second one is through partial fraction expansion of (23). Both methods require extremely tedious derivations. A simple alternative is presented in Appendix B which first expands the denominator of (23) as follows

$$\frac{1}{1 - S + (1-\mu)\mu^2 S^3} = \sum_{i=0}^{\infty} C_i S^i \tag{26}$$

with

$$C_0 = C_1 = C_2 = 1,$$

and

$$C_i = C_{i-1} - (1-\mu)\mu^2 C_{i-3} \qquad i \geqq 3. \tag{27}$$

From (19), (23), (26), and (27)

$$p_m = \mu^2 C_{m-2} - \mu^3 C_{m-3} \qquad m \geqq 3. \tag{28}$$

Equations (27) and (28) provide an attractive way to evaluate the probability coefficients p_m's. What is more, p_m can be obtained without first calculating p_{m-1}, p_{m-2}, etc. It is interesting to note that for any error rate,

$$p_2 = \mu^2$$
$$p_3 = p_4 = (1-\mu)\mu^2$$
$$p_m > p_{m+1} \qquad m \geqq 4.$$

Thus, the probability that the VMR will generate an alarm during the second measuring period is always the largest, regardless of the error rate. The probability decreases monotonically at later measuring periods.

The cumulative distribution function of $\mathbf{M}$ is

$$F_{\mathbf{M}}(m) = P\{\mathbf{M} \leqq m\}$$

$$= \sum_{k=1}^{m} p_k.$$

Since the duration of each measuring period is not greater than $t_0 = 100$ ms, the length of the timer,

$$P\{\text{VMR has generated an alarm in } mt_0 \text{ ms}\} \geqq \sum_{k=0}^{m} p_k.$$

This equation can be used to plot the lower bound of the alarm probability as a function of time.

2.4 Distribution of violation measuring time

The distribution of the measuring time $\mathbf{T}$, assuming $\mathbf{N} = n$ and $\boldsymbol{\varepsilon} = \epsilon$, is considered next. If we let $\mathbf{Y}$ be the number of error bits prior to the nth error, then $\mathbf{Y}$ has the negative binomial distribution

$$P\{\mathbf{Y} = y\} = \binom{y + n - 1}{n - 1} \epsilon^n (1 - \epsilon)^y.$$

The time elapsed for the nth error to occur,

$$\mathbf{T} = \frac{\mathbf{Y} + n}{\gamma},$$

has the probability-density function (PDF)

$$P\{\mathbf{T} = t\} = \gamma \binom{\gamma t - 1}{n - 1} \epsilon^n (1 - \epsilon)^{\gamma t - n}. \tag{29}$$

Equation (29) is the distribution of the discrete violation measuring time $\mathbf{T}$ given that $\mathbf{N} = n$ and $\boldsymbol{\varepsilon} = \epsilon$. The T4M VMR has the additional condition $\mathbf{T} \leqq t_0 = 100$ ms; i.e., each measuring period is no greater than 100 ms. Let this censored random variable be denoted by $\mathbf{T}_c$. It is now desirable to find the distribution of $\mathbf{T}_c$, given that $\mathbf{N} = n$, $\boldsymbol{\varepsilon} = \epsilon$, and $\mathbf{T}_c \leqq t_0$. Unfortunately, this task is difficult to perform in the discrete sample space. However, since each information bit is 3.65 ns long while the $\mathbf{T}_c$ of interest is in milliseconds, the discrete censored random variable can be considered continuous for ease of calculation. From the Poisson theorem, (11) can be approximated by the Poisson distribution

$$P\{\mathbf{N} = n\} = \frac{e^{-\gamma \epsilon t}(\gamma \epsilon t)^n}{n!}. \tag{30}$$

Let $\mathbf{Y}_i$, $i = 1, 2, \cdots, n$ represent the time from the $(i-1)$th error to the ith error, then its PDF is given by

$$f_{\mathbf{Y}_i}(t) = \gamma \epsilon e^{-\gamma \epsilon t}.$$

Through the use of the characteristic functions, it is easy to see that the sum

$$\mathbf{T} = \sum_{i=1}^{n} \mathbf{Y}_i$$

has the gamma distribution

$$f_{\mathbf{T}}(t) = \frac{(\epsilon\gamma)^n}{(n-1)!} t^{n-1} e^{-\epsilon\gamma t} \qquad 0 \leqq t < \infty.$$

By successive integration by parts, it can be shown that

$$\int_{t_0}^{\infty} f_{\mathbf{T}}(t) dt = e^{-\epsilon\gamma t_0} \sum_{k=0}^{n-1} \frac{(\epsilon\gamma t_0)^k}{k!}.$$

Thus, the censored random variables $\mathbf{T}_c$ has the PDF

$$f_{\mathbf{T}_c}(t) = \begin{cases} f_{\mathbf{T}}(t) + \delta(t - t_0) e^{-\epsilon\gamma t_0} \displaystyle\sum_{k=0}^{n-1} \frac{(\epsilon\gamma t_0)^k}{k!} & t \leqq t_0 \\ 0 & t > t_0, \end{cases} \tag{31}$$

where $\delta(t - t_0)$ is the delta function. Its characteristic function $T(\omega)$ is

$$T_c(\omega) = \frac{(\epsilon\gamma)^n}{(\epsilon\gamma - j\omega)^n} \left(1 - e^{-(\epsilon\gamma - j\omega) t_0} \sum_{k=0}^{n-1} \frac{(\epsilon\gamma - j\omega)^k t_0^k}{k!}\right) + e^{-(\epsilon\gamma - j\omega) t_0} \sum_{k=0}^{n-1} \frac{(\epsilon\gamma t_0)^k}{k!}.$$

The mean η_{t_c} is given by

$$\eta_{t_c} = \left.\frac{dT_c(\omega)}{jd\omega}\right|_{\omega=0} = \frac{n}{\epsilon\gamma} - \frac{1}{\epsilon\gamma} e^{-\epsilon\gamma t_0} \sum_{k=1}^{n} \frac{k(\epsilon\gamma t_0)^{n-k}}{(n-k)!}. \tag{32}$$

The variance $\sigma_{t_c}^2$ can be evaluated similarly. The first term on the right of (32) is the mean value of $\mathbf{T}$. The second term is present because of the additional restriction $\mathbf{T} \leqq t_0$. At the alarm-error-rate threshold, $\eta_{t_c} \approx 97$ ms, $n/\epsilon\gamma = 100$ ms, the contribution of the second term is about 3 ms.

2.5 Distribution of the alarm time

Let $\mathbf{T}_0$ represent the time it takes the VMR to generate an alarm at a given error rate. It is desired to find the PDF of $\mathbf{T}_0$. Let $\mathbf{T}_i$, $i = 1, 2, \cdots, \mathbf{M}$, represent the time from the $(i-1)$th to the ith measuring interval, neglecting the 3-ms waiting time. The PDF of $\mathbf{T}_i$ is given in (31). The alarm time is then

$$\mathbf{T}_0 = \sum_{i=1}^{\mathbf{M}} \mathbf{T}_i.$$

Note that $\mathbf{T}_0$ is the sum of a random number of random variables.[4,5] Through the use of conditional probability, since $\mathbf{M}$ and $\mathbf{T}_i$'s are independent, the PDF of the random sum has a compound distribution

$$f_{\mathbf{T}_0}(t) = \sum_{m=0}^{\infty} p_m f_{\mathbf{T}_c}^{(m)}(t),$$

where p_m is given in (28) and $f_{\mathbf{T}_c}^{(m)}(t)$ is the m-fold convolution of $f_{\mathbf{T}_c}(t)$ with itself. The characteristic function of $\mathbf{T}_0$ is

$$T_0(\omega) = \sum_{m=0}^{\infty} p_m [T_c(\omega)]^m. \tag{33}$$

The right side of (33) is the Taylor expansion of $P(S)$ obtained in (23) with S replaced by $T_c(\omega)$. Thus,

$$T_0(\omega) = P[T_c(\omega)]. \tag{34}$$

The mean and the variance of $\mathbf{T}_0$ are

$$\begin{aligned} \eta_{t_0} &= \frac{1+\mu}{\mu^2}\,\eta_{t_c} \\ \sigma_{t_0}^2 &= \frac{1+\mu}{\mu^2}\,\sigma_{t_c}^2 + \frac{(1-\mu)(1+3\mu+\mu^2)}{\mu^4}\,\eta_{t_c}^2, \end{aligned} \tag{35}$$

where η_{t_c} is given in (32). Equation (35) is used to plot Fig. 3 which shows the mean alarm time versus the error rate. It can be seen that the mean alarm time decreases very fast as the error rate increases. The total alarm probability after time t is

$$\begin{aligned} P\{\mathbf{T}_0 \le t\} &= \int_0^t f_{\mathbf{T}_0}(t)dt \\ &= \sum_{m=0}^{\infty} p_m \int_0^t f_{\mathbf{T}_c}^{(m)}(t)dt. \end{aligned} \tag{36}$$

2.6 Waiting time distribution

In the above analyses, the 3-ms waiting intervals have not been taken into account. The waiting timer is triggered after each counter overflow. The distribution of the waiting periods is studied next. Let $\mathbf{W}$ be the number of times the waiting timer is triggered before a VMR alarm is generated, assuming that $\mathbf{M} = m$. The last three measuring periods before a VMR alarm should be 011 [notations are defined before (15)] and the waiting timer is definitely triggered once. Let

A_l = the event that 11 does not occur in l measuring intervals.

This event occurs if the counter does not overflow in the first measuring interval, followed by the event A_{l-1}, or the counter overflows in the

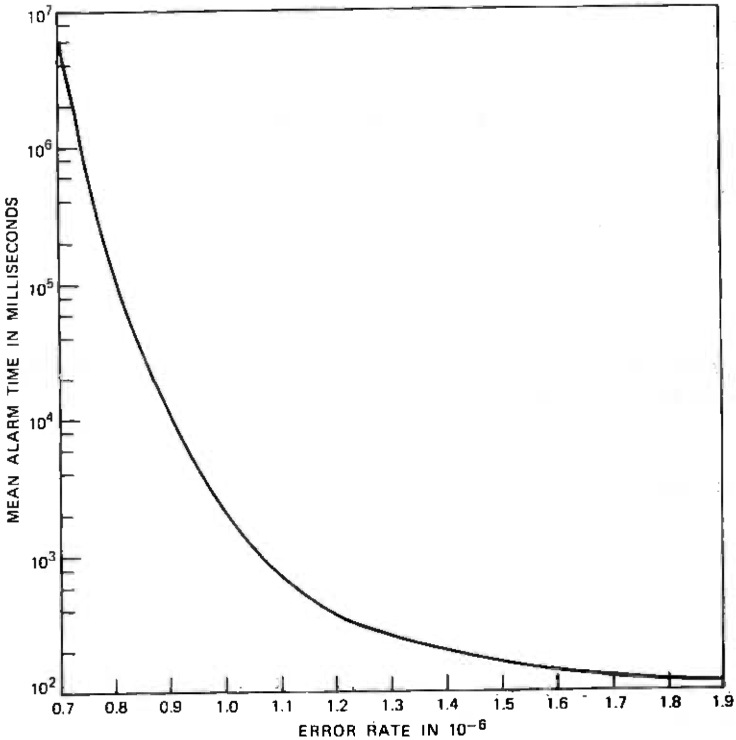

Fig. 3—Expected alarm time vs error rate.

first interval but not the second interval, followed by the event A_{l-2}. Let

$$a_l = P\{A_l\},$$

then

$$a_l = \mu(1-\mu)a_{l-2} + (1-\mu)a_{l-1} \qquad l \geqq 2. \tag{37}$$

The generating function $A(S)$ is defined as

$$A(S) = \sum_{l=0}^{\infty} a_l S^l \qquad -1 \leqq S \leqq 1.$$

Multiplying (37) by S^l and summing from $l = 2$ to infinity,

$$\sum_{l=2}^{\infty} a_l S^l = \mu(1-\mu)S^2 \sum_{l=2}^{\infty} a_{l-2}S^{l-2} + (1-\mu)S \sum_{l=2}^{\infty} a_{l-1}S^{l-1}. \tag{38}$$

Since $a_0 = a_1 = 1$, (38) can be written as

$$A(S) - S - 1 = \mu(1-\mu)S^2 A(S) + (1-\mu)S[A(S) - 1],$$

then

$$A(S) = \frac{1 + \mu S}{1 - (1 - \mu)S - \mu(1 - \mu)S^2}.$$

Therefore, each $P\{A_l\}$, $l \geqq 2$, can be obtained by the method indicated in Appendix B. Let $\mathbf{X}$ be the number of times the waiting timer is triggered in l measuring periods, given that the event A_l is true, then

$$P\{\mathbf{X} = j | A_l\} = \frac{P\{\mathbf{X} = j, A_l\}}{P\{A_l\}}. \tag{39}$$

Let $P\{\cdot|0\}$ denote the conditional probability assuming the counter does not overflow in the first measuring interval, and $P\{\cdot|1, 0\}$ denote the conditional probability assuming the counter overflows in the first but not the second interval. The numerator of (39) can be written as

$$\begin{aligned} P\{\mathbf{X} = j, A_l\} &= P\{\mathbf{X} = j, A_l|1\}P\{1\} + P\{\mathbf{X} = j, A_l|0\}P\{0\} \\ &= \mu P\{\mathbf{X} = j, A_l|1\} + (1 - \mu)P\{\mathbf{X} = j, A_l|0\}. \end{aligned} \tag{40}$$

However,

$$\begin{aligned} P\{\mathbf{X} = j, A_l|1\} &= P\{\mathbf{X} = j, A_l|1, 1\}P\{1|1\} \\ &\qquad + P\{\mathbf{X} = j, A_l|1, 0\}P\{0|1\} \\ &= 0 + (1 - \mu)P\{\mathbf{X} = j - 1, A_{l-2}\} \end{aligned} \tag{41}$$

$$P\{\mathbf{X} = j, A_l|0\} = P\{\mathbf{X} = j, A_{l-1}\}. \tag{42}$$

Insert (41) and (42) into (40); then,

$$\begin{aligned} P\{\mathbf{X} = j, A_l\} &= \mu(1 - \mu)P\{\mathbf{X} = j - 1, A_{l-2}\} \\ &\qquad + (1 - \mu)P\{\mathbf{X} = j, A_{l-1}\}. \end{aligned} \tag{43}$$

Let

$$p_{j,l} = P\{\mathbf{X} = j, A_l\}.$$

Equation (43) can be written as

$$p_{j,l} = \mu(1 - \mu)p_{j-1,l-2} + (1 - \mu)p_{j,l-1}.$$

Following the derivation of (38), we obtain

$$\begin{aligned} \sum_{j=1}^{\infty} \sum_{l=2}^{\infty} p_{j,l} S_1^j S_2^l &= \mu(1 - \mu)S_1 S_2^2 \sum_{j=1}^{\infty} \sum_{l=2}^{\infty} p_{j-1,l-2} S_1^{j-1} S_2^{l-2} \\ &\qquad + (1 - \mu)S_2 \sum_{j=1}^{\infty} \sum_{l=2}^{\infty} p_{j,l-1} S_1^j S_2^{l-1}. \end{aligned} \tag{44}$$

Define the bivariate generating function $A(S_1, S_2)$ as

$$A(S_1, S_2) = \sum_{j=0}^{\infty} \sum_{l=0}^{\infty} p_{j,l} S_1^j S_2^l.$$

Since

$$\begin{aligned} p_{j,l} &= 0 & j > l,\ j = 1, 2, \cdots \\ p_{0,l} &= (1-\mu)^l & l = 0, 1, 2, \cdots \\ p_{1,1} &= \mu, \end{aligned}$$

eq. (44) can be reduced to

$$\begin{aligned} A(S_1, S_2) - \frac{1}{1-(1-\mu)S_2} - \mu S_1 S_2 &= \mu(1-\mu)S_1S_2^2 A(S_1, S_2) \\ &\quad + (1-\mu)S_2\left[A(S_1, S_2) - \frac{1}{1-(1-\mu)S_2}\right]. \end{aligned}$$

Therefore,

$$A(S_1, S_2) = \frac{1 + \mu S_1 S_2}{1-(1-\mu)S_2 - \mu(1-\mu)S_1S_2^2}. \tag{45}$$

An iterative expression similar to that given in Appendix B can be obtained for the evaluation of $p_{j,l}$, and, hence, $P\{\mathbf{X} = j | A_l\}$ according to (39). Note that $P\{\mathbf{X} = j | A_l\} = 0$ for $j > l/2 + 1$.

An example is given below. When $\epsilon = \epsilon_0$, $\mu = \frac{1}{2}$, it was shown in (24) that on the average six measuring periods are required for the VMR to generate an alarm. During the last three periods (011), the waiting timer is triggered once. It is desirable to find the distribution of **X** in the first three periods. From (37) and (45),

$$\begin{aligned} P\{A_3\} &= 1 - 2\mu^2 + \mu^3 \\ p_{03} &= (1-\mu)^3 \\ p_{13} &= 3\mu(1-\mu)^2 \\ p_{23} &= \mu^2(1-\mu) \\ p_{33} &= 0 \\ E\{\mathbf{X}|A_3\} &= \sum_{i=0}^{3} i \times P\{\mathbf{X} = i | A_3\} \\ &= \frac{\mu(1-\mu)(3-\mu)}{1-2\mu^2+\mu^3}. \end{aligned}$$

At the threshold, $u = \frac{1}{2}$,

$$E\{\mathbf{X}|A_3\} = 1.$$

Thus, in the first three measuring intervals, the waiting timer is expected to be triggered once. In the last three intervals (011), the waiting timer is definitely triggered once. Hence, if the alarm occurs at the sixth measuring interval, then

$$E\{\mathbf{W}|\mathbf{M} = 6\} = 2. \tag{46}$$

Equation (46) says when $\epsilon = \epsilon_0$, the waiting timer shall be, on the average, triggered twice before an alarm is generated.

2.7 Statistics of alarm release and oscillation

To avoid oscillatory alarms near the error threshold, a release timer with duration $d > t_0$ is used to measure the violation rate when the VMR is in the alarm condition. The alarm is released only after the release timer times out and the counter does not overflow. Let ν be the probability of counter overflow during the measuring period d. From (12)

$$\nu \approx 1 - \Phi\left(\frac{n - \gamma d\epsilon}{\sqrt{\gamma d\epsilon(1 - \epsilon)}}\right).$$

Let $\mathbf{K}$ represent the number of measuring periods before the VMR stops alarming; i.e., the VMR will release the alarm at the $(\mathbf{K} + 1)$th period. Then,

$$\begin{aligned} h_k &= P\{\mathbf{K} = k\} \\ &= (1 - \nu)\nu^k \qquad k = 0, 1, 2, \cdots. \end{aligned} \tag{47}$$

Thus, $\mathbf{K}$ is governed by a geometric distribution with generating function

$$H(s) = \frac{1 - \nu}{1 - \nu S}. \tag{48}$$

The distribution of the alarm-release time $\mathbf{D}$ (assuming the error rate remains constant) will be derived first. Let $\mathbf{D}_i$ represent the time from the $(i - 1)$th to the ith counter overflow during the alarm state. The distribution of $\mathbf{D}_i$ is given by (29) and its generating function is

$$D_i(s) = \frac{\epsilon S^{1/\gamma}}{1 - (1 - \epsilon)S^{1/\gamma}}. \tag{49}$$

The alarm-release time is again given by a random sum

$$\mathbf{D} = \sum_{i=0}^{\mathbf{k}} \mathbf{D}_i + d, \tag{50}$$

where by definition, $\mathbf{D}_0 = 0$. Since $\mathbf{K}$ and the $\mathbf{D}_i$'s are independent, the generating function of $\mathbf{D}$ is

$$\begin{aligned} D(s) &= S^d \sum_{k=0}^{\infty} h_k \left(\frac{\epsilon S^{1/\gamma}}{1 - (1 - \epsilon)S^{1/\gamma}}\right)^{kn} \\ &= S^d H[D_i(S)]. \end{aligned} \tag{51}$$

The PDF of $\mathbf{D}$ is the compound distribution

$$f_{\mathbf{D}}(x) = \sum_{k=1}^{\infty} h_k \gamma \binom{\gamma(x - d) - 1}{kn - 1} \epsilon^{kn}(1 - \epsilon)^{\gamma(x-d)-kn}. \tag{52}$$

The mean and the variance of $\mathbf{D}$ are

$$\eta_d = \frac{\nu}{1 - \nu} \times \frac{n}{\epsilon\gamma} + d \tag{53}$$

$$\sigma_d^2 = \frac{\nu}{1 - \nu} \times \frac{n}{\epsilon^2\gamma^2} \times \left(\frac{n}{1 - \nu} + 1 - \epsilon\right). \tag{54}$$

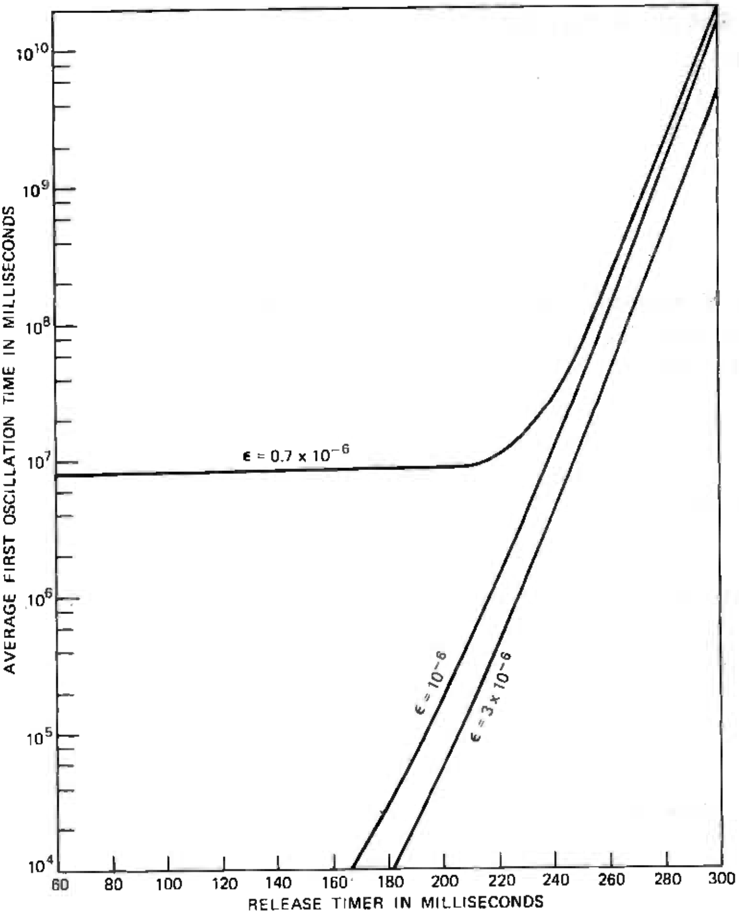

Fig. 4—Average first-oscillation time vs duration of release timer.

The first oscillation time $\mathbf{T}_a$, i.e., the time it takes for an alarming VMR to release and then generate another alarm, assuming the error rate remains constant, is

$$\mathbf{T}_a = \mathbf{D} + \mathbf{T}_0. \tag{55}$$

Its PDF is simply the convolution

$$f_{\mathbf{T}_a}(t) = f_{\mathbf{D}}(t) * f_{\mathbf{T}_0}(t).$$

The mean and the variance of $\mathbf{T}_a$ are

$$\eta_{t_a} = \eta_d + \eta_{t_0}. \tag{56}$$

$$\sigma_{t_a}^2 = \sigma_d^2 + \sigma_{t_0}^2. \tag{57}$$

Equation (56) is employed to plot Fig. 4 which shows the expected first oscillation time versus the duration of the release timer d with the error rate as the parameter. When $\epsilon = 10^{-6}$, if $d = 330$ ms, alarm oscillation is expected to occur once in 187 years; if $d = 1$ second, alarm oscillation is extremely unlikely to occur.

The time from an initial alarm state to the ith alarm oscillation is $i \times \mathbf{T}_a$, whose distribution can be easily obtained from that of $\mathbf{T}_a$.

2.8 Pseudorandom signal switching statistics

As described in 2.1, after the pseudorandom signal is switched in, if the VMR is back in-frame, immediately the violation counter is reset and starts counting again until the free-running release timer of duration d times out. Since the in-frame condition can occur anytime within the interval 0 to d, the time spent to count the violations is uniformly distributed between 0 and d. When the release timer times out, the number of violations counted is a mixture distribution obtained through randomization[5] of the parameter t in (30)

$$P\{\mathbf{N} = n \,|\, \boldsymbol{\varepsilon} = \epsilon\} = \int_0^d \frac{e^{-\gamma\epsilon t}(\gamma\epsilon t)^n}{n!} \times \frac{1}{d}\, dt$$
$$= \frac{1}{\gamma\epsilon d}\left(1 - e^{-\gamma\epsilon d} \sum_{i=0}^{n} \frac{(\gamma\epsilon d)^i}{i!}\right). \tag{58}$$

The PDF $f_\varepsilon(\epsilon)$ of the error rate $\boldsymbol{\varepsilon}$ is usually unknown. If $f_\varepsilon(\epsilon)$ is given or can be estimated empirically, (58) can be randomized by $f_\varepsilon(\epsilon)$.

$$P\{\mathbf{N} = n\} = \int_0^{\cdot} P\{\mathbf{N} = n \,|\, \boldsymbol{\varepsilon} = \epsilon\} f_\varepsilon(\epsilon) d\epsilon, \tag{59}$$

where the upper integration limit is determined by the domain of ϵ. From (59), the probability $P\{\mathbf{N} < n\}$ that the counter does not overflow, i.e., the pseudorandom signal will be switched out, can be evaluated.

2.9 Generalizations

All the above derivations are general enough so that if one requires the counter to overflow consecutively more than twice (with the waiting timer triggered each time the counter overflows) before an alarm is generated, the results can be easily extended. For example, if the VMR generates an alarm after k consecutive counter overflows, then (24) becomes

$$E\{\mathbf{M}\} = \frac{1 - \mu^k}{(1 - \mu)\mu^k},$$

and the probability coefficients are

$$\begin{aligned} p_m &= 0 \qquad m = 0, 1, \cdots, k-1 \\ p_k &= \mu^k \\ p_{k+1} = p_{k+2} &= \cdots = p_{2k} = (1-\mu)\mu^k \\ p_m &> p_{m+1} \qquad m \geqq 2k+1 \end{aligned}$$

III. DISCUSSION

As discussed in the introduction, one of the main functions of the VMR is to generate alarms when it detects that the line performance is below a predetermined objective. However, the digital line performance objective is usually set in terms of a threshold bit-error rate which cannot be directly measured in service. Equation (8) establishes the relationship between the bit-error rate and the parity-violation rate for a digital line employing parity-checking digits. Figure 1 shows that for the parity-check structure used in the T4M system and for bit-error rates below 10^{-3}, there is almost a one-to-one correspondence between a bit error and a parity violation. This implies that the parity-checking scheme is effective in determining digital transmission line performance.

When the T4M VMR parity violations exceed a specified threshold in two consecutive measuring intervals, an alarm is generated. This is normally followed by an automatic transfer of the failed line to a spare line if the latter is available. In general, each spare line will protect several service lines to reduce system cost. Thus, a so-called "hard" alarm threshold, which clearly distinguishes between error rates slightly above and below the threshold, is desirable because it is unlikely to cause an alarm at error rates below the threshold. In this case, the spare line will be available to protect more serious failures on other service lines. It also takes less time for a VMR with a hard threshold to generate alarms when the error rates are above the threshold. Equation (14) gives the probability of the parity-violation counter overflow as a function of the error rate and the duration of the measuring interval. Figure 2 is a plot of (14) and exhibits the desirable hard threshold characteristics. As the error rate varies from 0.6×10^{-6} to 2×10^{-6}, the probability of counter overflow changes from 0.0001 to 0.999.

When a catastrophic failure occurs on a line, its VMR should generate an alarm as soon as possible so that an automatic transfer to a spare line can take place without trunk disconnection. When an error rate just above the threshold is detected, little harm will be done if the VMR takes longer to announce an alarm. Equation (35) obtains the mean alarm time as a function of the error rate. From Fig. 3 it can be seen that the mean alarm time of the T4M VMR reduces very fast with increasing error rates. Note that if an error rate of 0.7×10^{-6} (slightly below the threshold) persists for hours, eventually an alarm will be generated because the alarm threshold is not infinitely hard.

The amount of hysteresis required in releasing an alarm is an important part of VMR design. The release timer should be long enough so that oscillation between alarm request and alarm release is unlikely to occur. It should also be short enough so that alarms are not unnecessarily prolonged. Equation (56) gives the expected oscillation time as a sum of the mean alarm time and the mean release time, both of which are functions of the error rate and the length of the release timer. Figure 4 shows that when the duration of the release timer is greater than three times that of the parity-violation measuring interval, alarm oscillation is not likely to occur at any constant error rates. This is due to the fact that the mean alarm time is large for error rates below the alarm threshold while the mean release time is long for error rates above the alarm threshold.

APPENDIX A

The T1 Outstate (1.544 Mb/s) VMR counts 16 bipolar violations (violations occurring within a 0.3-ms interval are counted only once) in 85 ms to generate an alarm. The T2 (6.312 Mb/s) VMR generates a low-error alarm if it counts 32 bipolar violations in 5 seconds (violations occurring within a 3.2-μs interval are counted only once). Since the error rates of interest are near the threshold, it can be assumed that no two violations occur "close" to each other. The 3A-RDS (44.736 Mb/s) VMR generates an alarm if it counts 31 parity violations in 2 seconds. These alarm rules are simpler than that for the T4M VMR, hence, the alarm statistics of these VMRs are also easier to derive. For the VMR of each system, a probability of counter overflow μ can be derived as in (14). This probability is also the probability of alarm. The three alarm rules have identical mathematical models; hence, no separate discussions are necessary.

Let $\mathbf{M}$ represent the number of elapsed measuring periods before the VMR generates an alarm; i.e., the VMR will generate an alarm at the $(\mathbf{M} + 1)$th period. Then,

$$\begin{aligned} p_m &= P\{\mathbf{M} = m\} \\ &= \mu(1 - \mu)^m \qquad m = 0, 1, 2, \cdots. \end{aligned}$$

$\mathbf{M}$ is governed by a geometric distribution. Most other statistics discussed in Section II can be derived similarly.

Because of the simplicity of the geometric distribution, given a probability of alarm p, the number of elapsed periods k before the probability p is reached can be obtained explicitly,

$$
\begin{aligned}
p &\leqq \sum_{m=0}^{k} p_m \\
&= \sum_{m=0}^{k} \mu(1-\mu)^m \\
&= 1-(1-\mu)^{k+1}.
\end{aligned}
$$

Therefore,

$$k \leqq \frac{ln(1-p)}{ln(1-\mu)} - 1.$$

In each of the first k measuring intervals, the counter will not overflow when the measuring timer times out. Thus, the total alarm probability as a function of elapsed time can be plotted easily as opposed to evaluating (36) for the T4M VMR.

APPENDIX B

This appendix derives an iterative expression to calculate the probability coefficients p_i's discussed in Section 2.3. Specifically, given that

$$P(S) = \sum_{i=0}^{\infty} p_i S^i \tag{60}$$

and

$$P(S) = \frac{\sum_{j=0}^{m} a_j S^j}{1 + \sum_{i=1}^{n} b_i S^i} \tag{61}$$

it is desired to obtain the p_i's in terms of the a_i's and the b_i's. Let the denominator of (61) be expanded as follows

$$\frac{1}{1 + \sum_{i=0}^{n} b_i S^i} = \sum_{i=0}^{\infty} C_i S^i.$$

C_i, $i = 0, \cdots, n-1$, can be determined through long division or by comparing the coefficients of the S^i's in

$$1 = \left(1 + \sum_{i=1}^{n} b_i S^i\right)\left(\sum_{i=0}^{\infty} C_i S^i\right).$$

For $i \geqq n$,

$$C_i = -\sum_{k=1}^{n} b_k C_{i-k}.$$

Therefore

$$P(S) = \sum_{j=0}^{m} a_j S^j \times \sum_{i=0}^{\infty} C_i S^i. \tag{62}$$

Compare (60) and (62), p_i, $i = 0, 1, \cdots, m-1$ can be determined easily. For $i \geqq m$

$$\begin{aligned} p_i &= \sum_{h=0}^{m} a_h C_{i-h} \\ &= \sum_{h=0}^{m} a_h \left[- \sum_{k=1}^{n} b_k C_{i-h-k} \right] \\ &= - \sum_{h=0}^{m} \sum_{k=1}^{n} a_h b_k C_{i-h-k}. \end{aligned}$$

p_i can be calculated by computer without knowing p_{i-1}, p_{i-2}, etc.

REFERENCES

1. *Transmission Systems for Communications*, Technical Staff of Bell Telephone Laboratories, 4th ed., Winston-Salem, N. C.: Western Electric Company, 1970.
2. M. A. Rich and J. M. Trecker, "The T4M Digital Line Termination," ICC 75 Conf. Record, San Francisco, June 16–18, 1975.
3. H. I. Maunsell, R. B. Robrock, and C. A. von Roesgen, "The M13 and M34 Digital Multiplexers," ICC 75 Conf. Record, San Francisco, June 16–18, 1975.
4. W. Feller, *An Introduction to Probability Theory and Its Applications*, 3rd ed., Vol. I, Wiley, 1968.
5. W. Feller, *An Introduction to Probability Theory and Its Applications*, 2nd ed., Vol. II, Wiley, 1971.

Contributors to This Issue

Allen H. Cherin, B.E.E., 1961, City College of New York; M.S.E.E., 1965, University of Vermont; Ph.D. (E.E.), 1971, University of Pennsylvania; Bell Laboratories, 1965—. Mr. Cherin is engaged in studies associated with the characterization, splicing, and packaging of optical fibers. Member, IEEE, OSA.

Ronald E. Crochiere, B.S. (E.E.), 1967, Milwaukee School of Engineering; M.S. (E.E.), 1968, and Ph.D. (E.E.), 1974, Massachusetts Institute of Technology; Raytheon, 1968–1970; M.I.T. Research Laboratory of Electronics, 1970–1974; Bell Laboratories, 1974—. Mr. Crochiere has worked on the design of microwave phase shifters, on digital network theory, and digital filter structures. He is presently engaged in research in speech communications and digital signal processing. Associate editor, IEEE G-ASSP Transactions. Member, Sigma Xi and IEEE G-ASSP Technical Committee on Digital Signal Processing.

G. S. Fang, B.S.E.E. 1967, National Taiwan University; PhD, 1971, Princeton University; Computer Sciences Corporation 1971–72; Bell Laboratories, 1972—. At Bell Laboratories, Mr. Fang has worked on high-speed digital transmission, protection switching, and microprocessor applications.

James L. Flanagan, Sc.D. (E.E.), 1955, Massachusetts Institute of Technology; Bell Laboratories, 1957—. Mr. Flanagan has worked in voice communications, acoustics, and digital techniques for signal coding and transmission. He is Head, Acoustics Research Department. Fellow, IEEE; Fellow, Acoustical Society of America; Board of Governors, American Institute of Physics; member, Sigma Xi; Tau Beta Pi.

Franz T. Geyling, B.S., 1950, M.S., 1951, and Ph.D., 1954, Stanford University; Bell Laboratories, 1954—. Mr. Geyling has engaged in solid mechanics research and experimental stress analysis. From 1959 to 1970 he specialized in orbital mechanics and was responsible for tracking and control studies of missiles, satellites and spacecraft. He also contributed to the structural analysis of ground antennas and suspended underwater arrays. Since 1971, he has been engaged in continuum physics as applied to materials research. He is coauthor of a book and has served as associate editor of the SIAM and AIAA Journals, as well as chairman of the AIAA Astrodynamics Specialist Committee. Associate Fellow, AIAA; Member, APS, Rheol. Soc., ASME, SIAM, Phi Beta Kappa, Tau Beta Pi, Sigma Xi.

David J. Goodman, B.E.E., 1960, Rensselaer Polytechnic Institute; M.E.E., 1962, New York University; Ph.D. (E.E.), 1967, Imperial College, London; Bell Laboratories, 1967—. Mr. Goodman has studied various aspects of digital communications, including analog-to-digital conversion, digital signal processing, assessment of the quality of digitally coded speech, and error mechanisms in digital transmission lines. In 1974 and 1975, he was a Senior Research Fellow at Imperial College, London, England. Member, IEEE.

Sing-Hsiung Lin, B.S.E.E., 1963, National Taiwan University; M.S.E.E., 1966, and Ph.D., 1969, University of California, Berkeley; Bell Laboratories, 1969—. At the Electronics Research Laboratory, University of California at Berkeley, Mr. Lin engaged in research on antennas in plasma media and numerical solutions of antenna problems. At Bell Laboratories, Mr. Lin is working on wave propagation problems on terrestrial radio systems and earth-satellite radio systems. Member, IEEE, Sigma Xi, AIAA.

Barbara J. McDermott, B.A. (Psychology), 1949, University of Michigan; M.A. (Psychology), 1963, Columbia University; Bell Laboratories, 1959—. Ms. McDermott has worked on speech quality evaluation and multidimensional scaling analysis. Member, Acoustical Society of America.

Lloyd H. Nakatani, B.A. (Mathematics), 1964, Ph.D. (Psychology), 1968, University of California; Bell Laboratories, 1968—. Mr. Nakatani has worked on speech quality evaluation and on speech perception and synthesis research. Member, Acoustical Society of America.

Philip J. Rich, B.S., 1972, University of Illinois, M.S. (Physics), 1974, Georgia Institute of Technology; Bell Laboratories, 1974—. Mr. Rich is currently engaged in studies related to the characterization and splicing of optical fibers.

B. W. Stuck, S.B.E.E., S.M.E.E., 1969, Sc.D., 1972, Massachusetts Institute of Technology; Bell Laboratories, 1972—. Mr. Stuck has worked on problems in applied probability theory and mathematical physics. He is presently concerned with modeling and performance analysis of large digital systems. Member, SIAM, MAA, IEEE.

Susan A. Webber, B.A. (Mathematics), 1972, Vassar College; Bell Laboratories, 1973—. Miss Webber is engaged in scientific programming for laboratory computer systems dedicated to speech research.

Abstracts of Papers by Bell System Authors Published in Other Journals

CHEMISTRY

The Anodic Behavior of Gold in Sulfuric Acid Solutions Effect of Chloride and Electrode Potential. R. P. Frankenthal and D. E. Thompson, J. Electrochem. Soc., *123* (June 1976), pp. 799–804. Gold corrosion in the passive and transpassive potential regions is affected by Cl^-. Soluble Au(III) and $Au(OH)_3$ film are the reaction products. Chloride promotes dissolution and restricts film formation. Mechanism of O_2-evolution is different on a filmed than on a film-free surface.

Brillouin Scattering from Polymer Films. G. D. Patterson, J. Polym. Sci., Part A-2, Polym. Phys., *14* (1976), pp. 143–149. Many polymers cannot be prepared as clear amorphous blocks suitable for classical light-scattering studies. However, most linear polymers can be prepared as films which are somewhat transparent. With the advent of high-contrast multipass interferometers, these films can now be studied by Brillouin scattering. This work demonstrates the wide range of polymeric materials that can now be studied by Brillouin spectroscopy.

Direct Measurement of Spontaneous Predissociation Using Coaxial Laser-Molecular Beams. R. M. Lum and K. B. McAfee, Jr., J. Chem. Phys., *63*, No. 11 (December 1975), pp. 5029–5033. A laser-molecular beam technique has been devised to enable direct observation of radiationless transitions of isolated single molecular states. Spontaneous predissociation, detected as a modulation of the molecular beam, has been observed in Br_2 at laser wavelengths which produce selective excitation of the individual Br_2 isotopic species.

Neutron Scattering Study at High Pressure of the Structural Phase Transition in Paratellurite. D. B. McWhan, R. J. Birgeneau, W. A. Bonner, H. Taub,* and J. D. Axe,* J. of Phys. C. Lett, *8* (1975), pp. L81–L85. The dispersion relation for the transverse acoustic phonon mode propagating along $\langle 110 \rangle$ polarized along $\langle 1\bar{1}0 \rangle$ in TeO_2 has been measured at $P = 1$ atm, P_c (≈ 9.0 kbar), and $2P_c$ where P_c is the tetragonal-to-orthorhombic structural transition pressure. Measurements of the order parameter are consistent with a mean field theory of a pressure induced elastic instability. *Brookhaven National Laboratory.

COMPUTING

Integrated Injection Logic: A Bipolar LSI Technique. R. A. Pedersen, Computer, *9*, No. 2 (February 1976), pp. 24–29. Integrated Injection Logic (I^2L) is a novel bipolar circuit design approach to achieve high-density large-scale integration. As the basic logic unit, it uses multicollector npn transistors which are powered from merged multicollector lateral pnp transistors. I^2L can be fabricated with standard buried collector technology and is therefore compatible with conventional bipolar circuitry—digital or linear—on the same silicon chip.

ELECTRICAL AND ELECTRONIC ENGINEERING

Behavior of Tandem Buffers with Geometric Input and Markovian Output. J. Hsu and P. J. Burke, IEEE Trans. Commun., *COM-24* (March 1976), pp. 358–361. A discrete-time system of infinite-capacity buffers in tandem is studied. Input to the first buffer is geometric and the output for all but the last buffer (which can be arbitrary) is Markovian. The analysis shows that, in equilibrium, each buffer can be analyzed separately and independently.

Chemisorption and Schottky Barrier Formation of Ga on Si(111)7 × 7. G. Margaritondo, S. B. Christman, and J. E. Rowe, J. Vacuum Sci. Technol., *13* (January–February 1976), pp. 329–332. The chemisorption of gallium atoms on Si(111)7 × 7 was studied using photoemission, electron-energy-loss, LEED and Auger spectroscopy. Most of the states formed at the metal-semiconductor interface are due to the first 1–2 metal monolayers and need a microscopic-atomic bonding or surface-band-structure theoretical description.

A Comparison of Chemical Etches for Revealing (100) Silicon Crystal Defects. D. G. Schimmel, J. Electrochem. Soc., *123*, No. 5 (May 1976), pp. 734–741. Etch pit results of the Sirtl, Dash, Secco, and an experimental etch are compared for ⟨100⟩ silicon wafers after various device processing steps. Factors influencing etch-pit formation on silicon surfaces are discussed. A recommendation is given for the etch formation with the best etch-pit development.

Fabrication and Performance of Offset-Mask Charge-Coupled Devices. A.M. Mohsen and T. F. Retajczyk, Jr., IEEE J. Solid State Circuits, *SC-11* (February 1976), pp. 180–188. The use of the offset-mask technique to fabricate two-phase and uniphase charge-coupled device (CCD) electrode structures is described. A new two-phase electrode structure with polysilicon-electrodes and self-aligned gates for the peripheral circuits has been developed. The polysilicon offset-mask electrode structure is very attractive for charge-coupled memories. Compared to other two-polysilicon level CCD structures, it has a higher packing density, is more tolerant to intralevel shorts, and does not require large numbers of small contact windows to connect the gate electrodes to the phase bus lines.

High Repetition-Rate and Quasi-CW Operation of a Waveguide CO_2 TE Laser. P. W. Smith, C. R. Adams, P. J. Maloney, and O. R. Wood II, Opt. Commun., *16*, No. 1 (January 1976), pp. 50–53. We report operation of a waveguide CO_2 TE laser at excitation pulse repetition frequencies as high as 40 kHz. Quasi-continuous laser output was obtained yielding an average output power of 1.5 W from an active volume of 0.1 cc. Details of laser construction and excitation circuitry are given.

Hydrogen Embrittlement of Electroless Copper Deposits. Y. Okinaka and S. Nakahara, J. Electrochem. Soc., *123* (1976), pp. 475–478. Electroless copper deposits were investigated for ductility, impurity content, void distribution, and fracture surface morphology. It is concluded that the brittleness of electroless copper deposits is due to the internal hydrogen embrittlement rather than the incorporation of cuprous oxide or morphological effects.

Multicomponent Photopolymer Systems for Volume Phase Holograms and Grating Devices. W. J. Tomlinson, E. A. Chandross, H. P. Weber, and G. D. Aumiller, Appl. Opt., *15*, No. 2 (February 1976), pp. 534–541. Novel photopolymer systems for the fabrication of high-resolution volume phase holograms and gratings devices are reported. We use a mixture of components chosen to have differing reactivities and polarizabilities. The image-forming exposure results, ultimately, in a modulated chemical composition. Peak-to-peak refractive index differentials of up to 1.5 percent were achieved.

Multipoint Private Line Access Delays Under Several Interstation Disciplines. C. D. Pack and B. A. Whitaker, IEEE Trans. Commun., *COM-24* (March 1976), pp. 339–348. Performance objectives for some types of computer-communications networks are stated in terms of access-delay statistics which measure the grade of service experienced by stations bidding for access to a multipoint private line (MPL). Using simulation and some analysis, we examine the access delay statistics for an MPL under each of four service disciplines.

Observations on the Influence of Processing Steps on the Magnetic Hysteresis Parameters of a Co/Fe/Nb Alloy. M. R. Pinnel, IEEE Trans. Magn., *MAG-12* (May 1976), pp. 236–243. The variation of both magnetic and mechanical properties and microstructure of a Co/Fe/Nb alloy (Nibcolloy) with changes in processing has been characterized. Results indicate the use of a softening anneal prior to the final aging anneal can alter magnetic properties. A nonstability of coercivity to subsequent brief elevated temperature exposures of around 1000°C was also observed.

Profile Parameters of Implanted-Diffused Arsenic Layers in Silicon. R. B. Fair and J. C. C. Tsai, J. Electrochem. Soc., *123* (April 1976), pp. 583–586. Equations have been derived that describe the important variables that are required to characterize the diffusion of As-implanted layers for the surface doping concentration range $C_{TO} \gtrsim 1 \times 10^{19}$ cm^{-3}. In addition, data obtained from differential conductivity profile measurements and SIMS profile measurements have been used to obtain experimental parameters for these equations.

Qualitative Observations on the Diffusion of Copper and Gold Through a Nickel Barrier. M. R. Pinnel and J. E. Bennett, Met. Trans., *7A* (May 1976), pp. 629–635. The interdiffusion behavior in planar-layered couples of Cu/Ni/Au at temperatures between 150 and 750°C have been characterized. Results demonstrate that the nickel barrier layer retards but does not block the transport of copper to the gold surface. Possible mechanisms for the anomalous buildup of copper at the gold/nickel interface and gold at the copper/nickel interface are discussed.

Signaling and Switching As We Enter the Second Century. J. S. Ryan, Telecommun. J., *43*, No. 111 (March 1976), pp. 206–219. During the first century of the telephone, switching evolved from the 21-line New Haven switchboard to the 104,000-trunk No. 4 ESS, and signaling from voice alerting to CCIS. This centennial issue article traces the history and reviews the status of signaling and switching as we enter the second century.

A Study of Deep Levels in GaAs by Capacitance Spectroscopy. D. V. Lang and R. A. Logan, J. Electron. Mater., *4*, No. 5 (1975), pp. 1053–1066. We show how the DLTS capacitance spectroscopy technique can be used to detect small amounts of deep-level impurities in GaAs p-n junctions. The DLTS spectra associated with Cu, Fe, Cr, O, and two unidentified, but commonly occurring, deep levels in GaAs are shown. The LPE distribution coefficients are obtained for Cu, Fe, and Cr. The carrier capture cross sections for six levels are measured and give evidence for capture by multiphonon emission.

MATERIALS SCIENCE

Detection of Catalytic Oscillations by Differential Thermal Analysis. P. K. Gallagher and D. W. Johnson, Jr., Thermochim. Acta, *15* (May 1976), pp. 238–240. Oscillations in DTA curves associated with the oxidation of CO using Pt containing catalysts were observed. This offers a relatively quick and simple technique for studying instabilities that arise from the interaction of the catalytic mechanism and the exothermic nature of the reaction.

Kinetics of Formation of $LiFeO_2$ from $2Li_2CO_3 \cdot Fe_2O_3$ Mixture. P. K. Gallagher and D. W. Johnson, Jr., J. Amer. Ceram. Soc., *59* (March–April 1976), pp. 171–172. Mixtures of $2Li_2CO_3 \cdot Fe_2O_3$ were found to form $LiFeO_2$ at <600°C. Excess Li_2CO_3 did not react until higher temperatures. Isothermal and dynamic kinetic studies gave an activation energy of 42–50 kcal/mole. A model involving the rapid surface diffusion of Li_2CO_3 is proposed.

Diffusion Kinetics of Au Through Pt Films About 2000 and 6000 Å Thick Studied with Auger Spectrscopy. C. C. Chang and G. Quintana, Thin Solid Films, *31* (1976), pp. 265–273. Pt–Au couples with 2000 Å and 6000 Å Pt films were heat treated between 250° and 350°C in 1 atm N_2. Au was found to diffuse initially through Pt films <6000 Å by grain boundary migration and more than 10^{15} atoms cm^{-2} of Au crossed the Pt when the bulk of the Pt contained little Au ($\lesssim 1$ at.%). For 2250 Å Pt on Au, the time for half-saturation of the Pt surface with Au was $t(0.5) = 1.2 \times 10^{-7} \times \exp(0.96\ eV/kT)$ min.

Domain Wall Image Contrast in the SEM. D. C. Joy, H. J. Leamy, S. D. Ferris, D. E. Newberry,* and H. Yakowitz,* Appl. Phys. Lett., *28* (April 15, 1976), pp. 466–468. Contrast from domain walls in materials with cubic magnetic anisotropy has been observed in scanning electron microscope images. This contrast, which is visible in both the backscattered and absorbed current images, arises from the interaction of the convergent incident electron beam with the domains on either side of the wall. * National Bureau of Standards.

Ultranarrow, Forbidden, Singlet-Triplet Anticrossings in H_2. T. A. Miller and R. S. Freund, J. Chem. Phys., *63* (1975), pp. 256–263. Forbidden singlet-triplet anticrossings have been observed between different Zeeman sublevels of the i (3d) $^3\Pi_g$, $v = 1$, $N = 6$ and W(?) $^1\Sigma_g^+$, $v = 1$, $N = 4$ states of H_2. The anticrossings are quite sharp and hence allow accurate determinations of the states' zero field separation, linear and quadratic Zeeman parameters, coupling perturbation, and radiative lifetimes.

PHYSICS

The Determination of Energy-Level Shifts Which Accompany Chemisorption. Homer D. Hagstrum, Surface Sci., *54* (1976), pp. 197–209. This paper discusses the ionization limit with respect to which the electronic energy levels of an adsorbed complex on a solid surface should be referenced, and how this limit is defined and measured. This leads to a reasonable procedure for determining energy-level shifts, at least for simple systems.

The Linear Electric Field Effect for Low Spin Ferric Heme Compounds. W. B. Mims and J. Peisach*, J. Chem. Phys., *64*, No. 3 (February 1, 1976), pp. 1074–1091. Measurements were made on the linear electric field induced g shifts for a series of low-spin ferric heme compounds by the electron spin echo method on noncrystalline samples at liquid helium temperatures. Some of these samples consisted of proteins and protein derivatives; others were made from heme reacted with small ligand molecules. Analytic expressions relating the observed changes in spin echo amplitude to certain of the g^2-shift coefficients B_{ij} were derived. Results suggest the presence of extensive back bonding between the Fe^{3+} ion and the axial ligands of the heme complex. Results also suggest that myoglobin hydroxide is characterized by a crystal field which is exceptionally low for the $S = (1/2)$ ferric heme group of compounds.

* Departments of Pharmacology and Molecular Biology, Albert Einstein College of Medicine of Yeshiva University.

Elastic Constants of bcc ^{4}He. D. S. Greywall, Phys. Rev. B (Nucl. Phys.), *13* (February 1976), pp. 1056–1068. Longitudinal and transverse sound velocities were measured in single crystals of bcc ^{4}He with known orientation at 21.00 cm^3/mole and at 1.612 K. The temperature dependence of sound velocities along an isochore and along the melting curve was measured for several samples. No premelting effects were observed. The ratios of bcc ^{3}He to ^{4}He elastic moduli at the same molar volume are considerably larger than the classical ratio of unity but in excellent agreement with the quantum-mechanical calculations of Horner. Existing calorimetric data are compared with the present determination of the Debye temperature.

Isotope Abundances in Interstellar Molecular Clouds. P. G. Wannier, A. A. Penzias, R. A. Linke, and R. W. Wilson, Astrophys. J., *204*, No. 1 (February 15, 1976), pp. 26–42. We use the $J = 1 \rightarrow J = 0$ transitions of $^{12}C^{16}O$, $^{13}C^{16}O$, and $^{12}C^{18}O$ at $\approx$ 110 GHz to measure abundance ratios of carbon and oxygen isotopes throughout our galaxy. The measured values of $[^{12}C]/[^{13}C]$ seem to be different than the terrestrial values, suggesting significant galactic chemical evaluation since the birth of the sun.